BuMines OFR 184-82

PB83-136359

A minerals research contract report
November 1981

THE EFFECTS OF MOISTURE ON RADON EMANATION

INCLUDING THE EFFECTS ON DIFFUSION

Bureau of Mines Open File Report 184-82

Contract H0292024

Ford, Bacon & Davis Utah

BUREAU OF MINES ★ UNITED STATES DEPARTMENT OF THE INTERIOR

Minerals Health and Safety Technology

50272-101

REPORT DOCUMENTATION PAGE	1. REPORT NO. BuMines OFR 184-82	2.	3. Recipient's Accession No. PB83 136358

4. Title and Subtitle
The Effects of Moisture on Radon Emanation. Including the Effects on Diffusion

5. Report Date
November 1981

6.

7. Author(s)
Burton J. Thamer, Kirk K. Nielson, and Karen Felthauser

8. Performing Organization Rept. No.

9. Performing Organization Name and Address
Ford, Bacon & Davis Utah
375 Chipeta Way
Salt Lake City, UT 84108

Rogers and Associates Engineering Corp.
P.O. Box 330
Salt Lake City, UT 84110

10. Project/Task/Work Unit No.

11. Contract(C) or Grant(G) No.
(C) H0292024
(G)

12. Sponsoring Organization Name and Address
Office of Assistant Director--Minerals Health and Safety Technology
Bureau of Mines
U.S. Department of the Interior
Washington, DC 20241

13. Type of Report & Period Covered
Contract research, 10/79--11/81

14.

15. Supplementary Notes
Approved by the Director, Bureau of Mines, for placement on open file, November 2, 1982.

16. Abstract (Limit: 200 words)

Radon emanation coefficients of 0.02 to 0.55 were measured at moisture contents ranging from dry to saturation in 18 different ores. The emanation coefficients rose from a minimum when dry to a plateau usually starting at 5 to 20 percent of saturation. A model, using measured pore-size distributions, suggested that the radium mineralization may be confined to annular layers about 0.02 micrometers thick around pores. Radon's diffusion coefficient was determined as a function of moisture. The techniques involved comparing a disk's exhalation as a function of time whether or not the disk had a distributed source. The model was free of approximations and included the effects of porosity and adsorption. An increase of diffusion coefficient with moisture for one or two ores was explained in terms of a model's equation for the diffusion coefficient in terms of both volume and surface diffusion. Radon's adsorption coefficient was determined on a uranium ore.

17. Document Analysis a. Descriptors

Mining

Radon	Radioactive wastes	Gases
Uranium ores	Diffusion	Mine ventilation
Mineral deposits	Adsorption	Mining engineering

b. Identifiers/Open-Ended Terms
Radon emanantion coefficients
Radon diffusion
Uranium mining
Radioactive waste disposal

c. COSATI Field/Group 08I, 18F, 18H

18. Availability Statement	19. Security Class (This Report)	21. No. of Pages
Release unlimited by NTIS.		213
	20. Security Class (This Page)	22. Price

(See ANSI-Z39.18) See Instructions on Reverse OPTIONAL FORM 272 (4-77) (Formerly NTIS-35) Department of Commerce

The views and conclusions contained in this document are those of the authors and should not be interpreted as necessarily representing the official policies or recommendations of the Interior Department's Bureau of Mines or of the U.S. Government.

FOREWORD

This report was prepared by Ford, Bacon & Davis Utah, Inc., Salt Lake City, Utah, under USBM Contract number HO292024 . The contract was initiated under the Minerals Health and Safety Technology Program. It was administered under the technical direction of the Spokane Research Center with Robert C. Bates acting as Technical Project Officer. David J. Askin was the contract administrator for the Bureau of Mines. This report is a summary of the work recently completed as a part of this contract during the period October 1979 to November 1981. This report was submitted by the authors in November 1981.

The authors express their gratitude for the contributions of Robert F. Overmyer, Vern C. Rogers*, Emerson Cannon, Mary Lou Mauch*, and Craig M. Jensen*. The personnel of Rogers and Associates Engineering Corporation* were principally responsible for the material of Chapters 3 and 5.

The authors are indebted to the management of numerous mines for the samples of ore.

There are no patentable features in this report.

*Rogers and Associates Engineering Corporation, Salt Lake City, Utah

CONTENTS

FIGURES

TABLES

CHAPTER 1

INTRODUCTION

A groundwork for the studies reported here was laid in a 1980 survey of the world's literature on radon emanation and diffusion. The survey was directed principally toward the effects of moisture which is the subject of this report. The more important papers were ranked according to relevancy, there being sixty-three such on emanation and forty-six on diffusion. Another twenty-two articles also were reviewed or abstracted, but had insufficient relevancy to be ranked. The observations were frequently qualitative with respect to geological materials. However, the survey suggested that moisture increased emanation up to a point by stopping recoiling radon atoms within the pore rather than in the wall of the pore. Radon's flux from a material depends strongly on its diffusion therein. Moisture had been observed to depress the flux, but few quantitative studies had been made.

The present work is detailed in later chapters. Emanation coefficients were measured on both moist and dry-sample aliquots as planned, and on lump samples to assess the effects of sample crushing. However, due to restrictions of time and budget, at least 4 of the planned 11 moisture fractions for 9 of the 18 ore samples were omitted. The samples analyzed covered the same range, however, and provided an adequate basis for data interpretation and modeling. The de-emanation and drying procedure was also extended over a longer time period to permit complete drying of samples. Moisture uptake in the dried samples was considered due to its possible effect on the emanation coefficients.

The experimental work in diffusion required special attention to prevent leakage and diffusion in directions other than the direction to be investigated. Some samples had too little radium to be studied without using an artificial source. Equations were developed to aid in correlating observed diffusion coefficients in terms of its components, volume diffusion and surface diffusion.

Organization of the Report

This introductory chapter relates this work to the previous literature search and other on-going research. Chapter 2 describes the geology and mineralogy of the ore areas as well as the physical and radiological properties of the ores. Chapter 3 presents the observed effects of moisture on radon's emanation and Chapter 5 discusses the results. Chapter 4 describes and discusses the effects of moisture on radon's diffusion. Chapter 6 briefly summarizes the most significant

accomplishments of this work. Appendix A contains the pore-size distribution for the ores, this data being relevant to Chapters 3 and 5. Appendices B-G are computer programs used in Chapter 4 and Appendix H is one for Chapter 5.

CHAPTER 2

THE GEOLOGY, MINERALOGY AND OTHER PHYSICAL PROPERTIES OF THE URANIUM ORES

In order to perform the experimental work of this study, a selection of typical uranium ores was collected from operating mines in the United States and Canada. The purpose of this chapter is to describe these ores in terms of their locations, geology and mineralogy (Table 2-1) and other physical characteristics. Table 2-1 also contains the ore grades of the samples. The variation in emanation with various physical characteristics necessitates a detailed discussion of the collected ores. Factors that can possibly affect radon emanation include moisture, mineralogy, lithology, grain size, internal surface area, porosity, solubility of the ore, hygroscopicity of the ore, and the extent of weathering and fracturing. In addition to the following discussions on the ores collected, Tables 2-2 and 3-23 summarize the physical characteristics of each ore.

It should be realized that the various tested rock formations have variable physical properties. Compare the duplicate density and porosity figures of sample WC, Table 2-2. For this reason one small sample tested for a certain physical property may not necessarily be representative of another small sample used in experimentation. This is especially true of formations that are characterized by interbedded shale and sandstone. The best characterization of a formation is probably gained from the written description of that formation. The variable nature of the formation may cause variability in the emanation and diffusion data when different pieces of the same sample are used.

The major uranium deposit areas of the United States exist in the states of Wyoming, New Mexico, Utah and Colorado. Samples were collected from nine districts in these four states including: The Gas Hills, Powder River Basin, Crooks Gap, Ambrosia Lake, Laguna, Lisbon Valley, Slick Rock, Uravan and Ralston Buttes Districts. Additionally, one sample from the Bancroft area of Ontario, Canada, was tested during this program. All of these areas are described in more detail as to geologic occurrence, host rock classification, major structural features, mineralogy, nature of occurrence and theories of genesis in the following sections.

Wyoming Basins

The Wyoming Basins have the largest concentration of uranium resources in the United States. The four most important uranium mining districts are the Gas Hills District, the Powder River Basin, the Shirley Basin and the Crooks Gap area. Samples were collected from all but the Shirley Basin, since mining there is by open pit. Each of the other areas are discussed in the following sections.

TABLE 2-1. Identity of ores

Sample number	Location state - district	Mine company & name	Host formation (age)	Ore minerals	Sample ore grade %
WG1	Wyoming Gas Hills	Pathfinder's Lucky Mac	Upper Wind River (Eocene)	Uraninite coffinite	.5
WG2	Wyoming Gas Hills	Pathfinder's Lucky Mac	Upper Wind River (Eocene)	Uraninite	.04-.06
WG3	Wyoming Gas Hills	Pathfinders's Lucky Mac	Upper Wind River (Eocene)	Uraninite	.15 to .25
WP-1	Wyoming Powder River Basin	Exxon's Highland	Lower Fort Union (Paleocene)	Uraninite coffinite	.3 to .4
WP-2	Wyoming Power River Basin	Exxon's Highland	Lower Fort Union (Paleocene)	Uraninite coffinite	.05 to .15
WC	Wyoming Crooks Gap	Western Nuclear's Reserve	Lower Battle Springs (Eocene)	Uraninite coffinite	1.16
NM-S23-1	New Mexico Ambrosia Lake	United Nuclear Homestake Partner's Section 23	West Water Canyon of the Morrison (Jurassic)	Coffinite	.84
NM-S23-2	New Mexico Ambrosia Lake	United Nuclear Homestake Partner's Section 23	West Water Canyon of the Morrison (Jurassic)	Uraninite coffinite	.08 to .15
NM-S23-3	New Mexico Ambrosia Lake	United Nuclear Homestake Partner's Section 23	West Water Canyon of the Morrison (Jurassic)	Uranophane carnotite	1.00

TABLE 2-1. Identity of ores - CONTINUED

Sample number	Location state - district	Mine company & name	Host formation (age)	Ore minerals	Sample ore grade %
NM-P10-1	New Mexico Laguna	Anaconda's P-10	Jackpile Sand of the Morrison (Jurassic)	Coffinite uraninite	.5
NM-P10-2	New Mexico Laguna	Anaconda's P-10	Jackpile Sand of the Morrison (Jurassic)	Coffinite uraninite	.15 to .2
UB	Utah Lisbon Valley	Atlas' Big Buck	Lower Moss Back Member of the Chinle (Triassic)	Uraninite coffinite	.4 to .5
UL	Utah Lisbon Valley	Rio Algom's Lisbon	Lower Moss Back Member of the Chinle (Triassic)	Uraninite coffinite	.1 to .6
CD	Colorado Slick Rock	Union Carbide's Deremo-Snyder	Salt Wash Member of the Morrison (Jurassic)	Uraninite coffinite	.15 to .20
CK	Colorado Uravan	Union Carbide's King Solomon	Salt Wash Member of the Morrison (Jurassic)	Uraninite coffinite	.13
C-S	Colorado Ralston Buttes	Cotter Corp.'s Schwartzwalder	Idaho Springs (Precam-brian)	Pitchblende (uraninite)	.2
Mada	(Canada) Ontario Bancroft	Madawaska Mines Limited Madawaska	Faraday (Precam-brian)	Uraninite uranothorite	.07

TABLE 2-2. Physical properties of ores

Sample number	Dry bulk density (g/cm^3)[1]	Dry porosity (%)[1]	Specific surface (m^2/g)[1]	Air perm. par to b.p.[2]	Air perm. perp to b.p.[2]	H_2O perm. par to b.p.[4]	H_2O perm. perp to b.p.[4]
WG1	1.98	23.4	0.25	1290	42	0.514	0.392
WG2	2.16	16.7	23.3	____[3]	____[3]	Very low	Very low
WG3	2.04	24.4	3.1	____[3]	____[3]	0.241	0.526
WP-1	1.80	33.1	4.7	2120	1840	0.00581	0.0128
WP-2	1.84	27.8	3.4	____[3]	____[3]	0.00746	0.013
WC	2.28 2.30	13.5 12.0	6.5	____[3]	____[3]	0.00487	0.00203
NM-S23-1	2.26	16.4	9.33	0.48	3.2	----	----
NM-S23-2	1.85	23.5	4.55	2300	2590	----	----
NM-S23-3	2.34	10.4	16.6	----	----	----	----
NM-P10-1	2.23	14.2	7.91	0.16	0.07	----	----
NM-P10-2	2.16	12.5	18.0	550	250	----	----
UB	2.66	2.1	5.7	0.12	0.08	----	----
UL	2.54	4.3	26.6	0.50	0.07	----	----
CD	2.42	10.0	4.2	0.03	0.43	----	----
CK	2.25	15.5	10.9	3.3	1.6	----	----
CS	3.00	3.2	0.76	----	----	----	----
Mada	2.61	0.4	0.07	----	----	----	----
Synthetic ore	1.76	27.3	7.2	----	----	----	----

[1]Determined by Micrometrics, 5680 Goshen Springs Rd., Norcross, GA. 30093.
[2]In millidarcy, determined on dry samples by Core Laboratories, Inc., 10703 E. Bethany Dr., Aurora, CO. 80014; b.p. means bedding plane.
[3]Sample failed.
[4]In darcy, determined by Dames & Moore, Suite 200, 250 E. Broadway, Salt Lake City, UT 84111; b.p. means bedding plane.

Gas Hills District

The Gas Hills District has been the most productive district in Wyoming. It is divided into two portions, the East Gas Hills and the West Gas Hills Districts. They are located in eastern Fremont and western Natrona Counties, about 45 mi southeast of Riverton, Wyoming(11). The area is in the southeastern portion of the Wind River Basin on the western flank of the Dutton Basin Anticline.

The host rock for the uranium is yellowish to gray arkosic sandstones of the Wind River Formation of the lower Eocene Age. This formation outcrops at the surface over much of the basin. The sandstones are generally interstratified with lenses of mudstones and shales. The Wind River Formation consists of an upper and lower unit in this area(20). The lower unit varies from 0 to 130 ft in thickness and is dominated by grayish-green to light gray siltstone and claystone with some gray fine-grained sandstone. The upper unit is from 300 to 800 ft thick and tends to be coarser grained. It consists of medium- to very coarse-grained crossbedded arkosic sandstone with some intercalated mudstone, carbonaceous shale, and siltstone. Conglomerate beds can be found in places, especially in the East Gas Hills. The uranium ore is found largely in the upper unit of the Wind River Formation in a permeable sandstone near the base of the unit. Generally the sandstone is cemented by a pyritic gray clay but can be cemented with coarsely crystalline authigenic calcite in narrow zones.

While oxidized deposits have been mined in the past, they are largely mined out, and little if any underground mining is on-going in oxidized ores. Presently, most mineralization in the Gas Hills is in unoxidized roll fronts containing uraninite and coffinite. Many of these unoxidized deposits have been protected by their position beneath the water table. However, extensive mining in the area has greatly disturbed the water table and some of these deposits are now above the water table.

Uranium in the Gas Hills generally occurs in elongate roll front deposits. The uranium roll is bounded on the inside by the solution front and the altered barren interior. The exterior side grades to a protore having many characteristics in common with the ore zone but lacking the concentrated mineral deposition. An idealized roll front can be seen in Figure 2-1.

The roll fronts were formed when alkaline, highly mineralized, oxidizing ground water encountered a reducing environment. This caused deposition of the minerals that were in solution. In the Gas Hills area, a major reductant is felt to have been hydrocarbons which migrated along faults and fractures(31).

The associations of various minerals to the roll fronts are important(23). Consequently, the remaining portion of this section discusses these associations.

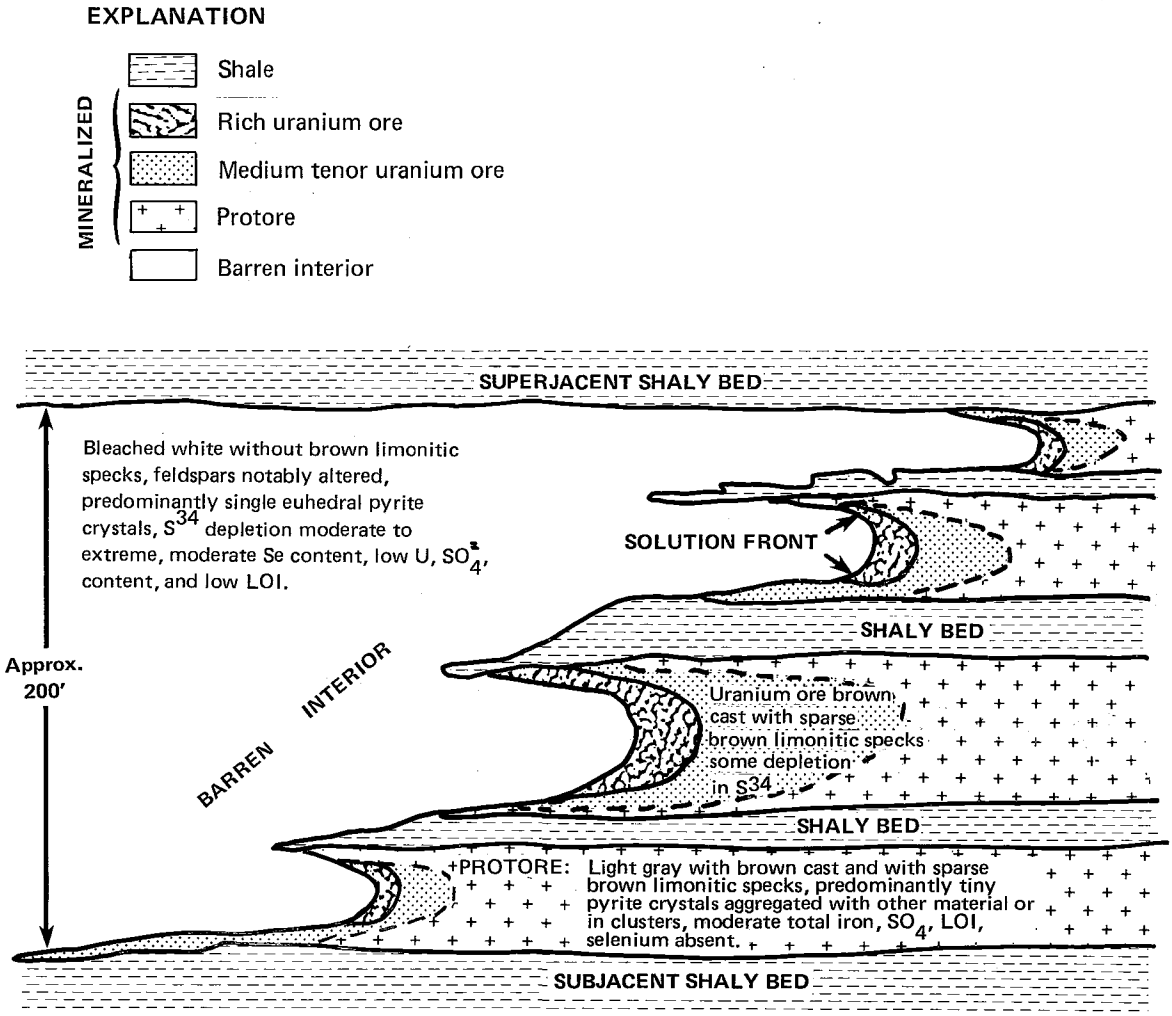

Figure 2-1. Idealized vertical section across a Gas Hills roll solution front.

The uranium is concentrated several feet beyond the front. In the ore area, the radiometric gamma and chemical assays for uranium are generally equal or the chemical assay is higher. Disequilibrium occurs on either side of the ore area where the radiometric assay is usually higher than the chemical assay. This disequilibrium is apparently due to an excess of Ra^{226} and Po^{210}. Thin layers of lignite and carbonaceous shale and elevated concentrations of iron, selenium, sulfur, molybdenum, organics, phosphorous, and arsenic are usually found in association with the uranium ore. Organic carbons and carbon dioxide are more abundant on the mineralized side of the front. Some iron is generally present as limonite in the mineralized zone and can be clearly seen as specks in the protore. The limonite is absent in the barren ground behind the solution front. This causes the barren interior to be a light drab gray. The mineralized ground is a dark-brown gray with small limonitic specks, and the protore is gray with limonitic specks. Pyrite in the altered barren zone behind the front occurs largely as untarnished discrete and nearly euhedral crystals. In mineralized ground the pyrite occurs generally as very fine aggregates of crystals which are coated black. Total iron correlates positively with the uranium.

The presence of total sulfur in high concentrations appears to have been instrumental in the precipitation of organic carbon and perhaps subsequently of the iron as pyrite and the uranium as uraninite. Hence, it also is positively correlated with iron and uranium. Enrichment in S^{32} over S^{34} in the barren interior and the abrupt reversal of this trend at the front may suggest a zone of intense bacterial activity at the front. It is believed that bacteriogenesis has played a strong role in the uranium deposition. Differential transport probably has also played a role in the isotope distribution. Calcium carbonate and sulfates also appear to have been mobilized and transported in the mineralizing solution, but are deposited farther from the front than the uranium. Phosphorus is generally associated with the uranium. Molybdenum is generally concentrated as a halo in front of the primary uranium mineralization.

Selenium, on the other hand, is most abundant in the barren interior, moderately abundant in the ore, and scarce in the protore. Arsenic and selenium tend to peak together.

Various theories for the origin and source of the uranium in these deposits have been proposed. While not all of the theories concur, they generally agree that(1) the "uranium was transported by ground water and leached from one or more of the following: 1) overlying tuffaceous rocks, 2) granitic rocks of nearby mountains, and 3) from arkosic sandstone derived from the granitic mountains." Different theories propose both diagenetic and epigenetic formation of the deposits(8).

As operations in the East Gas Hills are largely open pit, no samples were collected from this area. Three ore samples

were collected in the West Gas Hills area of Wyoming. They were all taken from Pathfinder's Lucky Mac Mine, which is a pit wall mine. The mine is just above the water table. One sample was taken from each of the three faces which were being worked at the time. Three different sandstone layers were sampled, representing a vertical spread of about 80 ft in the upper Wind River Formation.

The first sample, WG-1, was obtained from the No. 5 stope in the central sandstone lense. The average ore grade for this face was running about 0.5% with spots up to 1% or 2%. In this area the sandstone lenses seemed to be pinching out to claystone just ahead of the roll fronts. This was probably a factor in the higher concentrations of ore in this area. Generally, the major ore mineral was uraninite, with about one-third coffinite. Spots with more coffinite tended to be a darker chocolate-brown color and to be a higher grade ore. A scaler assay showed the grade for a small sample of this darker ore to be about 1.46%, while X-ray analysis showed an actual milling grade of 1.89%.

The second sample, WG-2, was obtained from the highest of the sandstone lenses in the 17-2 drift or heading. It was a much finer grained ore and also of a much lower grade averaging only 0.04 to 0.06%. Uraninite was the principal ore mineral. Since the ore had just been drilled and blasted, there was a lot of water in the area from the drilling. The scaler assay for this ore was 0.04% and the X-ray assay was 0.05%.

The third sample, WG-3, was taken from the 17-J stope, which was the lowest of the three sandstone layers sampled. It seemed to be a traditional roll front, not being pinched off like the sandstone lense where Sample WG-1 was taken. The sample was taken from the lower limb of the roll. The average ore grade for this locality is about 0.2% varying from 0.15 to 0.25%. Two samples were tested for uranium content. The scaler assays were 0.16% and 0.13% and the X-ray results were 0.17% and 0.12%. This area is characterized by a high concentration of molybdenum which usually runs from 0.002% to 0.05%, but is about 0.2% in this ore.

Since this area has high-beta ore in spots, it is not always stabilized. However, the ore in these deposits is in an area that is unaffected by surface leaching. Most deposits are associated with humus and coal and there tends to be more carbon trash associated with the rolls.

Powder River Basin

The Powder River Basin is a structural and physiographic basin in northeastern Wyoming. There are four major districts in the southern end of the basin where uranium mining has taken place: the Turnercrest-Ross, Monument Hill-Bear Creek, Highland Flats-Box Creek, and Pumpkin Buttes.

In 1965, the Monument Hill-Bear Creek area had produced over 90% of the total production from the Powder River Basin. Mining was largely in the Wasatch Formation of Eocene Age. Presently, there are some small open-pit mines in this area, but in general the Highland Flats-Box Creek District has become the most active area(11). This is the only district in the Powder River Basin where there are producing underground mines at this time. This district is located in Converse County about 25 mi north of Douglas, Wyoming.

Previously, mining in the Highland Flats-Box Creek District was almost entirely in the Wasatch Formation of Eocene Age. This formation outcrops at the surface over most of the area. The uranium mineralization occurred in thick lenses of coarse crossbedded arkosic sandstones which are interbedded with clay and siltstone. Calite cement is common in areas of uranium deposition. Hematite, limonite, manganese oxides, pyrite, and barite also are found as cementing material in the Wasatch sandstones(44). More recently, mining has been concentrated on the deeper deposits in the immediately underlying Fort Union Formation of Paleocene Age. Both the Wasatch and the Fort Union Formations were derived from the Laramie Range to the south. Samples were obtained from the Fort Union Formation since mining still is under way there.

The Fort Union outcrops at the surface closer to the margins of the basin, south and west of the Highland Flats area. The formation is divided into two units: an upper fine-grained siltstone unit and a lower coarser-grained unit. The upper unit consists of white weathering clayey siltstone and coal beds. The coal beds in this unit are extensively mined in the Powder River Basin. The lower unit is largely a fine-grained, clay-rich sandstone interbedded with silty claystone and minor coal. However, the uranium occurs in tan to reddish brown to gray, fine- to coarse-grained, arkosic, sandstones of fluvial origin in this lower unit. They are generally channel-type deposits where correlation of individual units across long distances is not possible. The mineralization tends to be more concentrated along the edges of the channels, where the sandstone thins. The mineralization in the Highland Flats area occurs largely in three sandstone beds in the Fort Union Formation. They occupy an interval from 110 to 180 ft thick in this area. While the individual sandstone beds vary on the average from very fine grained to very coarse grained and conglomeratic, they are fair to poorly sorted. Montmorillonite, nontronite (an iron-rich montmorillonite) and chamosite (a hydrous iron silicate) are all present in the formation, especially immediately above the clay-stone beds. The average mineral composition of the ore bearing sandstone is:(28)

Crystalline quartz	50 - 60%
Feldspar	20 - 30%
Chert and rock fragments	10 - 15%
Clay minerals	2 - 8%

Organic matter	0 - 3%
Mica and chlorite	1 - 2%
Green hornblende	0 - 2%
Other heavy minerals	1%

Most of the deposits mined in this area have been above the water table and have been oxidized. Those found most recently, both in the Wasatch and the Fort Union Formations, have been unoxidized(28). In fact, mines in the Fort Union are generally below the water table. Uraninite (pitchblende) and coffinite are the main ore minerals present in the Highland ore body(28). The minerals occur as thin layers deposited on the sand grains, clay or chamosite of the host rock. While a few more samples than not have an excess of chemically-determined uranium, the deposit appears to be generally in equilibrium. It is felt that the uranium deposits move gradually in the direction of ground water flow.

Most of the uranium occurs in roll fronts similar, at least in form, to those described for the Gas Hills. Once again the uranium was carried as an uranyl carbonate complex in alkaline, oxidizing bicarbonate-sulfate waters until they reached a major reductant. The major reductant in this area is felt to be hydrogen sulfide and pyrite. Anaerobic bacteria may have caused the formation of the hydrogen sulfide by using organic matter for energy and changing sulfate to sulfide. Coloring is different than in the Gas Hills with that behind the front being red and yellow brown. The red color is in the oxidized sandstone behind the front and is caused by the presence of hematite, an anhydrous iron oxide. The yellow-brown color is caused by the less stable goethite, a hydrous iron oxide found closer to the front, but still behind it. The sandstone in front of the roll is various shades of gray. The gray is caused by and varies with the uranium minerals and organic content. Often the sandstone overlying a roll is cemented by calcite. This differs from the Gas Hills, where claystones generally form the immediately confining upper layer. Concentrations of pyrite are very high in the ore zone. Organic carbon is concentrated ahead of the ore zone. Carbonate, sulfate, and manganese are all in greater concentrations in the mineralized zone than in the barren interior. Chromium is more concentrated in the limonite-hematite and protore zones. Selenium, as in the Gas Hills, is most abundant just before the front. Vanadium and lead are definitely associated with the uranium, unlike the Gas Hills. Molybdenum, however, does not seem to occur in analogous quantities. In the mineralized zone, the mass mean diameter of particles that make up the host rock tends to range between 340 to 420 microns. Behind the front it is between 410 to 500 microns. A larger zone of low- to medium-tenor ore seems to exist in the Powder River Basin at the expense of the high-grade ore.

As in the Gas Hills, both Oligocene and Miocene tuffs and the host sandstones themselves have been proposed as sources for

uranium. Thus, the timing as well as the source of the uranium deposition are in question. An Oligocene source has been favored by recent authors(28, 9).

Two samples were collected at Exxon Minerals' Highland Mine. The mine is 650 to 700 ft deep. Water is pumped from the mine at a rate of 400 to 450 gal/min. One sample was taken in the P1 drift 0634 at an elevation of 4,836 ft, about 535 to 545 ft below the surface. The average ore grade in this locality was 0.3% to 0.4%. It was in a medium-grained sand and was from the lower limb of a roll front. Calcareous sandstone was present above the ore. The second sample was taken in the P2 drift 0503 at an elevation of 4,867 ft. It was a lower grade ore (0.05% to 0.15%) on the upper wing of a roll. Clay galls were abundant. The uranium was in a crossbedded sandstone and some organics could be seen. It was bordering on unaltered, unoxidized protore.

Crooks Gap District

The Crooks Gap District is located in southcentral Wyoming, in the Green Mountains. It is south of the Gas Hills District and previously shared a mill with the Gas Hills. The mill is about 2 mi north of Jeffrey City and the mines are about 9 mi to the south. The district is in southeastern Fremont County. Crooks Gap is a water gap between Crooks Peak on the west and Sheep Mountain on the east. Most of the mining has occurred along the west and north flanks of Sheep Mountain(11).

The uranium is found in the lower member of the Battle Spring Formation of Eocene Age. This lower member is folded and faulted, whereas the younger member is not(9). In fact, it is much more severely folded and faulted than other host rocks. Dips of up to 20 deg have been noted. The Battle Spring Formation unconformably overlies the Fort Union Formation, or other formations where the Fort Union is absent. The lower member consists largely of conglomeratic arkose, cobble and boulder conglomerate and carbonaceous siltstone, all derived from older Precambrian, Cambrian and Paleozoic rocks. Fine- and coarse-grained layers alternate. Conglomerate lenses are sparser in the lower part of the member. Most of the uranium occurs in the part of the member composed of arkosic sandstones. Ores also are found in some conglomerate and mudstone layers. The formation dips at 10 deg to 20 deg toward the east beneath Sheep Mountain. Therefore, mines higher on the mountain tend to be deeper. The member is overlain by the younger member of the Battle Spring Formation, which outcrops higher on Sheep Mountain. Some uranium has been found in older formations near major faults.

Originally small near-surface ore bodies of uranophane and autinite were mined. Presently unoxidized ore bodies at or below the water table are mined. Primary ore minerals are uraninite and coffinite. As in other Wyoming Basins, lithologic

changes where permeability abruptly decreases have caused deposition of the minerals. Synclinal troughs and faults apparently have played more important roles in the localization of deposits.

Ore deposits in this area occur in tabular and poorly defined roll-type forms. A bleached-white altered sandstone behind the rolls can be seen, as in the Gas Hills. In the oxidized areas, the altered sandstone tends to be pinkish or red rusty colored. It should be noted that roll-front relationships are not as distinct as in either the Gas Hills or in the Powder River Basin. Feldspar alteration to kaolinite behind the front appears to be characteristic of this area. Pyrite and carbonaceous material have acted as reductants and played roles in the uranium deposition. Carbonaceous fragments, pyrite, calcite, and selenium are associated with the deposits. Molybdenum halos in front of the uranium mineralization are common in this district. Vanadium content is low in the Crooks Gap area. Calcium carbonate is concentrated in the mineralized areas. In altered ground the pyrite tends to be subhedral and replaced by marcasite.

Three theories for the source of the uranium are proposed: 1) tuffaceous rocks of Pliocene, Miocene and Oligocene Ages, 2) the arkosic host rock itself, and 3) uranium-bearing water from a deep-seated source. As in the Gas Hills and the Powder River Basin, the leaching of the tuffaceous rocks is the favored theory(46, 6).

One sample was collected from the Crooks Gap area, from Western Nuclear's Reserve Mine. At the time they were closing this mine and were going to work toward the access and remove all the pillars for ore. The sample was taken from one of these pillars in the A-1 stope at an elevation of 6,767 ft. This was approximately 243 ft below the surface of Sheep Mountain. It was above the water table and so was dry compared with the larger part of their operations, which are below the water table. Much of the formation tends to be less consolidated than in this area. The sample was taken from a roll in a sandstone bed about 18-in.-thick which was exposed on a pillar. The ore grade of the sample collected, as measured on a Beta scale, was 1.16%.

Grants Uranium Belt

The Grants Uranium Belt is located in northwestern New Mexico. This area is second behind the Wyoming Basins in available reserves. The belt is from 15 to 20 mi wide and extends from Gallup to the western edge of the Rio Grande trough(21). There are three main uranium producing areas in the belt: the Gallup, Grants and Laguna districts. We obtained samples from two of these districts.

Ambrosia Lake District

This district is located north of Grants, New Mexico. It is located on the Chaco Slope where the beds dip 2 to 5 deg to the northeast towards the San Juan Basin(21). The Chaco Slope is characterized by a series of elongated valleys separated by ridges or cuestas formed by the differential erosion of the slightly tilted sedimentary rocks. Shales generally underlie the valleys and the ridges are formed by the more resistant sandstone and limestones. These beds of Pennsylvanian Age and younger ages comprise a broad monocline locally modified by Tertiary folds and faults. The area is characterized by associated intrusive and extrusive rocks of the Mount Taylor and Zuni volcanic fields of Tertiary and Quaternary Ages.

The most important host formation for uranium in this area is the Jurassic Morrison Formation. The ore occurs largely in two distinct trends: the Poison Canyon and the Ambrosia Lake Trends. Ore in the Poison Canyon Trend occurs in the Poison Canyon sandstone, a tongue of the Westwater Canyon Member near the base of the Brushy Basin Shale Member of the Morrison. Ore in the Ambrosia Lake Trend occurs largely in the main body of the Westwater Canyon Member of the Morrison. Host rocks are medium- to coarse-grained, poorly sorted, feldspathic to arkosic sandstone with abundant pellets, pebbles and cobbles. The depth to the top of the Westwater Canyon Member varies from 300 to 1,500 ft in the mining area. Vertical permeability tends to be less than horizontal due to interbedded shale.

While mining has occurred mostly below the water table, some of it has been above. Much of the water occurs along joints in the sandstone. Unoxidized and oxidized deposits are mined. Presently, most ore is unoxidized. Coffinite is the principal ore mineral with minor amounts of uraninite.

Two different types of ore deposits characterize this area: the primary, trend or prefault ore; and the secondary, redistributed or postfault ore. The primary or trend ore is a dark gray to black well cemented deposit. Concentrated organic matter and calcite cement characterize this ore. These deposits are tabular and lenticular bodies which pinch and swell. They can be as long as 1,000 ft but are generally less than 200 ft. Thickness varies from a few inches to about 17 ft. While they usually conform to bedding they occasionally cross-cut. Primary ore tends to be high-grade ore, sometimes up to 10%. Mining grade averages about 0.3%.

Secondary ore is quite different from the primary. Much lower amounts of organic material are found and the rock is generally not well cemented. Both these characteristics make it hard to distinguish from barren rock. The secondary ore bodies are much larger than primary bodies. They can be up to 2,000 and 3,000 ft in length, several hundred feet in width, and up to 150 ft thick. These thick bodies are called stack

deposits and can be found as single masses or closely spaced ore layers. They are tabular in form. Ore grade tends to be about 0.4% with mining grades averaging between 0.15% and 0.2%.

The surrounding host rocks can be oxidized or unoxidized or both; and distinct relationships to the ores, as in Wyoming roll fronts, are more difficult to determine. Secondary ores probably were redistributed down dip from the primary ore by an oxidizing front similar to those in the Wyoming deposits, but different in that the rate of ground water migration greatly exceeded that of the migration rate of the oxidation front, resulting in the large uranium ore bodies. However, sharp transition zones from unoxidized gray rocks to buff and then to red, where the pyrite is oxidized to limonite and hematite, can be seen near the stack ores.

The genesis of the primary bodies is more difficult to determine. There is little doubt that the organic material and the pyrite played a role in the emplacement, but exactly what role is unknown. Both inorganic chemical precipitation and original fixation in the organic compounds with late coffinate formation have been proposed.

Thorium is scarce in these deposits. Mineral assemblages vary with the different ore body types and the oxidization state of the deposit. Fewer minerals are associated with the primary ore bodies. Table 2-3 lists associated minerals.

As in other areas the source for the uranium mineralization is in contention(21). Ash leach, syngenetic, granite leach, hydrothermal and source bed theories have all been proposed.

Three samples were taken in the Ambrosia Lake District from United Nuclear-Homestake Partners Section 23 Mine. All three samples were taken from the Westwater Canyon Member of the Morrison Formation. One sample represented a trend ore, one a redistributed ore, and one an oxidized ore. The trend ore was taken from the 780 level of the mine at coordinates 105 East and 1700 South. The ore grade of the sample taken was 0.84%. The secondary or redistributed sample was taken at the 650 level at coordinates 184 East 40 North. The ore grade in this locality varies from 0.08% to 0.15%. The oxidized sample was taken at the 780 level at coordinates 64 East and 2000 South. It is an oxidized premining high-grade ore. In this locality it often runs over 1%. Uranophone and carnotite are the ore minerals.

Laguna District

This district is located in the southeast corner of the Grants Mineral Belt. The area is about 50 mi west of Albuquerque. The district is located on the Acoma Sag in the southeastern corner of the San Juan Basin(21). Regional dip is about 2 deg to the north-northwest toward the San Juan

TABLE 2-3. Minerals in deposits in the Westwater Canyon Member listed according to environment[1]

Unoxidized Environment		Oxidized Environment			
		Premining		Postmining	
Prefault	Postfault	Deep	Surficial	Efflorescent	Other
Carbonaceous material	Coffinite	Tyuyamunite	Tyuyamunite	Zippeite	Tyuyamunite[2]
Coffinite	Uraninite	Metatyuyamunite	Metatyuyamunite	Zippeite-like	
Jordisite	Montroseite	Carnotite	Carnotite	Andersonite	
Pyrite	Paramontroseite	Gray Selenium	Red selenium	Bayleyite	
	Haggite	Cryptomelane	Cryptomelane	Uranopilite	
	Ferroselite		Autunite	Liebigite	
	Pyrite		Meta-autunite	Pascoite	
	Marcasite		Zellerite	Green "pascoite"	
	Barite[3]		Todorokite	Red selenium	
	Kaolinite		Gypsum	Ilsemannite	
	Calcite			Thenardite	
				Thermonatrite	
				Gypsum	

[1]Reference 21.
[2]X-ray powder pattern has broad lines but is similar to tyuyamunite. Mineral forms under films of water flowing from mine walls.
[3]Barite is classified as unoxidized because of its close association with montroseite.

Basin. Faulting is minor in this area. The same general stratigraphic sequence is present in this area as to the east in the Grants Ambrosia Lake area. However, mineralization in this area occurs in a slightly higher position, stratigraphically. It is contained largely in the Jackpile sandstone, the upper unit in the Morrison Formation(29). It is a fluvial deposit of fine- to medium-grained sandstone. Thin lines of mudstone are common. The cement is largely calcite near the bottom of the unit and grades to kaolinite toward the top. On fresh surfaces it is grayish white with a slight greenish cast. It intertongues with the underlying Brush Basin Member and is unconformably overlain by the Dakota Formation. As in other districts, organic remains are characteristic; however, they tend to be silicified and are only locally coalified.

Unoxidized deposits contain coffinite and uraninite ore minerals. Coffinite is the dominant ore mineral, with uraninite being associated more with partly weathered ores. Most deposits are above the water table and are oxidized, some to quite an extent. The oxidized mineral assemblage is like that in the near-surface oxidized Westwater Canyon deposits shown in Table 2-3. Uranium vanadates predominate; both tyuyamunite and metatyuyamunite are found. Also, as in the Westwater Canyon Member, a separate assemblage of postmining oxidized minerals exist. Some mining has occurred.

The deposits are generally tabular elongate bodies. Vanadium in the ore is generally contained in micaceous silicates and is only slightly positively correlated with uranium content. Ore running about 0.23% uranium has about 0.35% vanadium. Pyrite and carbonaceous material are closely associated with the ore.

Controlling features in localization seem to include the carbonaceous material, mudstone layers and lenses, bedding planes, facies changes in the sandstone, and in some cases weak intraformational faults. The age of implacement is apparently late Cretaceous to possible middle Tertiary time, after Dakota deposition and tilting and before or during early to middle Tertiary volcanism. Syngenetic, hydrothermal and volcanic-ash leaching are all possible deposition modes, as in other areas.

Two samples were collected in the Laguna District at Anaconda's P-10 mine, a pit-wall mine on the north side of the Paguate mine. Sampling was in the north part of the mine, which is in the upper part of the Jackpile sandstone. One sample, NM-P10-1, was collected from a primarily unoxidized area of the mine. It was about 25 ft northwest and then 60 to 90 ft northeast of station 2121 at the north end of the mine. The ore grade in this locality is approximately 0.5%. The main ore minerals are coffinite and uraninite.

The second sample, NM-P10-2, was taken from an area which was affected by postmining oxidation. It was 50 ft northwest

and then 20 to 40 ft northeast of station 2121. Ore grade in this locality was approximately 0.15% to 0.2%.

Paradox Basin

Many uranium mining districts are located in the Paradox Basin in southeastern Utah and southwestern Colorado. In fact, this area falls behind only the Wyoming basins and the Grants Mineral belt in estimated resources. The basin started to form during the Ancestral Rockies orogeny(15). The basin sank as the adjoining Uncompaghre Uplift rose. As the basin sank, it began to fill with massive deposits of gypsum and salt evaporites. During the Permian Age, sediments from the surrounding highlands were deposited in the basin, resulting in interbedded and interfingered sandstones and shales. Also during the Permian Age, tectonic forces started producing the salt domes and northwest-trending anticlines so characteristic of the area. During the Triassic period, classic red-bed deposits were laid down and the salt anticlines and domes developed further. Deposition in the basin continued through the Tertiary period.

Uranium mineralization has occurred in 18 geologic formations ranging from Permian to Cretaceous Ages(12). Largest production has come from the Salt Wash Member of the Jurassic Morrison Formation and the Shinarump and Moss Beck Members of the Triassic Chinle Formation. The deposits tend to cluster in groups or trends, most notably the Uravan and Lisbon Valley (or Big Indian) belts. Our samples were taken from these belts.

Lisbon Valley (Big Indian) District or Belt

For the period 1948 through 1977, the largest production of uranium ore from the Paradox Basin was from the Lisbon Valley or Big Indian area. This area is located along the Lisbon Valley salt anticline. It is in southeastern Utah in the larger Monticello uranium mining district(17).

While mineralization in this area has occurred in several formations, the Moss Back Member of the Chinle Formation is the most important ore-bearing horizon. This formation is of Triassic Age and unconformably overlies the Cutler Formation. The Moss Back Member is a fluvial deposit which varies in thickness from 20 to 150 ft. It consists of gray to greenish-gray, fine- to medium-grained quartzes, and conglomerate sandstones; minor mudstone, siltstone and limestone pebble conglomerates also are present. The ore is usually found within a short distance from the contact with the underlying Cutler Formation. The calcite-rich sandstone tends to be comparatively impermeable; fracturing of the formation probably allowed penetration of the ore-bearing solutions.

Presently the principal ore minerals in this area are uraninite, coffinite, and the associated vanadium minerals

corvusite and montroseite. The ores are dark gray to black. Uraninite generally fills interstices and replaces carbonaceous debris, calcite and detrital grains. The vanadium fills interstices and replaces calcite in the sandstone matrix.

Oxidized deposits are not common in the Chinle due to the consolidated, impermeable nature of the formation. Ore bodies mined in this area include 1) bedded, lenticular and tabular bodies, 2) rolls, and 3) log-shaped masses. Tabular deposits are more common in this area than in the Wyoming Basins. Individual ore bodies do not tend to be as obviously related to paleostructures and carbonaceous material as in the Wyoming Basins. Minerals associated with the ore include chalcopyrite, pyrite, molybdenum, galena and greenockite.

Various plausible theories exist on the mode of the uranium mineralization. One theory suggests that the source for mineralization was water that rose updip from an unspecified source beneath or within the Moenkopi to its eroded edge where it joins with the Moss Back. Other theories purport that the mineralizing solutions moved downward to the Moss Back from overlying deposits which have been eroded. Still others feel that these deposits are early diagenic in origin, formed by leaching of uranium and humic substances from the tributary drainages into the underlying sands of the main channels. The uranium itself may have been derived from igneous terrain, volcanic sediments, magmatic solutions, or underlying salts.

Two samples were collected from this district, one from the Big Buck Mine and one from the Lisbon Mine. The Big Buck Mine is located on the southeast flank of the anticline. It is accessed by an incline in the side of a hill. It is an extension of the Mi Vida ore body, the site of the original discovery of the blackish unoxidized ore in the Paradox Basin. The mine is mostly played out but pod and fringe mining are still ongoing. The ore zone in this mine is from 9 to 20 ft thick in the lower 30 ft of the Moss Back. The beds are dipping at about 9 deg to the southwest. The ore bodies are irregular shaped tabular deposits. The highest grade areas are associated with carbonaceous trash, which could be seen at the sample location. The ore grade of the sample collected was about 0.4% to 0.5% as measured by a T-probe. Vanadium concentrations tend to be particularly high in this area, the vanadium-to-uranium ratio being 2 to 1.

The second sample was taken from Rio Algom's Lisbon Mine. This mine was not discovered until 1965 since it is on the northwest side of the anticline which is on the downthrown side of the Lisbon Valley fault, which strikes along the axis of the anticline. Mining occurs at depths of 2,600 to 2,800 ft in the lower Moss Back Member of the Chinle Formation. This mine is below the water table. The sample was taken in an area

where medium- to coarse-grained sandstone predominated with interbedded fine-grained siltstone and mudstones. Ore grades in the 2 to 3 ft interval sampled varied from 0.1% to 0.6%. Vanadium concentrations in this mine tend to be low.

Slick Rock District

This district is in the most productive district of those located in the Uravan Mineral Belt. The Uravan Belt, located largely in southwestern Colorado, has yielded a major proportion of the uranium from the Paradox Basin, second only to the Lisbon Valley Belt. The Slick Rock District is largely in San Miguel County in the southern portion of the belt. Included in this district is the Sage Plains area, the site of current major production.

The host rock for mineralization in this area is the Salt Wash Member of the Morrison Formation of Jurassic Age. Over half the production in the Paradox Basin has come from this unit. It consists of interbedded reddish-brown to grayish-green fluvial sandstone and mudstones. The richest uranium mineralization has occurred in the upper sandstone lenses of the Salt Wash Member.

The ore minerals are unoxidized uraninite and coffinite found below the water table. As in the other uranium mining district, oxidized deposits were mined in the past. Ore deposits are found in tabular and roll-type forms. While rolls are more common than in the Lisbon Valley area, tabular deposits predominate. The deposits are up to 15 ft high and several hundred ft long. Uranium has averaged about 0.22% to 0.30%. Associated minerals include pyrite, marcasite and montroseite. Vanadium is common in these deposits and is estimated to be about 1.8%. Small amounts of selenides and molybdenum are also present in the ore zones. Copper occurring largely as malachite and azurite are more abundant in this region than in the other parts of the Uravan Ore Belt, with grades of up to 0.3%. Coalified matter is common in the ores.

Deposits seem to be localized at impermeable boundaries of the sandstone host rock. They are usually underlain or overlain by mudstones and occur in sandstones which are about 50% mudstone.

Both diagenetic and epigenetic models have been proposed for these deposits. Everything from the presence of hydrogen sulfide to the occurrence of pressure changes has been used to explain the primary reason for localization.(30, 22, 1) Even the original source of the uranium is in question and includes hydrothermal magmatic sources, basement rock, and volcanic ash.

A sample was taken from the Deremo No. 2 section of the Deremo-Snyder mine in the Sage Plain area of the Slick Rock District. It was taken in the 2420 stope approximately 700 ft

below the surface. The water table is approximately 200 ft below the surface. The sample was taken from the upper sand, an apparent channel deposit. Uranium-to-vanadium ratios run about 1 to 8 in this upper sand.

Uravan District

This district is in the north-central section of the Uravan Mineral Belt in western Montrose County. Three areas (Long Park, Club Mesa, and the Dolores Bench) are the most productive. Currently, the largest production comes from the King Solomon Mine on the Dolores Bench(12).

As is generally the case in Colorado deposits, the host rock is the Salt Wash Member of the Morrison Formation. These fluvial sandstones outcrop in this area high on the cliffs. On the Dolores Bench most ore deposits are found in the upper lenses of the member, generally in the upper 15 to 20 ft.

While the major ore minerals being mined in the area at the present time are uraninite and coffinite, this is the one area where small amounts of yellow oxidized uranium minerals were observed in the sample face. They were seen replacing a log. Generally the unoxidized deposits are found at depth, near or below the water table. Uranium for the district averages about 0.28%(12). Deposits are found in tabular, irregular, and roll-type forms. Greenish-gray mudstone usually underlies the ore bodies which are generally 4 ft thick, 75 ft wide, and 20 ft long. Fossil carbon is abundant. Vanadium occurs at levels of about 1.6% V_2O_5.

As with the Slick Rock District and all other districts in the Uravan Mineral Belt, considerable controversy exists over the mode of implacement, localization of, and the source of the uranium.

One sample was taken from the King Solomon Mine. This mine is well above the water table and water must be pumped to the mine. However, the deposits show the black coloring characteristic of uraninite and coffinite. Some yellow uranium minerals were seen replacing a fossilized log. The sample was taken from a very distinct roll front. A probe reading in the sample barrel indicated a 0.13% ore grade.

Ralston Buttes District - Colorado

The Ralston Buttes District is located in northcentral Colorado on the Colorado Front Range, northwest of Golden, Colorado. This district has had the richest production in Colorado east of the Continental Divide(45). The district is in northwestern Jefferson County. The Schwartzwalder Mine, in the northeastern part of the district, has produced about 97% of the Front Range uranium(60).

The host rock for the uranium at the Schwartzwalder Mine is contained in a transition zone between hornblende gneisses and mica schists of the Precambrian Idaho Springs Formation. The rocks in this transition zone consist of garnet-biotite gneiss, quartzite, and quartz-biotite schist. These rocks are often referred to as "Schwartz" rocks. The Schwartz rocks are more competent and denser than either of the enclosing units, and for this reason faulting and fracturing have formed more integral, discrete structures in the Schwartz rock(50). This apparently accounts for the characteristically abrupt end to mineralization at the mica schist contact and the end, within 16 to 20 ft, of the hornblende-gneiss contact.

The primary ore mineral is pitchblende (uraninite) with minor coffinite. Relatively minor amounts of secondary minerals have also been associated with the near-surface oxidized zones of the deposits. These oxidized zones are not generally any deeper than 50 ft(45).

The deposits at the Schwarzwalder Mine are hydrothermal, structurally controlled fracture and fault deposits. The mineralization occurs largely along the Illinois fault and tension fractures or "horsetails" in the hanging wall block of the fault(59). The breccia zones adjoining the faults and fissures contain most of the uranium. It occurs as thin layers coating breccia fragments, crystals of ankerite and the walls of thin veinlets in the breccia. The uranium probably was carried as a molecular carbonate complex. Gangue minerals are quartz, calcite, ankerite, siderite, red hematite, and potassic feldspar. The sequence of mineralization is felt to be: pyrite, carbonates and feldspar, pitchblende and jordesite (molybdenite), base metal sulfides, pyrite and calcite. High concentrations of organics do not typify this deposit.

The more accepted theory for the genesis of the uranium deposit generally has switched from that of a subsurface magmatic source to a meteoric hydrothermal source. Higher concentrations of molybdenum, instead of thorium and rare earths, smaller unit cells of pitchblende, and the presence of argon in muscovite in the veins, all support the meteoric model. Questions still abound about the source for the uranium. Overlying tuffs and ashes, granitic uplands, and the host rocks themselves have all been proposed.

One sample was collected from a stope in the Schwartzwalder Mine, just above the Steve mining level, opened in the late 1950's. The typical ore grade for this stope was 0.2%. The host rock was very friable and large pieces could not be obtained. This level is well below the water table.

Haliburton-Bancroft District - Canada

The Haliburton-Bancroft uranium district is located in southeastern Ontario, Canada in Hastings, Haliburton and

Peterborough counties. The district is from 38 to 88 miles north of Lake Ontario(39). It is one of only a few areas in the world where uranium is produced from deposits of the general pegmatitic class. The Madawaska Mine, the mine from which we obtained our sample, was formerly the Faraday uranium mine. It is located in the northeastern part of the district in Faraday township, Hastings County, about four miles southwest of Bancroft. The first large-scale operation in the district began production in 1956(16). Faraday uranium mines began production in April 1957. Under their original contract with Eldorado Mining and Refining Limited they were to deliver $29,754,800 worth of uranium concentrates.

The economic uranium occurs largely in granite-syenite-pegmatite dikes of Precambrian age. These dikes occur in a halo of metamorphic rock surrounding the Faraday Granite. At the Madawaska Mine, these dikes cut intrusive Faraday metagabbro-metadiorite. The containing Grenville meta-sediments consist of paragneiss shoots, amphibolite and marble in this area. The pegmatite is composed mainly of feldspars, silicates, and quartz in varying quantities. Accessory minerals include magnatite, zircon sphene, pyrite, marcasite, hematite, calcite, anhydrite, uraninite, uranothorite, thorite, allanite and secondary uranophane(2). Ore shoots are erratically distributed in the dikes. They generally occur in a medium grained granite or syenite, well hematized with 10 to 30% mafic crystals of pyroxene, amphibole and/or relics of the host rock. Their size varies from 50 to 350 ft in length, 5 to 40 ft wide and 50 to 200 ft high.

More recently ore has been found in anhydrite dikes which cross cut amphibolites. They are generally found at the 1,050-ft level of the mine and below. Apparently, the anhydrite crystallized early in the pegmatite dikes(27).

Most of the mine is below the water table. The major ore minerals are uraninite and uranothorite. The uranium is usually associated with areas rich in pyroxene or magnetite, zirconium, titanium and iron. Locally the ore is associated with quartz rich zones with abundant pyrite and pyrrhotite, allanite, rare earths and niobium.

The uranium-to-thorium ratio is fairly constant at 2/1. Secondary uranophane is occasionally found coating fracture surfaces in the ore bodies. It also occurs in vugs in the upper levels of the mine. The presence in the lower portions of the mine suggest a deuteric origin or some of the uranaphane(39).

All deposits in the district are epigenetic with a probable genetic relationship to granite intrusions of the area. It is felt that the dikes themselves where formed largely by replacement but partially by fissure filling(37). Due to the widespread occurrence of the deposits in different forms

in the district it is felt that an early coextensive sediment rather than a magma may have provided the source for some of the rarer elements(37). In any case, the migration and concentration of the elements was probably fueled by heat from intruding granitic rocks. Others felt the deposits are primarily of granitic or pegmatitic origin(24). It is likely that these deposits are caused by a combination of granitic-pegmatite, metasomatic and hydrothermal effects.

The samples were taken from the 1,050 ft level in shrinkage stope #714. This locality averages about .07% uranium.

The synthetic ore was made as described in Chapter 4 under Experimental Techniques.

CHAPTER 3

MEASUREMENT OF MOISTURE EFFECTS ON RADON EMANATION COEFFICIENTS

The stopping of direct- or indirect-recoil atoms by water in the rock pores appeared to be the primary mechanism of moisture effects on radon emanation coefficients suggested by a survey of the world's literature on emanation. In order to precisely define the emanation coefficient and remain consistent with this mechanism, emanation was defined as the fraction of total radon recoil atoms which were free to diffuse in the rock pores. The pore space included both air-filled and water-filled regions. The emanation could occur by direct recoil, indirect recoil, or diffusion mechanisms. The effects of moisture on the transport of radon through the pores to permit its escape from the rock was a separate experimental effort, described in Chapter 4.

The objective of the emanation coefficient measurements described in this chapter was to experimentally demonstrate their dependence on the moisture content of the ores over the entire moisture range from dryness to complete saturation. The following sections of this chapter describe the experimental design, laboratory procedures and results of emanation measurements on the natural and synthetic ores described in Chapter 2.

Experimental Design

The experimental design provided for two main experimental sequences. One was aimed at measuring emanation coefficients at ten different moisture contents using replicate aliquots of a crushed sample of the given ore. The other was aimed at demonstrating the effect on the emanation coefficient, if any, due to crushing the ore samples. Figure 3-1 illustrates these two experimental sequences.

As indicated, two sets of eleven samples each were prepared from the crushed, air-dried ore to provide two replicate measurements at each of eleven moisture contents. An estimate of the ore porosity was made from separate lumps of the ore to determine the saturation moisture content. The moisture was added to pairs of each of twenty sample fractions in approximate ten percent increments of saturation, with the eleventh fractions being used without any moisture addition. After emanation measurements on each sample fraction, they were again measured in the dry state to assess variation among the replicate fractions. A single sample fraction was used at the end of this procedure to measure the uranium content and estimate the uranium/radium ratio of the ore.

The lump samples were used in duplicate to determine an emanation coefficient at ambient moisture and at dryness on unground samples. The lumps were then crushed in the manner

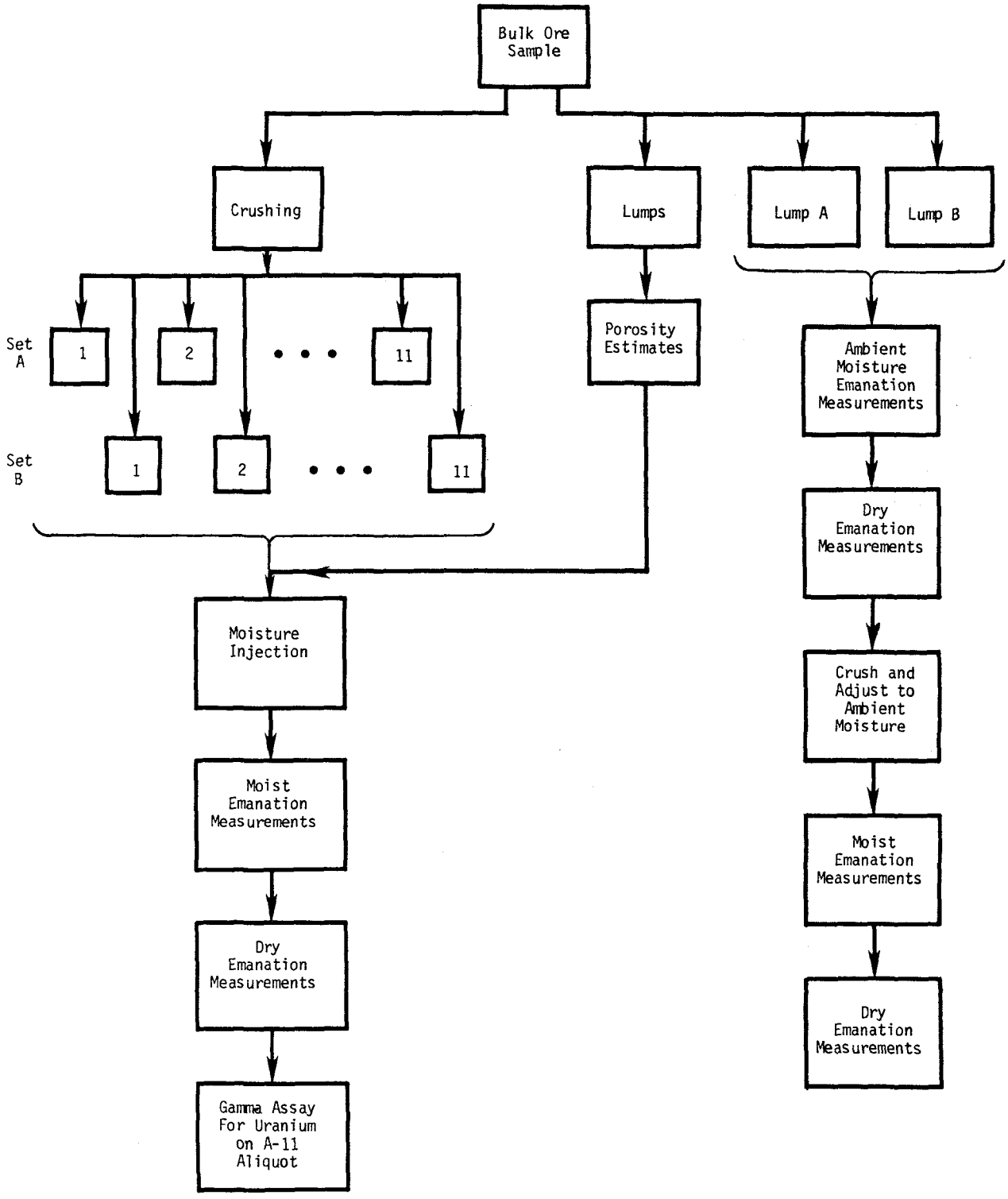

FIGURE 3-1. Sample handling and radon emanation measurement sequence for each of the eighteen ore samples.

used in the other sequence, remoistened to their ambient moisture level, and used for remeasurement of emanation coefficient in the moist and dry states. A comparison of emanation coefficients was thus obtained for each ore for crushed versus lump samples at both ambient moisture and at dryness.

Laboratory Procedures

The method used for measuring emanation coefficients has been used previously(5), and entailed determining the emanated fraction of the total radon from the difference between two sets of gamma counts of the ore. For the first set of gamma counts, the radon and daughters were kept in equilibrium with the radium parent by means of a sealed can. For the second set, the free gaseous radon was removed by vacuum de-emanation. Because the vacuum de-emanation procedure also removed the moisture from the sample, it was resealed and directly used again in the same manner for measurement of the dry emanation coefficient. Figure 3-2 illustrates this experimental procedure.

The ore samples were sealed in 8.2-cm diameter by 4.1-cm metal cans (1/2-lb. fish cans) at the appropriate moisture content using a commercial mechanical can sealer. An aluminum foil liner was used inside the cans to facilitate later transfer of the sample to a new can. After an equilibration period of 30-60 days, the first triplicate set of gamma counts was conducted to determine the total equilibrium radon activity. The can was also leak tested just prior to or after the first set of counts to assure accuracy of the total radon measurement. The agreement among the three counts was then checked, as indicated in Figure 3-2, to assure adequate precision before continuing. Additional counts were performed when the standard deviation exceeded three times the statistical uncertainty expected for the set. Approximately five percent of the sets required additional counts.

The sample cans were next opened and placed inside a vacuum drying chamber for de-emanation and moisture removal. After the ores had dried to constant weight, they were immediately transferred to new cans by lifting out the foil liner and were resealed. A second set of counts as then conducted on the samples within 4 to 24 hours was indicated in Figure 3-2, to complete the moist emanation determination. The dry sealed sample was then allowed to equilibrate for another 30-day period and the emanation coefficient was similarly measured for the dry sample.

Emanation coefficients were calculated from the gamma-ray counting data as

$$Em = \frac{R_1 - R_2}{R_1} \qquad (3\text{-}1)$$

and

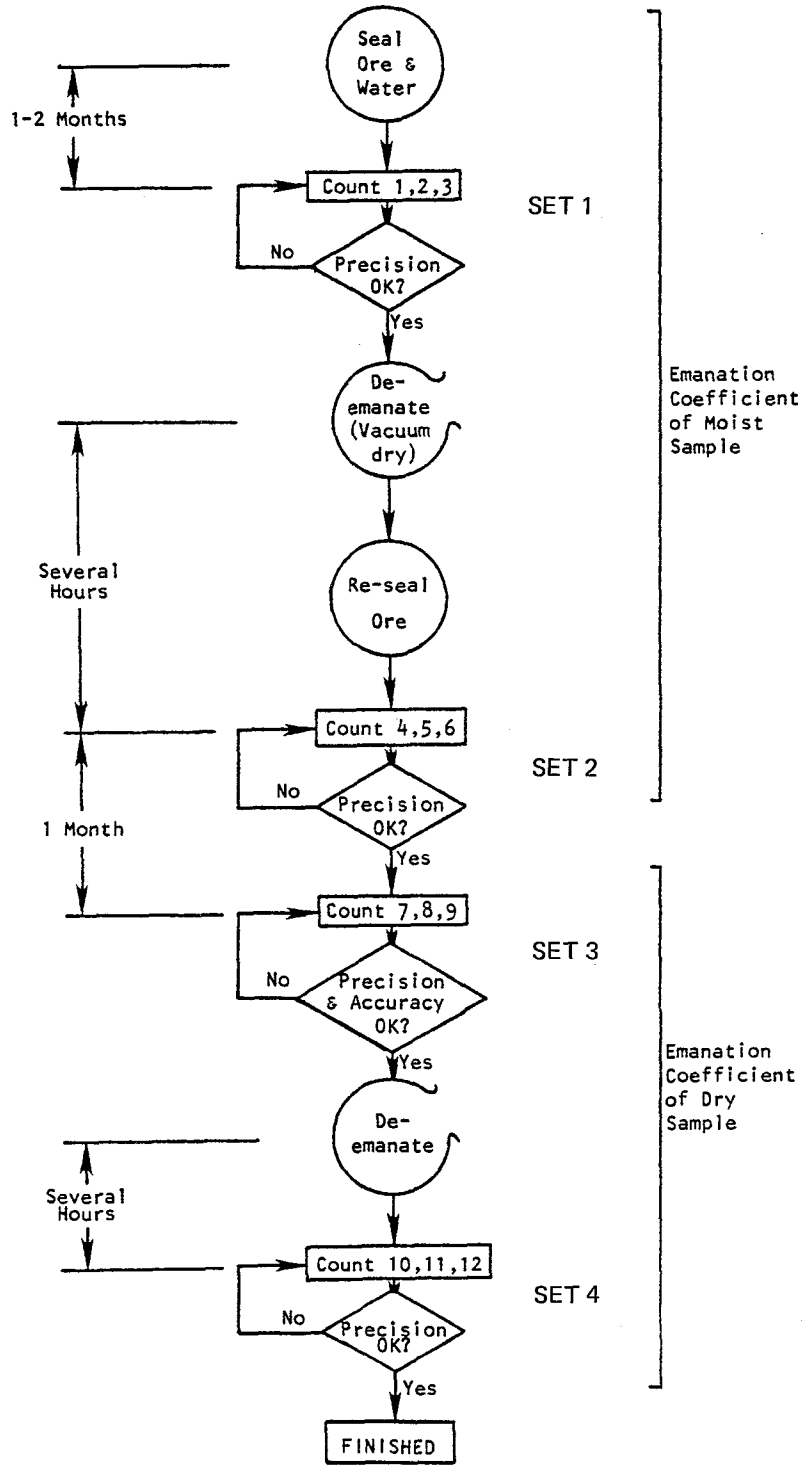

FIGURE 3-2 - Flowchart of the radon emanation measurement procedure.

$$E_d = \frac{R_3 - R_4}{R_3} \qquad (3\text{-}2)$$

where E_m and E_d are the emanation coefficients of the moist and dry samples, respectively, and R_1, R_2, R_3 and R_4 are the mean radon activities (pCi/g dry mass) determined from the four respective sets of counts illustrated in Figure 3-2. Because the samples were at equilibrium, R_1 and R_3 were calculated directly from the gamma-ray counting data and the net dry sample mass. Values for R_2 and R_4 were determined by averaging equilibrium-corrected radon daughter activities which accounted for the ingrowth of bismuth-214, the nuclide actually being counted, between the time of resealing the can and the time of the count. This correction had the form

$$R_{i2} = R'_{i2} - (R_1 - R'_{i2})B, \qquad (3\text{-}3)$$

where R_{i2} is the corrected radon activity (pCi/g dry mass) from count i, immediately after de-emanation, R'_{i2} is the observed activity of bismuth-214 from count i, and B is the bismuth-214/radium-226 activity ratio for the ingrowth time interval, from resealing to counting, as calculated from the Bateman equation(7). Selected values for B are listed in Table 3-1.

TABLE 3-1. Activity ratios of bismuth-214/radium-226 for correcting for bismuth-214 ingrowth after de-emanation

Time, Min	Ratio	Time, Min	Ratio
60	0.0015	400	0.0405
90	0.0038	450	0.0465
120	0.0068	500	0.0525
150	0.0102	600	0.0643
180	0.0137	700	0.0760
210	0.0173	800	0.0876
240	0.0210	900	0.0990
270	0.0247	1000	0.1100
300	0.0283	1200	0.1320
330	0.0320	1400	0.1540
360	0.0356	1600	0.1750

The uncertainty in the moist emanation coefficients was estimated as

$$\Delta E_m = \left[\frac{(\Delta R_1)^2 + (\Delta R_2)^2}{(R_1 - R_2)^2} + \frac{(\Delta R_1)^2}{R_1^2} \right]^{\frac{1}{2}} \quad (3\text{-}4)$$

where ΔR_1 is the larger of either the statistical precision of the radon measurement in the first three counts or their actual standard deviation and ΔR_2 is the corresponding uncertainty among the second set of counts. The uncertainty in the dry emanation coefficients was similarly defined using corresponding definitions of ΔR_3 and ΔR_4.

The moisture contents (M) of the samples, expressed as fractions of the saturation moisture content, were determined as

$$M = \frac{M_m - M_d}{P\ M_d} \quad (3\text{-}5)$$

where M_m is the net mass of the moist sample (g), M_d is the net mass of the dry sample (g), and P is the total porosity of the sample (cm^3/g), which is numerically equal to the saturation moisture content (g water/g dry sample).

Several specific laboratory procedures were unique to this study or otherwise require detailed description. These include the sample preparation methods, the leak-testing procedure, the gamma-assay procedures, and the vacuum-drying procedure and apparatus. The following sections give these descriptions.

Sample Preparation

Bulk samples were received in the form of large lumps of ore measuring 5-30 cm diameter. Several small lumps were typically sampled separately and maintained at ambient moisture for use in the lump/crushed emanation experiment. These were immediately sealed for equilibration at their ambient moisture. The remaining ore lumps were crushed to smaller particles on the order of 2-3 mm and allowed to air dry over a period of seven days in a dry outdoor environment. Crushing of several of the soft sandstone ores was accomplished by hand-crushing of the lumps. Harder ores were crushed with a jaw crusher. After the drying period, each ore was thoroughly mixed and was then coned and quartered to select 22 equivalent aliquots representative of the crushed sample mass. The aliquots were then weighed into the tared aluminum foil can liners with a precision of $\pm$ 0.01 g. Distilled water was added gravimetrically to each aliquot just prior to sealing the sample can. Typical sample masses were on the order of 250 g.

Because of geometric restrictions, considerably less mass of the lump samples was sealed in the sample cans. The typical

mass was about half that of the crushed aliquots. The geometry of the resulting radon-daughter activity distribution in the can was approximately equivalent for the lump samples and for the crushed aliquots, both of which approximately filled the can volume. However, when the lump samples were crushed for the comparison measurements on the same sample, the resulting crushed ore approximately half filled the can. The resulting geometry difference was observed to affect the counting efficiency in the lump/crushed emanation comparisons.

Porosity Estimates

In order to add appropriate quantities of water to the crushed sample aliquots in the initial preparation of the samples, an estimate of the saturation moisture content, or porosity was needed. Porosity estimates were made by vacuum-drying several lumps of the given ore, and then vacuum saturating the ore with either water or acetone. After draining the excess surface liquid from each lump, it was weighed, dried, and re-weighed to estimate the mass of liquid contained in its pores. The vacuum saturation method consisted of placing the dry ore lump inside a chamber, evacuating the chamber, and then allowing the water or acetone to enter the chamber until the sample was immersed. Samples were allowed to remain in the liquid for up to several hours, or until visible disintegration occurred.

It was observed that water required a long time period to penetrate some ores, even with the vacuum saturation method. The penetration was checked by splitting the lumps after weighing to visually observe whether the centers were wet. Acetone penetrated to a greater extent, but still failed to penetrate some of the hard-rock ores of low porosity. In other cases, the liquids caused swelling of the ores which altered their normal porosity. The total ore porosities were therefore adjusted later for the purposes of data analysis using the porosity data obtained by mercury intrusion porosimetry. Although this latter method was generally considered more reliable, it was seen to be biased in several cases due to inhomogeneity among the sample lumps. Porosities were also measured by mercury intrusion porosimetry on several crushed samples to better define a representative estimate of total porosity for these samples.

Leak Testing

All sealed sample cans were checked for radon leakage just prior to their de-emanation. Leak testing was accomplished by sealing eight sample cans inside a larger (4.6 liter) can fitted with a sampling port. A 20-liter chamber was also used occasionally to screen 54 cans at a time. After three days inside the larger can, a sample was collected with a Lucas Cell and counted to determine the radon concentration in the larger can. When an elevated radon concentration was noted, the sample

cans were placed into individual leak-test cans to identify the leaking can. Out of approximately 800 cans which were leak tested, three leaking cans were identified.

One of the leaking cans had a leak rate of 340 pCi/day, which was about one percent of the total radon activity in the can, but about seven percent of the gaseous, emanated radon in the can. The can seams were sealed with vacuum wax and the sample was allowed to re-equilibrate. The other two leaking cans were both synthetic ore samples which were reacting with the aluminum foil can liners and building up a high gas pressure, as evidenced by the bulging can lids. These cans were opened, resealed in new cans and re-equilibrated without subsequent leakage problems.

Radon measured in the leak test chambers was frequently elevated above background levels. In such cases, a calculation was made which attributed all of the leaking radon to the single can known to contain the lowest gaseous radon concentration. If the resulting leak rate amounted to more than five percent of the gaseous radon production rate, the sample cans were split to identify the source of the leak. The result usually indicated that lower level leaks from many or all of the cans had combined to give the high result but none of the individual cans had a leak which significantly affected the measured emanation coefficient.

Gamma-Ray Analysis

Gamma-ray analyses of all the ore samples were accomplished using a 13 cm x 13 cm NaI(Tl) scintillation detector coupled to a multichannel analyzer. The detector was shielded by 20 cm of steel, and was fitted with an annular plastic collar for reproducible sample positioning near the detector surface. Areas of the 609-keV peak from bismuth-214 were integrated by the multichannel analyzer, along with appropriate background regions on each side. Net peak areas were computed by subtracting the approriate multiples of the background areas from the peak area, and statistical uncertainties were computed as the square root of the sum of the peak and weighted background areas. Typical counting times were 10 minutes.

In order to randomize counting errors, the triplicate counts on each sample were not done sequentially. Instead, the can was removed from the chamber after each count and replaced by a different sample. A standard sealed tailings sample was counted after each 10-15 ore samples and was used to normalize the given set of data. Gain shifts or other systematic errors were thus detected and controlled by use of the standards, and long-term calibration changes were also avoided.

The counting system was calibrated using a 157.7 g sealed sample of a standard pitchblende ore in the same geometry as the

uranium ore samples. The standard has been well characterized (43, 32) and shown to contain 6060 ± 40 dpm/g radium-226 and an equilibrium quantity of uranium-238. Inter-laboratory comparisons of standard samples showed the calibration to give results within three percent of those obtained at Pacific Northwest Laboratory by a multi-dimensional spectrometer system(58), and in nominal agreement with NBL uranium ore standards counted at the Bureau of Mines facility in Denver. The latter comparison was hampered by geometry differences between the standards. The comparison therefore relied on calculated factors to correct for the geometry differences, and was estimated to be uncertain by 10-15 percent.

Determination of the uranium/radium equilibrium ratio for each ore was based on direct gamma spectroscopy of one of the crushed aliquots of each ore. This method was chosen for the uranium determinations because it was considered the most accurate basis of comparison with the larger body of radium data, and because it would utilize exactly the same sample in the same geometry.

The uranium/radium equilibrium measurements utilized a shielded 30-cm^3 Ge(Li) gamma-ray spectrometer to analyze the 1001-keV peak from protactinium-234m to estimate uranium and the 934-keV peak from bismuth-214 to estimate radium in the sealed samples. Because the pitchblende ore standard was reported to be in close equilibrium for these nuclides(43), it was used as the standard for direct comparison of the activity ratios. Count intervals varied from 10 to 1000 min to get adequate data for the 1001-keV peak.

Vacuum Drying of Ore Samples

A vacuum drying system was used for de-emanation and drying of ore samples in order to completely remove gaseous radon and moisture vapors from the pores, and to thoroughly dry the ores without exposing them to elevated temperatures. Previous reports(5, 40) have indicated that heating tends to anneal ores and also drive away hygroscopic water, both of which could lower the emanation coefficient.

The vacuum dryer consisted of a 13-liter aluminum chamber connected to a large capacity cold trap and vacuum pump. The cold trap was maintained at about -78°C by a dry-ice and alcohol bath. Typical pressures inside the system reached 1 μm Hg after the first few hours of drying. Samples became cool during the first 12-24 hours due to water evaporation, but returned to ambient temperature upon approaching dryness. Typical samples required 24-36 hours to dry. The standard drying itme used for all moist samples was 48 hours. A 24-hour period was used for the already dry samples, for which de-emanation was the only objective. Twenty sample cans were accommodated in the drying chamber.

It was noted that some ores, particularly loose sandstones, and conglomerates, tended to explosively fracture or dissociate during the early stage of vacuum drying, ejecting small quantities of ore powder from the sample cans. The sample loss was usually limited to samples in the 10-20 percent saturation range, and only occurred during the first de-emanation when moisture was present. By weighing all samples before and after drying, however, and by calculating emanation coefficients on a dry mass basis (pCi/g), the effects of the small mass losses were avoided.

Results

The initial estimates of sample porosity determined by vacuum saturation were compared with porosities measured by mercury intrusion porosimetry to determine from the known water contents the fractional saturation of the samples. The comparison of the porosity measurements is summarized in Table 3-2. The porosities by vacuum saturation represent the value measured by either water or acetone saturation which had the best precision or which was visually observed to best avoid the difficulties of swelling or incomplete liquid penetration. The porosities measured by mercury intrusion into lump samples were obtained from the Micromeritics Materials Analysis Laboratory (Norcross, GA) in connection with the pore size distribution analysis which was conducted on one lump of each ore. The complete pore size distributions measured on these samples are tabulated in Appendix A, and were used in the application of the mathematical model in Chapter 5. The mercury intrusion measurements on the crushed samples were performed by Ceramatec, Inc. (Salt Lake City, UT) to verify or assist in choosing a representative porosity for the ore. Duplicate analyses by each of the outside laboratories on one sample gave an estimate of the reproducibility on a separate or lump aliquot of the same ore.

As indicated in Table 3-2, considerable variation was observed in some of the porosity measurements. This was partly due to the inhomogeneity among the ore lumps used for the analyses, and partly due to the experimental difficulties in making the porosity measurements. The representative value was usually chosen from the vacuum saturation data because the lumps used in these analyses were chosen from the lump ores which were crushed for the emanation measurements. The mercury intrusion data from the crushed samples were chosen whenever sample swelling, incomplete penetration, or other experimental difficulties were suspected. The mercury intrusion data for the lump samples were used in cases of similar questionable accuracy. The pore size distribution data in Appendix A were normalized to the representative value of the total porosity in Table 3-2 for application of the model.

TABLE 3-2. Comparison of porosity measurements on ore samples

Ore Sample	Porosity, cm^3/g			
	Vacuum Saturation Lump[1]	Hg Intrusion Lump	Hg Intrusion Crushed	Representative Value
WP-1	0.184 ± 0.002	0.184	ND	0.184
WP-2	0.178 ± 0.011	0.151	ND	0.178
WG-1	0.133 ± 0.024	0.118	ND	0.133
WG-2	0.118 ± 0.013	0.077	0.089	0.118
WG-3	0.127 ± 0.036	0.119	ND	0.127
WC	0.081 ± 0.008	0.056,0.059	ND	0.081
UB	0.053 ± 0.049	0.0079	0.026	0.026
UL	0.012 ± 0.003	0.0171	0.015,0.027	0.027
CK	0.065 ± 0.025	0.069	0.060	0.065
CD	0.038 ± 0.004	0.041	ND	0.041
NM-P10-1	0.040 ± 0.009	0.064	ND	0.064
NM-P10-2	0.165 ± 0.020	0.058	ND	0.058
NM-S23-1	0.057 ± 0.005	0.072	ND	0.072
NM-S23-2	0.134 ± 0.020	0.127	0.054	0.134
NM-S23-3	0.077 ± 0.017	0.045	ND	0.077
CS	0.0043± 0.0018	0.0107	0.0052	0.0107
OM	0.001 ± 0.001	0.0017	0.0028	0.0028
SYN-3	0.125 ± 0.020	0.155	ND	0.155

[1]Means and standard deviations from five lumps.
ND = Not determined.

The emanation coefficients measured on the lump ore samples are presented in Table 3-3 and are compared with the corresponding coefficients after the lumps were crushed. The expectation was that crushing the samples might increase the emanation coefficients by reducing particle sizes, opening up blind pores, or increasing the accessibility of internal, radium-bearing cementing material to air. As indicated in Table 3.3, the opposite trend was observed. The indicated decrease in emanation coefficients after crushing was interpreted as an artifact of the measurement technique, however, and not as an actual decrease in emanation due to crushing.

The decrease in emanation coefficients measured on crushed samples was attributed to a geometry effect in counting the gamma activity in the sealed cans. The cans were counted at a very small incremental distance above the detector face, causing any vertical positioning variations to significantly affect the geometric efficiency (solid angle) of the analysis. Because the ore lumps were not shaped in cylinders to match the can shape, considerable void volume was present in the cans containing the ore lumps. However, the vertical distribution of

TABLE 3-3. Comparison of emanation coefficients for lump and crushed samples under moist and dry conditions

Ore Sample		Moisture Sat'n	Radon Emanation Coefficient				$E_{crushed}/E_{lump}$	
			Moist		Dry			
			Lump	Crushed[1]	Lump	Crushed[1]	Moist	Dry
WP-1	A	0.70	0.46	0.33	0.29	0.32	0.72	1.10
	B	.72	.52	.38	.35	.34	0.73	0.97
WP-2	A	.51	.68	.50	.45	.25	0.73	0.56
	B	.48	.60	.47	.40	.25	0.78	0.63
WG-1	A	.16	.042	.064	.023	.013	1.5	0.57
	B	ND	ND	ND	ND	ND	ND	ND
WG-2	A	.34	.45	.29	.30	.37	0.64	1.23
	B	.37	.40	.30	.28	.42	0.75	1.50
WG-3	A	.47	.39	.29	.28	.39	0.74	1.39
	B	.28	.34	.17	.15	.05	0.50	0.33
WC	A	.24	.29	.14	.087	ND	0.48	ND
	B	.29	.30	.14	.057	ND	0.47	ND
UB	A	.55	.40	.23	.22	.055	0.58	0.25
	B	.26	.23	.11	.11	ND	0.48	ND
UL	A	.71	.20	.12	.10	.082	0.60	0.82
	B	.44	.36	.21	.17	.16	0.58	0.94
CK	A	.88	.18	.11	.044	.069	0.61	1.57
	B	.91	.22	.12	.072	.067	0.55	0.93
CD	A	.49	.60	.39	.32	.14	0.65	0.44
	B	.52	.43	.28	.20	.09	0.65	0.45
NM-	A	.37	.50	.36	.30	.15	0.72	0.50
P10-1	B	.81	.55	.42	.27	.19	0.76	0.70
NM-	A	.21	.16	.10	.073	.034	0.63	0.47
P10-2	B	.22	.38	.26	.081	.055	0.68	0.68
NM-	A	.74	.51	.47	.24	.24	0.92	1.00
S23-1	B	.52	.55	.44	.30	.25	0.80	0.83
NM-	A	.10	.65	.57	.51	.43	0.88	0.84
S23-2	B	.05	.34	.26	.24	.14	0.76	0.58
NM-	A	.70	.24	.18	.14	.105	0.73	0.77
S23-3	B	.65	.44	.30	.30	.25	0.68	0.83
CS	A	.39	.50	.34	.10	ND	0.68	ND
	B	.48	.21	.15	.20	.064	0.71	0.32
OM	A	.54	.051	ND	.023	ND	ND	ND
	B	ND	.081	ND	.019	ND	ND	ND

ND = Not determined

[1]Crushed to 2-3 mm diameter particles.

activity was similar to that for the completely filled cans of crushed ores. When the lumps were crushed and resealed, however, the ore was packed more efficiently into the bottom part of the can, leaving most of the void volume at the top. When the loss of gaseous radon activity was measured by de-emanating these crushed samples, the main loss was determined from the most distant, and therefore the least sensitive part of the can. The observed emanation coefficients for the crushed samples therefore appeared to be lower than the ones for the original lumps.

The large variation evident in the data in Table 3-3 further complicates quantitative interpretations. The variation was high because of the inhomogeneity among ore lumps, as indicated by comparing emanation coefficients between the replicate (A and B) lumps. The variation was also increased by possible rearrangements of the relative lump positions in the cans during handling. The fact that the crushed/lump emanation ratios are also highly variable is expected, since the relative heights of crushed ore in the sealed cans varied widely.

The magnitudes of the emanation ratios in Table 3-3 are consistent with the expected geometry effect. Although certain ores may have suffered increased emanation due to crushing which was masked by the geometry difficulty, the precision of the data precludes making any corrections for such an increase, or even stating that the increase was significant.

The results of the main body of emanation coefficient measurements on the replicate crushed aliquots of each ore are presented in Tables 3-4 through 3-21. The moistures were determined from equation 3-5, and the emanation coefficients from equations 3-1 and 3-2. Although the ore samples were vacuum dried in the process of the first de-emanation, they picked up sufficient moisture from the laboratory atmosphere during the weighing and the re-sealing procedure to affect the "dry" set of emanation measurements in some cases. The moisture content, as a fraction of the saturation moisture, was therefore tabulated for the supposedly dry samples in Tables 3-4 to 3-21.

The reliability of the measured emanation coefficients was assured by several of the experimental procedures. The leak test procedure assured that radon gas was sufficiently contained in the sample cans to avoid significant errors in the resulting emanation coefficient measurements. The triplicate counting of each can in random sequences guarded against all replicate counts being biased due to sample positioning. The method for determining the emanation coefficients avoided dependence on the accuracy of the gamma calibration, although this was accurately determined, as described previously.

The use of actual standard deviations among the triplicate counts, in place of gamma-peak statistics whenever the standard deviation was larger, allowed actual counting errors to be

TABLE 3-4. Emanation coefficients measured for sample WP-1

Moisture, Saturation	Emanation Coefficient[1]	Moisture, Saturation	Emanation Coefficient	Moisture, Saturation	Emanation Coefficient
0.000	0.34	0.015	0.38	0.48	0.58
.006	.37	.015	.39	.56	.56
.009	.37	.016	.37	.57	.54
.010	.37	.016	.35	.66	.54
.011	.39	.068	.48	.67	.57
.013	.38	.068	.50	.75	.55
.013	.34	.157	.55	.79	.52
.014	.38	.159	.55	.87	.59
.014	.35	.250	.53	.88	.57
.014	.38	.280	.54	.96	.55
.014	.37	.360	.55	.98	.54
.014	.31	.390	.56	1.07	.55
.015	.35	.470	.56	1.08	.55

[1]Typical relative standard deviation was 3.4% for a single point, based on counting statistics.

TABLE 3-5. Emanation coefficients measured for sample WP-2

Moisture, Saturation	Emanation Coefficient[1]	Moisture, Saturation	Emanation Coefficient	Moisture, Saturation	Emanation Coefficient
0.00	0.30	0.086	0.35	0.70	0.46
.00	.26	.20	.47	.70	.49
.00	.24	.21	.46	.79	.45
.001	.23	.30	.47	.80	.47
.015	.28	.38	.45	.90	.46
.015	.27	.40	.48	.91	.49
.015	.33	.49	.48	1.00	.50
.016	.26	.51	.47	1.01	.49
.016	.28	.59	.45	1.11	.50
.017	.32	.61	.47	1.11	.51

[1]Typical relative standard deviation was 7.7% for a single point, based on counting statistics.

TABLE 3-6. Emanation coefficients measured for sample WG-1

Moisture, Saturation	Emanation Coefficient[1]	Moisture, Saturation	Emanation Coefficient	Moisture, Saturation	Emanation Coefficient
0.000	0.028	0.11	0.087	0.56	0.117
.001	.019	.11	.121	.61	.077
.001	.028	.17	.068	.65	.075
.002	.020	.17	.107	.76	.075
.004	.024	.26	.097	.85	.092
.005	.026	.27	.080	.89	.081
.005	.021	.36	.100	.94	.082
.005	.021	.41	.075	.96	.134
.005	.023	.49	.098	1.06	.130
.008	.019	.54	.097	1.08	.101

[1]Typical relative standard deviation was 9.8% for a single point, based on counting statistics.

TABLE 3-7. Emanation coefficients measured for sample WG-2

Moisture, Saturation	Emanation Coefficient[1]	Moisture, Saturation	Emanation Coefficient	Moisture, Saturation	Emanation Coefficient
0.000	0.13	0.063	0.16	0.71	0.21
.011	.13	.064	.17	.71	.23
.012	.19	.096	.22	.81	.26
.012	.15	.300	.25	.83	.21
.013	.17	.360	.27	.91	.29
.016	.17	.410	.23	.91	.20
.017	.13	.430	.23	.99	.28
.057	.13	.500	.24	1.01	.28
.059	.21	.510	.21	1.13	.27
.061	.21	.600	.20	1.22	.25
.061	.17	.610	.25	1.24	.26

[1]Typical relative standard deviation was 19% for a single point, based on counting statistics.

TABLE 3-8. Emanation coefficients measured for sample WG-3

Moisture, Saturation	Emanation Coefficient[1]	Moisture, Saturation	Emanation Coefficient	Moisture, Saturation	Emanation Coefficient
0.001	0.034	0.005	0.028	0.55	0.110
.001	.020	.005	.050	.55	.134
.001	.034	.052	.065	.65	.105
.002	.018	.052	.072	.66	.110
.002	.068	.160	.104	.73	.101
.004	.036	.220	.104	.76	.117
.004	.049	.260	.101	.86	.097
.004	.097	.280	.102	.86	.143
.004	.008	.360	.089	.94	.111
.004	.088	.460	.147	.96	.103
.005	.031	.460	.090	1.06	.157
.005	.027	.510	.123	1.06	.092

[1]Typical relative standard deviation was 11% for a single point, based on counting statistics.

TABLE 3-9. Emanation coefficients measured for sample WC

Moisture, Saturation	Emanation Coefficient[1]	Moisture, Saturation	Emanation Coefficient	Moisture, Saturation	Emanation Coefficient
0.004	0.066	0.007	0.044	0.42	0.161
.004	.058	.008	.068	.61	.158
.004	.055	.009	.056	.61	.171
.004	.057	.010	.045	.81	.151
.005	.063	.200	.144	.83	.158
.005	.039	.200	.166	1.02	.150
.005	.044	.310	.198	1.05	.144
.006	.048	.320	.192	1.22	.137
.007	.052	.410	.162	1.22	.156

[1]Typical relative standard deviation was 3.6% for a single point, based on counting statistics.

TABLE 3-10. Emanation coefficients measured for sample UB

Moisture, Saturation	Emanation Coefficient[1]	Moisture, Saturation	Emanation Coefficient	Moisture, Saturation	Emanation Coefficient
0.02	0.033	0.04	0.012	0.36	0.059
.02	.053	.04	.027	.38	.079
.03	.019	.04	.019	.61	.040
.03	.024	.04	.023	.63	.129
.03	.042	.05	.013	.77	.097
.04	.047	.06	.044	.97	.156
.04	.026	.07	.072	1.15	.153
.04	.019	.20	.081	ND	ND
.04	.033	.20	.032	ND	ND

[1]Typical relative standard deviation was 17% for a single point, based on counting statistics.

ND = Not determined.

TABLE 3-11. Emanation coefficients measured for sample UL

Moisture, Saturation	Emanation Coefficient[1]	Moisture, Saturation	Emanation Coefficient	Moisture, Saturation	Emanation Coefficient
0.02	0.079	0.04	0.071	1.13	0.162
.03	.070	.04	.072	1.19	.154
.03	.064	.04	.079	1.31	.198
.03	.081	.04	.067	1.35	.164
.03	.077	.19	.081	1.57	.160
.03	.079	.91	.162	1.57	.186
.04	.095	.91	.157	1.77	.146
.04	.092	1.04	.153	1.79	.186
.04	.066	1.07	.171	2.00	.157

[1]Typical relative standard deviation was 11% for a single point, based on counting statistics.

TABLE 3-12. Emanation coefficients measured for sample CK

Moisture, Saturation	Emanation Coefficient[1]	Moisture, Saturation	Emanation Coefficient	Moisture, Saturation	Emanation Coefficient
0.01	0.057	0.02	0.076	0.31	0.206
.01	.062	.02	.100	.49	.199
.02	.082	.03	.091	.50	.184
.02	.091	.03	.068	.69	.184
.02	.064	.09	.136	.69	.180
.02	.086	.09	.141	.89	.190
.02	.061	.19	.193	.90	.191
.02	.092	.20	.164	1.09	.177
.02	.090	.30	.210	1.10	.173

[1]Typical relative standard deviation was 5.1% for a single point, based on counting statistics.

TABLE 3-13. Emanation coefficients measured for sample CD

Moisture, Saturation	Emanation Coefficient[1]	Moisture, Saturation	Emanation Coefficient	Moisture, Saturation	Emanation Coefficient
0.01	0.068	0.01	0.112	0.48	0.23
.01	.111	.02	.062	.57	.28
.01	.093	.02	.098	.66	.25
.01	.130	.12	.200	.67	.26
.01	.104	.12	.210	.76	.25
.01	.105	.21	.220	.76	.29
.01	.118	.21	.240	.84	.27
.01	.111	.30	.260	.85	.26
.01	.123	.33	.240	.99	.27
.01	.102	.42	.210	1.03	.26
.01	.110	.48	.230	1.05	.25
.01	.111	ND	ND	ND	ND

[1]Typical relative standard deviation was 3.4% for a single point, based on counting statistics.

ND = Not determined.

TABLE 3-14. Emanation coefficients measured for sample NM-P10-1

Moisture, Saturation	Emanation Coefficient[1]	Moisture, Saturation	Emanation Coefficient	Moisture, Saturation	Emanation Coefficient
0.01	0.16	0.02	0.22	0.34	0.42
.01	.21	.02	.23	.36	.45
.01	.22	.02	.23	.46	.47
.02	.18	.02	.24	.50	.46
.02	.20	.16	.40	.64	.45
.02	.21	.19	.43	.65	.48
.02	.21	.21	.43	.71	.47
.02	.21	.22	.43	.77	.46

[1]Typical relative standard deviation was 3.9% for a single point, based on counting statistics.

TABLE 3-15. Emanation coefficients measured for sample NM-P10-2

Moisture, Saturation	Emanation Coefficient[1]	Moisture, Saturation	Emanation Coefficient	Moisture, Saturation	Emanation Coefficient
0.001	0.127	0.01	0.126	1.6	0.43
.001	.146	.01	.119	1.6	.44
.001	.150	.15	.350	1.9	.46
.001	.136	.15	.370	1.9	.45
.001	.154	.44	.390	2.2	.43
.001	.144	.47	.390	2.2	.45
.002	.138	.73	.260	2.4	.47
.004	.135	.79	.420	2.5	.44
.004	.139	1.02	.430	2.7	.45
.005	.126	1.10	.440	2.7	.43
.009	.126	1.31	.460	3.0	.46
.010	.141	1.32	.430	3.0	.45

[1]Typical relative standard deviation was 2.3% for a single point, based on counting statistics.

TABLE 3-16. Emanation coefficients measured for sample NM-S23-1

Moisture, Saturation	Emanation Coefficient[1]	Moisture, Saturation	Emanation Coefficient	Moisture, Saturation	Emanation Coefficient
0.01	0.33	0.02	0.31	0.71	0.53
.01	.33	.02	.32	.72	.53
.01	.34	.02	.32	.87	.53
.01	.34	.02	.32	1.02	.55
.02	.28	.02	.33	1.03	.54
.02	.30	.38	.49	1.04	.54
.02	.30	.38	.51	1.21	.54
.02	.30	.47	.51	1.31	.56
.02	.30	.55	.52	ND	ND

[1]Typical relative standard deviation was 1.2% for a single point, based on counting statistics.

ND = Not determined.

TABLE 3-17. Emanation coefficients measured for sample NM-S23-2

Moisture, Saturation	Emanation Coefficient[1]	Moisture, Saturation	Emanation Coefficient	Moisture, Saturation	Emanation Coefficient
0.005	0.17	0.01	0.27	0.53	0.36
.008	.23	.02	.23	.56	.38
.008	.23	.02	.26	.62	.37
.008	.24	.02	.26	.67	.40
.008	.29	.12	.37	.71	.33
.009	.21	.13	.36	.72	.38
.009	.23	.22	.37	.83	.37
.010	.23	.22	.37	.85	.41
.010	.24	.32	.38	.90	.38
.010	.25	.33	.36	.94	.39
.010	.25	.43	.38	1.04	.34
.010	.26	.44	.35	1.05	.41

[1]Typical relative standard deviation was 2.1% for a single point, based on counting statistics.

TABLE 3-18. Emanation coefficients measured for sample NM-S23-3

Moisture, Saturation	Emanation Coefficient[1]	Moisture, Saturation	Emanation Coefficient	Moisture, Saturation	Emanation Coefficient
0.01	0.18	0.02	0.20	0.81	0.26
.01	.19	.04	.18	.91	.28
.02	.16	.18	.26	.93	.25
.02	.16	.32	.26	1.02	.26
.02	.16	.32	.28	1.03	.25
.02	.17	.41	.26	1.15	.26
.02	.18	.42	.27	1.15	.27
.02	.18	.55	.25	1.28	.28
.02	.18	.58	.28	1.30	.26
.02	.18	.66	.28	1.45	.26
.02	.19	.76	.27	1.45	.26
.02	.19	.79	.26	ND	ND

[1]Typical relative standard deviation was 7.2% for a single point, based on counting statistics.

ND = Not determined.

TABLE 3-19. Emanation coefficients measured for sample CS

Moisture, Saturation	Emanation Coefficient[1]	Moisture, Saturation	Emanation Coefficient	Moisture, Saturation	Emanation Coefficient
0.06	0.105	0.08	0.118	0.53	0.212
.06	.106	.08	.120	.57	.218
.07	.100	.08	.121	.61	.215
.07	.114	.08	.124	.69	.229
.07	.116	.39	.180	.70	.219
.07	.118	.39	.184	.80	.214
.07	.123	.45	.199	.82	.219
.07	.129	.50	.210	.91	.236
.08	.117	.50	.220	.92	.217

[1]Typical relative standard deviation was 3.2% for a single point, based on counting statistics.

TABLE 3-20. Emanation coefficients measured for sample OM

Moisture, Saturation	Emanation Coefficient[1]	Moisture, Saturation	Emanation Coefficient	Moisture, Saturation	Emanation Coefficient
0.03	0.028	0.09	0.028	0.52	0.081
.04	.040	.09	.041	.62	.049
.04	.047	.10	.035	.75	.050
.05	.034	.11	.049	.95	.050
.05	.041	.12	.050	.98	.053
.05	.054	.18	.066	1.07	.040
.06	.027	.23	.066	1.21	.048
.07	.041	.24	.047	ND	ND
.08	.040	.31	.060	ND	ND

[1]Typical relative standard deviation was 19% for a single point, based on counting statistics.

ND = Not determined.

TABLE 3-21. Emanation coefficients measured for sample SYN-3

Moisture, Saturation	Emanation Coefficient[1]	Moisture, Saturation	Emanation Coefficient	Moisture, Saturation	Emanation Coefficient
0.0	0.076	0.49	0.196	0.69	0.23
.0	.085	.49	.137	ND	ND
.0	.040	.58	.168	ND	ND

[1]Typical relative standard deviation was 18% for a single point, based on counting statistics.

ND = Not determined.

incorporated into the final uncertainty estimate. The actual standard deviations were typically larger than predicted by counting statistics, particularly for ores with high activity. For such ores, the peak statistics usually yielded relative uncertainties of less than one percent.

There appeared to be a residual component of about 1-2 percent relative variation which was superimposed on the uncertainty attributed to counting statistics. This may have been due to ore inhomogeneity, which was typically expressed by 5-10 percent relative variation among radium activities of replicate ore aliquots. An analysis of variance was used to partition out the inter-aliquot variation in emanation coefficients. The residual variation, attributed to uncertainty in replicate counts of individual cans, exceeded that expected from the gamma peak statistics by 1-2 percent. The typical relative uncertainties associated with the emanation measurements were estimated from equation 3-4 for each ore and are reported at the bottom of Tables 3-4 to 3-21.

As indicated in the tables, the emanation coefficients ranged from about 0.02 to 0.55. These microscopic emanation coefficients were always lower at low moistures, and increased to a higher constant value in the 5-20 percent saturation range in most cases. Moisture increases above this range caused no further change in the emanation coefficients because all recoil atoms with proper trajectories were already being stopped by the water in the pores. On a macro-scale, the quantity of radon escaping from an ore body would be expected to decrease near saturation due to the lowered diffusion rate for radon gas in the saturated medium. The diffusion rate is independent of the emanation coefficient, however, which only describes the fraction of radon entering into the air or water filled pore space. The data in Tables 3-4 to 3-21 were summarized by averaging all emanation coefficients representing dry ores, and also those representing the plateau region of the emanation-moisture curve for each ore. Emanation coefficients in the transition region, which varied due to moisture, were avoided. The results of this summary are presented in Table 3-22. As indicated, the differences in emanation due to moisture greatly exceeded the uncertainties in the average moist and dry emanation coefficients. The ratios of the moist to dry emanation coefficients varied from 1.38 to 4.19, with a mean ratio of 2.3. Radon emanation was thus increased, on the average, by more than a factor of two by the presence of moisture.

Little correlation was observed between the emanation coefficients and the total porosity of the ore samples. A least-squares linear regression of the emanation coefficients for the moist samples on the total (fractional) porosity yielded a correlation coefficient of $r = 0.38$, with a slope of 1.03 and an intercept of 0.18. A similar regression using the dry emanation coefficients yielded a correlation coefficient of 0.47, with a slope of 0.84 and an intercept of 0.06. Qualitatively, the

emanation coefficients were generally higher for highly porous samples than for samples of low porosity.

Similar attempts at finding simple correlations between the moist emanation coefficient and other parameters showed even less correlation. Regression of the emanation coefficient on the specific surface areas (m^2/g) of the ores had a correlation coefficient of 0.10, a slope of 0.0019, and an intercept of 0.26. Regression of the emanation coefficient on the uranium content of the ore (weight-percent uranium) had a correlation coefficient of 0.17, a slope of 0.049 and an intercept of 0.25. Regression of the emanation coefficient on the radium activity in the ore (pCi/g) had a correlation coefficient of 0.12, a slope of 1.0×10^{-5}, and an intercept of 0.26. Regression of the emanation coefficient on the uranium/radium equilibrium ratio had a correlation coefficient of -0.22, a slope of -0.14, and an intercept of 0.43.

TABLE 3-22. Average dry and moist emanation coefficients and their ratios

Ore Sample	E_d, mean±S.D.	(n)[1]	E_m, mean±S.D.	(n)[1]	Ratio, E_m/E_d
WP-1	0.36 ±0.02	(17)	0.55 ±0.02	(20)	1.53
WP-2	.28 ± .03	(10)	.47 ± .02	(19)	1.68
WG-1	.023± .003	(10)	.095± .019	(20)	4.13
WG-2	.17 ± .03	(14)	.24 ± .03	(19)	1.41
WG-3	.042± .026	(14)	.112± .019	(20)	2.67
WC	.053± .009	(13)	.161± .017	(14)	3.04
UB	.032± .016	(16)	.13 ± .03	(4)	4.19
UL	.077± .009	(14)	.166± .015	(13)	2.16
CK	.078± .015	(13)	.189± .012	(10)	2.42
CD	.104± .018	(15)	.25 ± .02	(17)	2.40
NM-P10-1	.21 ± .02	(13)	.46 ± .02	(8)	2.19
NM-P10-2	.136± .010	(14)	.44 ± .02	(18)	3.24
NM-S23-1	.32 ± .02	(14)	.53 ± .02	(12)	1.66
NM-S23-2	.24 ± .03	(16)	.37 ± .02	(20)	1.54
NM-S23-3	.178± .012	(14)	.26 ± .01	(21)	1.46
CS	.116± .008	(13)	.219± .007	(11)	1.89
OM	.040± .009	(14)	.055± .012	(11)	1.38
SYN-3	.067± .024	(3)	.18 ± .04	(4)	2.73

[1] n is the number of determinations.

It was concluded that the emanation coefficient data required interpretation in terms of the more basic parameters of the ore. The pore size distribution data listed in Appendix A

provided the necessary information, which was used in connection with a cylindrical pore model to describe the emanation characteristics and moisture effects for the ore samples. The development and application of this model are described in Chapter 5.

The results of the high-resolution gamma-ray spectroscopy on a single aliquot of each ore are presented in Table 3-23. The gamma counting provided the ratio of the uranium and radium activities, which was used with mean radium content of the crushed ore samples to estimate the uranium content of each ore. The radium contents were determined in the course of the emanation measurements when the sealed, equilibrated ore samples were counted.

TABLE 3-23. Measurement of the uranium/radium equilibrium activity ratios for the eighteen ores

Ore Sample	Radium[1] (pCi/g)	Uranium/Radium Activity Ratio[2]	Uranium[3] (wt. %)	Original Moisture (wt. %)
WP-1	370±10	1.07 ±0.14	0.12 ±0.02	15.1
WP-2	320±10	0.83 ±0.17	0.080±0.017	9.4
WG-1	2040±170	1.19 ±0.12	0.72 ±0.10	3.0
WG-2	37±4	1.27 ±0.21	0.014±0.003	8.1
WG-3	74±6	1.60 ±0.27	0.035±0.007	8.0
WC	5400±200	0.95 ±0.09	1.53 ±0.15	1.6
UB	3620±140	0.96 ±0.10	1.04 ±0.11	0.4
UL	570±30	0.92 ±0.16	0.16 ±0.03	0.5
CK	730±30	0.95 ±0.13	0.20 ±0.03	5.5
CD	550±30	0.95 ±0.14	0.16 ±0.03	1.9
NM-P10-1	4560±150	0.99 ±0.08	1.35 ±0.12	3.5
NM-P10-2	2160±170	0.90 ±0.07	0.58 ±0.06	3.0
NM-S23-1	4400±600	1.25 ±0.10	1.65 ±0.27	3.3
NM-S23-2	320±10	1.41 ±0.17	0.14 ±0.02	0.5
NM-S23-3	440±20	1.26 ±0.17	0.17 ±0.03	6.2
CS	3180±150	0.73 ±0.10	0.70 ±0.10	0.3
OM	142±13	1.46 ±0.26	0.063±0.012	0.15
SYN-3	61±2	0.051±0.023	$(9.7 \pm 4.4) \times 10^{-4}$	0.0

[1]Mean of 36 to 66 individual gamma counts using the 609-keV peak from bismuth-214.

[2]Calculated from a single count using the 1001-keV protactinium-234m peak for uranium and the 934-keV bismuth-214 peak for radium.

[3]Calculated from the uranium/radium activity ratio.

As indicated, the equilibrium ratios for the ores were near or slightly greater than unity (especially for Gas Hills ores) for most of the Wyoming ores, and approximately equal to unity for the Utah and Colorado ores. The ratio for the hard-rock ore from the Schwartzwalder mine was significantly below unity. The New Mexico ores had ratios from slightly below unity for the Laguna area to significantly above unity for the Ambrosia Lake area. The Canadian ore also had a ratio significantly above unity. As expected, the ratio for the synthetic ore indicated that the tailings used in its preparation were about 95 percent depleted in uranium activity.

CHAPTER 4

THE EFFECTS OF MOISTURE ON RADON'S DIFFUSION COEFFICIENTS

Theoretical Review

Radon's diffusion is considered for a medium of porosity p in the absence of convective flow. Volume diffusion is within the air of the pores. The possible coexistence of surface diffusion also is included since it has been postulated for radon even to a degree exceeding that of volume diffusion(40), and also has been observed near room temperature for an organic compound on carbon(49) and gases on compounds(10) or metals(33, 47).

The Equation of Continuity with Both Volume and Surface Diffusion

The effective diffusion coefficient of a porous medium may be defined in terms of Fick's first law. The macroscopic flux J (atoms/cm^{2}s) due to radon's volume diffusion in the air of the pores is, therefore, given as

$$J_v = - D_{ev} \partial C/\partial x \qquad (4\text{-}1)$$

where D_{ev} is the effective volume diffusion coefficient (cm^2/s),

C is the radon concentration in the pore air (atoms/cm^3), and

x is the direction of maximum concentration gradient.

It might be noted that radon's volume diffusion in the crystal lattice of inorganic substances, specifically geological materials, is completely negligible compared with that in pore air. Radon's volume diffusion in the moisture of a pore also is negligible since the diffusion coefficient in pure water is four orders of magnitude less than that in pure air. Hence, only the pore air will be considered in volume diffusion.

A simple model constructed with the aid of Figure 4-1 is useful in assessing physical relationships. The tortuosity is defined to be the ratio of the average path length to the straight-line length in the direction of the maximum concentration gradient. The porosity is the volume fraction

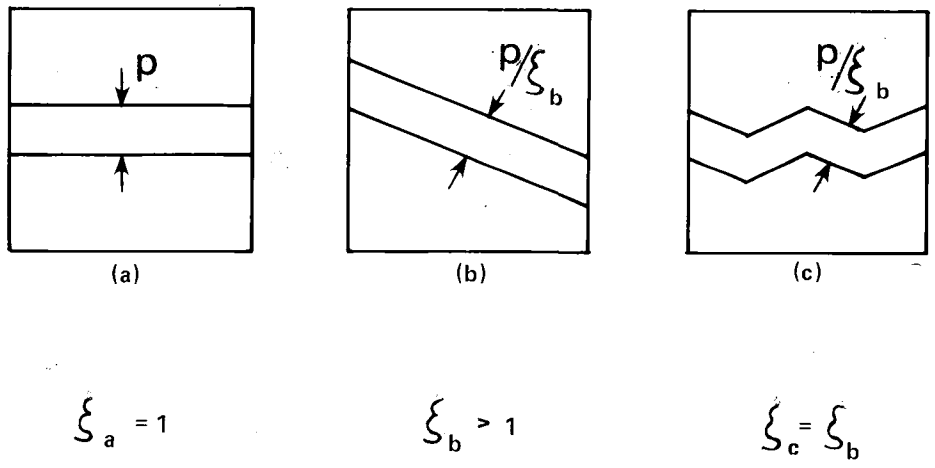

Figure 4-1. -(a), -(b), -(c). Considerations of porosity and tortuosity in volume diffusion

of the bulk material that is occupied by interconnecting air; it is different from Chapter 3's "total porosity" P. See Figure 4-1-a, b, and c. A unit cube is pictured with two different tortuosities. The porosity is represented by a single straight channel having the depth of the cube. The width of the channel is equal to the porosity p for $\xi=1$; i.e., the channel's orientation completely in the direction of the maximum concentration gradient as shown in Figure 4-1-a. In this case, the flux J_v (atoms/ cm^2s) coming off the right-hand side of the cube is $J_{av} = -p\ D_a\ \partial C/\partial x$ (where D_a is radon's diffusion coefficient (cm^2/s) in free air) because Fick's first law is only operative in the channel. The width of the channel must be p/ξ for a tortuosity other than unity (Figure 4-1-b). The length of the channel is increased by the factor ξ, thus decreasing the concentration gradient along the channel's length by the same factor. Thus, the flux J_v coming off the right-hand side of the cube in this case is

$$J_v = -fD_a(p/\xi)(1/\xi)\partial C/\partial x = -(fpD_a/\xi^2)\partial C/\partial x \qquad (4\text{-}2)$$

where f is a factor equal to, or less than, unity due to a nonuniform width.

Comparing equations 4-1 and 4-2 yields

$$D_{ev} = fpD_a/\xi^2 \qquad (4\text{-}3)$$

Equations 4-2 and 4-3 are also valid if the pore or channel zigzags (Figure 4-1-c).

Fick's first law for surface diffusion may be obtained by extensions of the treatments of J.C. Fisher(13) and V. Levy(25). These investigators considered a planar geometry, but the circular cross-section of a pore is appropriate here (Figure 4-2). It is assumed that the surface in question is the surface of the solid rather than a moisture-air interface. Fisher considered surface diffusion in a layer of thickness Δ (cm) of no definite physical meaning, but in the case of uranium ores the layer could be no more than a sparsely populated monomolecular film of radon atoms. The direction of surface diffusion of the adsorbed radon atoms is in the direction of the pore axis which has a tortuosity ξ with respect to the direction of maximum concentration gradient. Fick's first law applied to surface diffusion gives the following microscopic flux j_s (atoms/cm^2s) at the annulus:

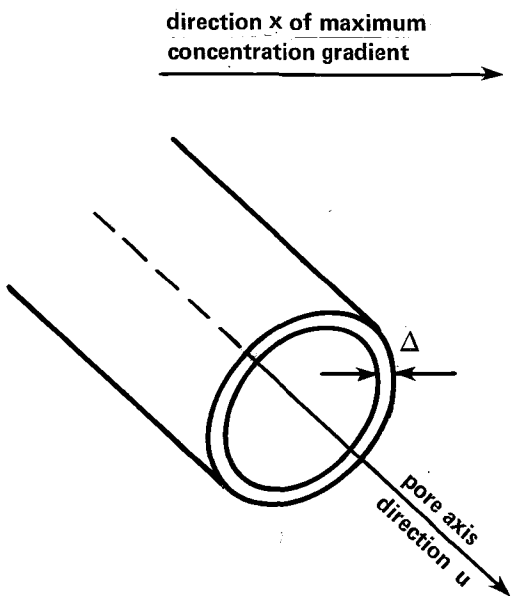

Figure 4-2. The surface diffusion at an average pore of diameter θ

$$j_s = - d_s \partial C_s / \partial u \qquad (4\text{-}4)$$

where d_s is the microscopic surface diffusion coefficient (cm^2/s),

C_s is the number of radon atoms/cm^3 in the surface layer of thickness Δ, and

$\underline{u}$ is the distance (cm) along the pore.

Including the effect of tortuosity gives

$$\partial C_s / \partial u = (1/\xi) \partial C_s / \partial x \quad . \qquad (4\text{-}5)$$

It is assumed for simplicity that there is a distribution of pores of uniform diameter θ (cm) and they occur at a concentration of $\underline{n}$ pores/cm^2 in a plane that is perpendicular to the direction $\underline{x}$ of maximum concentration gradient. The macroscopic surface flux J_s (atoms/cm^2s) due to surface diffusion in the experimentally observed direction $\underline{x}$ may be taken as

$$J_s = -(n\pi\theta\Delta d_s/\xi) \partial C_s / \partial x \qquad (4\text{-}6)$$

from equations 4-4 through 4-5. Letting the sample's total surface area per unit volume of sample be G (cm^2/cm^3), leads to the relation

$$G = n\pi\theta\xi \qquad (4\text{-}7)$$

Combining equations 4-6 and 4-7 gives

$$J_s = - (G\Delta d_s/\xi^2) \partial C_s / \partial x \qquad (4\text{-}8)$$

Adsorption in the sparsely populated monomolecular film is justifiably assumed to be linear so that equilibrium requires that

$$\rho k = G\Delta C_s/C \qquad (4\text{-}9)$$

where ρ is the bulk density (g/cm^3) of the matrix, and $\underline{k}$ (cm^3/g) is the distribution coefficient, i.e., the ratio of the number of adsorbed radon atoms per gram of dry matrix divided by the number of radon atoms per cm^3 of pore air.

Combining equations 4-8 and 4-9 yields the relation

$$J_s = -(\rho k d_s/\xi^2)\partial C/\partial x \qquad (4\text{-}10)$$

The total radon flux J_{tot} ($atoms/cm^2 s$) is the sum of that from volume diffusion (equation 4-2) and that from surface diffusion (equation 4-10), i.e.,

$$J_{tot} = J_v + J_s \qquad (4\text{-}11)$$

which, in this model, results in

$$J_{tot} = -(1/\xi^2)(fpD_a + \rho k d_s)\partial C/\partial x \qquad (4\text{-}12)$$

The total effective diffusion coefficient D_e (cm^2/s) is therefore a composite from volume and surface diffusion, i.e.,

$$D_e = (1/\xi^2)(fpD_a + \rho k d_s) \qquad (4\text{-}13)$$

where D_e is defined from

$$J_{tot} = -D_e \partial C/\partial x \qquad (4\text{-}14)$$

Although radon's diffusion in the moisture of the pores is neglected, radon's absorption in the moisture can be evaluated from

$$C_w/C = k_w \qquad (4\text{-}15)$$

where C_w is the number of radon atoms per cm^3 of pore water, and k_w is radon's distribution coefficient (cm^3/cm^3) in water (0.225 at 25°C)(42).

The mobile radon concentration per unit of bulk volume of the matrix is pC from the pore air plus $G\Delta C_s = \rho kC$ (equation 4.9) from the absorbed surface layer of radon plus $\rho_w C_w = \rho_w k_w C$ (equation 4-15) from radon dissolved in the water where ρ_w is the volume fraction of moisture in the bulk matrix. Hence the equation of continuity may be written as

$$(\partial/\partial t)(pC+\rho kC+\rho_w k_w C) = - \partial J_{tot}/\partial x - \lambda(pC+\rho kC+\rho_w k_w C) + E_\mu S \qquad (4\text{-}16)$$

where λ is radon's decay constant ($2.098 \times 10^{-6} s^{-1}$, 57)

E_μ is the microscopic emanation coefficient, i.e., the fraction of the recoiling radon atoms that reach the interconnecting porosity and remain there for diffusion, and

S is the strength of the distributed radon source in ^{226}Ra $d/cm^3 s$.

Combining equations 4-14 and 4-16 gives the equation of continuity in the form

$$\partial C/\partial t = D_{obs}\partial^2 C/\partial x^2 - \lambda C + E_\mu S/(p+\rho k+\rho_w k_w) \qquad (4\text{-}17)$$

where

$$D_{obs} = D_e/(p+\rho k+\rho_w k_w) \qquad (4\text{-}18)$$

is the experimentally measured diffusion coefficient and, according to the present model,

$$D_{obs} = (fpD_a+\rho kd_s)/\{\xi^2(p+\rho k+\rho_w k_w)\} \qquad (4\text{-}19)$$

from equation 4-13. It should be remembered that the porosity p is the volume fraction of the bulk material that is not filled with either solid or liquid.

The Determination of the Diffusion Coefficient D_{obs} Using the Sample's Own Production of Radon

The experimental arrangement was basically that of Stranden in which a slab of the material was exposed on its flat surface to flowing air which was then sampled for radon determinations(48). His measurements suffered from the inaccuracies of measuring low levels of radioactivity because the radon

exhalation was in the steady state in flowing gas. It was therefore decided to first seal the disc to build up radon to a much higher equilibrium state in a tightly confined, closed system. Samples of the flowing air were to be taken at intervals after the seals had been removed from both flat surfaces. It was unnecessary and operationally undesirable to take samples from the instant that the seals were removed. The possibility of opening a previously sealed, equilibrated, uraniferous sample also has been suggested by R.F. Holub and B.T. Brady(18).

Radon's diffusion was to be measured in only one direction at a time because the directionality of diffusion in ores was to be investigated as well as the effect of moisture. A cylindrical disc of the ore or other material to be investigated was permanently sealed on its curved sides, but only covered with removable end plates at the flat surfaces. The assembly was further sealed externally. The leak rate was 0.1 to 0.2 percent per day on the average. It is shown in Appendix B that no matter what might be the different leak rates and gaps at the two flat surfaces during equilibration, the relationship that should hold rigorously after the removal of the end plates at time zero is:

$$(EXR_{t_1}-EXR_{ss})/(EXR_{t_2}-EXR_{ss}) =$$

$$e^{-\lambda(t_1-t_2)}\left[\sum_{n=0}^{\infty} e^{-(2n+1)^2\pi^2 D_{obs} t_1/L^2}/\{1+\lambda L^2/((2n+1)^2\pi^2 D_{obs})\}\right] \Bigg/$$

$$\sum_{n=0}^{\infty} e^{-(2n+1)^2\pi^2 D_{obs} t_2/L^2}/\{1+\lambda L^2/((2n+1)^2\pi^2 D_{obs})\} \quad (4\text{-}20)$$

where L is the thickness of the disc and EXR_{ss} is the exhalation rate in the steady state, i.e., after a very long period of time. The flow rate of sweep air is made high enough to keep the radon concentration substantially zero at the disc's planar surface. Research has shown that the exhalation rate is not otherwise influenced by the rate of flow of sweep air. The left-hand side of the equation is experimentally obtained from pairs of points from times t_1 and t_2 and the right-hand side contains only the observed diffusion coefficient as an unknown. Values of the observed diffusion coefficient are calculated from program BJT06*PRE315.6 which includes a search technique (Appendix C). One of each pair of points should be on the upper, straight-line portion of the curve of log EXR versus log t and the other should be on the steep portion. The effects of decay on the exhalation rate are comparable to those of diffusion for values of $D_{obs} < \lambda L^2/\pi^2$ or about 10^{-6} cm^2/s for a 1-inch disc. If the disc is contained in a tightly fitting

cup to which it is sealed, then the removal of the end plate allows the use of equation 4-20 with a value of L of twice the thickness of the disc.

The Determination of the Diffusion Coefficient D_{obs} Using Injected Radon

It not infrequently happens that the disc of an experimental material gives exhalation rates in the method of the preceding section that are too low in radon for accurate counting. In such a case the accuracy may be improved by injecting radon from an artificial source such as a radon bubbler and allowing the sealed sample to stand for a day or so before the experiment. A uniform concentration C_o of radon is achievable in the pore gas of the sample provided that any fractional rate of radon leakage per day from the sample is much less than $3D_{obs}/L^2$ in comparable units, for example, about 1/day if $D_{obs} = 10^{-4}$ cm^2/s and L = 2.5 cm. In this case it can be shown (Appendix D) that the following relationship exists at times t_1 and t_2 following the removal of the end plates:

$$(EXR-EXR_{NI})_{t_1}/(EXR-EXR_{NI})_{t_2} =$$

$$\sqrt{t_2/t_1}\, e^{-\lambda(t_1-t_2)}\left[1+2\sum_{n=1}^{\infty}(-1)^n e^{-n^2L^2/4D_{obs}t_1}\right] \Bigg/ \left[1+2\sum_{n=1}^{\infty}(-1)^n e^{-n^2L^2/4D_{obs}t_2}\right] \qquad (4\text{-}21)$$

where EXR_{NI} represents the exhalation rate at the time in question in a separate experiment with No Injection of radon but substantially complete equilibration of the sample's own radon, i.e., the measurement of the preceeding section with any leakage during equilibration much less than λ, and L is the thickness of the disc if both planar surfaces are exposed. As in the preceding section, the use of equation 4-21 utilizes pairs of points for the left-hand side of the equation and a computer program (BJT06*UC359PROG3.1) (Appendix E) to search out the value of the observed diffusion coefficient that satisfies the equation. Its use will be illustated for the first two ores of this chapter's Experimental Results. Also as in the preceding section, one of the pair of points should be on the upper, straight line portion of the curve of log EXR versus log t and the other should be on the steep portion. The value of L should be twice the disc thickness if the disc is contained in a cup.

Range of Observable Values

In both of the above methods the maximum or minimum determinable value for the observed diffusion coefficient is largely determined by how thick or thin a disc can be made, i.e., the value of L in equation 4-20 or 4-21. If $t_{1/2}$ is the midpoint of the steep part of the curve of log EXR versus log t, then the observed diffusion coefficient is of the order of $L^2/(3t_{1/2})$. The minimum value for L with a friable uranium ore is about 2 cm and the minimum value of $t_{1/2}$ is roughly 300 seconds. As high a value of $L^2/(3t_{1/2})$ as the diffusion coefficient for pure air could easily be measured. A minimum value of about 10^{-5} cm^2/s for the observed diffusion coefficient could be observed if the maximum value of $t_{1/2}$ was restricted to 1 day.

Experimental Work

Experimental Techniques

The experimental arrangement is shown in block form in Figure 4-3. The location of the flowmeter aided in having the exhalation chamber and the disc in a pulsation-free air stream. The disc sample with only its sides sealed (Figure 4-4a) or with all but one end sealed (Figure 4-4b) was located on the axis of the exhalation chamber by means of spacers. The disc was vertically centered as well when both ends of the disc were open (Figure 4-4a), but this adjustment may not have been perfect. Hence, a 60-ml flow-through flask served as a mixing chamber which was desirable when the exhalation chamber had two exit lines (Figure 4-4a) but was unnecessary when it had one (Figure 4-4b). The exhalation chamber was 8.25 cm in diameter and 4.45 cm in inside height. It was mounted on thick foam rubber to eliminate any vibrations. Its top end was removable to allow the emplacement or removal of the sample. The top's seal was of the tongue-in-groove type aided with silicone stopcock grease or vaseline. Two C clamps also were mounted on opposite sides of the vertical axis to ensure a tight seal. The seal and proper flow of air out of the mixing chamber were checked at the outset of each experiment.

A needle valve was located downstream of the reduction valve on the tank of aged, compressed air. A single Gilmont flowmeter together with its calibration curve was used throughout each experiment with a nearly constant flow of air. Therefore, absolute errors in calibration were largely self-canceling on the left-hand side of equations 4-20 and 4-21 and other flow-calibration errors were minor. Tygon tubing was used for all lines. The sampling time was corrected for the transit time from the exhalation chamber to the scintillation cell. The air was humidified prior to entering the exhalation chamber for all but dehydrated samples. The humidistat consisted of a bubble tower containing a concentration of sulfuric acid to give a relative humidity (usually about 90 percent) that would

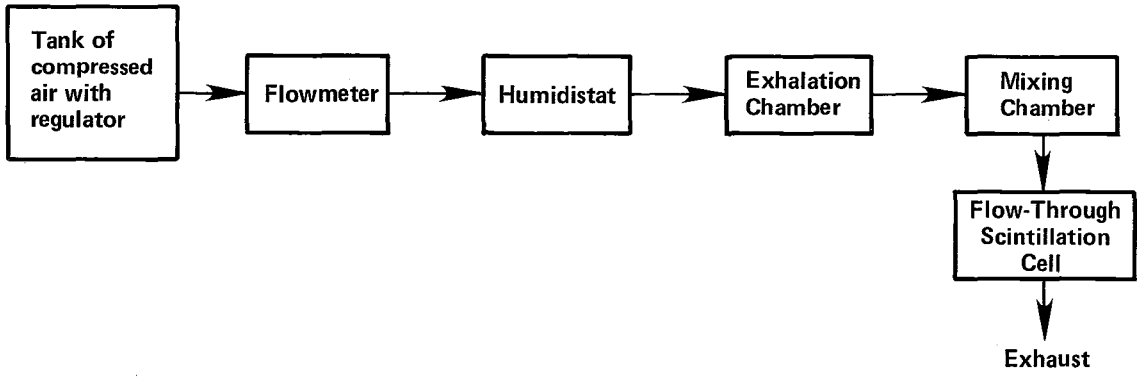

Figure 4-3. Apparatus for measuring the diffusion coefficient of a disc sample.

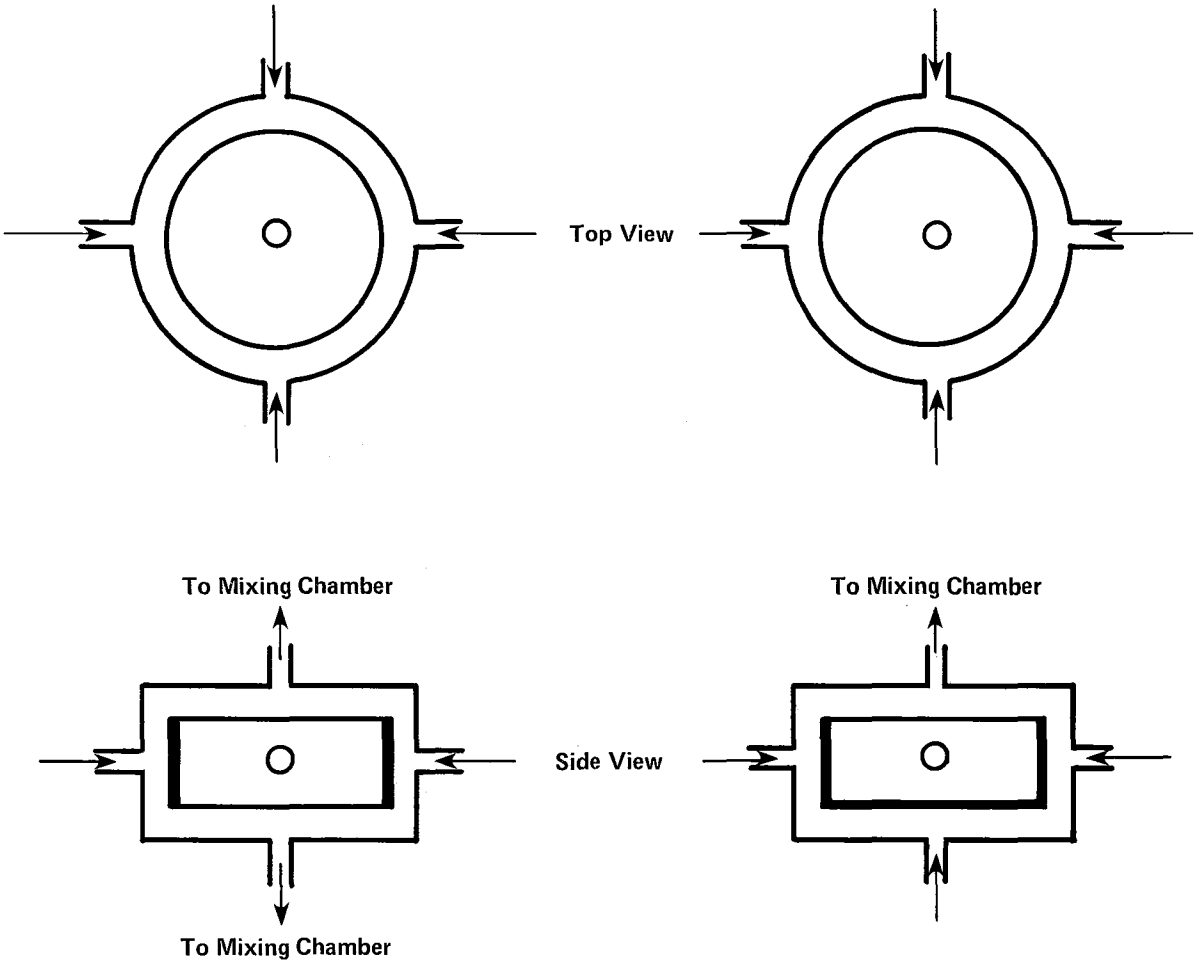

Figure 4-4. Air flow at the exhalation chamber (a) for a disc open at both ends, or (b) for a disc open at only one end.

not appreciably alter the moisture content of the sample. A little glass wool at the exit of the bubble tower prevented the carry-over of spray. A disc's moisture content changed inapprecially (less than 1 percent of moisture saturation) during the hours of measurement when the data to be used in the calculations were obtained. Errors from this source are thought to be negligible.

Each scintillation cell was of a flow-through type made from a 50-ml Erlenmeyer flask. See Figure 4-5. The phosphor coating extended up to the neck of the flask. The translucent coating had been applied from a thin slurry of zinc sulfide in diluted acrylic lacquer, then allowed to dry. In addition, some of the scintillation cells had aluminized plastic film wrapped around the outside to increase the reflection of scintillation pulses when the grab sample was counted with a photomultiplier tube. Aluminum foil was sealed on the interior surface of the rubber stopper to minimize the absorption of radon by rubber.

Connections to glass were aided with vaseline or silicone stopcock lubricant and connections were coated externally with epoxy cement or paraffin. The counting efficiencies of several dozen such scintillation cells were intercalibrated by circulating radon through them in series in a leak-free Tygon system having a peristaltic pump and counting them in the usual manner. A radon-filled scintillation cell was typically sealed by joining the two Tygon tubes of Figure 4-5 with a short, suitable sleeve and coating the connection with paraffin. The absolute counting efficiency of the reference scintillation cell was 55 percent(19); it was somewhat higher if the cell had the aluminized plastic film on the side.

The scintillation cells were counted 3.5 to 4 hours after sampling to achieve equilibrium with radon's alpha emitting daughters down to lead-210. The cells were counted with a photomultiplier tube in a radon flask counter, the latter being connected to a scaler rate meter. The counts were made in the middle of the plateau of counts versus high voltage. Corrections were made for the instrument background (about 0.1 c/m). Corrections also were made for each cell's own background by flushing and sealing it with the aged tank air and counting the cell in 3.5 to 4 hours.

Since variety was sought in the types of ores to be measured, there were likewise different degrees of machineability in producing the discs for measurement. The two chosen ores from Wyoming, Gas Hills ore no. 1 and Crooks Gap ore no. 1, were readily cut with saws but a little crumbling occurred at the edges due to their friability. By contrast the Utah Big Buck ore was dense, hard, and difficult to machine but the dimensions became comparatively precise. One disc for each ore was machined with its axis (direction of diffusion) parallel to the bedding plane; the other disc for that ore was

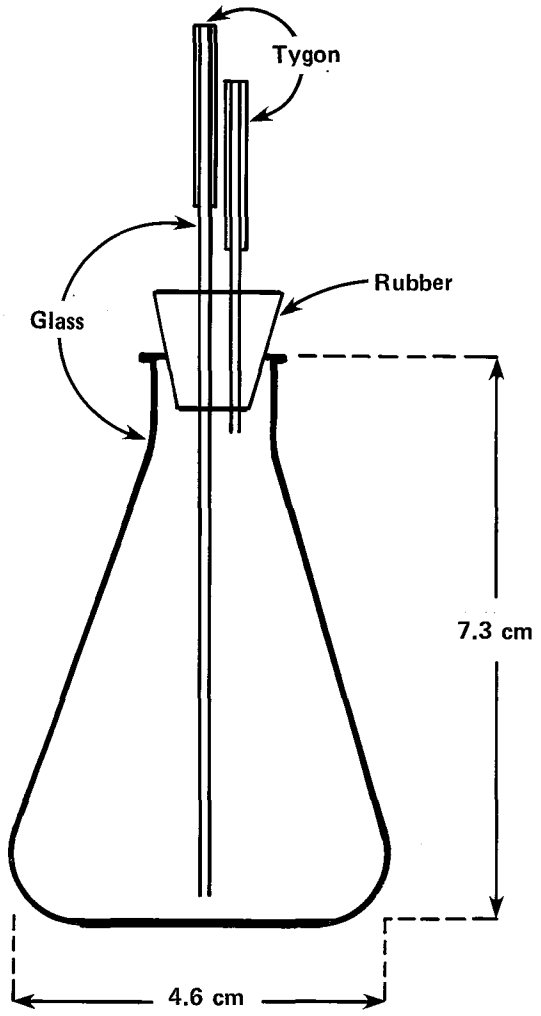

Figure 4-5. A flow-through scintillation cell (approximately full size).

obtained within 2 to 12 cm of the first in a perpendicular orientation with respect to the bedding plane. However, there is evidence from the geology of the areas (Chapter 2), from the emanation work (Chapters 3 and 5) and elsewhere that strong inhomogeneities may exist within such distances within an ore. Indeed it is probable that such inhomogeneities existed within a single diffusion disc the typical dimensions of which were 6.5 cm in diameter and 2.6 cm in thickness.

A more homogeneous disc was obtained from a synthetic "ore" that was made in the following way. A dry mix was made from 40 weight percent Portland cement (Type 2)(3), 30 percent 0.1 mm Vitro uranium tailings and 30 percent 0.1 mm sand of rounded particles. Water containing 0.5 percent of casein glue was mixed with the latter in the ratio of 20/100 for the water/dry mix ratio. The resulting mixture was pressed at 2,500 psi for 15 minutes. The small amount of glue prevented the pressed material from cracking or crumbling as it was removed from the mold. The disc was cured in moisture-saturated air at room temperature for two weeks, then dried at 85° to 90° C for a week, and finally dried in the vacuum desiccator for a week, all of which produced a constant weight and but slowly changing properties(53). The product was free of cracks and had a fine, uniform texture.

The moisture content of the discs was determined with respect to the weight of the dried disc from a week in a drying oven at 95° C and a further week in a vacuum desiccator at room temperature. The percentage of moisture saturation was calculated from the bulk density and the dry porosity as given in Table 2-2 for the same ore. The desired amount (if any) of water was added as the disc was sealed in its glass sleeve and end plates prior to the equilibration to develop the equilibrium concentration of radon. There was some uncertainty in the porosity and therefore the percentage of moisture saturation because it was impractical to determine the porosity on the disc itself.

The diffusion results for a given ore and direction of diffusion were obtained with the selfsame disc no matter what the moisture content. Hence, such results should be more amenable to correlation than those between different diffusion directions of the same ore, for example, because of the different discs and unpredictable inhomogeneities of the samples. The distribution coefficient k was determined on the ore for which the most diffusion results were obtained, i.e., the Wyoming Gas Hills ore no. 1. The air and/or water permeabilities for most of the ores in both diffusion directions have been reported in Table 2-2, but these were done on samples other than the radon-diffusion discs themselves. Some ores fractured during attempts to measure air permeabilities.

The discs of the natural ores all were run with both end faces exposed during the exhalation run (Figure 4-4a). In

most cases that had the beneficial effect of increasing the counting rate of the grab samples. The counting rate also could have been increased by decreasing the flow rate of sweep air, but the latter was maintained high enough so that the concentration of mobile radon in the air at the sample's surface was less than 1 percent of the sample's average. This was to experimentally satisfy the boundary conditions for the mathematical solutions, i.e., equations 4-20 and 4-21. The best seal of the sample's side was with a close-fitting glass ring to which the ore was sealed with silicone stopcock lubricant or vaseline. Glass or plexiglass end plates were likewise sealed to the glass ring with silicone stopcock lubricant or vaseline in the pre-experiment equilibration period during which time the assembly was covered with a thick layer of paraffin as well. The paraffin was quickly removed along with the end plates at the inception of measurements. The use of aluminum foil in place of the glass ring was not as free of leaks. If the side seal was a thick layer of paraffin that was left in place during the measurements, then the standard deviation of the observed diffusion coefficient was much worse and the average was lower. Since radon's diffusion coefficient in paraffin is low (1.3×10^{-6} cm^2/s)(34), the latter effect is consistent with the paraffin originally absorbing some of the sample's radon, then exhaling it during the measurements. This is particularly likely because radon's distribution coefficient between paraffin and air is appreciable $(1.4 \pm 0.5) cm^3/cm^3$(51).

The disc of synthetic ore previously mentioned is the only disc the radon diffusion of which was investigated in a cup, Figure 4-4b. The disc was sealed to the cup with small amounts of paraffin and vaseline. The end plate prior to the determination was glass with or without a stopcock for radon injection.

When there was two or three weeks of sealed equilibration before the exhalation experiment, about 30 percent of the planar surface of the disc sometimes became discolored with a film of surface-diffusing vaseline. It is estimated that this film was 0.1 mm or less in thickness. To estimate the time t for radon to diffuse through the film, the rule of thumb $\bar{t} = L^2/(3D)$ could be used with paraffin's published value for D, i.e., 1.3×10^{-6} cm^2/s(34), which probably overestimates the time. Thus, a period of a half minute or less was required and this was generally an order of magnitude less than the shortest times of our calculations. Errors from this source were probably not serious considering that less than half of the exhaling surface was so affected and the relative standard deviation in our determination of the diffusion coefficient was usually greater than 10 percent.

The relationships between Fick's first and second laws involve the term $p + \rho k + \rho_w k_w$ (equations 4-16 through 4-19) for both volume and surface diffusion. Although the porosity

$\underline{p}$ and density ρ are known for each ore, the radon distribution coefficient $\underline{k}$ (cm^3/g) generally is not. Hence, a method was devised for determining $\underline{k}$ and the technique was applied to ore WG1 in which the radon diffusion was the most completely studied of the ores of this report. A weight W_{ore} (g) of the ore crushed to particles of 1 mm or less in size was sealed in an absorption tube and allowed to develop the mobile radon of the experiment during a day or so. The absorption tube was then connected in a loop in series with a leak-free peristaltic pump and two scintillation cells using Tygon tubing to minimize unwanted absorption of radon. The pump was run for an hour or more after which the scintillation cells were serially removed with about a half hour of further circulation between these two events. The agreement of the radon counting rates in these two scintillation cells using counting by a standard method and corrections for cell efficiencies, etc., gave evidence of a uniform distribution of mobile radon in the remaining system whose known air volume is designated as V_{al} including the interconnecting porosity of the sample. The average of the two scintillation-cell readings (designated R_1) was then a measure of the concentration of mobile radon in the air of the remaining system. Two new scintillation cells of known total added volume V_a' were inserted in the train in the second part of the experiment. The air was again circulated and these scintillation cells were removed and counted as with the first pair. The average reading of this pair of scintillation cells is designated R_2. A small correction is added to R_1 to include "grown in" mobile radon in R_1', the concentration of mobile radon that the system would have had at the last two samplings if the added volumes were not there. Considerations of material balance give the relationship

$$R_1'(V_{al}+kW_{ore}) = R_2(V_{al}+V_a'+kW_{ore}) \qquad (4\text{-}22)$$

which may be rearranged to give

$$k = \{R_2V_a'/(R_1'-R_2) - V_{al}\}/W_{ore} \qquad (4\text{-}23)$$

Please see the Experimental Results under WG1 for further details.

Experimental Results

The exhalation rate is conveniently given in terms of counts per minute in a reference scintillation cell at a given flow rate, but could be converted to atoms per second if desired. Standard deviations based on counting statistics are included. The recorded exhalation rates are from counts of radon-222 plus its daughters polonium-218 and bismuth-214 in equilibrium. The data are used in this form for determining

diffusion coefficients, but must be divided by three in correlations with the emanation coefficient. Unless otherwise noted, the source of radon was the sample's own radium which yielded an equilibrium radon concentration upon standing in the sealed state.

The Disc of Synthetic Ore

This disc of 40 percent cement, 30 percent tailings, and 30 percent sand was 2.0 cm thick and had a diameter of 4.4 cm. The tailings material had been washed with water in classifying it to the 0.1 mm size prior to the pressing because the clay-like material was difficult to comminute otherwise. This may have contributed to the low radium content of this disc the equilibrium radon content of which gave the data of Table 4-1 at 46 cm^3/min of air flow. The disc was contained in a cup as in Figure 4-4b. The data were too sparse and inaccurate to yield a diffusion coefficient from equation 4-20. However, it was useful to give values of EXR_{NI} for equation 4-21 when the disc was injected at atmospheric pressure with about 1 microcurie of radon, equilibrated for a day, and again run in the cup in the exhalation apparatus. Table 4-2 contains the data of exhalation rate EXR for the injected run as well as interpolated values for no injection. The values for EXR_{NI} were comparatively small and could have been neglected.

Table 4-3 contains a dozen combinations of points of times t_1 and t_2 together with their calculated values of observed diffusion coefficients calculated from equation 4-21. The average at the 22°C and 0.85 atm of the experiment was 1.2×10^{-3} cm^2/s with a relative standard deviation of 11 percent over a range of time from 4 to 69 minutes. The data of Table 4-2 has been plotted in Figure 4-6 along with a curve calculated from equation 4-21 and $D_{obs} = 1.21 \times 10^{-3}$ cm^2/s (program BJT06*UC359PROG9.1) (Appendix F). The agreement between the observed and calculated results is good for the first hour of observations.

The No. 1 Ore of Wyoming Gas Hills (WG1)

Diffusion Parallel to the Bedding Plane

The Dry Disc. - The disc with its axis parallel to the bedding plane had a thickness of 2.58 cm and a diameter of 6.6 cm. The diffusion coefficient had previously been determined on it with the moisture of the disc as machined as described later. The disc was dried for this run, sealed and equilibrated to produce its own equilibrium concentration of radon before obtaining the data of Table 4-4. The rate of diffusion was too high and the counting rates too low to determine the diffusion coefficient from these data. As with the disc of synthetic ore, however, these data were interpolated to give values of EXR_{NI} for equation 4-21 when the disc was injected at atmospheric pressure with radon, allowed to stand in

TABLE 4-1. Exhalation data for the disc of dried synthetic ore after developing its own equilibrium radon concentration

(24°C, 0.85 atm)

Diffusion time (min)	Exhalation rate (c/min)[1]
1.4	2.8 ± 1.6
2.9	4.1 ± 1.4
6.0	0.2 ± 1.2
16.0	3.3 ± 1.2
25.5	1.0 ± 1.0

[1]For 46 cm^3/min of flow rate

TABLE 4-2. Exhalation data for the disc of dried synthetic ore with injected radon

(22 ± 1°C, 0.85 atm)

Diffusion time (min)	EXR (c/min)*	EXR_{NI} (c/min)[1]
3.9	641. ± 9.	1.1
6.7	627. ± 10.	0.8
11.6	382. ± 8.	0.6
19.2	281. ± 9.	0.5
30.0	162. ± 4.	0.4
46.0	88. ± 2.	0.3
69.0	37. ± 2.	0.3
100.0	23. ± 1.	0.2
154.0	14.8 ± 0.7	0.2
233.0	9.9 ± 0.7	0.1
359.1	11.6 ± 0.6	0.1
727.2	5.8 ± 0.7	0.1
960.2	4.3 ± 0.4	0.1
1,510.1	3.7 ± 0.6	0.1
2,603.0	0.8 ± 0.4	0.0

[1]For 100 cm^3/min of flow rate

TABLE 4-3. Observed diffusion coefficents (cm^2/s) calculated from Table 4.2 for the disc of dried synthetic ore

($22 \pm 1^{o}C$, 0.85 atm)

Time (min) of point 2 =	30.0	46.0	69.0
Time (min) of point 1			
3.9	1.17×10^{-3}	1.11×10^{-3}	1.07×10^{-3}
6.7	1.52×10^{-3}	1.30×10^{-3}	1.19×10^{-3}
11.6	1.24×10^{-3}	1.14×10^{-3}	1.09×10^{-3}
19.2	1.38×10^{-3}	1.17×10^{-3}	1.10×10^{-3}

Av. $D_{obs} = (1.21 \pm 0.13) \times 10^{-3}$ cm^2/s

TABLE 4-4. Exhalation data for the dried disc of WG1 with the axis parallel to the bedding plane after developing its own equilibrium radon concentration

($23.5^{o}C$, 0.85 atm)

Diffusion time (min)	Exhalation rate (c/min)[1]
1.3	10.8 ± 1.6
2.8	4.2 ± 1.2
4.8	0.9 ± 1.0
9.8	0.7 ± 0.7

[1]For 1,540 cm^3/min of flow rate

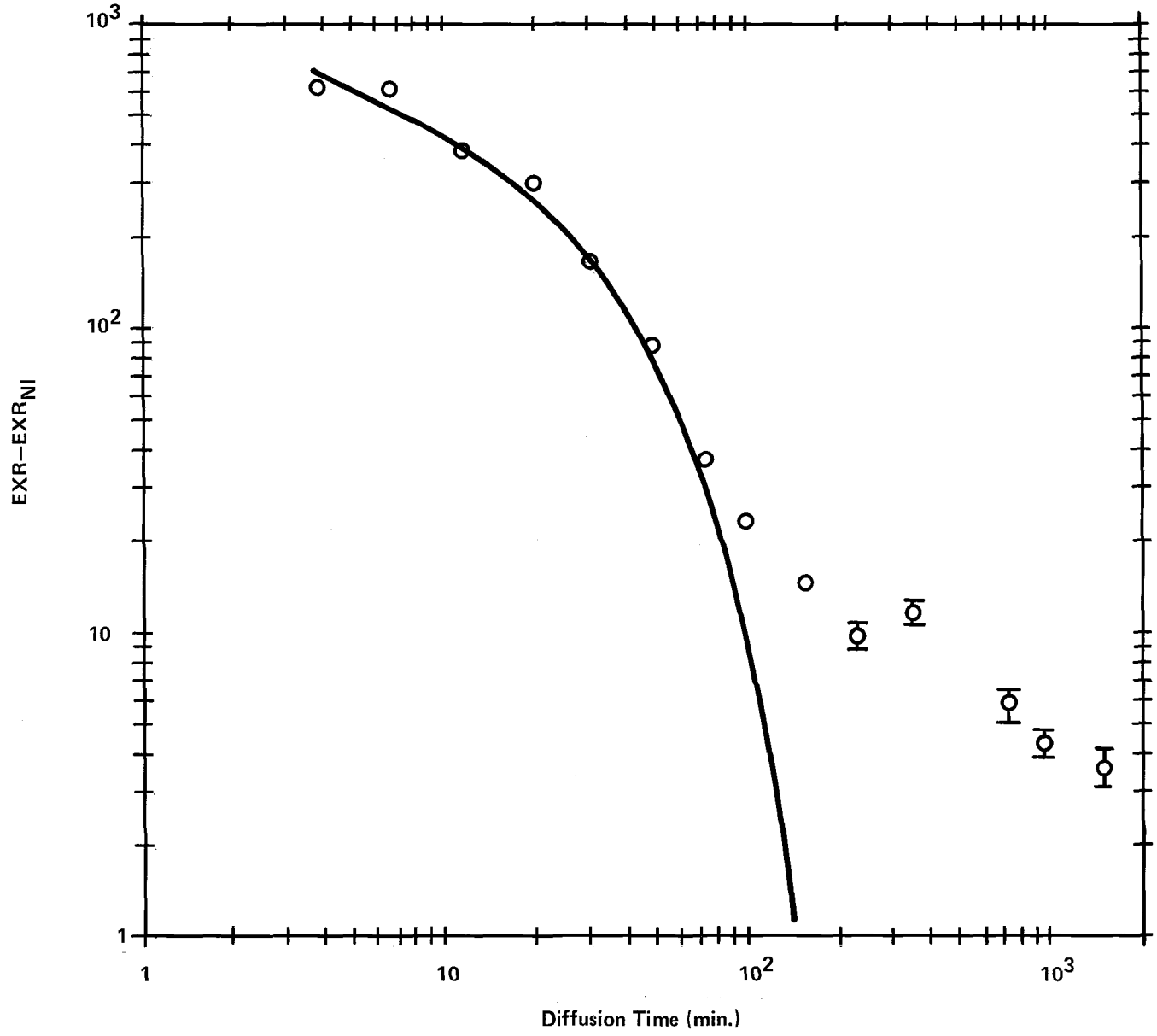

Figure 4-6. Data and curve for synthetic ore. Curve calculated with $D_{obs}=1.21x10^{-3}cm^2/s$

the sealed state for a day, and again run in the exhalation apparatus. Table 4-5 contains the data for the injected run as well as interpolated values for no injection at the new flow rate. The values for EXR_{NI} could have been ignored as they might have been in the case of the synthetic ore.

Eighteen combinations of times t_1 and t_2 are contained in Table 4-6 together with their calculated results from equation 4-21. The average observed diffusion coefficient was 7.1 x 10^{-4} cm^2/s with a relative standard deviation of 20 percent over a range of 4 to 52 minutes. The data of Table 4-5 has been plotted in Figure 4-7 along with a curve calculated from equation 4-21 and D_{obs} = 7.12 x 10^{-4} cm^2/s.

The Disc with 17.0 Percent of Moisture Saturation. - The sealed disc was first equilibrated with the applied moisture and its own source of radon before the end plates and external paraffin were removed. The data of Table 4-7 then was obtained for use with equation 4-20. The same general ranges of values for t_1 and t_2 as those for the dry disc were used with the data at this degree of moisture saturation (Table 4-8). The observed diffusion coefficients from the 25 combinations of t_1 and t_2 averaged 4.4 x 10^{-4} cm^2/s with a relative standard deviation of 36 percent. Figure 4-8 contains a plot of the data of Table 4-7 together with a curve calculated from equation 4-20 and D_{obs} = 4.40 x 10^{-4} cm^2/s (program BJT06*UC359PGM1.1) (Appendix G).

The Disc with 29.6 Percent of Moisture Saturation. - This was the degree of moisture saturation of the disc as machined, then sealed for equilibration. Table 4-9 contains the data obtained after equilibration and removal of the end plates and excess paraffin. In order to minimize the effects of poor counting statistics, the points for t_2 (Table 4-10) were taken somewhat longer than usual after those of t_1. However, the effects on the average observed diffusion coefficient (3.0 x 10^{-4} cm^2/s) were not large. The data and calculated curve have been plotted in Figure 4-9.

The Disc with 67.4 Percent of Moisture Saturation. - Table 4-11 contains the data from which the average value of the observed diffusion coefficient was 3.34 x 10^{-4} cm^2/s (Table 4-12). The data and calculated curve have been plotted in Figure 4-10.

Diffusion Perpendicular to the Bedding Plane

The Disc with 12.9 Percent of Moisture Saturation. - This disc had a thickness of 2.63 cm and a diameter of 6.8 cm. Table 4-13 contains the exhalation data from which the calculations yielded the average observed diffusion coefficient of 7.15 x 10^{-4} cm^2/s from Table 4-14. The data and calculated curve have been plotted in Figure 4-11.

TABLE 4-5. Exhalation data for the dried disc of WG1 with the axis parallel to the bedding plane after injection with radon

(23°C, 0.85 atm)

Diffusion time (min)	EXR (c/min)[1]	EXR_{NI} (c/min)[1]
1.7	18,290. ± 90.	13.
2.7	11,090. ± 80.	7.
3.7	8,850. ± 70.	4.
4.7	7,010. ± 60.	3.
6.7	4,960. ± 40.	2.
8.7	3,930. ± 30.	1.
11.7	2,650. ± 30.	1.
14.7	2,550. ± 20.	1.
17.7	1,730. ± 20.	0.
20.7	1,840. ± 20.	0.
23.7	1,430. ± 10.	0.
29.7	980. ± 10.	0.
51.7	448. ± 7.	0.
119.7	245. ± 6.	0.
227.7	113. ± 2.	0.
462.6	67.3 ± 1.	0.
1,390.7	10.1 ± 0.5	0.

[1]For 720 cm^3/min of flow rate

TABLE 4-6. Observed diffusion coefficients (cm^2/s) for the dried disc of WG1 with the axis parallel to the bedding plane

(23^oC, 0.85 atm)

Time (min) Point 2 =	23.7	29.7	51.7
Time (min) of point 1			
3.7	9.80×10^{-4}	9.13×10^{-4}	6.58×10^{-4}
4.7	9.10×10^{-4}	8.60×10^{-4}	6.28×10^{-4}
6.7	8.07×10^{-4}	7.80×10^{-4}	5.83×10^{-4}
8.7	7.47×10^{-4}	7.38×10^{-4}	5.58×10^{-4}
11.7	5.56×10^{-4}	6.18×10^{-4}	4.93×10^{-4}
14.7	7.18×10^{-4}	7.17×10^{-4}	5.25×10^{-4}
Av. D_{obs} = $(7.12 \pm 1.43) \times 10^{-4}$ cm^2/s			

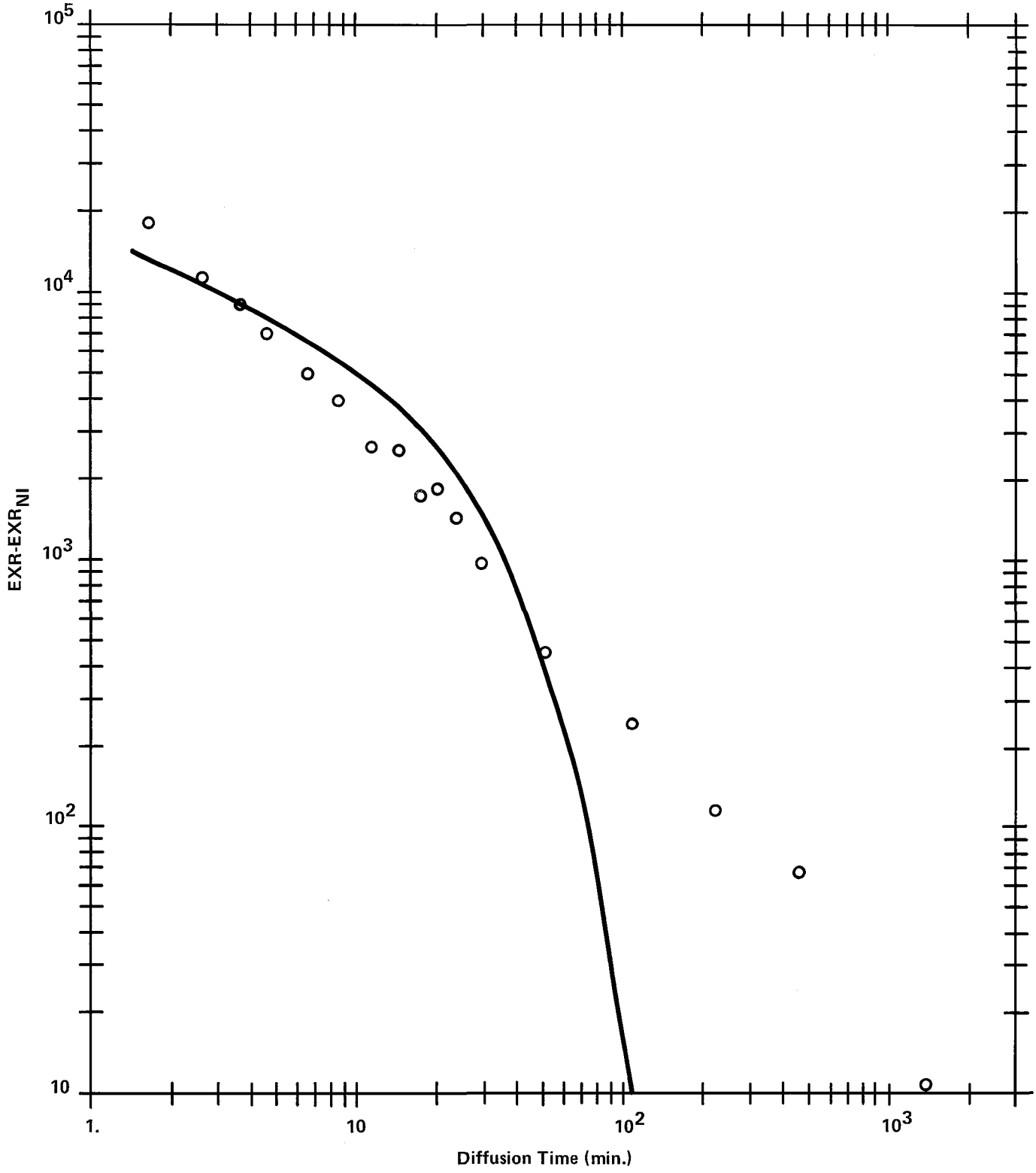

Figure 4-7. Dry disc of WG1 with axis parallel to bedding plane.
Curve calculated for $D_{obs}=7.12\times10^{-4}cm^2/s$.

TABLE 4-7. Exhalation data for 17.0 percent of moisture saturation in disc WG1 with the axis parallel to the bedding plane

(23°C, 0.85 atm)

Diffusion time (min)	Exhalation rate (c/min)[1]
1.6	261. ± 5.
3.6	93. ± 3.
5.2	70. ± 3.
7.6	49. ± 2.
10.1	32. ± 2.
12.6	28. ± 2.
16.6	24. ± 2.
21.6	12. ± 1.
26.6	18. ± 1.
34.6	12. ± 1.
44.6	8.9 ± 0.7
59.6	10.0 ± 0.7
79.6	5.8 ± 0.5
109.6	7.4 ± 0.5
157.6	4.7 ± 0.3
179.6	3.4 ± 0.3
1,500.0	0.4 ± 0.2 = EXR_{ss}

[1]For 610 cm^3/min of flow rate

TABLE 4-8. Observed diffusion coefficients (cm^2/s) with 17.0 percent of saturation in disc WG1 and the axis parallel to the bedding plane

(23^oC, 0.85 atm)

Time (min) of point 2 =	26.6	34.6	44.6	59.6	79.6
Time (min) of point 1					
3.6	7.45×10^{-4}	6.98×10^{-4}	5.97×10^{-4}	3.81×10^{-4}	3.62×10^{-4}
5.2	6.95×10^{-4}	6.64×10^{-4}	5.70×10^{-4}	3.60×10^{-4}	3.47×20^{-4}
7.6	5.77×10^{-4}	5.81×10^{-4}	5.08×10^{-4}	3.10×10^{-4}	3.13×10^{-4}
10.1	3.56×10^{-4}	4.49×10^{-4}	4.13×10^{-4}	2.30×10^{-4}	2.62×10^{-4}
12.6	3.02×10^{-4}	4.28×10^{-4}	3.97×10^{-4}	2.14×10^{-4}	2.52×10^{-4}

Av. $D_{obs} = (4.40 \pm 1.59) \times 10^{-4}$ cm^2/s

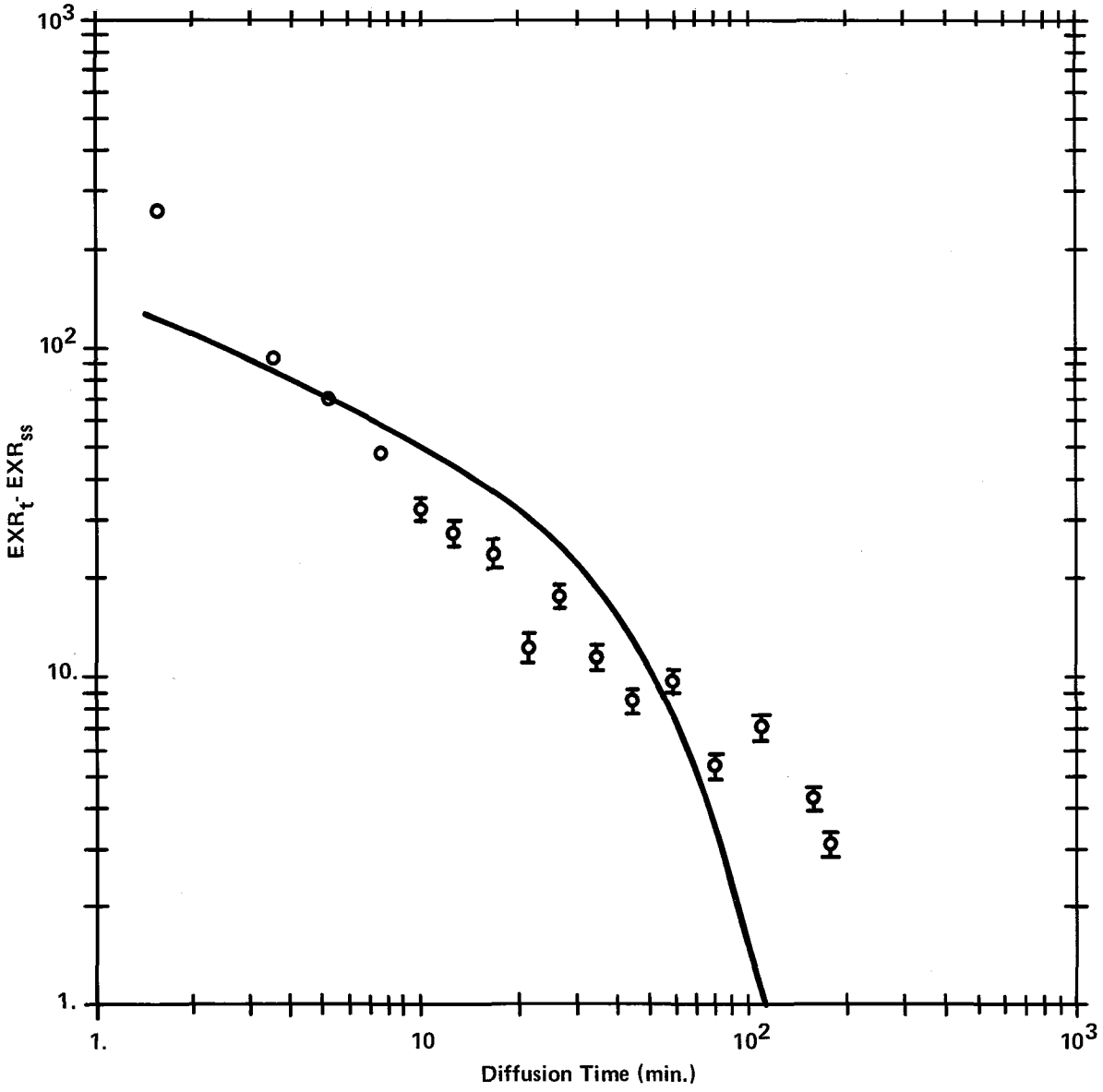

Figure 4-8. Disc WG1 with 17.0% moisture saturation and axis parallel to bedding plane. Curve calculated for $D_{obs}=4.40\times10^{-4}cm^2/s$

TABLE 4-9. Exhalation data for 29.6 percent of moisture saturation in disc WG1 with the axis parallel to the bedding plane

(23°C, 0.85 atm)

Diffusion time (min)	Exhalation rate (c/min)[1]
5.0	12. ± 1.
7.8	9. ± 1.
10.0	5.4 ± 0.8
11.8	3.5 ± 0.7
14.0	5.4 ± 0.7
15.8	5.1 ± 0.8
18.3	3.3 ± 0.7
23.0	2.0 ± 0.6
28.0	1.8 ± 0.5
38.0	2.3 ± 0.5
53.0	1.6 ± 0.5
71.5	0.9 ± 0.4
98.0	1.2 ± 0.7
158.0	0.8 ± 0.1
545.0	0.42 ± 0.05
1,184.0	0.40 ± 0.05
1,350.0	0.27 ± 0.05
1,588.0	0.41 ± 0.06
3,244.0	0.39 ± 0.05
4,298.0	0.34 ± 0.05
4,328.0	0.31 ± 0.05
	EXR_{SS} = 0.33

[1]For 3,000 cm^3/min of flow rate

TABLE 4-10. Observed diffusion coefficients (cm^2/s) with 29.6 percent of saturation in disc WG1 and the axis parallel to the bedding plane

(23^oC, 0.85 atm)

Time (min) of point 2 =	53.0	71.5	98.0	158.0
Time (min) of point 1				
5.0	4.82×10^{-4}	4.91×10^{-4}	2.75×10^{-4}	2.11×10^{-4}
10.0	3.34×10^{-4}	3.92×10^{-4}	1.96×10^{-4}	3.73×10^{-4}
14.0	3.89×10^{-4}	4.29×10^{-4}	2.24×10^{-4}	1.81×10^{-4}
18.3	2.58×10^{-4}	2.08×10^{-4}	1.57×10^{-4}	1.44×10^{-4}

Av. $D_{obs} = (2.97 \pm 1.16) \times 10^{-4}$ cm^2/s

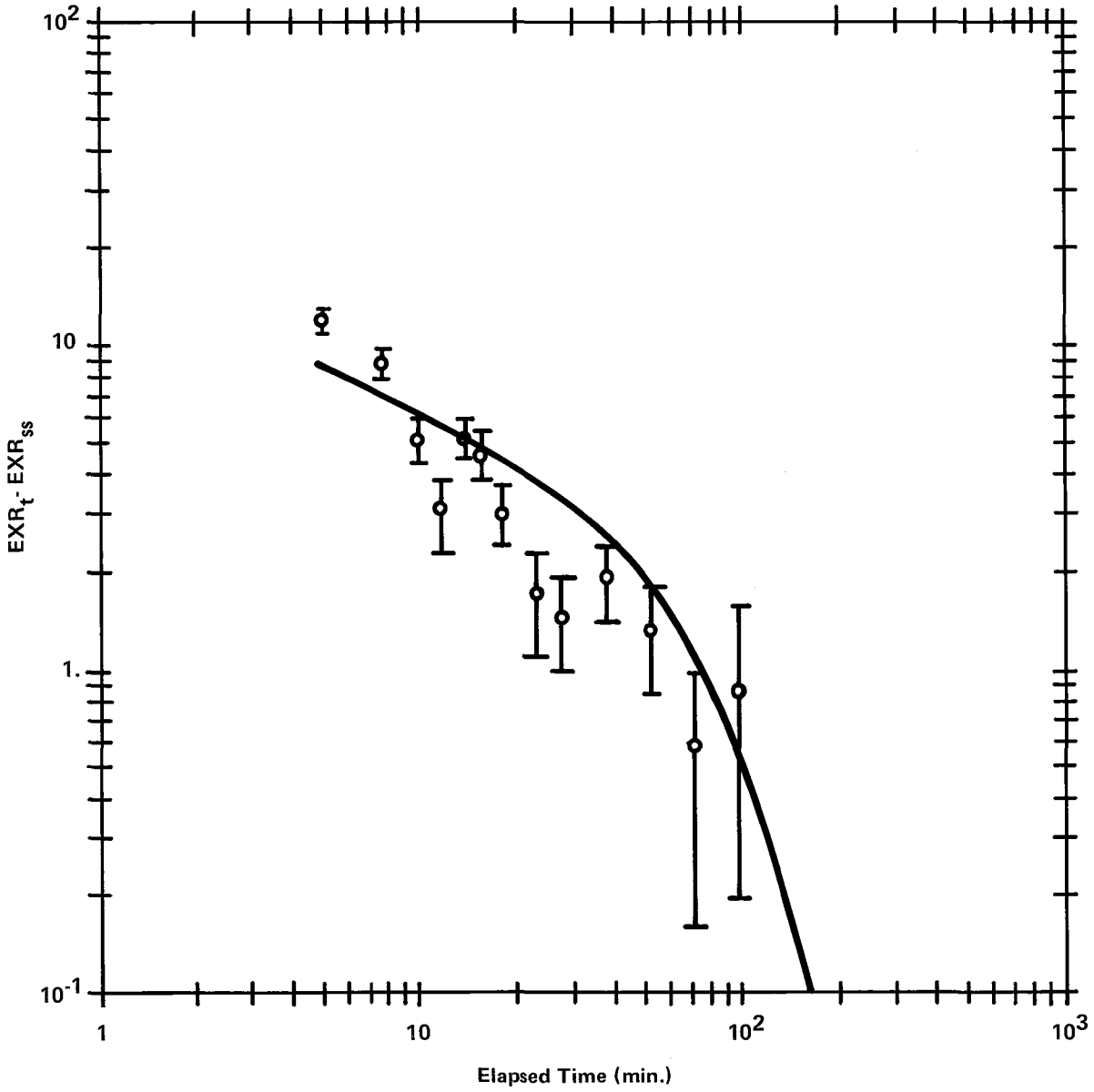

Figure 4-9. Disc WG1 with 29.6% moisture saturation and axis parallel to bedding plane. Curve calculated for $D_{obs}=2.97 \times 10^{-4} cm^2/s$

TABLE 4-11. Exhalation data for 67.4 percent of moisture saturation in disc WG1 with the axis parallel to the bedding plane

(23°C, 0.85 atm)

Diffusion time (min)	Exhalation rate (c/min)[1]
3.1	610. ± 10.
5.1	369. ± 6.
7.2	306. ± 5.
9.2	238. ± 5.
13.4	177. ± 3.
19.1	145. ± 4.
23.1	116. ± 3.
27.6	99. ± 3.
33.1	79. ± 3.
48.1	51. ± 2.
64.1	46. ± 2.
104.1	26. ± 2.
163.1	17. ± 1.
228.1	14. ± 1.
331.1	11.8 ± 0.4
469.1	8.6 ± 0.4
1211.1	4.9 ± 0.2
2907.0	4.3 ± 0.2
3181.0	4.8 ± 0.2
	EXR_{ss} = 4.6

[1]For 269 cm^3/min of flow rate

TABLE 4-12. Observed diffusion coefficients (cm^2/s) with 67.4 percent of saturation in disc WG1 and the axis parallel to the bedding plane

(23^oC, 0.85 atm)

Time (min) of point 2 =	48.1	64.1	104.1	163.1
Time (min) of point 1				
5.1	5.23×10^{-4}	3.85×10^{-4}	2.99×10^{-4}	2.17×10^{-4}
7.2	5.17×10^{-4}	3.81×10^{-4}	2.96×10^{-4}	2.16×10^{-4}
9.2	4.74×10^{-4}	3.47×10^{-4}	2.78×10^{-4}	2.04×10^{-4}
13.4	4.38×10^{-4}	3.18×10^{-4}	2.61×10^{-4}	1.94×10^{-4}

Av. D_{obs} = $(3.34 \pm 1.10) \times 10^{-4}$ cm^2/s

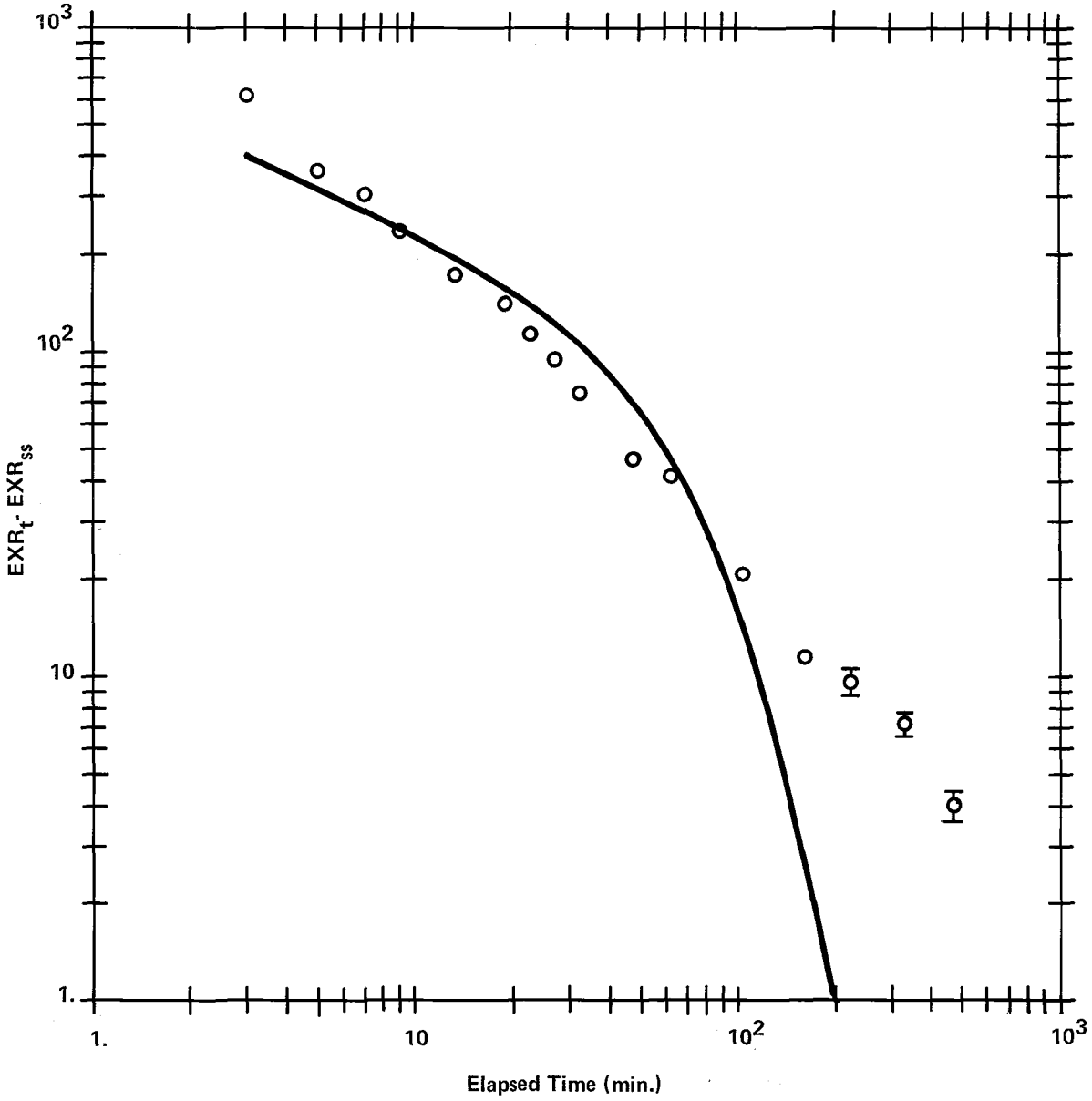

Figure 4-10. Disc WG1 with 67.4% moisture saturation and axis parallel to bedding plane. Curve calculated for $D_{obs}=3.34x10^{-4}cm^2/s$

TABLE 4-13. Exhalation data for 12.9 percent of moisture saturation in disc WG1 with the axis perpendicular to the bedding plane

(24°C, 0.85 atm)

Diffusion time (min)	Exhalation rate (c/min)[1]
1.3	524. ± 8.
2.8	198. ± 4.
4.8	88. ± 3.
6.8	56. ± 2.
8.8	41. ± 2.
11.8	29. ± 2.
15.8	23. ± 2.
20.8	16. ± 2.
26.8	10. ± 2.
34.8	8. ± 1.
44.8	8. ± 2.
59.8	5. ± 1.
79.8	2.7 ± 0.9
109.8	1. ± 1.
139.8	0.3 ± 1.0
169.8	0.7 ± 1.0
	EXR_{ss} = approx. 0

[1]For 1210. cm^3/min of flow rate

TABLE 4-14. Observed diffusion coefficients (cm^2/s) with 12.9 percent of saturation in disc WG1 and the axis perpendicular to the bedding plane

(24^oC, 0.85 atm)

Time (min) of point 2 =	26.8	34.8	44.8	59.8	79.8
Time (min) of point 1					
2.8	1.40×10^{-3}	1.11×10^{-3}	8.42×10^{-4}	7.17×10^{-4}	6.05×10^{-4}
4.8	1.123×10^{-3}	8.92×10^{-4}	6.70×10^{-4}	5.91×10^{-4}	5.14×10^{-4}
6.8	9.81×10^{-4}	7.79×10^{-4}	5.80×10^{-4}	5.26×10^{-4}	4.66×10^{-4}
8.8	8.97×10^{-4}	7.08×10^{-4}	5.21×10^{-4}	$4.84.10^{-4}$	4.36×10^{-4}
11.8	7.90×10^{-4}	6.16×10^{-4}	4.43×10^{-4}	4.30×10^{-4}	7.37×10^{-4}

Av. $D_{obs} = (7.15 \pm 2.48) \times 10^{-4}$ cm^2/s

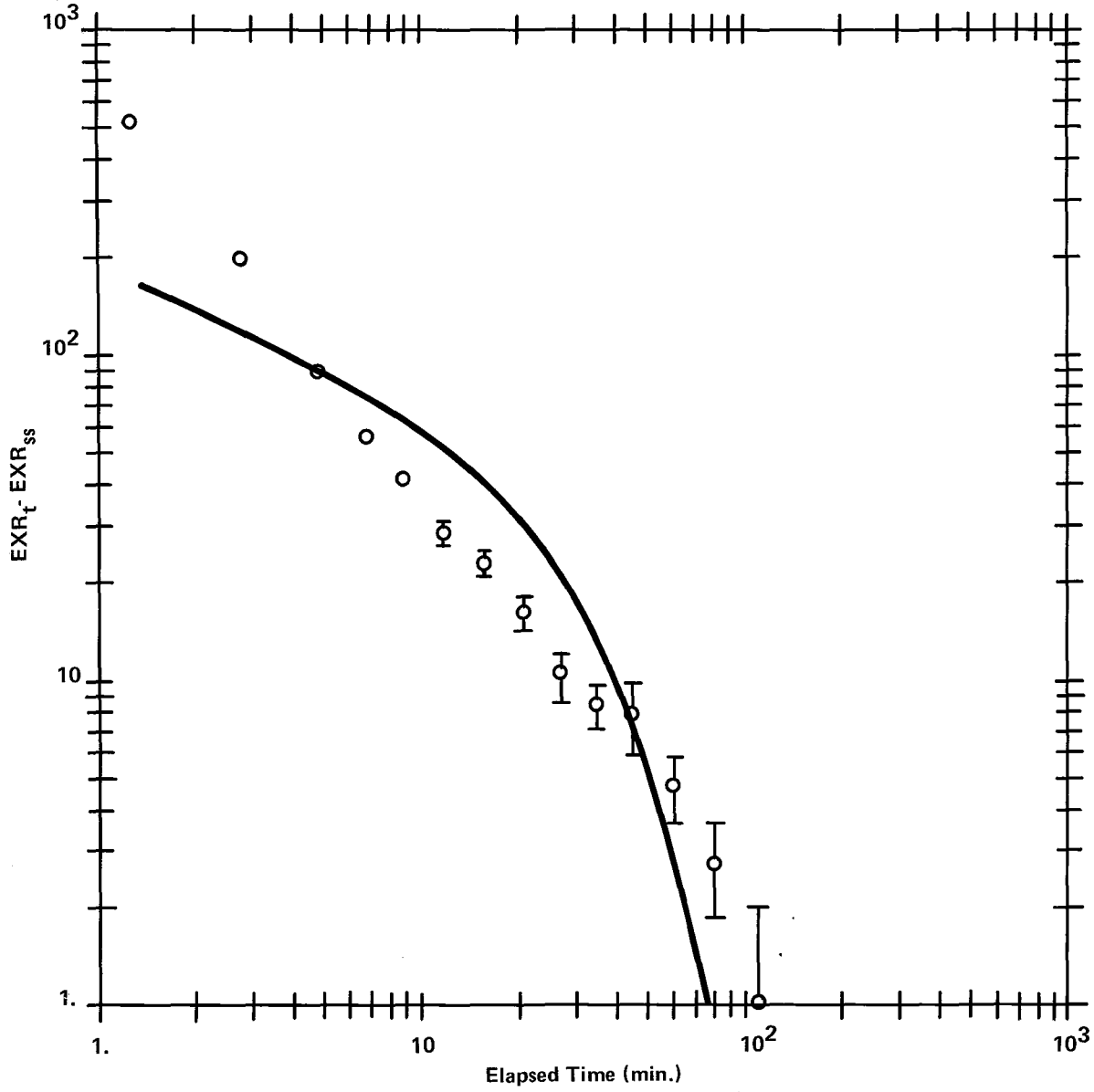

Figure 4-11. Disc WG1 with 12.9% moisture saturation and axis perpendicular to bedding plane. Curve calculated for $D_{obs}=7.15x10^{-4}cm^2/s$

The Disc with 29.5 Percent of Moisture Saturation. - Table 4-15 contains the exhalation data from which the calculations of Table 4-16 gave an average observed diffusion coefficient of 2.58×10^{-4} cm^2/s. Figure 4-12 contains the data and calculated curve.

Radon's Distribution Coefficient for Ore WG1

The weight W_{ore} was 37.7 g of which 2.803 weight percent was moisture. Its dry bulk density was 1.9776 g/cm^3 and its dry porosity was 23.41 percent. The volumes V_{a1} and V_a' were 80 ± 5 cm^3 and 121 ± 5 cm^3, respectively. The first two scintillation cells gave values of 4,477 and 4,817 for R_1', that is, an average of $4,647 \pm 240$. The last two scintillation cells gave values of 2,192 and 2,311 for R_2 at the same time of reference, that is an average of $2,252 \pm 85$. (The errors from counting statistics were negligible.) The value of the distribution coefficient k_{tot} for the whole sample was calculated from equation 4-23 to be (0.90 ± 0.44) cm^3/g including the propagation of errors. This includes some absorption by the small amount of the sample's moisture since water's absorption coefficient at the 25°C of the experiment is 0.22 cm^3/g(42). Using the law of mixtures enables the calculation of just moist WG1 ore's distribution coefficient to be (0.91 ± 0.45) cm^3/g where the air space is intended to include the air of the pores. This is (2.36 ± 1.16) cm^3/cm^3 in dimensionless units.

The Ore of Utah Big Buck (UB)

Diffusion Parallel to the Bedding Plane

The Dry Disc. - The disc with its axis parallel to the bedding plane had a thickness of 2.70 cm and a diameter of 6.7 cm. Its data (Table 4-17) was obtained for use with equation 4-12 and led to the results of Table 4-18. The data and curve calculated from the average observed diffusion coefficient of $(4.41 \pm 0.71) \times 10^{-5}$ cm^2/s have been plotted in Figure 4-13.

The Disc with 93.0 Percent of Moisture Saturation. - The data (Table 4-19) gave rise to the calculated results of Table 4-20. The average observed diffusion coefficient of $(1.21 \pm 0.39) \times 10^{-4}$ cm^2/s resulted in the curve of Figure 4-14.

Diffusion Perpendicular to the Bedding Plane

The Dry Disc. - This disc had a thickness of 2.70 cm and a diameter of 6.6 cm. Table 4-21 contains the data from which the results of Table 4-22 were obtained. The curve of Figure 4-15 was calculated with 5.19×10^{-4} cm^2/s for the average observed diffusion coefficient.

TABLE 4-15. Exhalation data for 29.5 percent of moisture saturation in disc WG1 with the axis perpendicular to the bedding plane

(25°C, 0.85 atm)

Diffusion time (min)	Exhalation rate (c/min)[1]
8.7	160. ± 4.
12.7	100. ± 3.
17.7	102. ± 3.
27.7	88. ± 3.
37.7	65. ± 3.
47.7	48. ± 2.
57.7	42. ± 2.
67.7	39. ± 2.
81.7	37. ± 2.
101.7	29. ± 2.
131.7	24. ± 2.
181.7	22. ± 1.
241.7	17. ± 1.
297.7	16. ± 1.
626.7	11.9 ± 0.8
1617.0	8.6 ± 0.3
2757.0	9.6 ± 0.3
3062.0	8.8 ± 0.2
	EXR_{ss} = 9.1 ± 0.2

[1]For 305. cm^3/min of air flow

TABLE 4-16. Observed diffusion coefficients (cm^2/s) with 29.5 percent of saturation in disc WG1 and the axis perpendicular to the bedding plane

(25^oC, 0.85 atm)

Time (min) of point 2 =	47.7	57.7	67.7	81.7
Time (min) of point 1				
8.7	3.73×10^{-4}	3.29×10^{-4}	2.81×10^{-4}	2.28×10^{-4}
12.7	2.43×10^{-4}	2.28×10^{-4}	1.95×10^{-4}	1.56×10^{-4}
17.7	3.30×10^{-4}	2.93×10^{-4}	2.49×10^{-4}	2.01×10^{-4}
Av. D_{obs} = $(2.58 \pm 0.64) \times 10^{-4}$ cm^2/s				

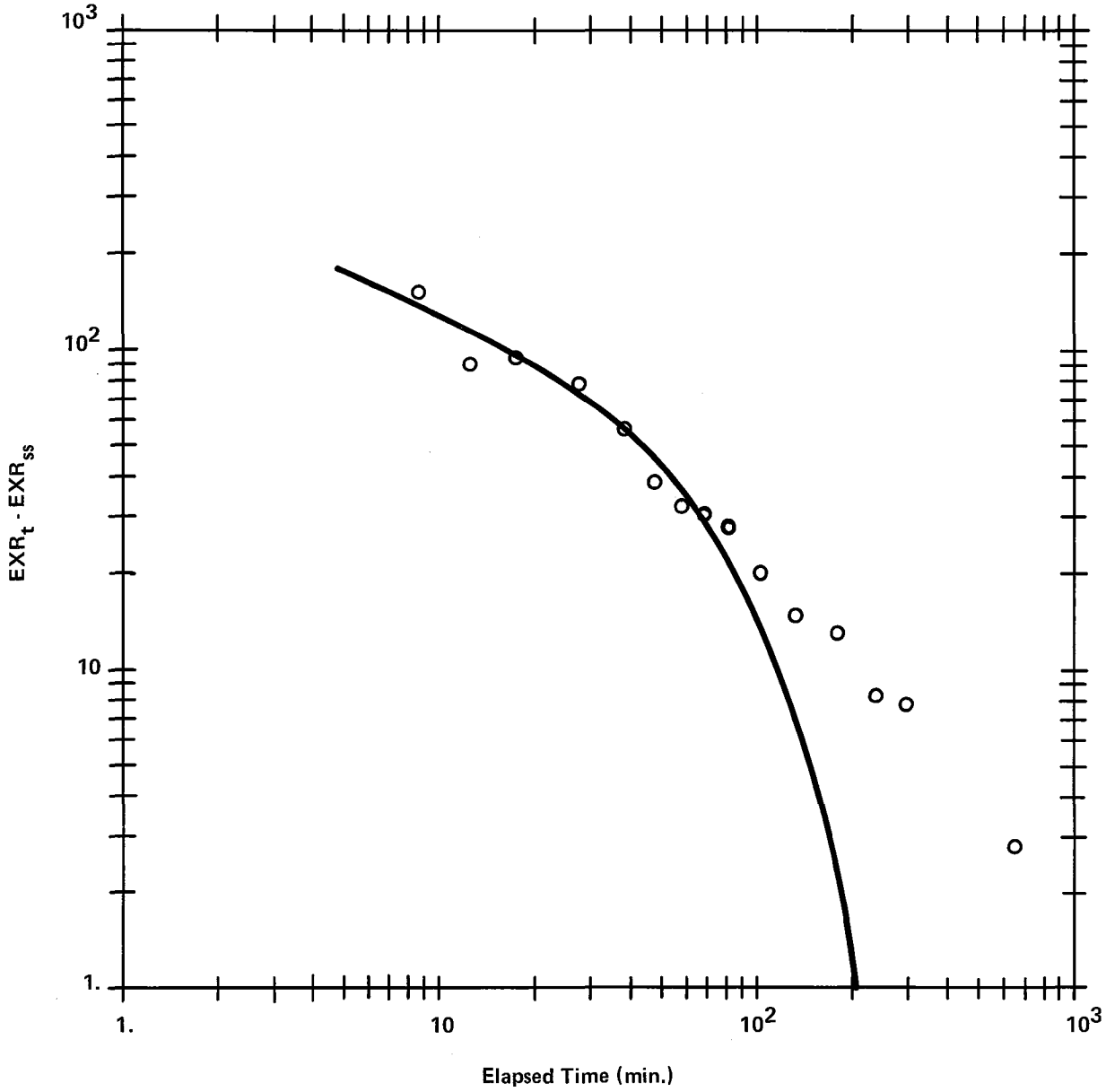

Figure 4-12. Disc WG1 with 29.5% moisture saturation and axis perpendicular to bedding plane. Curve calculated for $D_{obs}=2.58x10^{-4}cm^2/s$

TABLE 4-17. Exhalation data for dried disc UB with the axis parallel to the bedding plane

(24.5°C, 0.85 atm)

Diffusion time (min)	Exhalation rate (c/min)[1]
2.4	93. ± 3.
3.9	71. ± 3.
6.4	59. ± 2.
9.4	47. ± 2.
14.4	44. ± 2.
22.4	35. ± 2.
34.4	22. ± 2.
51.3	25. ± 2.
67.3	18. ± 1.
116.2	12. ± 1.
175.2	17. ± 1.
395.4	5.3 ± 0.7
607.4	4.0 ± 0.6
1,354.0	2.4 ± 0.4
1,667.0	2.2 ± 0.6
2,500.0	1.5 ± 0.3 = EXR_{ss}

[1]For 360 cm^3/min of air flow

TABLE 4-18. Observed diffusion coefficients (cm^2/s) with the dried disc UB having its axis parallel to the bedding plane

(24.5 °C, 0.85 atm)

Time (min) of point 2 =	395.4	607.4
Time (min) of point 1		
3.9	4.94×10^{-5}	3.71×10^{-5}
6.4	5.20×10^{-5}	3.86×10^{-5}
9.4	5.01×20^{-5}	3.75×10^{-5}

Av. D_{obs} = $(4.41 \pm 0.71) \times 10^{-5}$ cm^2/s

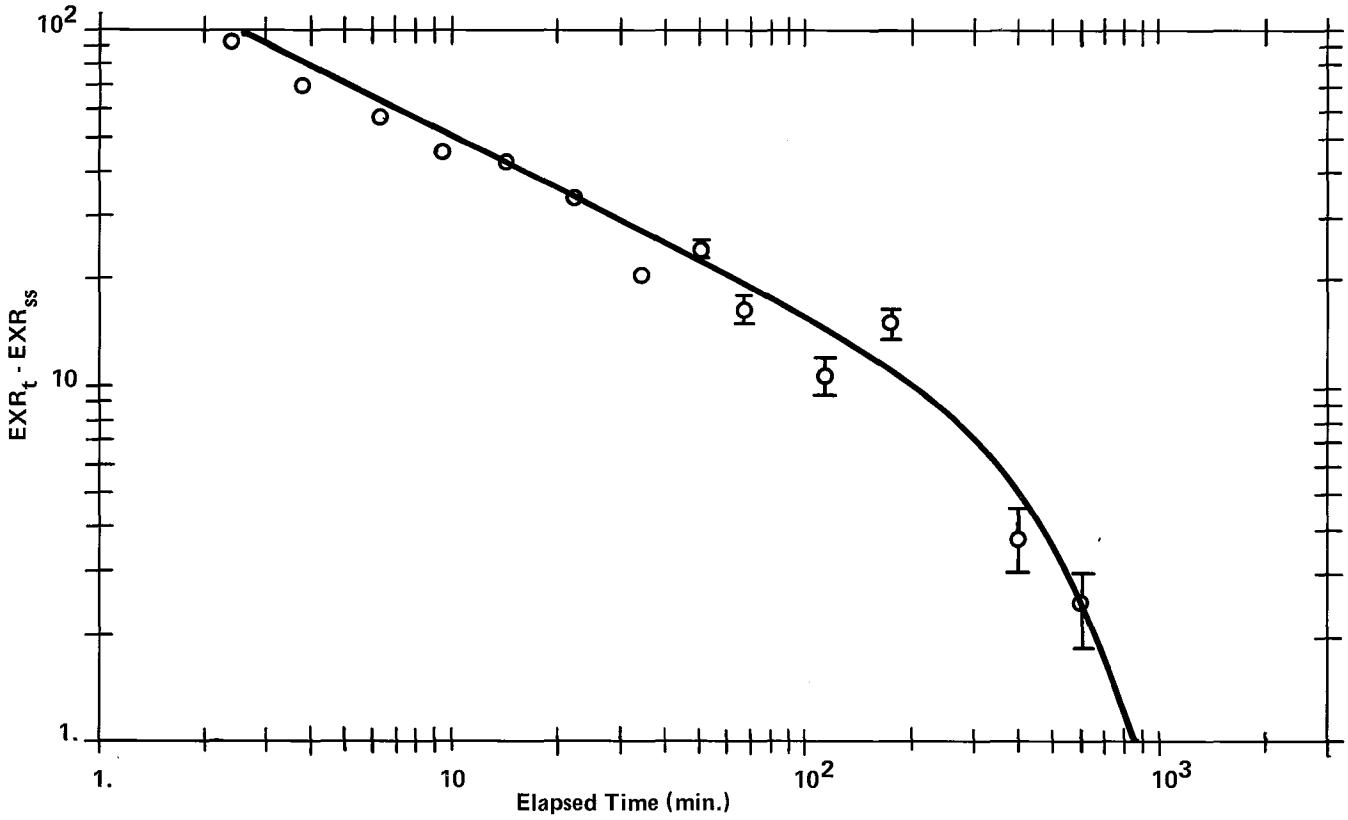

Figure 4-13. Dry disc of UB with axis parallel to bedding plane. Curve calculated for $D_{obs} = 4.41 \times 10^{-5}$ cm^2/s.

TABLE 4-19. Exhalation data for 93.0 percent of moisture saturation in disc UB with the axis parallel to the bedding plane

(23°C, 0.85 atm)

Diffusion time (min)	Exhalation rate (c/min)[1]
4.6	1410. ± 20.
7.6	1060. ± 20.
12.6	810. ± 10.
19.6	570. ± 10.
30.6	348. ± 6.
46.6	299. ± 6.
70.6	186. ± 4.
106.6	136. ± 4.
160.6	88. ± 4.
245.6	61. ± 2.
362.6	42. ± 1.
544.6	25.8 ± 0.9
993.1	16.0 ± 0.7
1893.0	12.9 ± 0.5
2719.0	12.1 ± 0.7
3337.0	11.6 ± 0.6
	EXR_{ss} = 11.0

[1]For 171 cm^3/min of air flow

TABLE 4-20. Observed diffusion coefficients (cm^2/s) with 93.0 percent of saturation in disc UB having its axis parallel to the bedding plane

($23^{o}C$, 0.85 atm)

Time (min) of point 2 =	160.6	245.6	362.6	544.6
Time (min) of point 1				
4.6	1.80×10^{-4}	1.30×10^{-4}	9.87×10^{-5}	7.97×10^{-5}
7.6	1.76×10^{-4}	1.28×10^{-4}	9.73×10^{-5}	7.88×10^{-5}
12.6	1.74×10^{-4}	1.27×10^{-4}	9.68×10^{-5}	7.83×10^{-5}

Av. $D_{obs} = (1.21 \pm 0.39) \times 10^{-4}$ cm^2/s

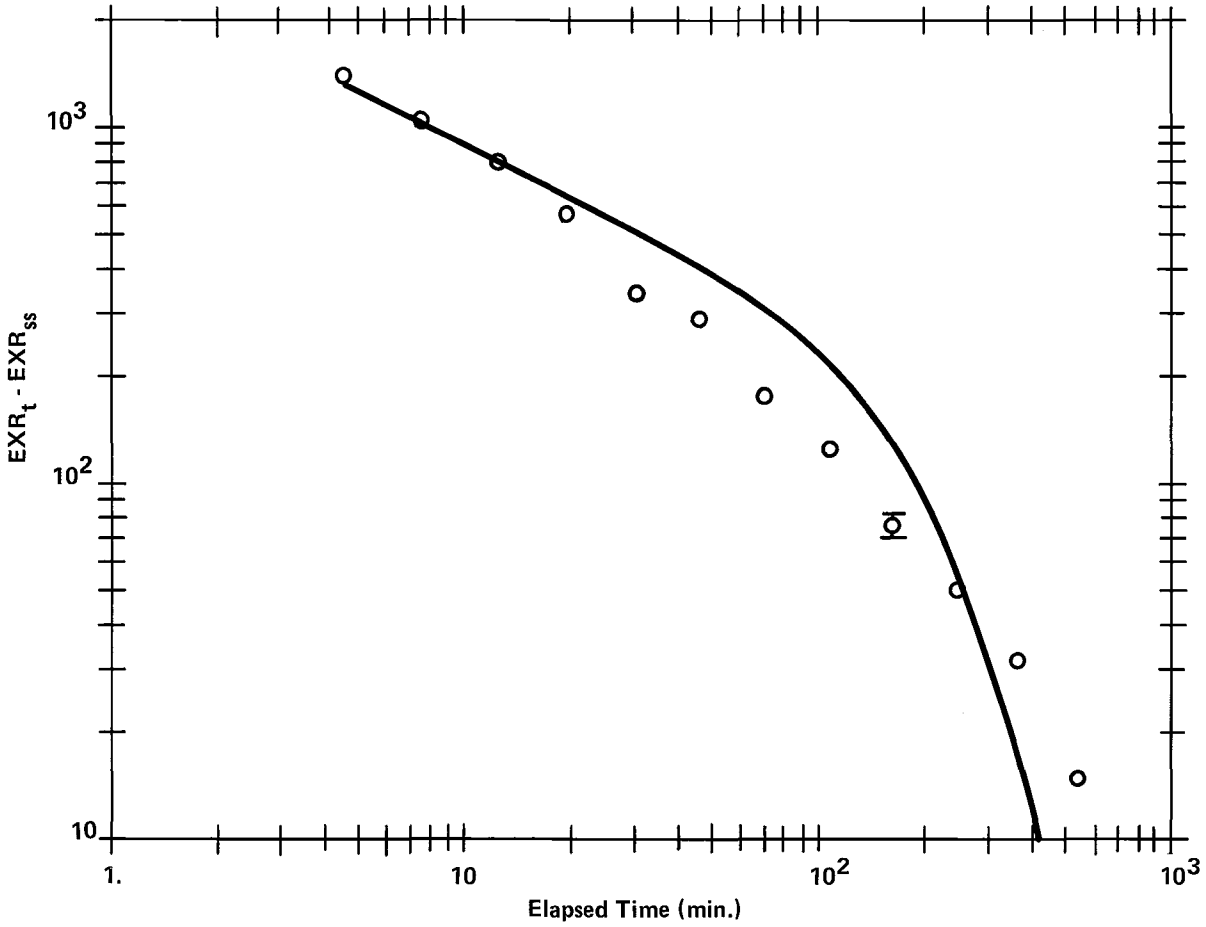

Figure 4-14. Disc UB with 93.0% moisture saturation and axis parallel to bedding plane.

Curve calculated for $D_{obs} = 1.21 \times 10^{-4}$ cm^2/s.

TABLE 4-21. Exhalation data for dried disc UB with axis perpendicular to the bedding plane

(23°C, 0.85 atm)

Diffusion time (min)	Exhalation rate (c/min)[1]
2.9	570. ± 10.
6.9	340. ± 9.
14.9	208. ± 5.
30.9	75. ± 3.
62.9	27. ± 1.
98.9	15. ± 1.
148.9	8. ± 1.
231.9	6.4 ± 0.4
345.0	4.5 ± 0.4
484.9	2.4 ± 0.2
1,362.0	1.3 ± 0.5
1,382.0	1.8 ± 0.6
	EXR_{ss} = 1.3

[1]For 240 cm^3/min of air flow

TABLE 4-22. Observed diffusion coefficients (cm^2/s) for dried disc UB having its axis perpendicular to the bedding plane

(23^oC, 0.85 atm)

Time (min) of point 2 =	30.9	62.9	98.9	148.9
Time (min) of point 1				
2.9	8.09×10^{-4}	5.69×10^{-4}	4.24×10^{-4}	3.35×10^{-4}
6.9	7.64×10^{-4}	5.48×10^{-4}	4.11×10^{-4}	3.27×10^{-4}
14.9	7.91×10^{-4}	5.32×10^{-4}	3.97×10^{-4}	3.17×10^{-4}

Av. $D_{obs} = (5.19 \pm 1.83) \times 10^{-4}$ cm^2/s

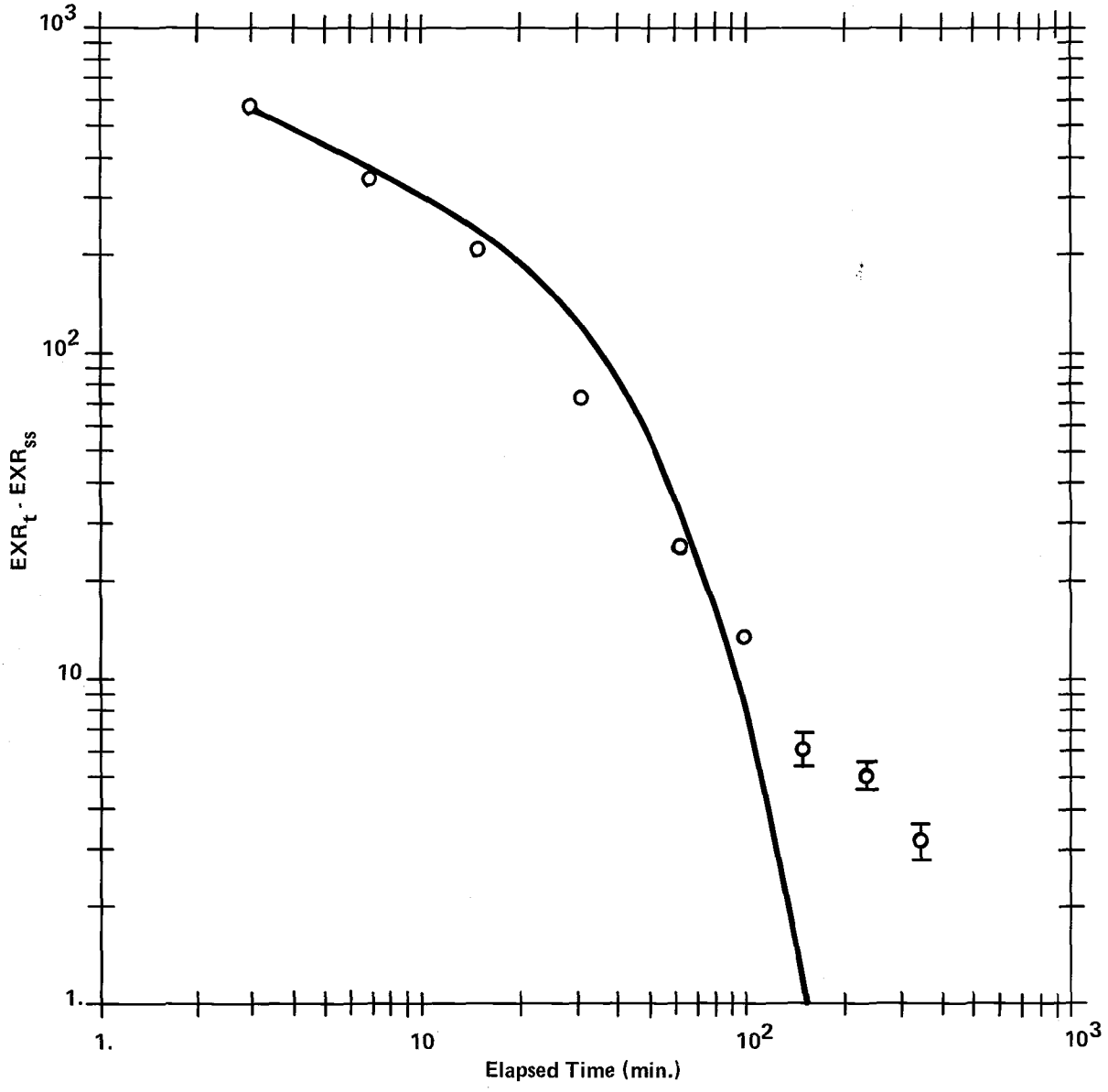

Figure 4-15. Dry disc of UB with axis perpendicular to bedding plane.

Curve calculated for D_{obs} = (5.19 $\pm$ 1.83) x 10^{-4} cm^2/s.

The Disc with 62.1 Percent of Moisture Saturation. - Table 4-23 contains the data obtained on the disc with the as-machined moisture content. The calculations are summarized in Table 4-24, giving (4.08 $\pm$ 1.46) x 10^{-4} cm^2/s for the average observed diffusion coefficient. Figure 4-16 contains the plotted data and calculated curve.

The No.1 Ore of Wyoming Crooks Gap (WC1)

The Dry Disc Parallel to the Bedding Plane

The disc had a thickness of 2.60 cm and a diameter of 6.5 cm. The data obtained in the dry state is in Table 4-25 and the calculations are summarized in Table 4-26. The average observed diffusion coefficient of (6.96 $\pm$ 2.91) x 10^{-4} cm^2/s gave the curve of Figure 4-17.

The Disc Parallel to the Bedding Plane and Having 64.1 Percent of Moisture Saturation

Table 4-27 contains the data from the disc with the as-machined moisture content. The calculated results are contained in Table 4-28. The average observed diffusion coefficient of (9.49 $\pm$ 3.90) x 10^{-4} cm^2/s gave the curve of Figure 4-18.

Discussion of Results

The Correlation of Steady-State Exhalation Rates with Microscopic Emanation Coefficients

As previously stated, the accurate measurement of exhalation rates in the steady state is hampered by low counting rates and therefore poor accuracy. Although the present methods do not require accurate steady-state values, it is interesting to apply an internal check on these values (Table 4-29 and Figure 4-19). The values of the microscopic emanation coefficient of Figure 4-19 are estimated from the equation

$$E_\mu = (SSEXR)/\{(No\ pCi\ Ra/g)\rho_{bulk}(\lambda D_{obs})^{\frac{1}{2}}\tanh\{(\lambda/D_{obs})^{\frac{1}{2}}L/2\}\} \quad (4\text{-}24)$$

where ρ_{bulk} is the sample's bulk density (g/cm^3) and

SSEXR is defined below Table 4-29.

The estimates for a given disc increase in a qualitative sense from the dry state as moisture is added. However, the values do not always agree quantitatively with those of Chapter 3. It would not be expected that an ore's curve in Figure 4-19 would rise markedly higher for the disc axis perpendicular to

TABLE 4-23. Exhalation data for 62.1 percent of moisture saturation in disc UB with the axis perpendicular to the bedding plane

(23°C, 0.85 atm)

Diffusion time (min)	Exhalation rate (c/min)[1]
4.5	1920. ± 20.
7.5	720. ± 10.
12.5	630. ± 10.
19.5	490. ± 10.
30.5	289. ± 8.
46.5	164. ± 6.
70.5	104. ± 3.
106.5	72. ± 2.
160.5	48. ± 1.
241.5	34. ± 1.
359.5	24.6 ± 0.8
414.5	29.6 ± 0.7
566.5	18.9 ± 0.8
1,401.0	18.3 ± 0.8
1,916.0	17.1 ± 0.8
2,833.0	15.8 ± 0.6
3,341.0	21.2 ± 0.7
	EXR_{ss} = 18.0

[1]For 165 cm^3/min of air flow

TABLE 4-24. Observed diffusion coefficients (cm^2/s) with 62.1 percent of moisture saturation in disc UB having its axis perpendicular to bedding plane

(23^oC, 0.85 atm)

Time (min) of point 2 =	46.5	70.5	106.5	160.5
Time (min) of point 1				
4.5	7.18×10^{-4}	5.41×10^{-4}	3.93×10^{-4}	2.95×10^{-4}
12.5	5.14×10^{-4}	4.09×10^{-4}	3.07×10^{-4}	2.39×10^{-4}
19.5	5.32×10^{-4}	4.08×10^{-4}	3.02×10^{-4}	2.35×10^{-4}

Av. D_{obs} = $(4.08 \pm 1.46) \times 10^{-4}$ cm^2/s

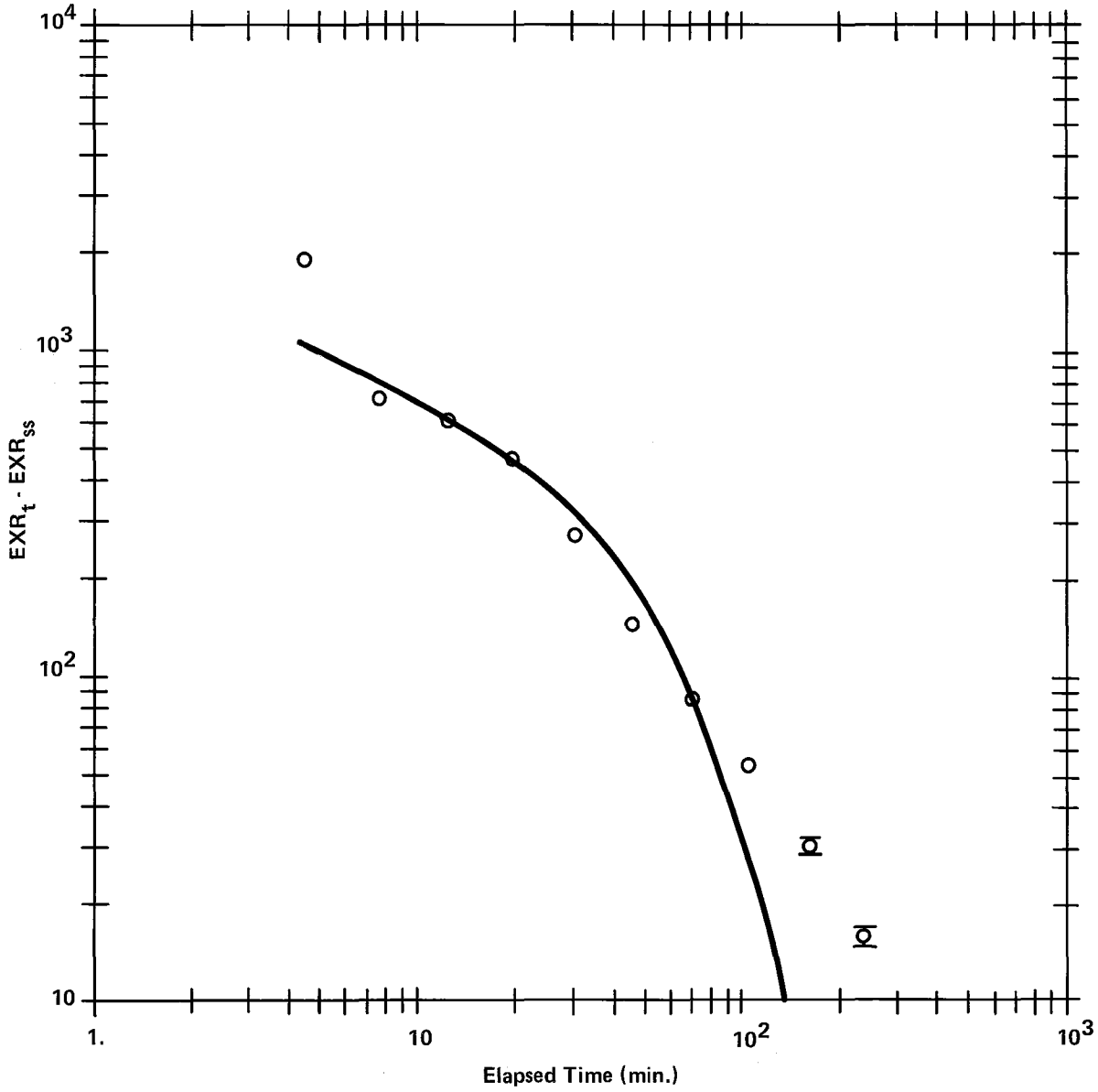

Figure 4-16. Disc UB with 62.1% of moisture saturation and with axis perpendicular to bedding plane.

Curve calculated for $D_{obs} = 4.08 \times 10^{-4}$ cm^2/s.

TABLE 4-25. Exhalation data for dried disc WC with the axis parallel to the bedding plane

(24.5°C, 0.85 atm)

Diffusion time (min)	Exhalation rate (c/min)[1]
2.7	530. ± 10.
4.2	363. ± 9.
6.7	225. ± 7.
9.7	132. ± 4.
14.7	97. ± 3.
22.2	57. ± 2.
33.7	29. ± 2.
50.7	20. ± 1.
75.7	13. ± 1.
113.7	9.0 ± 0.7
170.7	7.0 ± 0.7
263.7	3.8 ± 0.7
385.7	3.3 ± 0.6
578.7	3.2 ± 0.6
1,249.0	1.8 ± 0.6
1,630.0	2.4 ± 0.5
1,868.0	1.7 ± 0.5
2,807.0	1.8 ± 0.53
4,175.0	1.8 ± 0.55
	EXR_{ss} = 1.8

[1]For 780 cm^3/min of air flow

TABLE 4-26. Observed diffusion coefficients (cm^2/s) for the dried disc WC with its axis parallel to the bedding plane

(24.5^oC, 0.85 atm)

Time (min) of point 2 =	22.2	33.7	50.7	75.7	113.7
Time (min) of point 1					
2.7	1.275×10^{-3}	1.043×10^{-3}	0.745×10^{-3}	0.548×10^{-3}	0.393×10^{-3}
4.2	1.176×10^{-3}	0.980×10^{-3}	0.703×10^{-3}	0.520×10^{-3}	0.375×10^{-3}
6.7	1.028×10^{-3}	0.883×10^{-3}	0.636×10^{-3}	0.476×10^{-3}	0.345×10^{-3}
9.7	0.788×10^{-3}	0.743×10^{-3}	0.539×10^{-3}	0.412×10^{-3}	0.304×10^{-3}

Av. $D_{obs} = (6.96 \pm 2.91) \times 10^{-4}$ cm^2/s

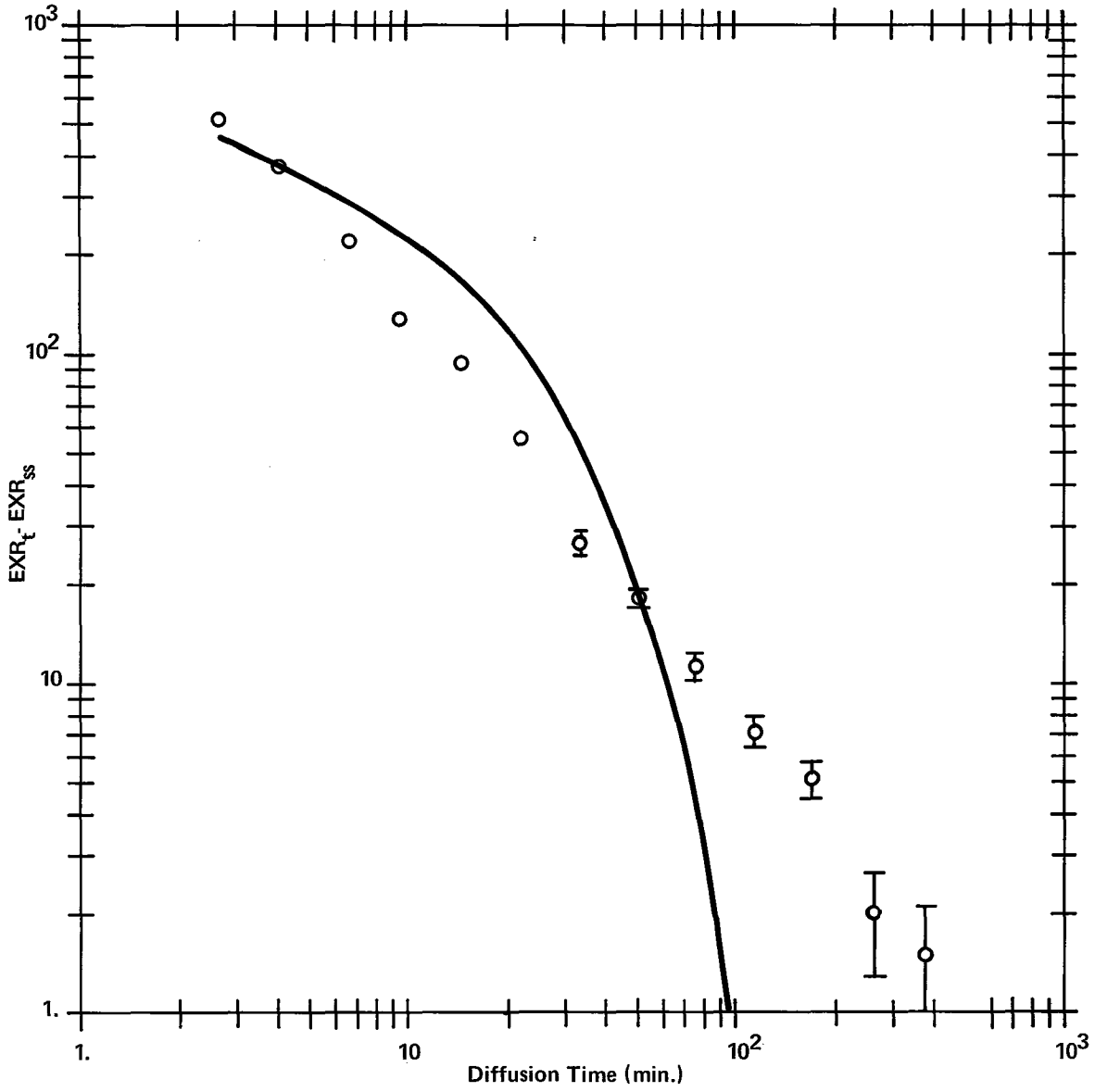

Figure 4-17. Dry disc of WC with axis parallel to bedding plane.
Curve calculated for $D_{obs}=6.96x10^{-4}cm^2/s$.

TABLE 4-27. Exhalation data for 64.1 percent of moisture saturation in disc WC with the disc axis perpendicular to the bedding plane

(22°C, 0.85 atm)

Diffusion time (min)	Exhalation rate (c/min)[1]
3.1	770. ± 10.
5.1	372. ± 9.
9.1	176. ± 6.
14.1	140. ± 5.
21.6	67. ± 3.
32.8	41. ± 2.
49.7	35. ± 2.
91.2	26. ± 1.
148.0	24. ± 1.
233.0	21.2 ± 0.9
361.0	20.7 ± 0.7
542.0	22.0 ± 0.5
849.0	16.0 ± 0.6
	EXR_{ss} = 19.0

[1]For 257 cm^3/min of air flow

TABLE 4-28. Observed diffusion coefficients (cm^2/s) with 64.1 percent of moisture saturation in disc WC with its axis parallel to bedding plane

($22^{o}C$, 0.85 atm)

Time (min) of point 2 =	21.6	32.8	49.7	91.2
Time (min) of point 1				
3.1	1.68×10^{-3}	1.34×10^{-3}	0.917×10^{-3}	0.566×10^{-3}
5.1	1.37×10^{-3}	1.14×10^{-3}	0.783×10^{-3}	0.495×10^{-3}
9.1	1.08×10^{-3}	0.946×10^{-3}	0.645×10^{-3}	0.420×10^{-3}

Av. D_{obs} = $(9.49 \pm 3.90) \times 10^{-4}$ cm^2/s

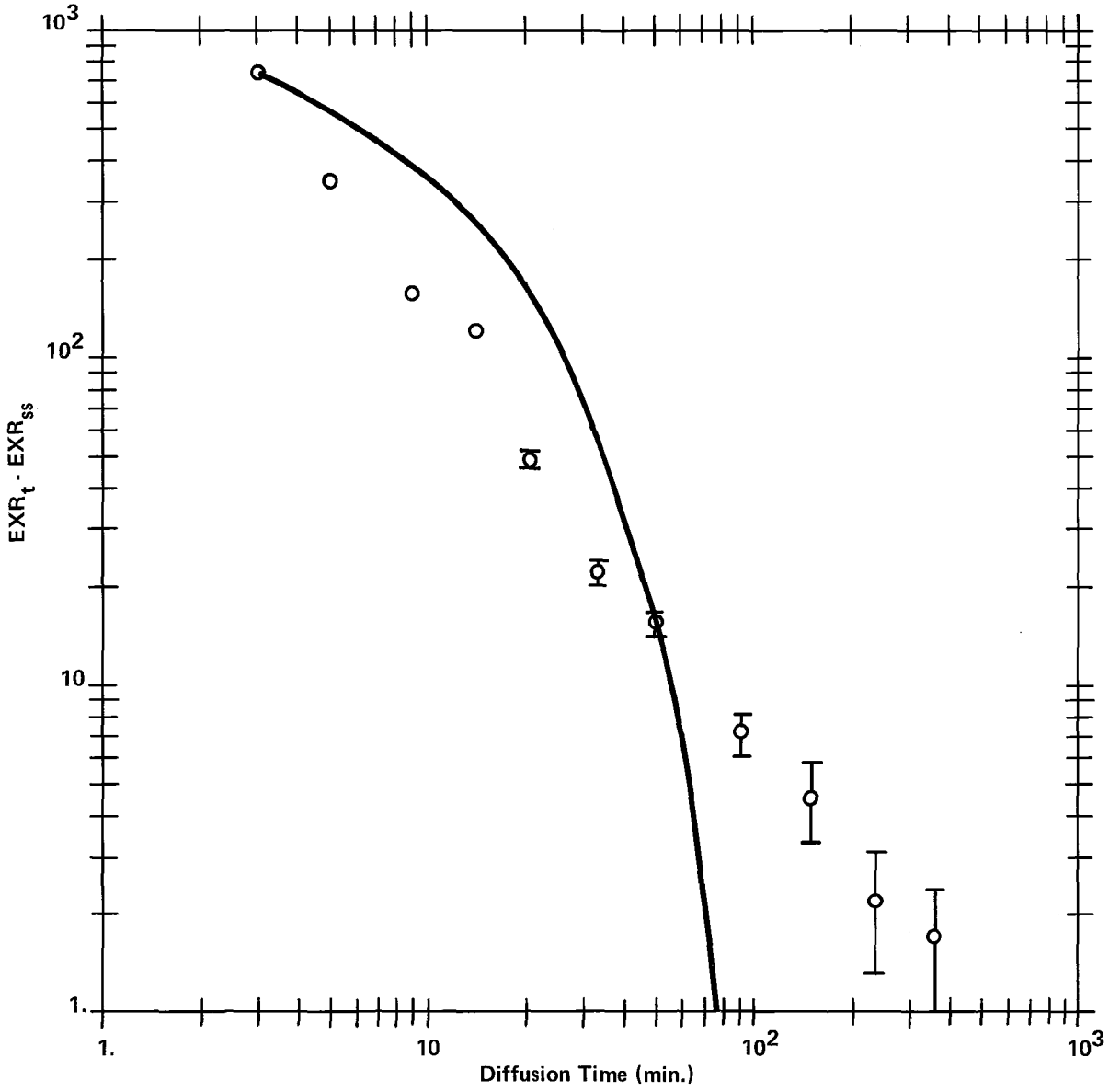

Figure 4-18. Disc WC with 64.1% of moisture saturation and with axis parallel to bedding plane. Curve calculated with $D_{obs}=9.49x10^{-4}cm^2/s$.

TABLE 4-29. Observed values of steady-state exhalation rates

Disc	% of sat	EXR_{ss}(c/min)[a] including Rn daughters	From Table	10^4xSSEXR (Rn pCi/cm^{2}s)[b]
WG1 (par)	0.0	0.0	4-4	0.
WG1 (par)	17.0	0.5	4-7	3.
WG1 (par)	29.6	2.0	4-9	11.
WG1 (par)	67.4	2.5	4-11	14.
WG1 (perp)	12.9	approx. 0	4-13	0.
WG1 (perp)	29.5	5.6	4-15	30.
UB (par)	0.0	1.1	4-17	6.
UB (par)	93.0	3.8	4-19	21.
UB (perp)	0.0	0.6	4-21	4.
UB (perp)	62.1	5.9	4-23	35.
WC1 (par)	0.0	2.8	4-25	17.
WC1 (par)	64.1	9.8	4-27	59.

[a]Calculated for an air flow of 500 cm^3/min

[b]The steady-state exhalation rate in Rn pCi/cm^{2}s can be shown to be

$$\text{SSEXR (Rn pCi/cm}^2\text{s)} = \frac{0.0219\ EXR_{ss}(\text{c/min})}{(\text{cell eff.})\ A_{tot}}$$

where the reference cell efficiency (cell eff.) = 0.55 in this diffusion work and A_{tot} is the total exposed area (cm^2) of the disc.

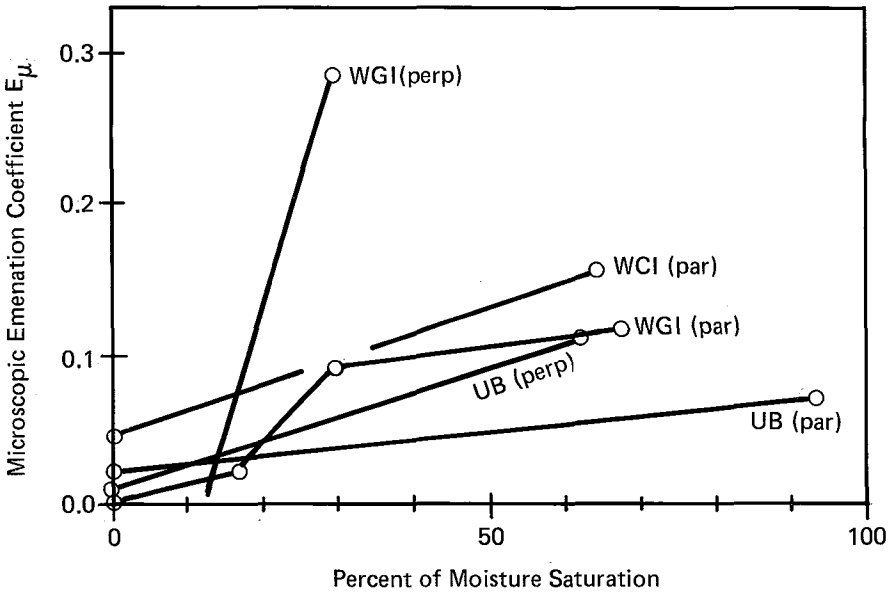

Figure 4-19. · Microscopic Emanation Coefficients Estimated from the Steady-State Exhalation Rates.

the bedding plane than it does for the other orientation as it does for ore WG1. Therefore, the highest value for WG1 in the perpendicular orientation is suspect although the effect on the calculation of the diffusion coefficient (equation 4-20) is small in this case (Table 4-16). The comparison between curves in Figure 4-19 has limited validity because of non-identical pieces of ore and their inhomogeneities.

Agreement with Theory

The Synthetic Ore

The data agrees very well with equation 4-21 up to an hour's time (Figure 4-6 and Table 4-3). This demonstrates a validity of the method with injected radon for at least this material which is significantly different from the other materials in being comparatively uniform. This method has also been applied with about the same relative error to pulverized bentonite and sand containing moisture(51).

The data suggests a source of radon other than the disc at times greater than one hour at which time the exhalation rate is about 5 percent of that of the initial measurement. This small, slowly dying, additional exhalation is probably due to radon initially absorbed in the small amount of paraffin and vaseline that was used to seal the disc to the surrounding glass. This interpretation is consistent with radon's appreciable distribution coefficient k of 1.6 cm^3/g in paraffin(51) and its slow diffusion therefrom (1.3×10^{-6} cm^2/s)(34). Vaseline's behavior would be similar to that of paraffin in giving this tailing.

The Natural Ores

Although the relative standard deviation of the observed diffusion coefficient for the synthetic ore is good ($\pm$11 percent), the corresponding values for the natural ores average $\pm$32 percent with a range from $\pm$16 percent to $\pm$42 percent. The explanation is not simply due to the above tailing although tailing is often prominent (Figures 4-7, 4-10, 4-12, 4-15, 4-17, and 4-18). Neither is it due to poor counting statistics except in one or two cases (Figure 4-9). A principal reason is believed to be a variation in the diffusion coefficient throughout the diffusion disc whether or not Knudsen diffusion is appreciable. For example, uniformly ground and distributed Vitro uranium tailings have been examined by equation 4-20 to give a relative standard deviation for the observed diffusion coefficient of only $\pm$13 percent, thus showing the validity of this equation with at least a uniform powder(51). Another reason for the unfavorable results with natural ores is probably the inhomogeneity of the radon source within the disc. (Dry disc WG1 (parallel) did not appreciably suffer from the inhomogeneous radon source because injected radon was used and its relative standard deviation was comparatively small ($\pm$20 percent)).

The relationship between the observed diffusion coefficient D_{obs} of the equation of continuity (equation 4-17) and the effective diffusion coefficient D_e of Fick's first law for the macroscopic flux is equation 4-18. Table 4-30 contains calculated values of the effective diffusion coefficients for the disc of WG1 using a dry porosity of p = 0.234, a dry bulk density of 1.98 g/cm^3 (Table 2-2), k_{ore} = 0.91 cm^3/g (Experimental Results) and k_w = 0.22 cm^3/g.

Inhomogeneities in the ores are assumed to explain why diffusion perpendicular to the bedding plane has not consistently been less than that parallel to the bedding plane for the same ore and moisture content. Inhomogeneities must also play a role in the lack of correlation of the diffusion coefficient with the permeability to air or water (Table 2-2). It should be noted that the air and water permeabilities also show similar anomalies vis a vis the bedding plane probably because of inhomogeneities between different discs.

Unpredictable differences between different discs of the same ore have been described in the preceding paragraph. However, the behavior of the observed diffusion coefficient for the very same disc appears to be more coherent. A case in point is the plots of Figures 4-20 through 4-22 for diffusion parallel to the bedding plane since each such plot was obtained with a single disc. The main features of these curves may be reproduced from equation 4-19 which describes the observed diffusion coefficient in terms of diffusion in the pore air (D_a) and on the pore surface (d_s). The equation is valid for any degree of saturation including the dry state. The following can be approximated from it to the extent that $\underline{f}$, $\underline{k}$, d_s, and ξ are constant between the dry and moist states:

$$\frac{D_{obs,\%}}{D_{obs,dry}} \simeq \frac{\left(\frac{p}{p+\rho k+\rho_w k_w}\right)_{\%} \cdot \left(\frac{fD_a}{d_s}\right) + \left(\frac{\rho k}{p+\rho k+\rho_w k_w}\right)_{\%}}{\left(\frac{p}{p+\rho k}\right)_{dry} \cdot \left(\frac{fD_a}{d_s}\right) + \left(\frac{\rho k}{p+\rho k}\right)_{dry}} \qquad (4\text{-}25)$$

where % represents the degree of moisture saturation, and fD_a/d_s is higher the more important is volume diffusion and lower the more important is surface diffusion.

In the case of the ore of Figure 4-20, the quantity k is known from the section on experimental work to be 2.36 cm^3/cm^3. A curve that satisfies the data fairly well is obtained with 500 assumed for fD_a/d_s and has been drawn in that figure. The curve from equation 4-25 can be made to slope upward to satisfy the experimental data as in Figures 4-21 and 4-22 with an assumed value of fD_a/d_s that is less than unity. This corresponds to a relative dominance of surface diffusion according to equations 4-19 and 4-25. It also coincides with

TABLE 4-30. Calculated values of the effective diffusion coefficient for ore WG1

(25°C, 0.85 atm)

Direction of Diffusion vs. Bedding Plane	Percentage of Moisture Saturation	$D_{obs}(cm^2/s)$[1]	$D_e(cm^2/s)$
Parallel	0.0	7.12×10^{-4}	1.85×10^{-3}
Parallel	17.0	4.40×10^{-4}	1.12×10^{-3}
Parallel	29.6	2.97×10^{-4}	7.50×10^{-4}
Parallel	67.4	3.34×10^{-4}	8.14×10^{-4}
Perpendicular	12.9	7.15×10^{-4}	1.83×10^{-3}
Perpendicular	29.5	2.58×10^{-4}	6.51×10^{-3}

[1] See Experimental Results in this chapter

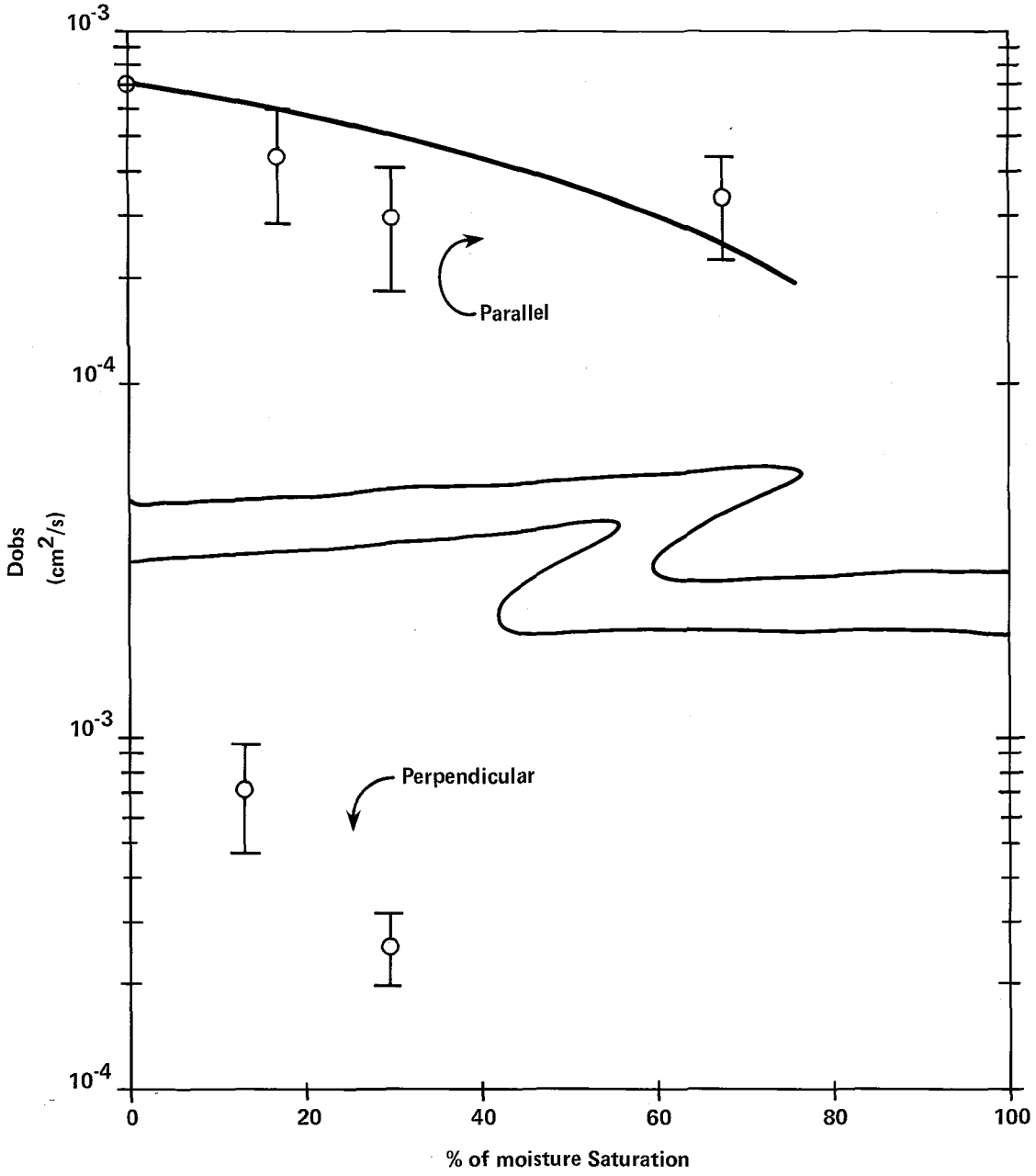

Figure 4-20. Radon's observed diffusion coefficient in two discs of ore from Wyoming Gas Hills ore No. 1.

($23 \pm 1^{\circ}C$, 0.85 atm)

Upper points: diffusion direction parallel to bedding plane; curve calculated from equation 4-25 with experimental $\rho k = 2.36$ and assumed $fD_a/d_s = 500$.

Bottom points: diffusion direction perpendicular to bedding plane.

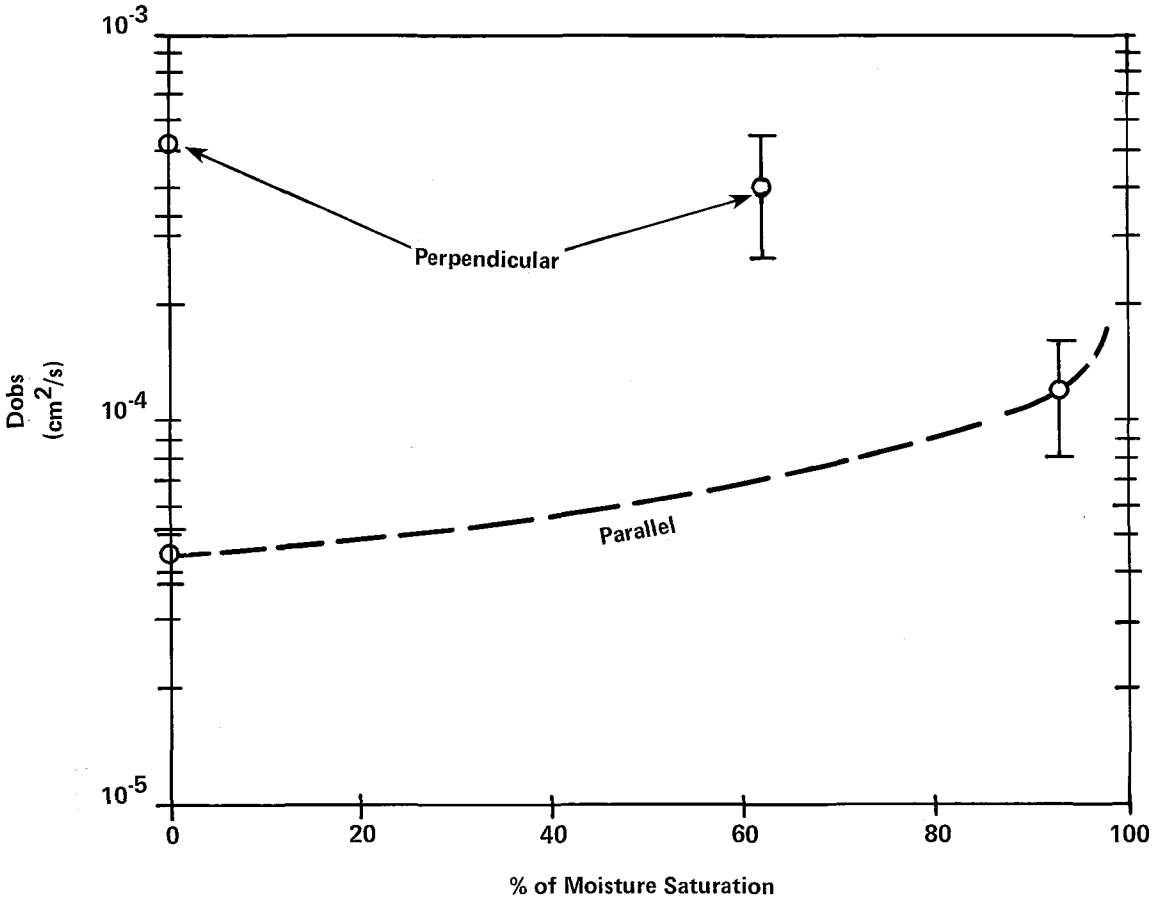

Figure 4-21. Radon's observed diffusion coefficient in two discs of ore from Utah Big Buck mine.

($23 \pm 1^{\circ}C$, 0.85 atm)

Bottom points: diffusion direction parallel to bedding plane; curve calculated from equation 4-25 with assumed values of $\rho k = 0.007$ and $f\ D_a/d_s = 0.1$.

Upper points: diffusion direction perpendicular to bedding plane.

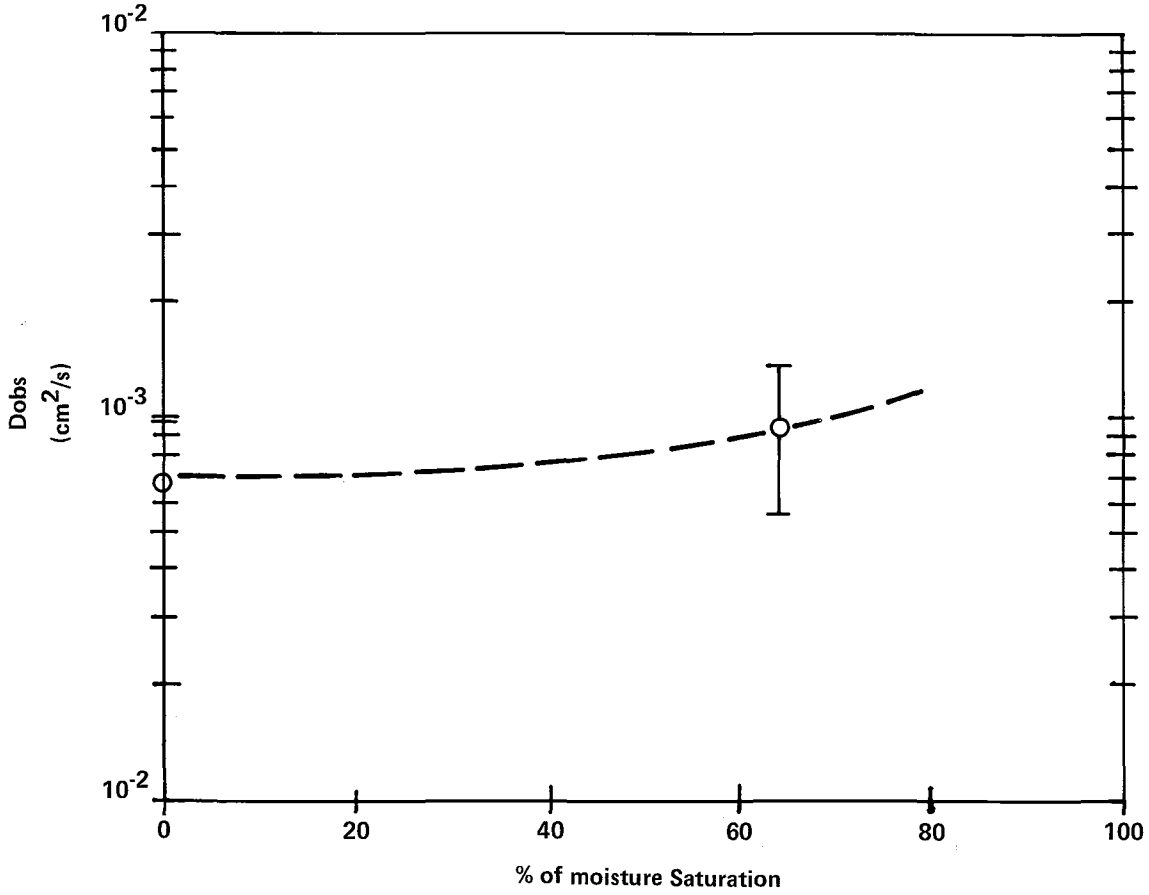

Figure 4-22. Radon's observed diffusion coefficient in Wyoming Crooks Gap ore No. 1 with the direction of diffusion parallel to the bedding plane.

($23 \pm 1^{o}C$, 0.85 atm)

Curve calculated from equation 4-25 with assumed values of $\rho k = 0.14$ and $fD_a/d_s = 0.1$.

larger specific surface areas for these ores (Table 2-2). Larger specific surface areas do not necessarily connote larger adsorption coefficients, as shown by the adsorption on charcoal of radon's sister elements, xenon and krypton(52). However, the present work suggests that larger specific surface areas may correlate with larger values of the surface diffusion coefficient.

Whether or not $D_{obs,\%}$ increases with moisture in equation 4-25, the total flux J_{tot} (equations 4-11 and 4-14) should nevertheless decrease because the application of equation 4-18 to equation 4-25 gives the following for the effective diffusion coefficient of equation 4-14 at a certain percentage of moisture saturation:

$$D_e \simeq \frac{\left[p\left(\frac{fD_a}{d_s}\right) + \rho k \right]_{\%} \cdot D_{obs,dry}}{\left(\frac{p}{p+\rho k}\right)_{dry} \cdot \left(\frac{fD_a}{d_s}\right) + \left(\frac{\rho k}{p+\rho k}\right)_{dry}} \quad . \qquad (4\text{-}26)$$

Equation 4-26 implies that as moisture increases and therefore the air porosity $p_{\%}$ decreases, the effective diffusion coefficient should vary monotonically with $p_{\%}$ provided that f, d_s, k and ξ are comparatively unaffected as would be expected.

Diffusional phenomena in this report have been considered in terms of a single volume-diffusion medium (air). It is possible that some natural ores can be better analyzed in terms of diffusing and virtually undiffusing pore gas as pictured by van Genuchten and Wierenga for liquids(55). The connection between the diffusing and virtually undiffusing gas would be through a slow, diffusion-controlled process as described in their mathematics.

CHAPTER 5

MATHEMATICAL MODELING OF RADON EMANATION

A mathematical model was developed to explain the observed effects of moisture on radon emanation coefficients. The model incorporates the generally accepted mechanisms of emanation, direct-recoil and indirect-recoil, and disregards the minor contributions expected to occur from diffusion of radon atoms through the rock matrix to pore surfaces.

The model is based on several of the key parameters measured on the ore samples in this study, including the bulk density (ρ), the total porosity, and the pore-size distribution, which was comprised of approximately fifty pore diameters (d_i) and their corresponding specific volumes (v_i). Other measured parameters such as the radium and uranium contents did not correlate well with the observed emanation coefficients. The specific surface area, which was related to the emanation coefficients, was also not used because corresponding information was contained, in greater detail with respect to pore sizes, in the pore-size distribution data.

The present model assumes a geometric configuration of parallel cylindrical pores whose diameters are defined by the measured pore-size distribution. A spherical-grain model was also considered due to the frequent occurrence of granular, sandstone uranium deposits. However, the absence of detailed grain size information and the requirement for extremely small grain sizes to explain the observed high emanation coefficients suggested that the modeling effort should be concentrated on the cylindrical pore model. The following sections present the theory and equations which describe this model, compare its predicted emanation coefficients with experimental results, and discuss interpretations of the fitted or variable parameters used in applying the model. The theory section also demonstrates that the model also applies to granular, sandstone ores by defining the porous emanating fraction of the ore to be the intergranular cementing material.

Theory and Equations

The process of radon emanation into a cylindrical pore containing water is illustrated schematically in Figure 5-1. The recoiling radon atom is considered to be emanated if, at the end of its trajectory, it comes to rest in an air-filled or water-filled region of the pore and is thus free to diffuse through the porous regions and escape from the ore. The diagram

illustrates several features of the model: The ore is considered to contain inert rock grains which contain no significant radium or porous space. The radium and uranium are considered to reside in the porous intergranular cementing material in annular regions of equal thickness (S) around each pore. Such uranium mineralization occurs by the precipitation of these minerals from solutions passing through the pores of the rock. The presence of moisture in the rock is considered to occur in layers of equal thickness (W) in all pores, thus filling the small pores first as the moisture content is increased.

The pores are randomly located as illustrated in Figure 5-1, but are spaced at maximum distance from each other. As the fraction of inert rock is increased, the pores must become closer together to maintain the same pore size distribution. Hence, a point is reached at which the annular radium source regions around each pore intersect each other, allowing emanation into more than one pore to occur from a single point of origin. Figure 5-1 illustrates the overlaping source regions but violates the maximum spacing criterion for the sake of simplicity. The minimum interpore spacing is achieved when the annular mineralized volume equals the total cementing material volume minus the pore volumes. The resulting parameters to be fitted for a given ore sample are therefore the inert rock fraction F_R (cm^3/cm^3), and the thickness of the mineral source layers around the pores.

Figure 5-1 illustrates several possible trajectories of interest for a recoiling radon atom. Trajectory A' depicts a radon recoil atom whose trajectory does not intersect a cylindrical pore, and which is therefore not emanated. Trajectory B' depicts a recoil atom which is stopped in the water-filled region of the pore and is therefore emanated. Trajectory C' is also properly oriented for emanation, but the recoil atom does not lose sufficient energy in the water and air filled regions to be stopped. It is therefore embedded in the rock of the opposite pore wall and is not emanated. Trajectory D' similarly depicts a recoil atom traversing the pore and penetrating the opposite rock surface. In this case, however, the penetration is shallow and the atom is able to diffuse or otherwise escape back into the pore through its damaged-rock path. The radon atom is therefore emanated by the indirect recoil mechanism. The model incorporates a threshold energy for rock impaction. Atoms striking a pore wall with less than the threshold energy are emanated by indirect recoil. The threshold energy is expressed as an equivalent range in rock, R_T.

The equation for calculating the emanation coefficient was derived in the following manner. The emanation coefficient, E, was defined as the number of radon atoms with appropriate energies and trajectories to stop in the pores, divided by the total number of radon atoms produced in the annular source regions around the pores. Because of the cylindrical symmetry of the parallel pores and the annular source regions, the

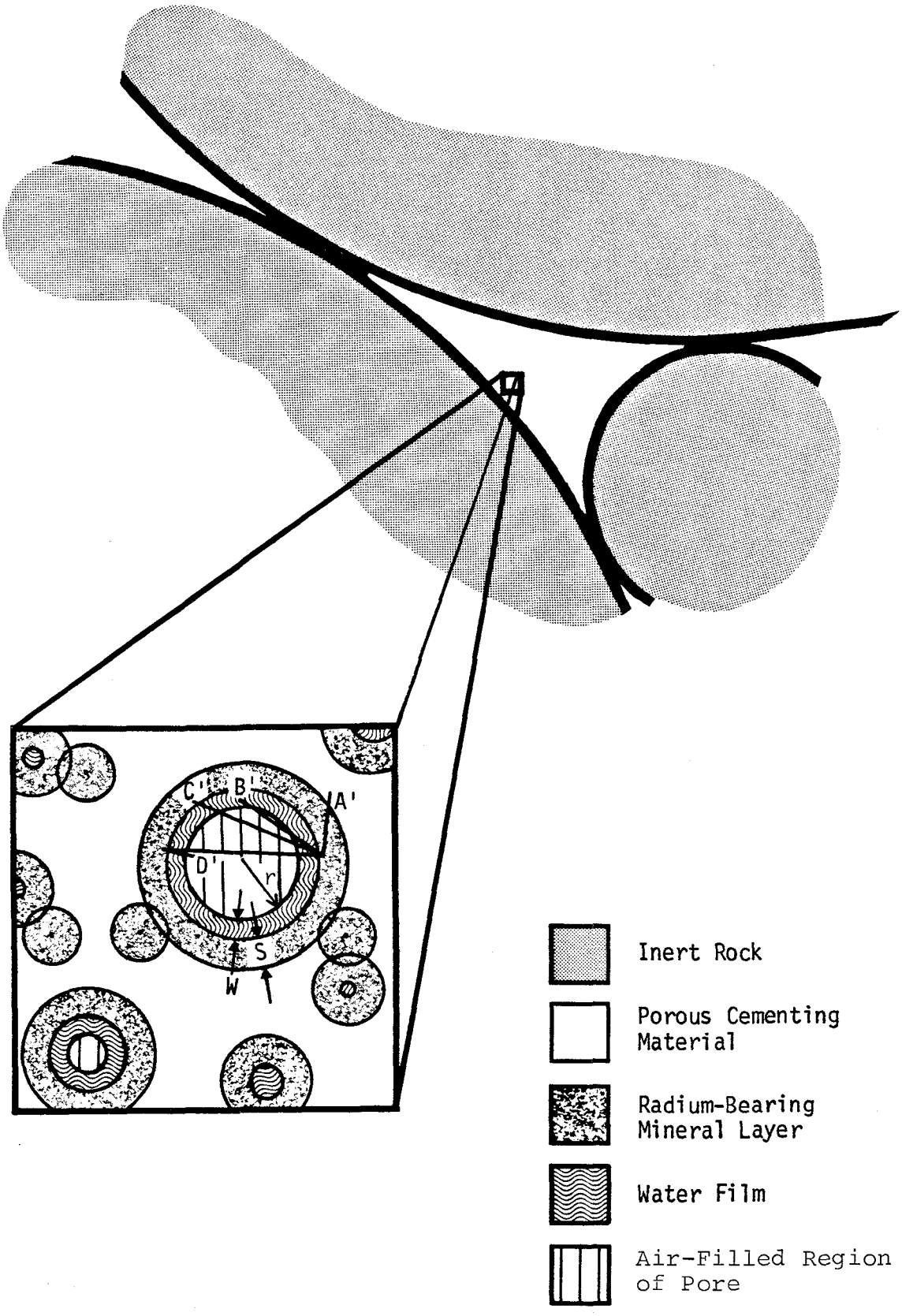

FIGURE 5-1. Schematic diagram of radon emanation into a partially saturated, cylindrical pore from an annular, radium-bearing mineral layer.

equation for E was simply written in two-dimensional form as:

$$E = \frac{\sum_i n_i A_i f_i}{Q} \qquad (5\text{-}1)$$

where,

$n_i = \frac{v_i \rho}{\pi r_i^2 (1-F_R)}$ (number of pores of radius r_i per unit area of cementing material)

$A_i = \pi\{(r_i+R')^2 - r_i^2\}$ (area of annular source region which can contribute to emanation)

$R' = \min(R,S)$ (minimum value of either R or S)

R = radon recoil range in rock (cm)

f_i = fraction of radon atoms produced in A_i which stop in pores

Q = total area of annular source regions per unit area of cementing material

The definition of Q depends on the interpore spacing. If the source regions do not overlap, Q can be written as the sum of the individual annular source areas per unit area of cementing material. When the source regions reach maximum overlap, the source area occupies all of the interpore space in the cementing material region. The value for Q in the intermediate range of minimal overlap was approximated by assuming that the annular source areas were additive until all interpore space was occupied by source material. The mathematical definition of Q was therefore:

$$Q = \min\left\{ \sum_i n_i \pi(\{r_i+S\}^2 - r_i^2),\ 1 - \sum_i n_i \pi r_i^2 \right\} \qquad (5\text{-}2)$$

The number of radon atoms produced in a given annular source having unit radium concentration (atoms/cm^2) that are emanated into a given pore was defined by integrating the emanation fraction originating at any point in the annulus over the area of the annulus:

$$f_i = \int_{r_i}^{r_i+R'} \int_0^{2\pi} f_{i,r}\, r\, dr\, d\phi \qquad (5\text{-}3)$$

The definition of the emanation fraction, $f_{i,r}$, requires three dimensional geometry to accommodate recoil trajectories which are not perpendicular to the pore axis. Figure 5-2 illustrates the geometric definitions for a recoil atom originating in the source area element $rdrd\phi$, and traveling a distance Z_r through the rock to reach the pore boundary. The fraction of atoms emanated from the source element is:

$$f_{i,r} = \frac{4}{2\pi^2} \int_0^{\cos^{-1}\left(\frac{r-r_i}{R}\right)} \left(\int_x^B d\psi \right) d\theta, \qquad (5\text{-}4)$$

where ψ can vary from zero (a trajectory intersecting the pore axis) to a maximum value which occurs when the trajectory is tangent to the pore surface. The angle θ can similarly range from zero to a maximum of $\pi/2$ or less, depending on the distance from the pore wall and the recoil range in the rock.

One additional constraint affects the integration limits A and B. This is the energy window required for a recoil atom with the proper trajectory to be emanated. The atom must have sufficient energy to reach the pore boundary, but less than the impaction threshold energy after it has traversed the pore. The limit B is determined by the distance from the point of origin to the pore surface, and is limited by the maximum recoil range in rock, R, in cases in which the recoil atom originates a large distance from the pore surface. The definition of B is thus:

$$B = \sin^{-1}\left[\frac{r_i}{r}\right] \qquad r < (R^2\cos^2\theta + r_i^2)^{\frac{1}{2}}$$

$$B = \cos^{-1}\left[\frac{r^2 - r_i^2 + R^2\cos^2\theta}{2rR\cos\theta}\right] \qquad r > (R^2\cos^2\theta + r_i^2)^{\frac{1}{2}} \qquad (5\text{-}5)$$

The definition of x is more complicated, and depends on the recoil atom having a low enough energy to not become impacted into the opposite pore wall. This requires a minimum pathway in rock of:

$$y = R - R_T, \qquad (5\text{-}6)$$

or an equivalent longer pathway in a less dense material such as water or air. Because the medium of the recoil pathway is now important, the distances traveled in rock, water and air must be considered. Figure 5-3 illustrates the two important types of trajectories through the single and dual phase regions of the pore.

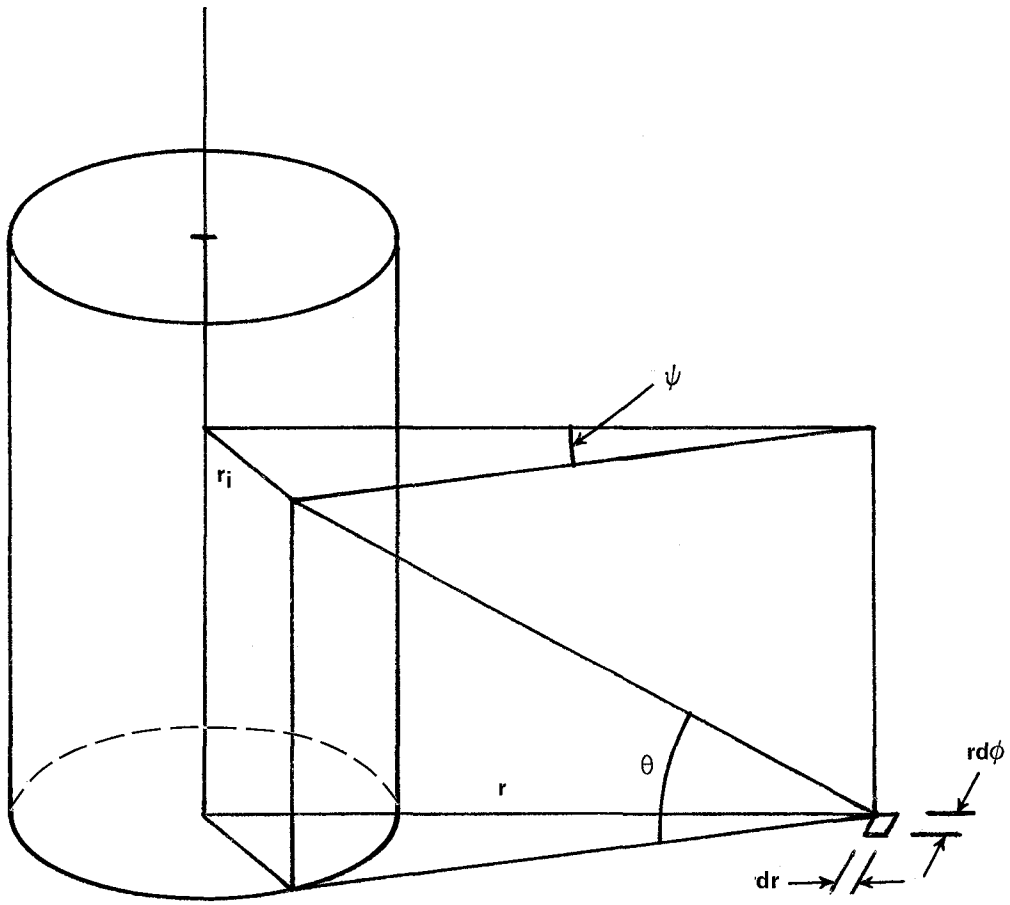

FIGURE 5-2. Cylindrical geometry used for emanation equation development.

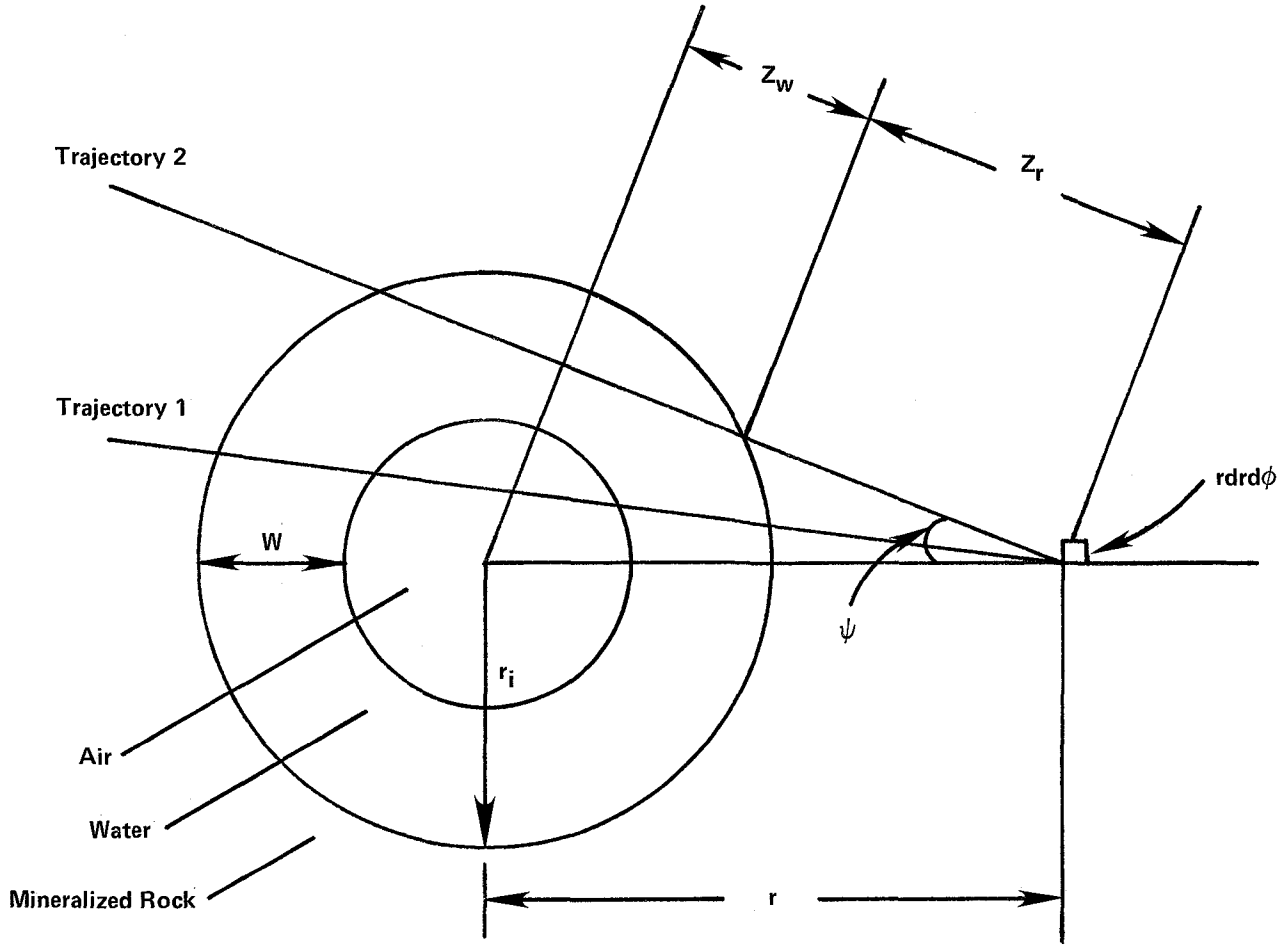

FIGURE 5-3. Recoil atom trajectories into water and air-filled pore regions (traj. 1) and water-filled pore region (traj. 2) from a source element.

Due to the small effect of air on the recoil range of radon, the effect of the air pathway was considered by adding a small increment to the water layer thickness based on the relative ranges in air and water and the radius of the air-filled region. The path lengths Z_r and Z_w were then determined from the equation

$$y = Z_r + 2aZ_w, \tag{5-7}$$

and the geometric relationships:

$$\cos\psi = \frac{r^2 - r_i^2 + Z_r^2\cos^2\theta}{2rZ_r\cos\theta} \tag{5-8}$$

$$\cos\psi = \frac{r^2 - (r_i - W)^2 + (Z_r + Z_w)^2\cos^2\theta}{2r(Z_r + Z_w)\cos\theta} \quad \text{(Trajectory 1)} \tag{5-9}$$

$$Z_w = \sec\theta\,(r_i^2 - r^2\sin^2\psi)^{1/2} \quad \text{(Trajectory 2)} \tag{5-10}$$

The constant (a) in equation 5-7 is the ratio of the recoil range in rock to that in water.

Combining equations 5-7, 5-8 and 5-9 yields a cubic equation for Z_r for trajectory 1 in terms of known parameters. Similarly combining equations 5-7, 5-8 and 5-10 yields a quartic equation in Z_r for trajectory 2 in terms of known parameters. The particular solutions to these equations which applied to the geometric constraints of this system were used when calculating the radon path lengths Z_{r1} and Z_{r2}, for the rock pathways for trajectories 1 and 2, respectively. The resulting definition of the integration limit x was then derived to be:

$$x = 0 \qquad r > r_i - 2aW + y\cos\theta \tag{5-11}$$

$$x = A \qquad r < r_i - 2aW + y\cos\theta$$

$$\text{and } A < \sin^{-1}\left(\frac{r_i - W}{r}\right)$$

$$\text{and } A < B$$

$$x = H \qquad r < r_i - 2aW + y\cos\theta$$

$$\text{and } A > \sin^{-1}\left(\frac{r_i - W}{r}\right)$$

$$\text{and } H < B$$

$$x = B \qquad r < r_i - 2aW + y\cos\theta$$

$$\text{and } A > B$$

$$\text{and } H > B$$

where $$A = \cos^{-1}\left[\frac{r^2 - r_i^2 + Z_{r1}^2\cos^2\theta}{2rZ_{r1}\cos\theta}\right]$$

and $$H = \cos^{-1}\left[\frac{r^2 - r_i^2 + Z_{r2}^2\cos^2\theta}{2rZ_{r2}\cos\theta}\right]$$

Combining equations 5-1, 5-2, 5-3 and 5-4, and integrating and simplifying yields the following expression for the emanation coefficient:

$$E = \frac{4\sum_i n_i\left[(r_i+R')^2 - r_i^2\right]\int_{r_i}^{r_i+R'} r \int_0^{\cos^{-1}\left(\frac{r-r_i}{R}\right)} (B-x)\, d\theta\, dr}{\min\left\{\sum_i n_i\pi\left[(r_i+S)^2 - r_i^2\right],\ 1 - \sum_i n_i\pi r_i^2\right\}} \qquad (5\text{-}12)$$

The integrals in equation 5-12 were evaluated numerically in a computer program listed in Appendix H to calculate emanation coefficients at various moisture contents. The program selected various fractions, F_s, of the saturation moisture content for a given ore and calculated an equivalent water film thickness, W, from the pore size distribution using the relationship:

$$F_s = \frac{\sum_i n_i \min(W, r_i)\left[2r_i - \min(W, r_i)\right]}{\sum_i n_i r_i^2} \qquad (5\text{-}13)$$

Comparison with Experimental Results

Exercising the model under a variety of conditions indicated that twenty equal increments were sufficient for evaluating the two numerical integrals in equation 5-12 to an uncertainty of less than a few percent. It also indicated that the variable fitting parameter S, the thickness of the

radium-bearing source region around each pore, determined the magnitude of the moisture effect, which was the ratio of emanation from the dry ore to that from the saturated ore. The other fitting parameter F_R, the fraction of inert rock in the ore, determined the magnitude or vertical position of the entire emanation versus moisture curve.

All other parameters defining the ore were measured, and were therefore held fixed when fitting the model to the observed data. The pore size distribution for the ore as listed in Appendix A was used by normalizing it to the representative value of the total porosity reported in Chapter 3. The pore size distribution determined the moisture content at which the moisture effect on emanation occurred. Predominantly small pore sizes shift the moisture effect region of the curve to higher moistures than in rocks with predominantly large pore sizes. Higher total porosities also shift the moisture effect region to higher moistures.

In order to apply the model, several parameters had to be defined. These included the ranges of a recoil radon atom in rock, in water and in air, and the radon range in rock which corresponded to the threshold energy for impaction. It was assumed in defining these parameters that the energy loss of the recoil atom was linear with distance traveled in a given medium, and that straggling was negligible.

The radon recoil range in rock was defined to be 0.036 micrometers (μm), as reported by Andrews and Wood(4), for the radon recoil range measured in $Na_2O \cdot CaO \cdot 6SiO_2$ glass. A supporting calculation using Lindhard, Scharff and Schott's (LSS) equations(26) and a matrix composed of 49% O, 2% Na, 5% Al, 35% Si, 2% K, 2% Ca, 3% Fe, and 2% U with a density of 2.7 g/cm^3 yielded a radon recoil range of 0.033 μm. Zimens(61) reported a similar value of 0.033 μm for thoron in iron hydroxide with a density of 3.3 g/cm^3. Recently Quet(35) reported higher ranges of 0.0654 μm for thoron in SiO_2, and suggested that the empirical formulation of Zimens(62) gave more reliable numbers than the LSS calculations. However, the value chosen above was based on laboratory measurements on a matrix similar to that expected for the uranium ores, and was considered the best choice under the circumstances of limited data.

Less controversy was apparent over the recoil ranges in water and air. An LSS calculation gave a recoil range of 0.075 μm in water, which was used in the present calculations, and was consistent with reported values(50). The radon recoil range in air was taken from Andrews and Wood(4) to be 64 μm.

The range of a radon atom in rock which was equivalent to the impaction threshold energy was assumed to be 0.01 μm. This was based on the estimate of Wahl(56) for the depth of the melted recoil pocket in rock. It was also supported indirectly by the data of Van Lint(54) on the threshold for introduction

of defects in silicon by electrons. This data suggested that the threshold was approximately 0.3 times the range. Using this fraction of the radon recoil range in rock also gave a value of approximately 0.01 μm for the impaction threshold.

Using the pore size distributions reported in Appendix A and the total porosities summarized previously, the cylindrical pore model was fitted to the measured emanation coefficients by varying S to achieve the correct magnitude of moisture effect and then F_R to normalize the resulting curve. The resulting calculated emanation coefficient curves are illustrated in Figures 5-4 through 5-21 for each of the eighteen ore samples. A typical error bar estimated from the counting statistics is plotted on each graph, and suggests that the counting uncertainty accounts for most of the observed scatter in the data.

The fit of the calculated emanation coefficient curve was generally good, but failed in a few cases to accurately represent the measured data. These biases were of several types. In Figure 5-4, for example, the plateau region was measured to begin at a slightly lower moisture than calculated from the model. This could result from using an excessively high porosity or an excessively small pore size distribution in the calculation. Although the pore size data were determined from different sample lumps than were used in emanation measurements, it was assumed that the size distribution was applicable, and that the same porosity estimate could be used to define the experimental moistures as was used to normalize the pore size distribution. Hence, the position of the shoulder of the curve may differ from the measured data primarily due to sample inhomogeneity. Figure 5-9 illustrates the effect of using two different pore size distributions, which were measured on replicate lumps of the WC ore sample.

For several of the ores, particularly WG1 (Figure 5-6), WG2 (Figure 5-7), and NM-S23-3 (Figure 5-18), the magnitude of the moisture effect could not be varied justifiably in the model using the mineral thickness parameter to match the measured data. This condition could also result from sample inhomogeneity between the emanation and porosity aliquots, due to biases in mineral thickness and pore size distribution. However, it could also result from the assumption in the model of a constant recoil range and impaction threshold for all of the ores. Due to local density variations in the mineralized region, the recoil ranges may actually vary sufficiently to cause the observed discrepancies. In the absence of more complete data to characterize these ranges, however, they were not considered to be a potential variable in the fitting process.

In general, the data fit the predictions of the model within the expected uncertainty. The values of the mineral thickness and the inert rock fraction obtained by applying the

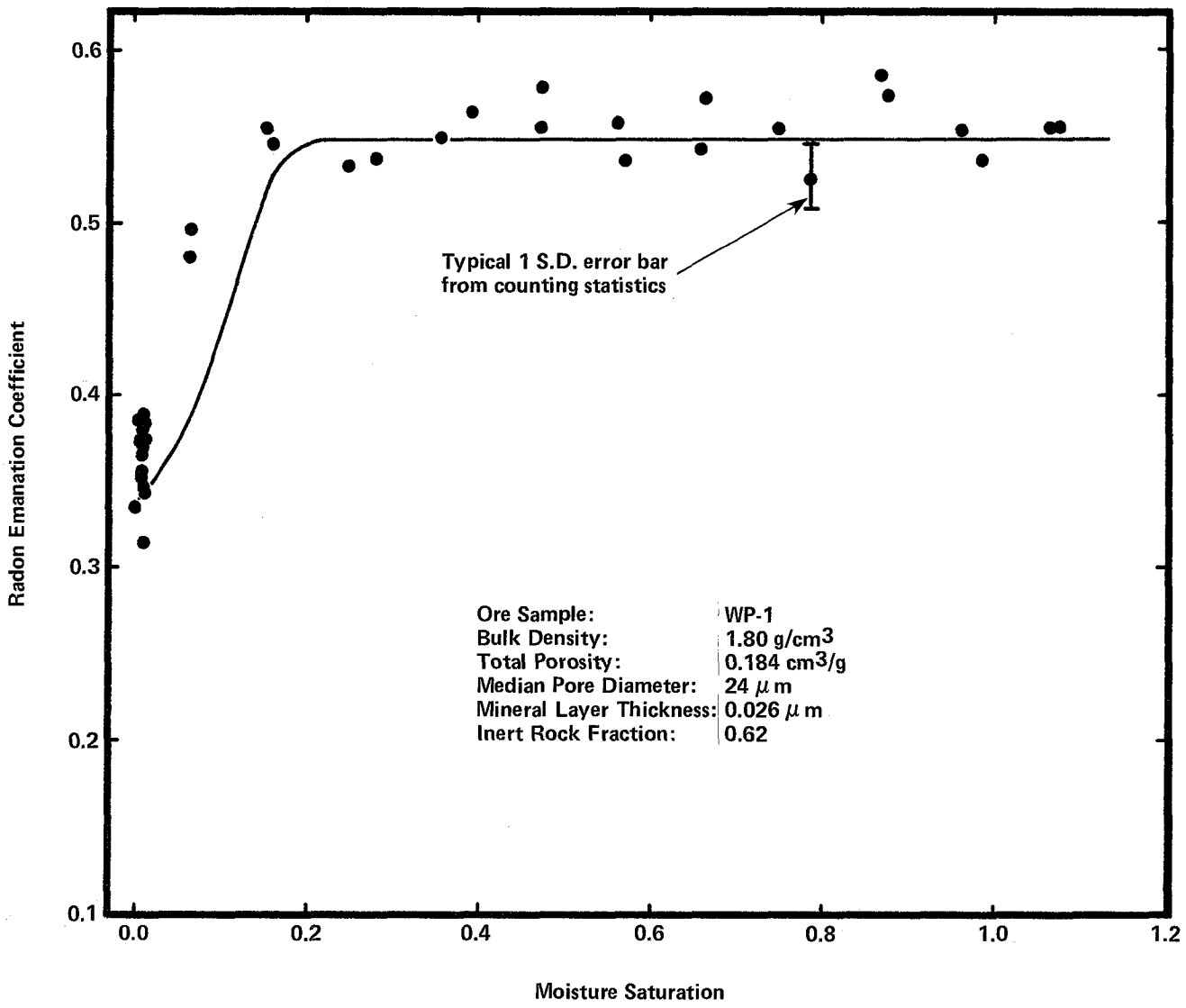

FIGURE 5-4. Comparison of Measured Emanation Coefficients with Calculated Emanation versus Moisture Curve for Ore Sample WP-1.

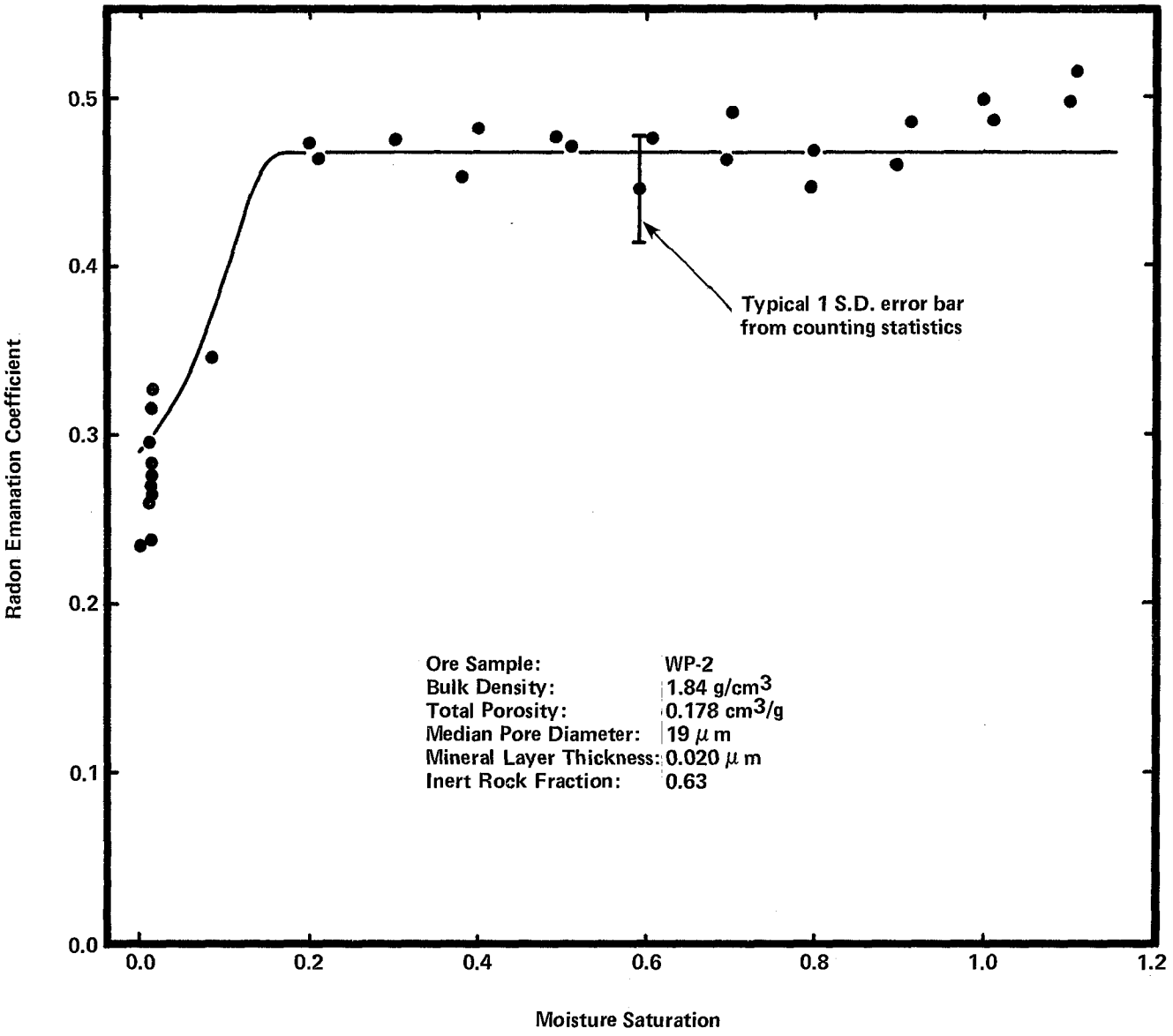

FIGURE 5-5. Comparison of Measured Emanation Coefficients with Calculated Emanation versus Moisture Curve for Ore Sample WP-2.

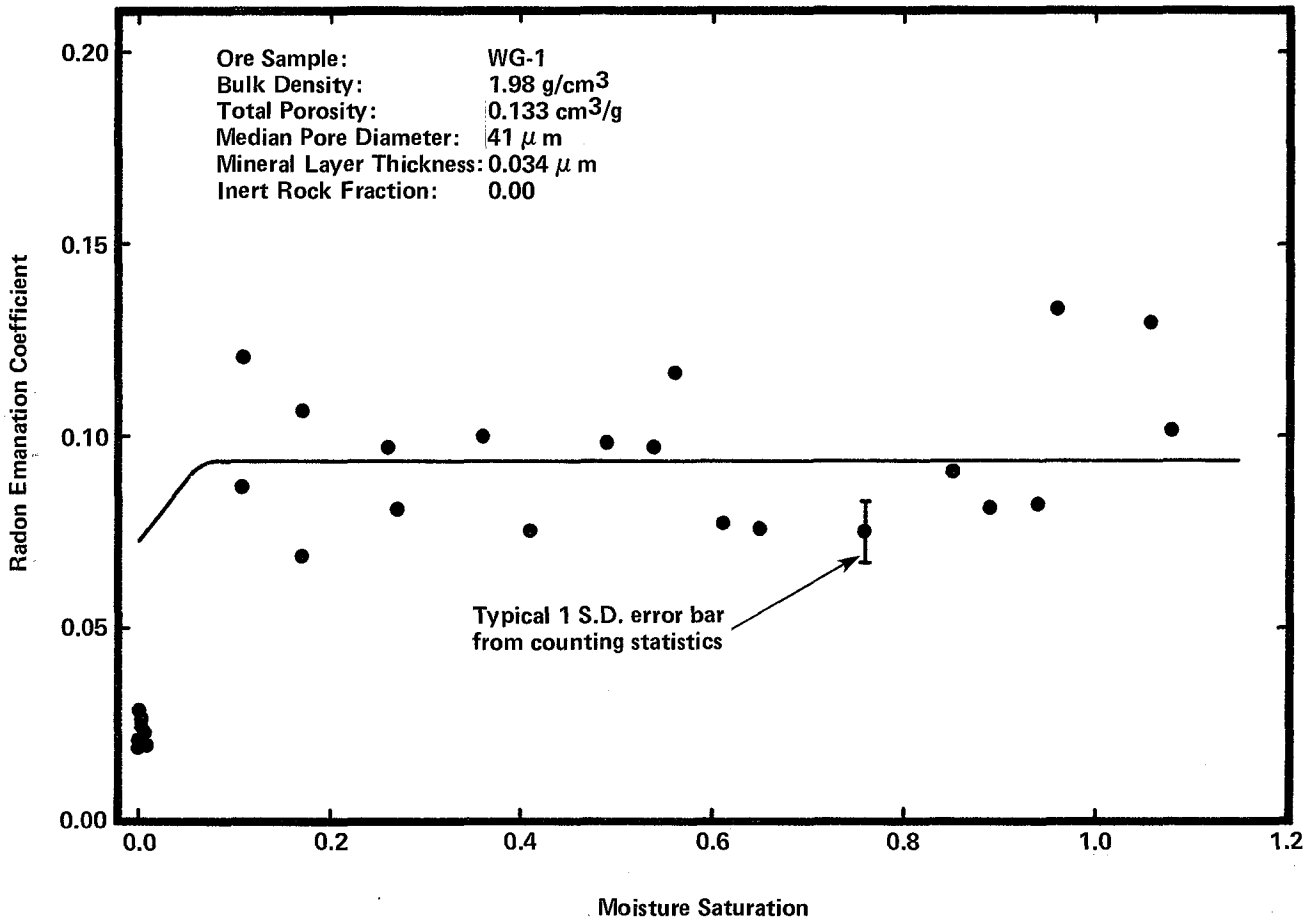

FIGURE 5-6. Comparison of Measured Emanation Coefficients with Calculated Emanation versus Moisture Curve for Ore Sample WG-1.

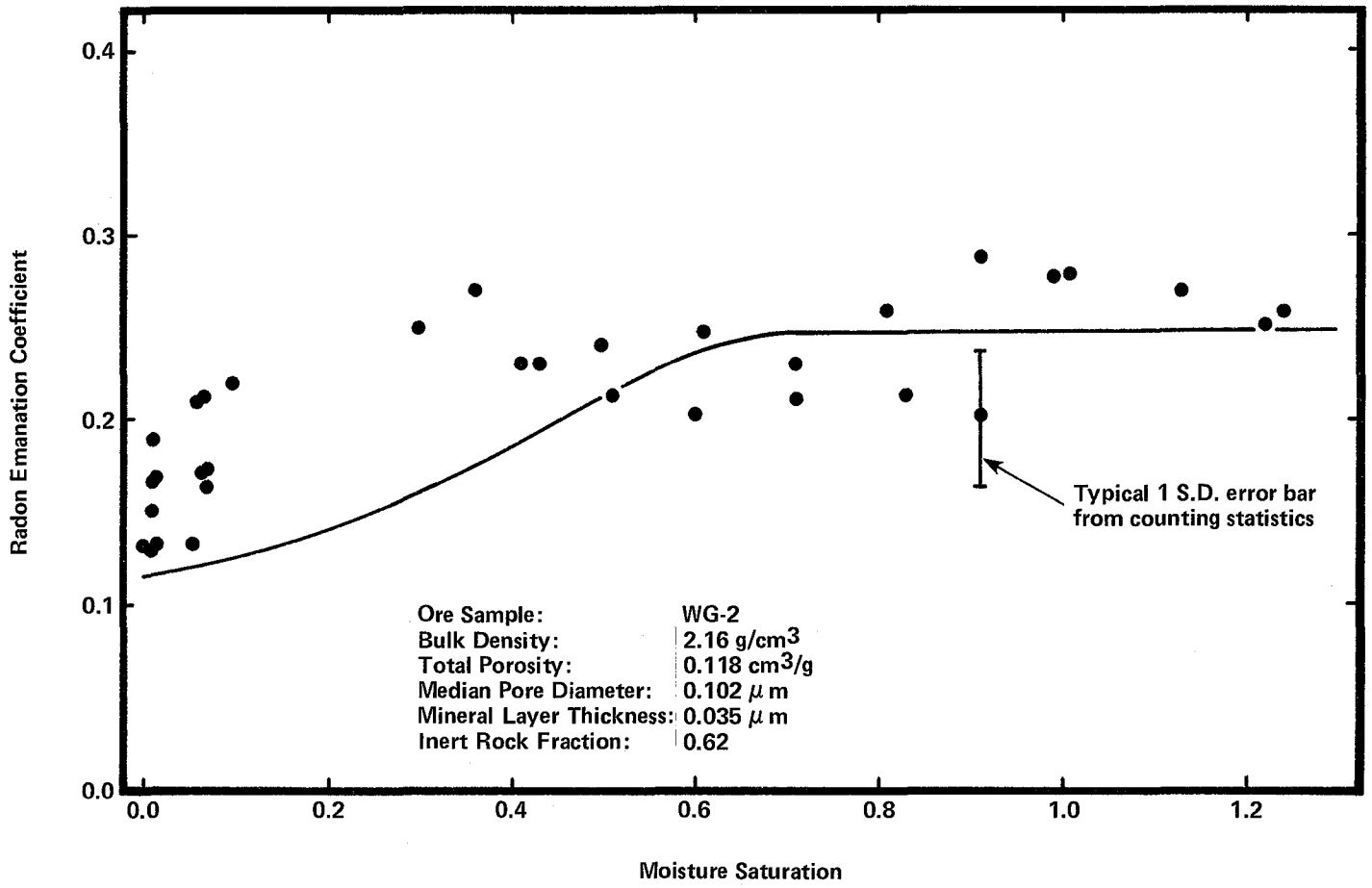

FIGURE 5-7. Comparison of Measured Emanation Coefficients with Calculated Emanation versus Moisture Curve for Ore Sample WG-2.

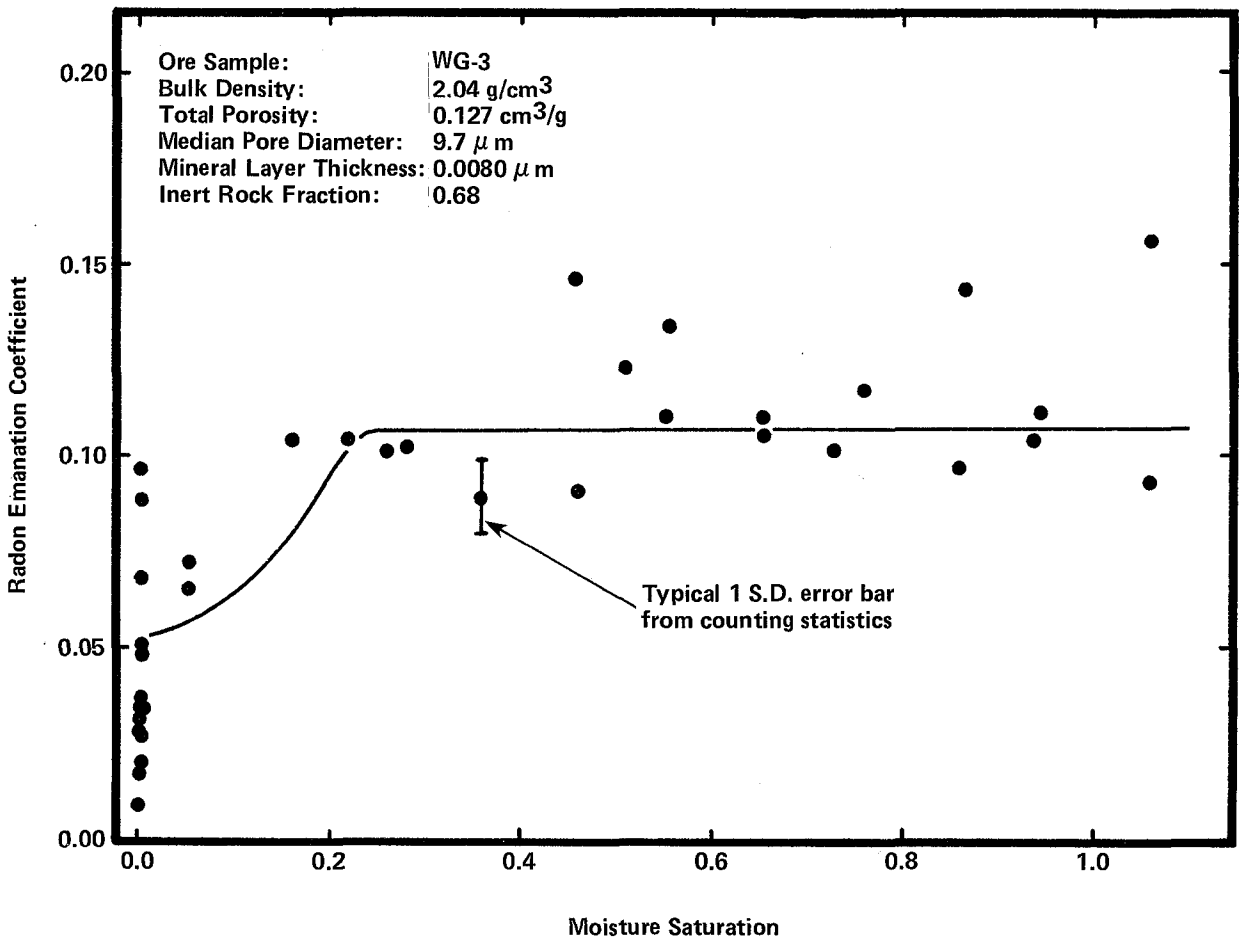

FIGURE 5-8. Comparison of Measured Emanation Coefficients with Calculated Emanation versus Moisture Curve for Ore Sample WG-3.

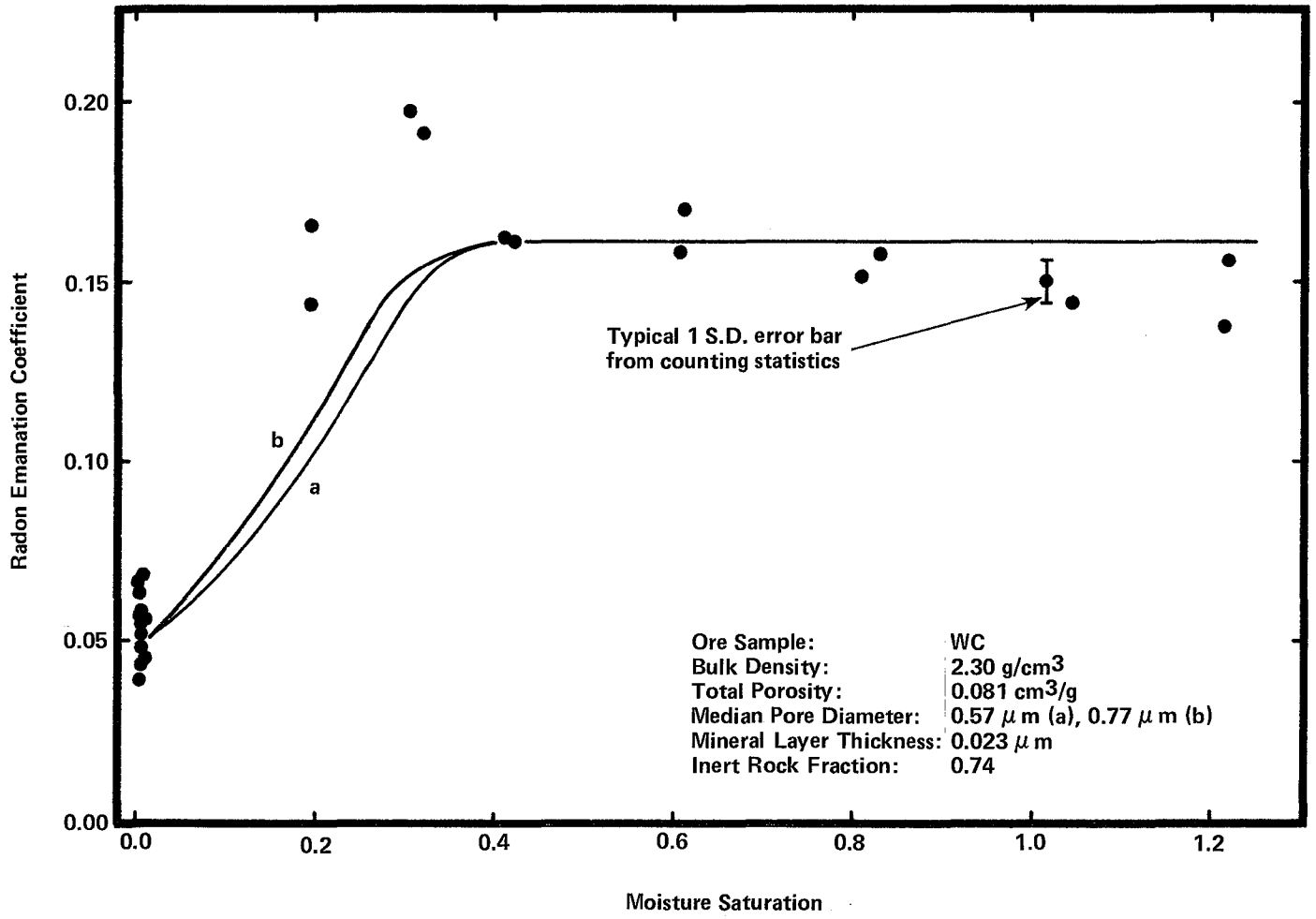

FIGURE 5-9. Comparison of Measured Emanation Coefficients with Calculated Emanation versus Moisture Curve for Ore Sample WC.

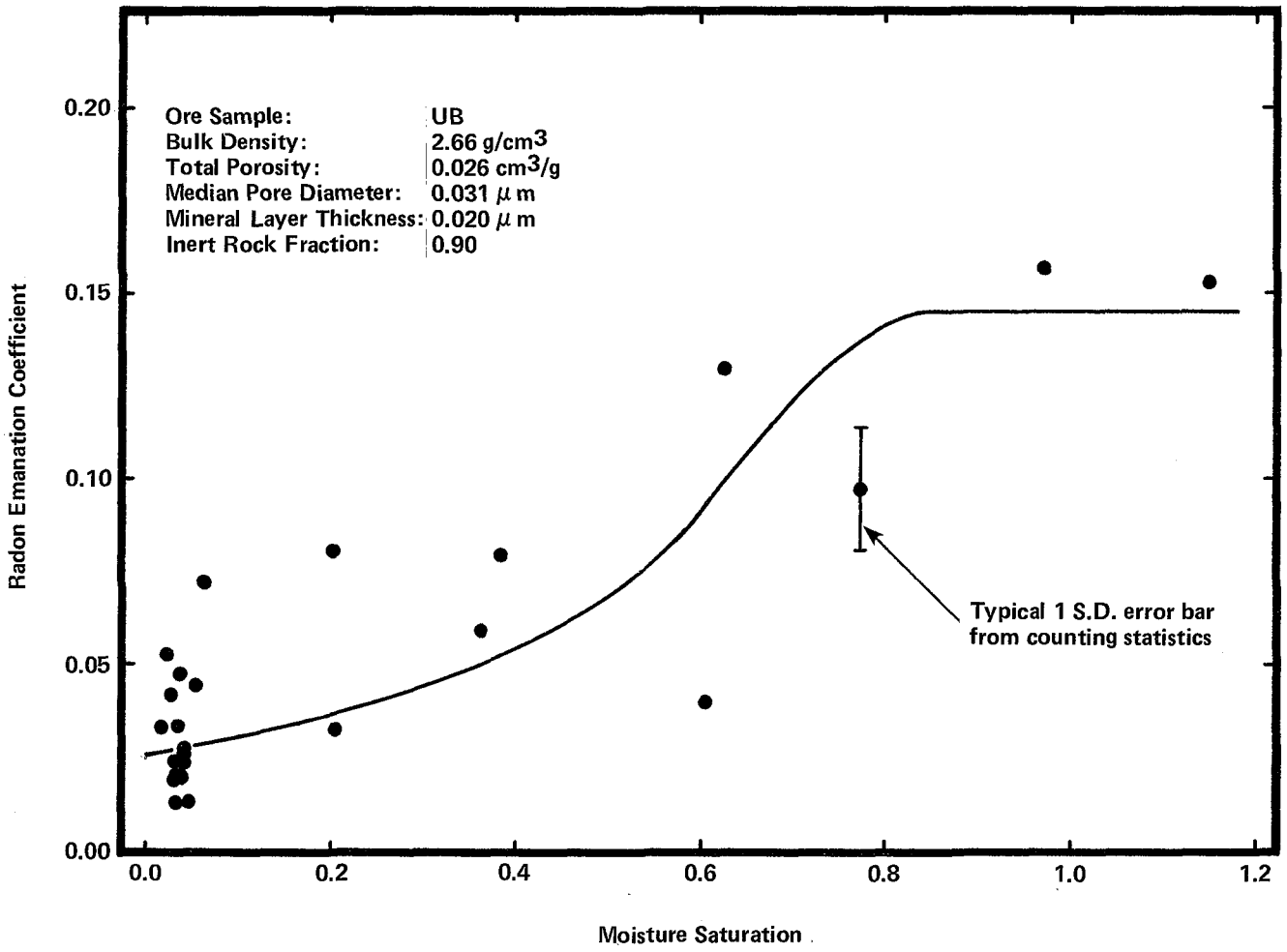

FIGURE 5-10. Comparison of Measured Emanation Coefficients with Calculated Emanation versus Moisture Curve for Ore Sample UB.

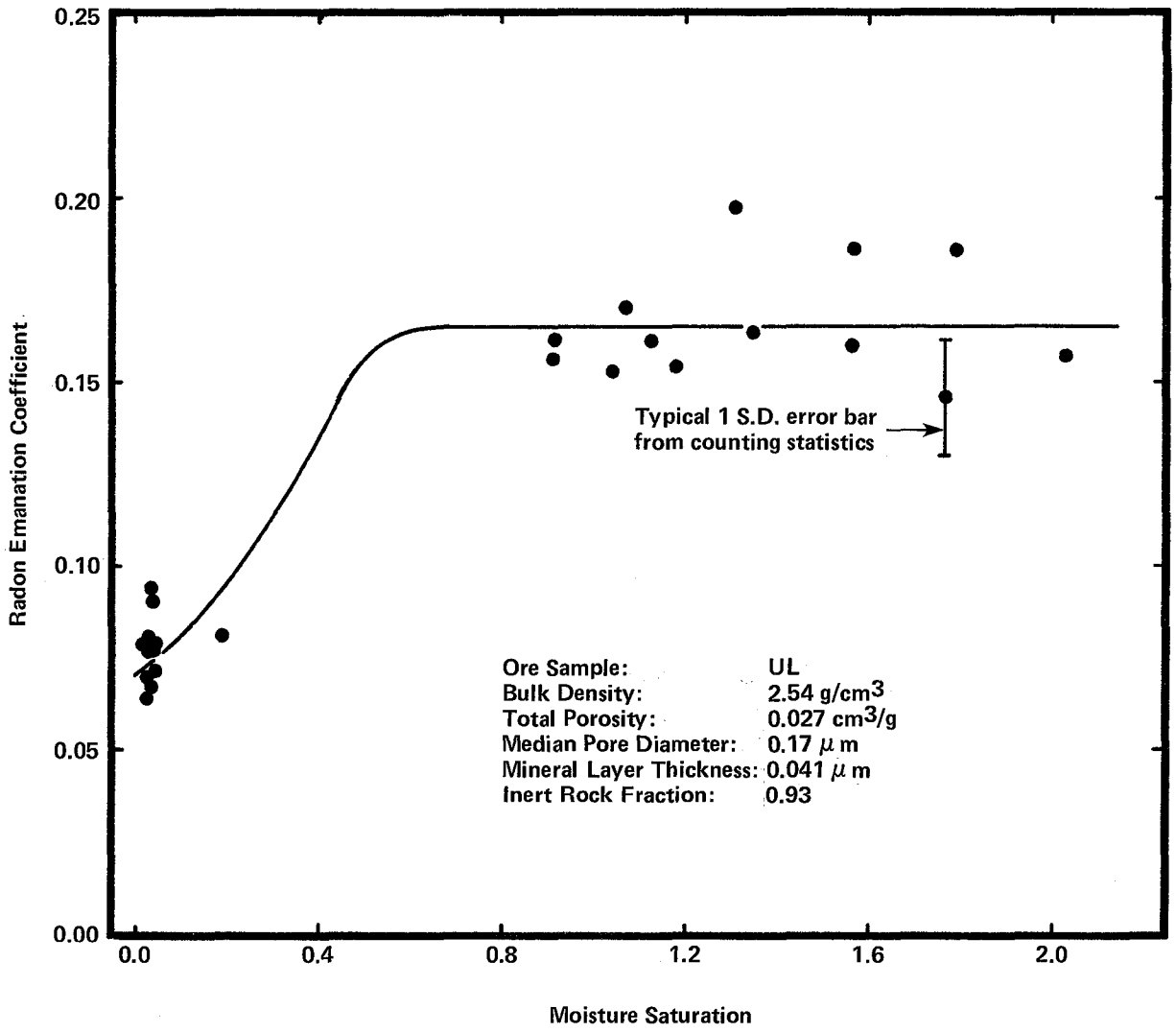

FIGURE 5-11. Comparison of Measured Emanation Coefficients with Calculated Emanation versus Moisture Curve for Ore Sample UL.

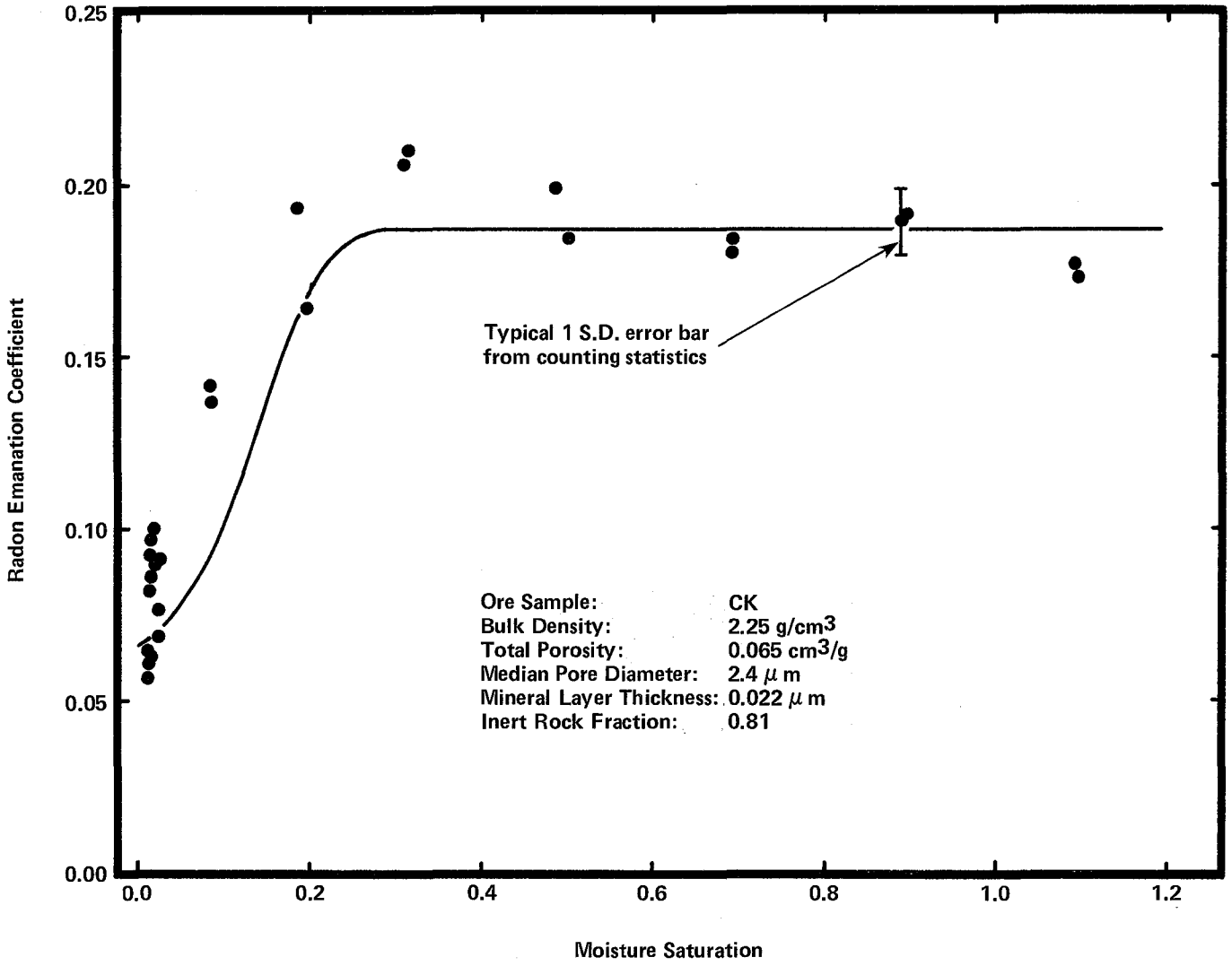

FIGURE 5-12. Comparison of Measured Emanation Coefficients with Calculated Emanation versus Moisture Curve for Ore Sample CK.

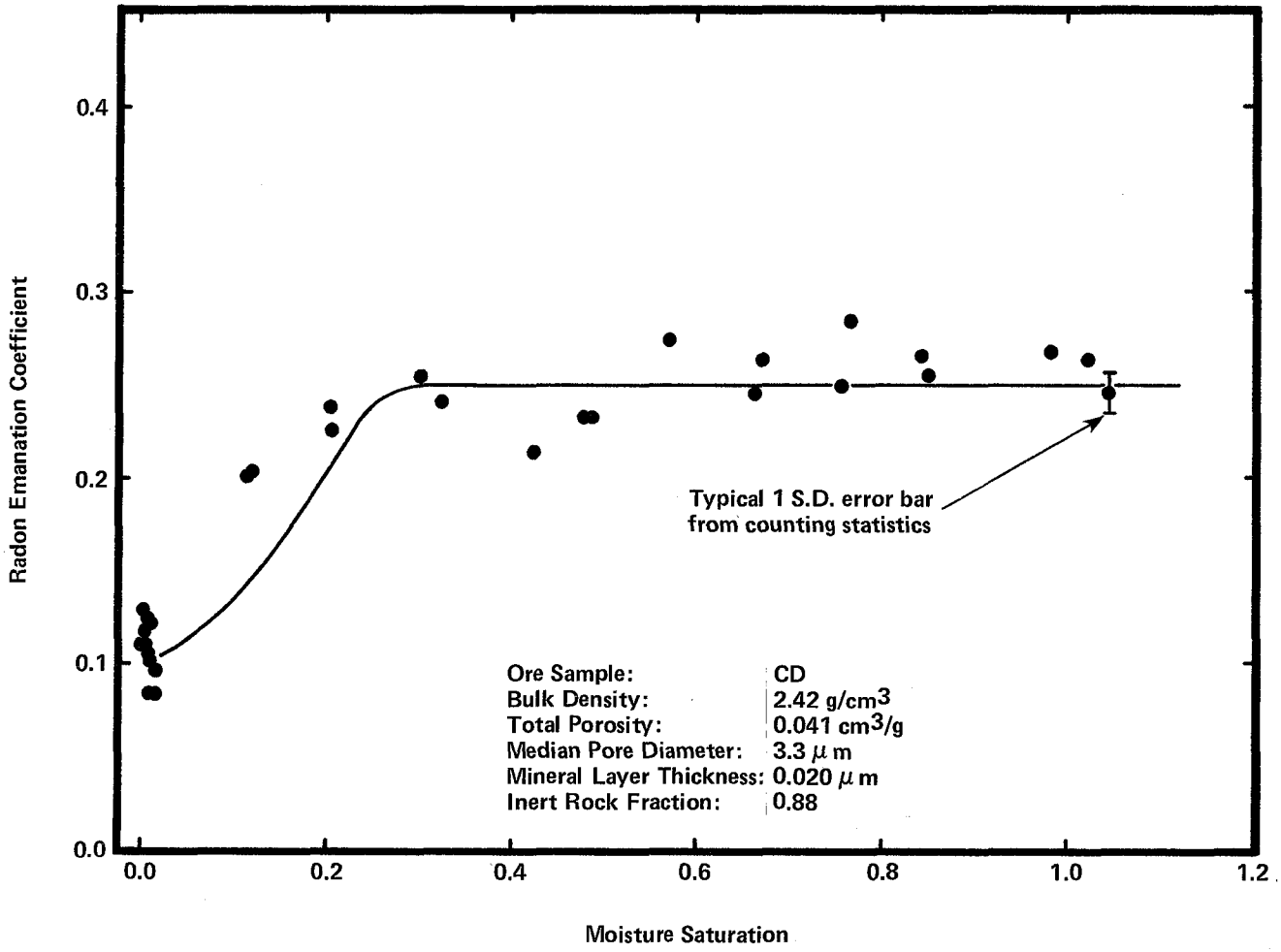

FIGURE 5-13. Comparison of Measured Emanation Coefficients with Calculated Emanation versus Moisture Curve for Ore Sample CD.

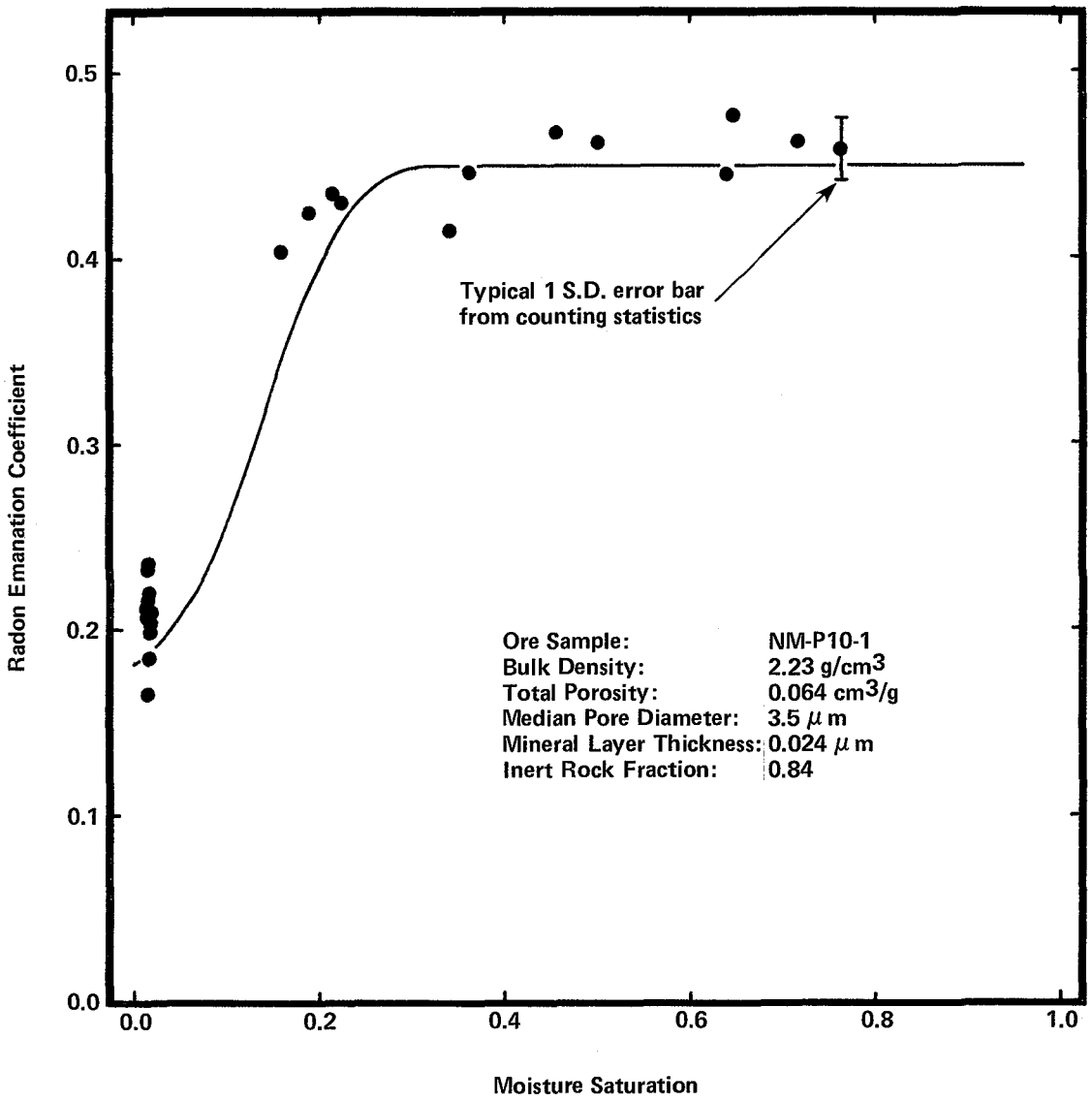

FIGURE 5-14. Comparison of Measured Emanation Coefficients with Calculated Emanation versus Moisture Curve for Ore Sample NM-P10-1.

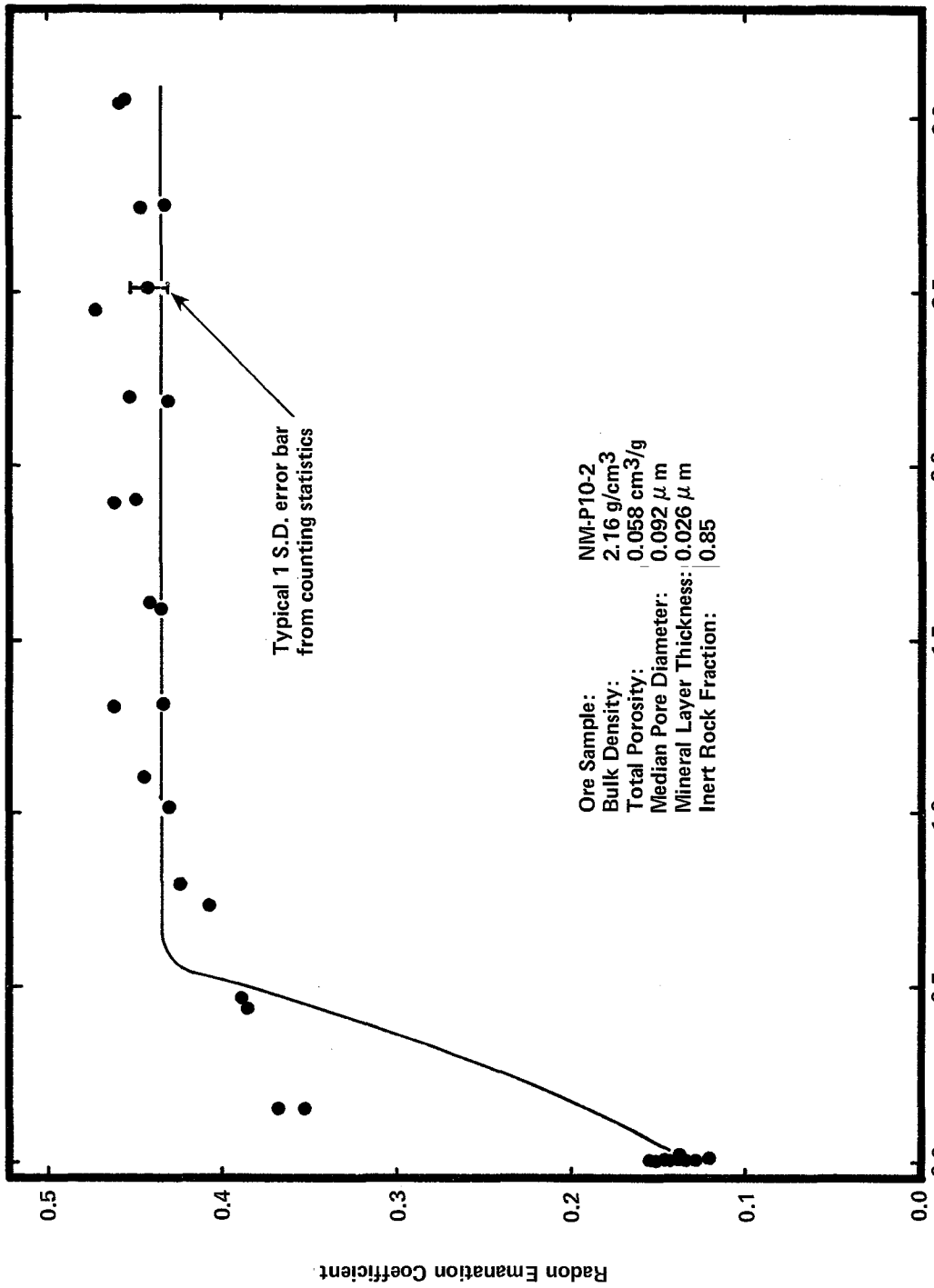

FIGURE 5-15. Comparison of Measured Emanation Coefficients with Calculated Emanation versus Moisture Curve for Ore Sample NM-P10-2.

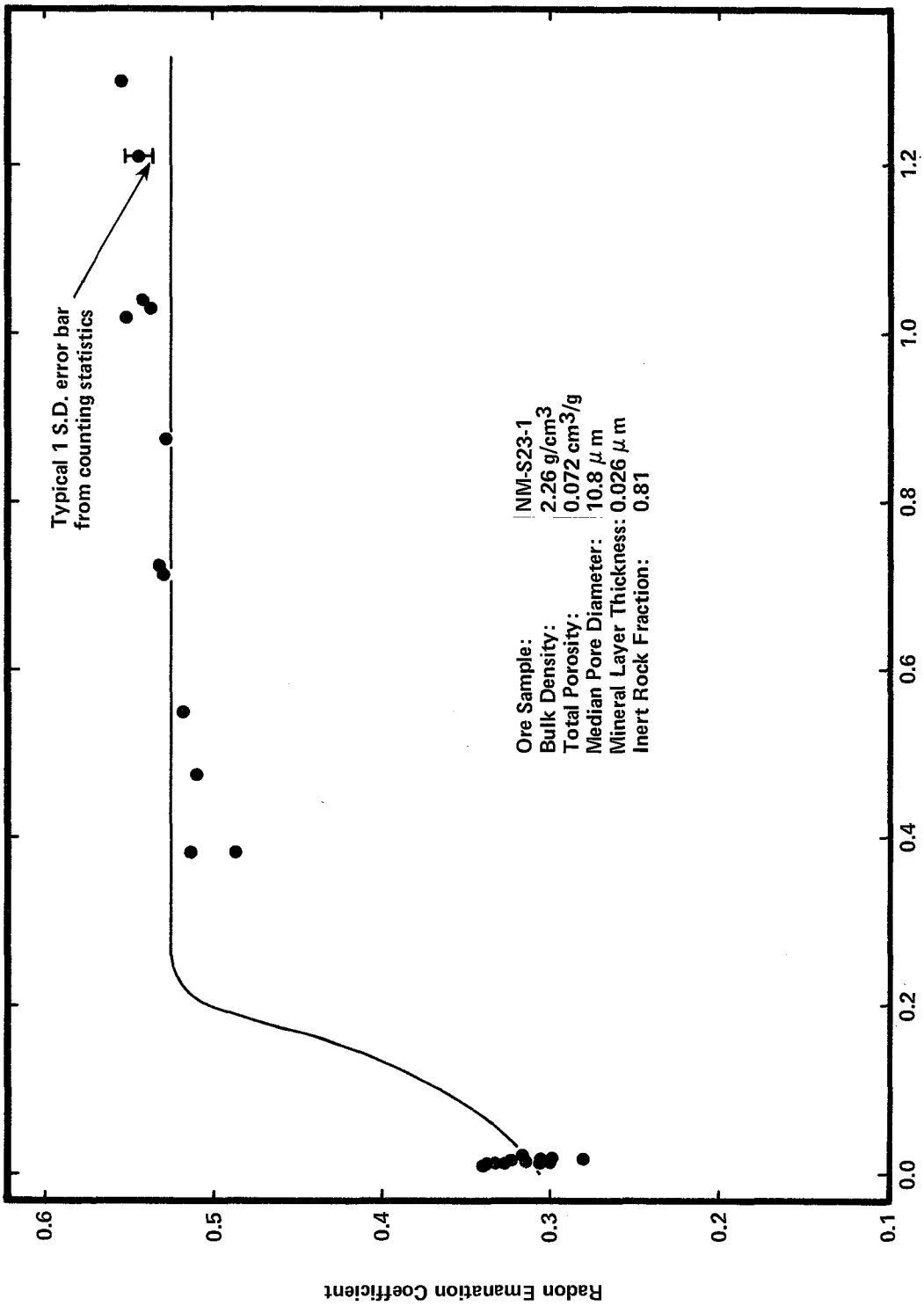

FIGURE 5-16. Comparison of Measured Emanation Coefficients with Calculated Emanation versus Moisture Curve for Ore Sample NM-S23-1.

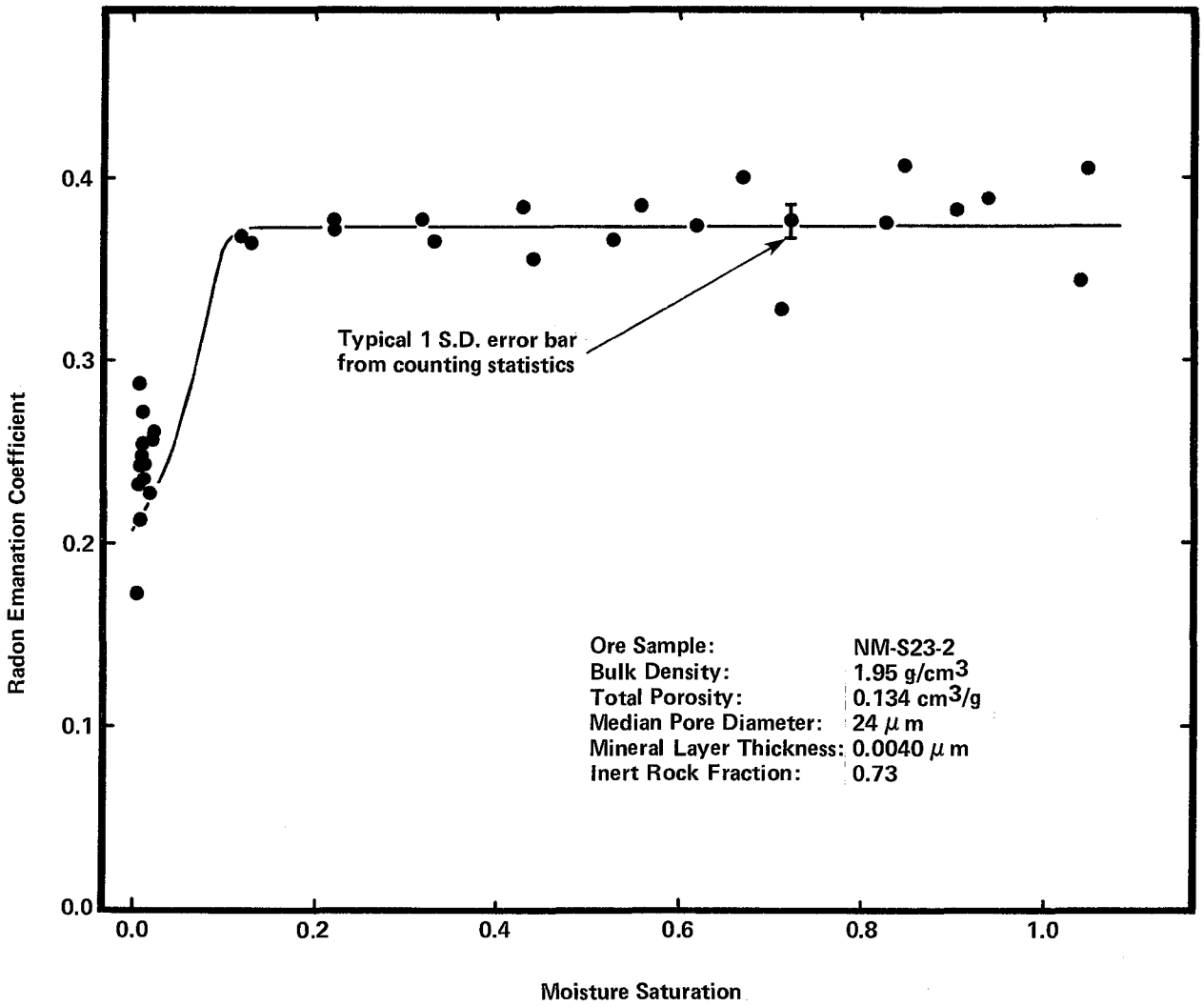

FIGURE 5-17. Comparison of Measured Emanation Coefficients with Calculated Emanation versus Moisture Curve for Ore Sample NM-S23-2.

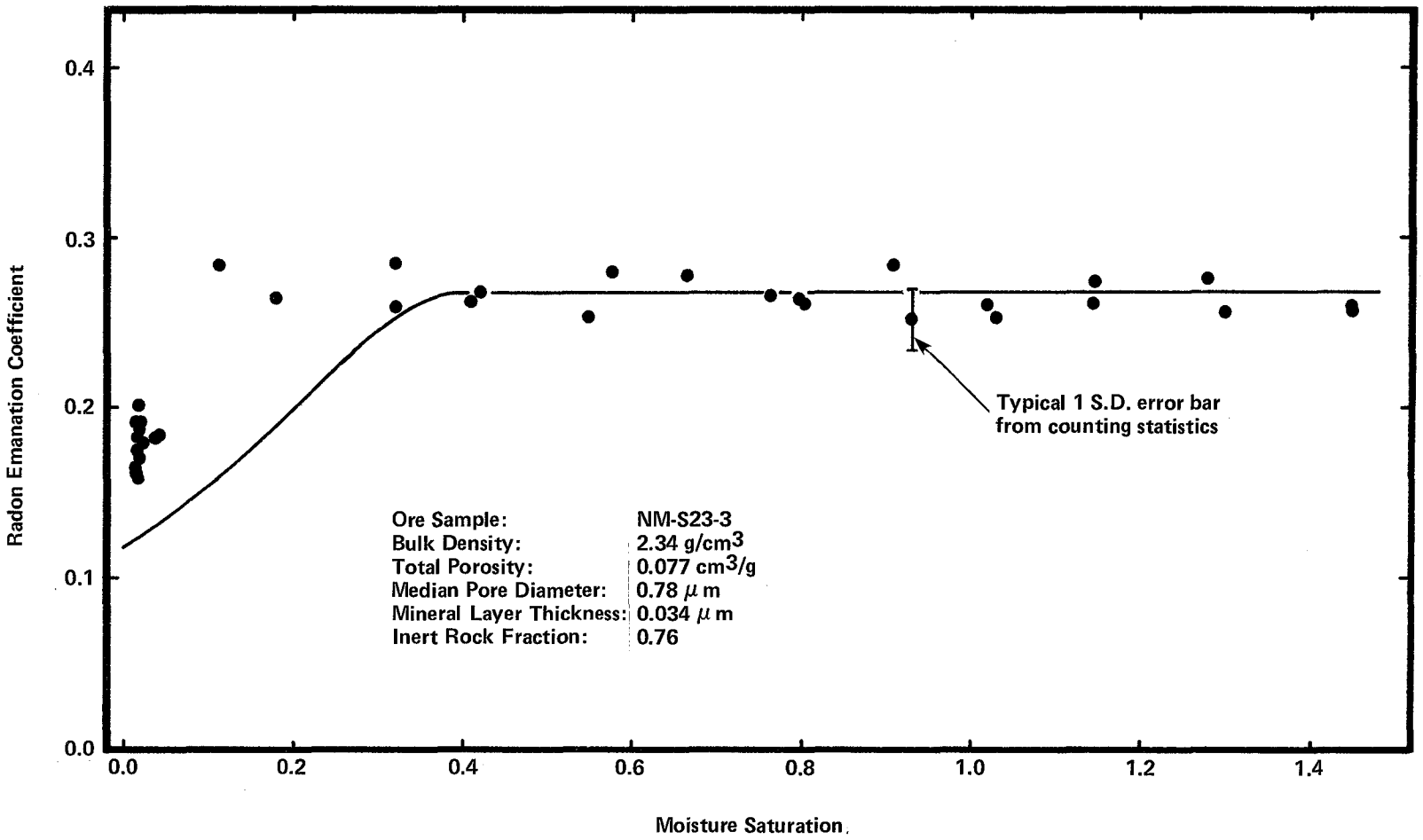

FIGURE 5-18. Comparison of Measured Emanation Coefficients with Calculated Emanation versus Moisture Curve for Ore Sample NM-S23-3.

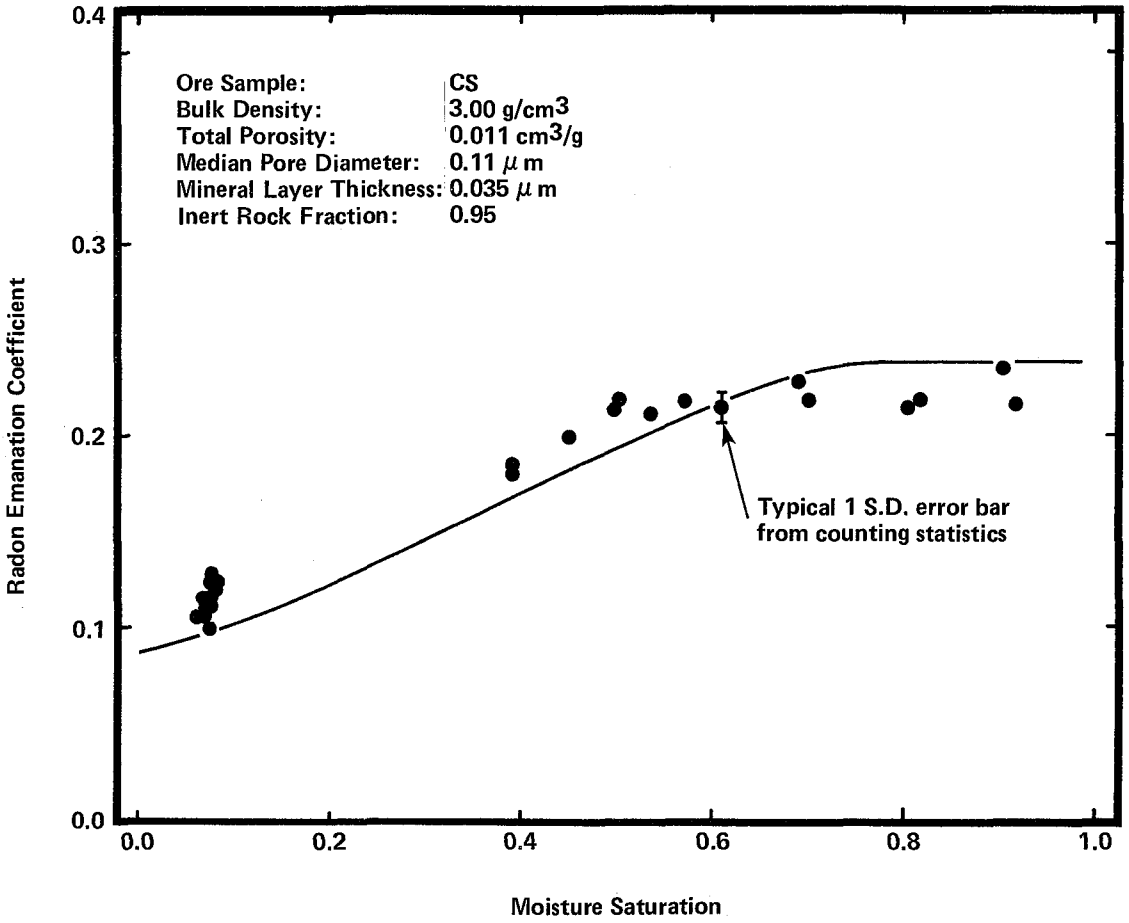

FIGURE 5-19.- Comparison of Measured Emanation Coefficients with Calculated Emanation versus Moisture Curve for Ore Sample CS.

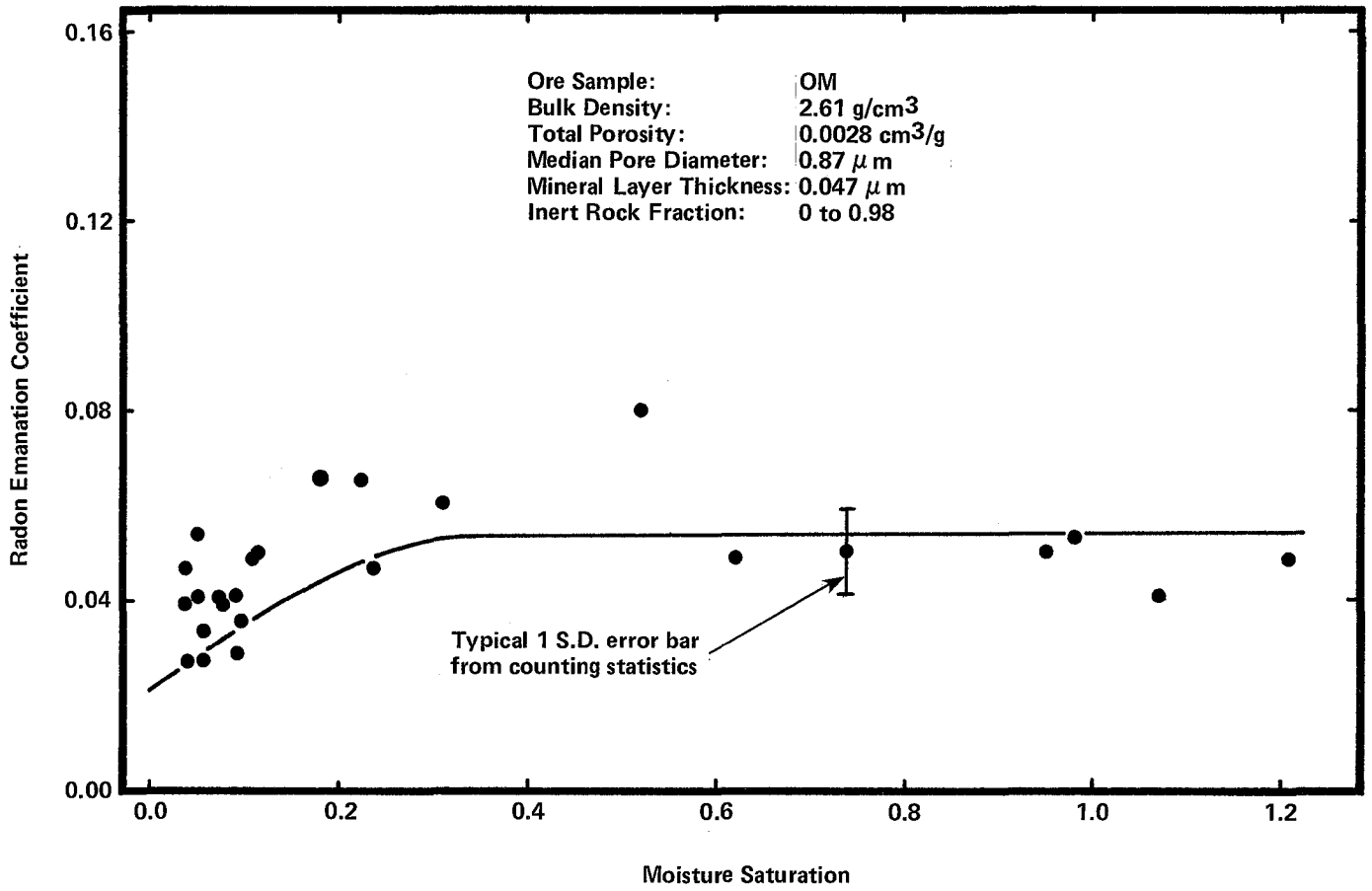

FIGURE 5-20. Comparison of Measured Emanation Coefficients with Calculated Emanation versus Moisture Curve for Ore Sample OM.

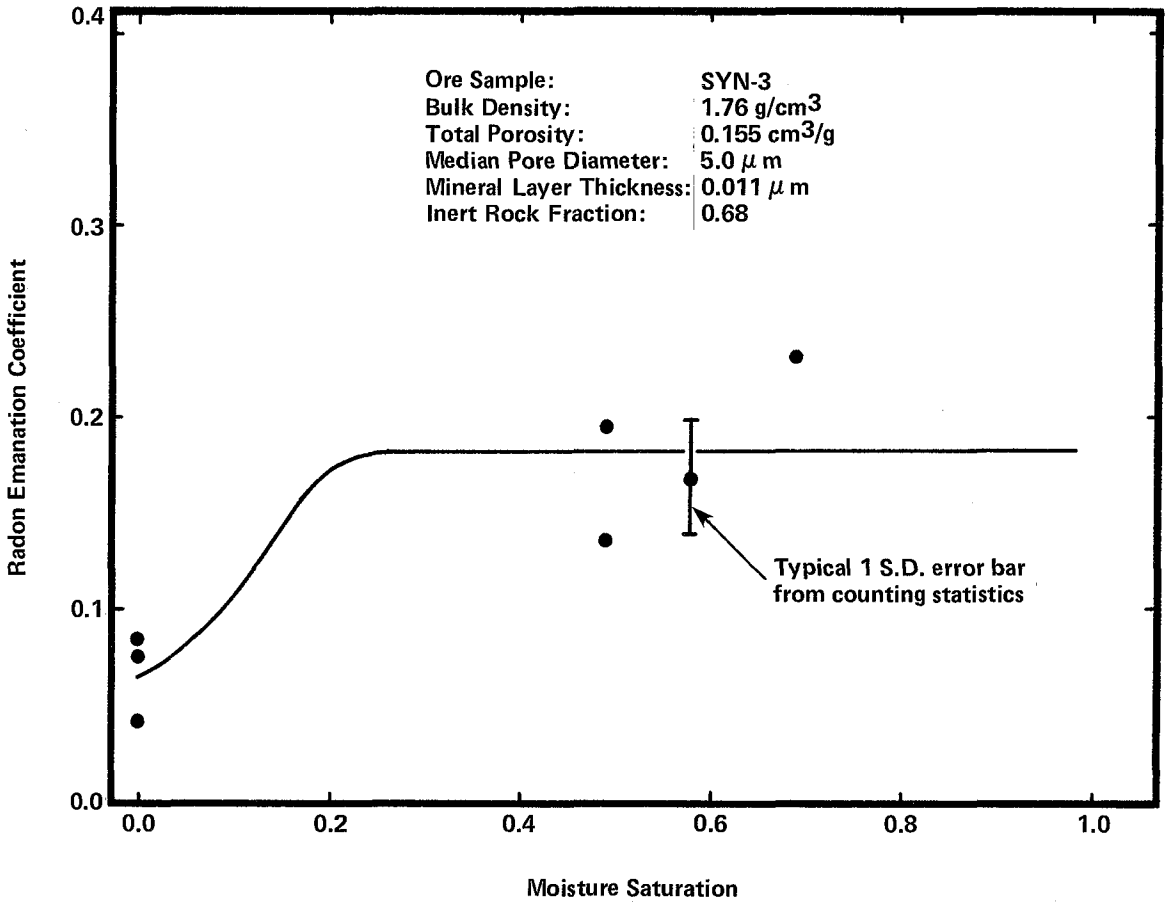

FIGURE 5-21. Comparison of Measured Emanation Coefficients with Calculated Emanation versus Moisture Curve for Ore Sample SYN-3.

model are tabulated in Table 5-1. As indicated, the inert fraction comprises most of the ore material. The inert rock can be interpreted to be the sand grain material in sandstone ores which only contain radium in the intergranular cementing material. In more homogeneous, hard rock ores, the inert rock fraction must be considered to be regions of non-porous rock, suggesting that pore development occurred in mineral inclusions which were more subject to the forces promoting pore development than the surrounding rock. The inert rock fractions were relatively constant for all ores, averaging 0.78 ± 0.11 for 16 of the ores. In the case of WG1, the inert fraction was pulled to zero in trying to fit the very low dry emanation coefficients. In the case of OM, the inert rock fraction could be varied over the indicated range without affecting the result. This suggested that the pores were so distantly spaced that no radium-bearing source regions from adjacent pores overlapped. The calculated average inert rock fraction is consistent with the similar fraction of coarse rock grains found in uranium mill tailings.

Mineral layer thicknesses were also remarkably similar, with an average thickness of 0.025 ± 0.011 μm for the eighteen ores. The mineral layer thicknesses were nearly always slightly less than the recoil range for a radon atom, a condition expected in order to explain the frequently high observed radon emanation coefficients.

The present model adequately explains the mechanism of moisture effects on radon emanation for most of the ores, particularly in consideration of the homogeneity difficulties associated with them. The mechanism appears to be the simple slowing down of the recoil atoms by the water as they traverse a pore. The water therefore affects both the direct recoil and indirect recoil contributions to radon emanation by the same means, that of reducing the energy of the recoiling atom. Other geometric models could be proposed to be more applicable to a given type of ore; however, the cylindrical pore model described here appears to be the most generally applicable model for a wide variety of ore types, and probably one of the simplest to describe mathematically.

TABLE 5-1. Mineral layer thickness and inert rock fractions estimated from the model

Ore Sample	Mineral Layer Thickness, μm	Inert Rock Fraction
WP-1	0.026	0.62
WP-2	.020	.63
WG-1	.034	.00
WG-2	.035	.62
WG-3	.008	.68
WC	.023	.74
UB	.020	.90
UL	.041	.93
CK	.022	.81
CD	.020	.88
NM-P10-1	.024	.84
NM-P10-2	.026	.85
NM-S23-1	.026	.81
NM-S23-2	.004	.73
NM-S23-3	.034	.76
CS	.035	.95
OM	.047	0.00-.98
SYN-3	.011	.68

CHAPTER 6

SUMMARY

The principal accomplishments and findings of this study are summarized in the following observations and conclusions.

- Radon emanation coefficients were consistently measured to be lower when ores were dry than they were when they were moistened to 5-20 percent of saturation. Emanation coefficients in dry ores ranged from 0.02 to 0.36, and in moist ores from 0.05 to 0.55.

- Radon emanation coefficients increased with increasing moisture throughout the low-moisture range, the extent of which depended on the pore size distribution. Finely porous ores exhibited moisture effects at moistures as high as 60 percent of saturation, while ores with predominantly coarser pores exhibited moisture effects only up to about 10 percent of saturation. Moisture variations above these ranges did not affect emanation coefficients.

- Observed emanation coefficients were explained in both magnitude and in moisture dependence by a cylindrical pore model which depended on annular water films on the pore surfaces to slow or stop recoiling radon atoms. Moisture in the pores affected emanation by both the direct recoil and indirect recoil mechanisms.

- Crushing of the ores to 2-3 mm diameter particles did not appear to significantly affect their emanation coefficients. An observed decrease in emanation after crushing was attributed to an alteration in geometry for the gamma-ray analyses.

- Application of the mathematical model for radon emanation to the uranium ores suggested that an average of 78 percent of the ore volume consisted of inert, non-porous rock, and that the radium mineralization was confined to annular layers of about 0.025 micrometers thickness around the cylindrical pores.

- The ore's own radon was used to determine radon's diffusion coefficient in the ore.

- It was demonstrated that injecting radon into the sample of ore may allow a more accurate determination of radon's diffusion coefficient.

- More precise determinations of the diffusion coefficient are obtained with more uniform materials like the employed synthetic ore or ground uranium tailings.

- A mathematical description was developed for the diffusion coefficient in terms of its components of volume diffusion in the pore air and surface diffusion on the pore walls. A form of this model was able to account for the diffusion coefficient either decreasing or increasing with the addition of moisture to the dry ore. In either case, the model still allows the flux to decrease with increasing moisture.

- Radon's adsorption coefficient was determined on a uranium ore (WG1) using the ore's own radon.

REFERENCES

1. Adler, H.H. Concepts of Genesis of Sandstone-Type Uranium Ore Deposits. Economic Geology, v. 58, No. 6, Sept-Oct 1963.

2. Alexander, R.L. Communication, Chief Geologist of Madawaska Mines Limited, 1980.

3. American Society for Testing Materials, conforming to specifications ASTM C-150 Type 2, Federal SS-C-192, Type 2, and A.A.S.H.O. M85-60 Type 2.

4. Andrews, J.N., and D.F. Wood. Mechanism of Radon Release in Rock Matrices and Entry into Groundwaters. Trans. Inst. Mining Metallurgy. v. B-81, 1972, pp. 198-209.

5. Austin, S.R., and R.F. Droullard. Radon Emanation from Domestic Ores Determined by Modifications of the Closed-Can, Gamma-Only Assay Method. U.S. Bureau of Mines, Report RI 8264, 1978, 74 pp.

6. Bailey, R.V. Review of Uranium Deposits in the Great Divide Basin-Crooks Gap Area, Wyoming, in Energy and Mineral Resources of the Southern Rocky Mountains. The Mountain Geologist, v. 9, No. 2 and 3, 1972, pp. 165-182.

7. Chase, G.D., and J.L. Robinowitz. Principles of Radio-isotope Methodology. Burgess Publishing Co., Minneapolis, Minnesota, 1967, pp. 177-178.

8. Childers, M.O., and R.V. Bailey. Classification of Uranium Deposits. Contributions to Geology, Wyoming Uranium, Issue II, v. 17, No. 2, 1979.

9. Davis, J.F. Uranium Deposits of Powder River Basin, Wyoming. Union Pacific Railroad Company, Twenty-Second Annual Field Conference, Wyoming Geological Association, 1970.

10. Delafoss, D. Surface Flow of Adsorbable Gases through Magnesium Chromite. Oxygen and Ammonia Surface Flows. J. Colloid Interface Sci., v. 63(1), 1978, pp. 1-6.

11. Elevatorski, E.A. Uranium Guidebook for Wyoming, MONOBRAS, 1976.

12. Elevatorski, E.A. Uranium Guidebook for the Paradox Basin, Utah-Colorado, MONOBRAS, 1978.

13. Fisher, J.C. Calculation of Diffusion Penetration Curves for Surface and Grain Boundary Diffusion. J. Appl. Phys., v. 22, January 1951, pp. 74-77.

14. Grocery store paraffin wax.

15. Hanshaw, B.B., and G.A. Hill. Geochemistry and Hydrodynamics of the Paradox Basin Region, Utah, Colorado and New Mexico. Chem. Geol., v. 4, 1969, pp. 263-294.

16. Hewitt, D.F. Geology of the Cardiff and Faraday Townships. Ontario Department of Mines, Annual Report 66, Part 3, 1957.

17. Hintze, L., ed. Guidebook to the Geology of Utah, Uranium Districts of Southeastern Utah. Utah Geological Society, No. 21, 1967.

18. Holub, R.F., and B.T. Brady. The Effect of Stress on Radon Emanation from Rock. J. Geophys. Res., v. 86, No. B3, March 19, 1981, pp. 1776-1784.

19. Holub, R.F. U.S. Bureau of Mines, Denver Federal Center, Denver, Colorado 80225.

20. Keefer, W.R. Stratigraphy and Geologic History of the Uppermost Cretaceous, Paleocene, and Lower Eocene Rock in the Wind River Basin, Wyoming. USGS Professional Paper 495-A, 1965.

21. Kelly, V.C., Chrm. Geology and Technology of the Grants Uranium Region. New Mexico Bureau of Mines and Mineral Resources, Memoir 15, 1963.

22. Kerr, P.F. Uranium Emplacement in the Colorado Plateau. Geological Society of America Bulletin, v. 60, No. 9, 1958, pp. 1075-1112.

23. King, J.W., and S. Ralph Austin. Some Characteristics of Roll-Type Uranium Deposits at Gas Hills, Wyoming. U.S. Energy Commission Resource Appraisal Branch, Oct 1965.

24. Lang, A.H., J.W. Griffith and H.R. Steacy. Canadian Deposits of Uranium and Thorium. Geol. Surv. Can. Econ. Geol. Series, No. 16, 1962.

25. Levy, V. Diffusion at Crystal Surfaces. Ch. 5 in L. Dobrzynski, ed., Handbook of Surfaces and Interfaces. Garland STPM Press, New York, v. 1, 1978.

26. Linchard, J., M. Scharff and H.E. Schott. Mat. Fys. Medd. Dan. Vid. Selsk. v. 33, 1963, p. 1.

27. Little, H.W. Anhydrite-Pegmatite Uranium Ore at Bancroft, Ontario. Econ. Geol. v. 64, 1969, pp. 691-695.

28. Longen, R.E., and A.L. Kidwell. Geology and Geochemistry of the Highland Uranium Deposit. Wyoming Geological Association, Earth Science Bulletin, Dec 1973, pp. 41-48.

29. Moench, R.H., and J.S. Schlee. Geology and Uranium Deposits of the Laguna District, New Mexico. USGS Professional Paper 519, 1967.

30. Noble, E.A. Genesis of Uranium Belts of the Colorado Plateau. International Geological Congress, Report of the Twenty-First Session, Part XV, Genetic Problems of Uranium and Thorium Deposits, 1960.

31. Paxton, Terry, and Jim Krouch. Lucky Mac Mine, personal communication to Karen Felthauser, 1980-81.

32. Percival, D.R., and D.B. Martin. Sequential Determination of Radium-226, Radium-228, Actinium-227, and Thorium Isotopes in Environmental and Process Waste Samples. Anal. Chem., v. 46, 1974, pp. 1732-1749.

33. Polak, A.J. Desorption and Surface Diffusion: Nitrogen on Tungsten (110). Report 1977, R-9789, UILU-ENG-77-2236, Order No. AD-A-56346, available from the National Technical Information Service, Springfield, Virginia.

34. Porstendoerfer, J. Diffusion Coefficients of Radon (Radon-222; Radon-220) in Some Solid Materials. Biophyzik, v. 5, 1968, pp. 248-254.

35. Quet, C., J. Rousseau-Violet and P. Bussiere. Recoil Emanating Power and Specific Surface Area of Solids Labeled by Radium Recoil Atoms. Radiochem. Radioanal. Letters, v. 23, 1975, pp. 359-368.

36. Robinson, S.C. A Genetic Classification of Canadian Uranium Deposits. Can. Mineralogist, v. 6, part 2, 1958, pp. 174-190.

37. Robinson, S.C. Economic Uranium Deposits in Grantic Dykes Bancroft. Can. Mineralogist, v. 6, Part 4, 1960, pp. 513-521.

38. Rogers, V.C., R.F. Overmyer, K.M. Putzig, C.M. Jensen, K.K. Nielson and B.W. Sermon. Characterization of Uranium Tailings Cover Materials for Radon Flux Reduction. Report NUREG/CR-1081 prepared for Argonne National Laboratory by Ford, Bacon & Davis Utah, January 1980.

39. Satterly, J. Radioactive Mineral Occurrences in the Bancroft Area, Ontario Department of Mines, Annual Report 65, Part 6, 1956.

40. Serdyukova, A.S., and Y.T. Kapitanov. Radon Isotopes and Short-Lived Products of Their Disintegration in Nature. Atomizdat, Moscow, 1969, translated for U.S. Department of Interior, Bureau of Mines, Washington, D.C., TT72-51014, 1978, 379 pp.

41. Serdyukova, A.S., and Y.T. Kapitanov, ibid., p. 62-63.

42. Serdyukova, A.S., and Y.T. Kapitanov, ibid., p. 16.

43. Sill, C.W., and F.D. Hindman. Preparation and Testing of Standard Soils Containing Known Quantities of Radionuclides. Anal. Chem., v. 46, 1974, pp. 113-118.

44. Sharp, W.N., and A.B. Gibbons. Geology and Uranium Deposits of the Southern Part of the Powder River Basin, Wyoming. USGS Bulletin 1147-D, 1964.

45. Sheridan, M., and Albee. Geology and Uranium Deposits of the Ralston Buttes District, Jefferson County, Colorado. USGS Professional Paper 520, 1967.

46. Stephens, J.G., and D.L. Healey. Geology and Uranium Deposits at Crooks Gap, Fremont County, Wyoming. UGGS Bulletin 1147-F, 1964.

47. Stornik, H., R. Stockmeyer and M. Monkenbusch. Motion of Hydrogen and Water Adsorbed in Fuel Cell Catalysts, Examined by Neutron Scattering. J. Mol. Struct., v. 60, 1980, pp. 443-448.

48. Stranden, E. A Simple Method for Measuring the Radon Diffusion Coefficient and Exhalation Rate from Building Materials. Health Phys., v. 37, August 1979, pp. 242-244.

49. Sudo, Y., J. Takagi, T. Serizawa and M. Suzuki. (Activiated Carbon Adsorption of Chlorinated Organics from Aqueous Solution.) Tokyo Kogyo Koto Semmon Gakko Kenkyu Kokokusho, v. 11, 1979, pp. 87-90; CA 92, 180144 (1980).

50. Tanner, A.B. Radon Migration in the Ground: A Review. The Natural Radiation Environment, J.A.S. Adams and W.M. Lowder, eds., University of Chicago Press, 1964, pp. 161-190.

51. Thamer, B.J., et al. Assessments of Stabilization Methods for Uranium Mill Tailings. Report FBDU-359 for U.S. Department of Energy by Ford, Bacon & Davis Utah, 1981.

52. Underhill, D.W. Correlation of the Specific Surface Area and Bulk Density of Commercial Charcoals with their Adsorption Capacity for Radioactive Krypton and Xenon. Nuc. Sci. Eng., v. 79, 1981, pp. 19-25.

53. U.S. Department of the Interior, Bureau of Reclamation. Concrete Manual, A Manual for the Control of Concrete Construction, Sixth Ed., Denver, Colorado, 1955.

54. Van Lint, V.A.J., T.M. Flanagan, R.E. Leadon, J.A. Naber and V.C. Rogers. Mechanisms of Radiation Effects in Electronic Materials. Wiley and Sons, New York, 1980, pp. 287-291.

55. Van Genuchten, M.T., and P.J. Wierenga. Mass Transfer Studies in Sorbing Porous Media I. Analytical Solutions. Soil Sci. Soc. Am., v. 40, No. 4, July-August 1976, pp. 473-480.

56. Wahl, A.C. Radioactivity Applied to Chemistry. Wiley and Sons, New York, 1951, pp. 284-310.

57. Walker, W.F., G.J. Kirouac and F.M. Rourke. Chart of the Nuclides. Knolls Atomic Power Laboratory, General Electric Company, Schenectady, New York 12345, 12th ed., revised to April 1977.

58. Wogman, N.A., D.E. Robertson and R.W. Perkins. A Large Detector, Anticoincidence Shielded Multidimensional Gamma-Ray Spectrometer. Nucl. Instr. Meth., v. 50, 1967, pp. 1-10.

59. Wright, J.H. Economic Geology of the Schwartzwalder Mine. Chief Geologist, Schwartzwalder Mine, Cotter Corporation, 1979.

60. Young, E.J. Genesis of the Schwartzwalder Uranium Deposit, Jefferson County, Colorado. Contributions to Geology, University of Wyoming, 1979.

61. Zimens, K.E. Surface Area Determination and Diffusion Measurements with Radioactive Inert Gases. Z. Phys. Chem., v. 192, 1943, pp. 1-55.

62. Zimens, K.E. Surface Area Determination and Diffusion Measurements with Radioactive Inert Gases. Z. Phys. Chem., v. A-191, 1942, pp. 95-128.

Appendix A. Pore size distributions

All ore samples in this study were analyzed by mercury intrusion porosimetry for their pore size distributions. These analyses were conducted by the Materials Analysis Laboratory of Micromeritics Instrument Corporation, Norcross, Georgia, using a mercury intrusion porosimeter. Selected data from the results of these analyses are presented for each ore sample in this appendix.

Several of the reported parameters require definition or clarification. The total intrusion volume was the porosity of the ore lump, and was compared with other measurements in the main text for selection of a representative value for the total porosity of the ore. The total pore area is the surface area of the pores assuming cylindrical geometry. The median pore diameter (volume) is the fifty-percentile value obtained from the volume distribution curve. The median pore diameter (area) is the fifty-percentile value obtained from the pore area distribution curve. The average pore diameter (4V/A) is obtained by the indicated volume/area ratio, which assumes the pores to be right circular cylinders. The bulk density was calculated from the sample mass (g) and volume (cm^3) at the initial mercury filling pressure, and the apparent (skeletal) density was similarly determined at the final, maximum pressure.

Column one of the data tables lists the actual mercury pressure for the given data point. Column two lists the pore diameters (μm) corresponding to the pressure values in column one. The pore diameters are based on the Washburn equation,

$$d = \frac{-4 \gamma \cos \theta}{P} \qquad \text{(A-1)}$$

where γ is the surface tension, θ is the contact angle, and P is the pressure. Column three lists the actual cumulative mercury volume intruded into the sample. Column four lists the cumulative pore surface area using the 4V/d relationship. Column five lists the mean pore diameters between two consecutive points from column two, which were used in connection with the differential volumes which are listed in the last column. The data in column six are simply the differential data from column three.

MICROMERITICS AUTO-PORE 9200 V2.00

FORD, BACON, & DAVIS UTAH INC INTRUSION (PRESSURIZATION) DATA SUMMARY
ORE WPI MAL #1285
PNTR NUMBER +330

TOTAL INTRUSION VOLUME =	+0.1836	CC/G
TOTAL PORE AREA =	+9.4513	SQ-M/G
MEDIAN PORE DIAMETER (VOLUME) =	+24.3435	MICROMETERS
MEDIAN PORE DIAMETER (AREA) =	+0.0057	MICROMETERS
AVERAGE PORE DIAMETER (4V/A) =	+0.0777	MICROMETERS
BULK DENSITY =	+1.8016	G/CC
APPARENT (SKELETAL) DENSITY =	+2.6922	G/CC

% CAPILLARY = +44.3743

PRESSURE PSIA	PORE DIAMETER MICRO-M	INTRUSION VOLUME CC/G	PORE SURFACE SQ-M/G	MEAN DIAMETER MICRO-M	DV
+1.4	+124.3780	-0.0003	-0.0000	+124.0590	-0.0003
+8.9	+19.8106	+0.0960	+0.0053	+72.0943	+0.0963
+16.9	+10.4547	+0.1292	+0.0141	+15.1326	+0.0333
+28.6	+6.1712	+0.1311	+0.0150	+8.3129	+0.0019
+53.6	+3.2964	+0.1368	+0.0198	+4.7338	+0.0057
+73.8	+2.3938	+0.1392	+0.0232	+2.8451	+0.0024
+99.4	+1.7781	+0.1407	+0.0261	+2.0860	+0.0015
+113.6	+1.5557	+0.1416	+0.0282	+1.6669	+0.0009
+128.6	+1.3749	+0.1422	+0.0299	+1.4653	+0.0006
+148.9	+1.1875	+0.1428	+0.0318	+1.2812	+0.0006
+179.4	+0.9853	+0.1437	+0.0352	+1.0864	+0.0009
+198.9	+0.8887	+0.1440	+0.0365	+0.9370	+0.0003
+239.6	+0.7376	+0.1444	+0.0381	+0.8132	+0.0003
+280.3	+0.6306	+0.1450	+0.0418	+0.6841	+0.0006
+308.7	+0.5727	+0.1456	+0.0459	+0.6016	+0.0006
+359.5	+0.4918	+0.1463	+0.0506	+0.5322	+0.0006
+407.3	+0.4340	+0.1469	+0.0561	+0.4629	+0.0006
+479.6	+0.3686	+0.1478	+0.0654	+0.4013	+0.0009
+549.9	+0.3214	+0.1485	+0.0729	+0.3450	+0.0006
+637.9	+0.2771	+0.1494	+0.0855	+0.2993	+0.0009
+728.7	+0.2426	+0.1501	+0.0955	+0.2599	+0.0006
+837.1	+0.2112	+0.1510	+0.1123	+0.2269	+0.0010
+966.1	+0.1830	+0.1520	+0.1318	+0.1971	+0.0010
+1117.5	+0.1582	+0.1523	+0.1405	+0.1706	+0.0004
+1294.3	+0.1366	+0.1539	+0.1830	+0.1474	+0.0016
+1492.6	+0.1184	+0.1546	+0.2043	+0.1275	+0.0007
+1712.3	+0.1032	+0.1556	+0.2395	+0.1108	+0.0010
+1969.2	+0.0898	+0.1568	+0.2924	+0.0965	+0.0013
+2287.7	+0.0773	+0.1578	+0.3398	+0.0835	+0.0010
+2619.8	+0.0675	+0.1591	+0.4105	+0.0724	+0.0013
+3017.8	+0.0586	+0.1598	+0.4542	+0.0630	+0.0007
+3491.6	+0.0506	+0.1611	+0.5483	+0.0546	+0.0013
+4014.6	+0.0440	+0.1621	+0.6314	+0.0473	+0.0010
+4630.0	+0.0382	+0.1639	+0.8138	+0.0411	+0.0019
+5362.6	+0.0330	+0.1658	+1.0244	+0.0356	+0.0019
+6183.1	+0.0286	+0.1674	+1.2283	+0.0308	+0.0016
+7076.9	+0.0250	+0.1689	+1.4613	+0.0268	+0.0016
+8161.2	+0.0217	+0.1702	+1.6778	+0.0233	+0.0013
+9465.2	+0.0187	+0.1715	+1.9274	+0.0202	+0.0013
+10857.1	+0.0163	+0.1727	+2.2129	+0.0175	+0.0012
+12542.1	+0.0141	+0.1740	+2.5405	+0.0152	+0.0012
+14432.2	+0.0122	+0.1752	+2.9159	+0.0132	+0.0012
+16659.3	+0.0106	+0.1761	+3.2426	+0.0114	+0.0009
+19179.5	+0.0092	+0.1767	+3.4963	+0.0099	+0.0006
+22124.5	+0.0080	+0.1774	+3.7858	+0.0086	+0.0006
+25479.8	+0.0069	+0.1780	+4.1157	+0.0075	+0.0006
+29362.6	+0.0060	+0.1786	+4.4918	+0.0065	+0.0006
+33831.5	+0.0052	+0.1795	+5.1316	+0.0056	+0.0009
+39091.6	+0.0045	+0.1804	+5.8640	+0.0049	+0.0009
+45040.3	+0.0039	+0.1813	+6.7024	+0.0042	+0.0009
+51882.7	+0.0034	+0.1824	+7.9845	+0.0037	+0.0012
+59736.2	+0.0030	+0.1836	+9.4513	+0.0032	+0.0012

MICROMERITICS AUTO-PORE 9200 V2.00

FORD, BACON & DAVIS #38178-080-S INTRUSION (PRESSURIZATION) DATA SUMMARY
WP2 MAL #1286
PNTR NUMBER +88

TOTAL INTRUSION VOLUME =	+0.1509	CC/G
TOTAL PORE AREA =	+3.5932	SQ-M/G
MEDIAN PORE DIAMETER (VOLUME) =	+18.9090	MICROMETERS
MEDIAN PORE DIAMETER (AREA) =	+0.0170	MICROMETERS
AVERAGE PORE DIAMETER (4V/A) =	+0.1680	MICROMETERS
BULK DENSITY =	+1.8417	G/CC
APPARENT (SKELETAL) DENSITY =	+2.5507	G/CC

% CAPILLARY = +51.5655

PRESSURE PSIA	PORE DIAMETER MICRO-M	INTRUSION VOLUME CC/G	PORE SURFACE SQ-M/G	MEAN DIAMETER MICRO-M	DV
+1.5	+121.8650	+0.0002	+0.0000	+121.8650	+0.0002
+2.0	+89.0382	+0.0035	+0.0001	+105.4520	+0.0033
+3.0	+59.2858	+0.0139	+0.0007	+74.1619	+0.0105
+4.0	+44.4371	+0.0257	+0.0016	+51.8614	+0.0118
+5.5	+32.3017	+0.0414	+0.0032	+38.3693	+0.0157
+7.0	+25.4261	+0.0588	+0.0057	+28.8638	+0.0174
+8.5	+20.9093	+0.0703	+0.0076	+23.1677	+0.0115
+10.4	+16.9925	+0.0804	+0.0098	+18.9509	+0.0100
+12.9	+13.6943	+0.0889	+0.0120	+15.3434	+0.0085
+15.9	+11.1093	+0.0952	+0.0140	+12.4018	+0.0063
+19.9	+8.8646	+0.1015	+0.0165	+9.9869	+0.0063
+24.9	+7.0969	+0.1063	+0.0189	+7.9807	+0.0048
+28.6	+6.1712	+0.1079	+0.0199	+6.6340	+0.0016
+38.7	+4.5699	+0.1116	+0.0227	+5.3706	+0.0037
+48.8	+3.6230	+0.1140	+0.0250	+4.0965	+0.0024
+58.8	+3.0086	+0.1159	+0.0274	+3.3158	+0.0020
+73.8	+2.3962	+0.1177	+0.0300	+2.7024	+0.0018
+88.9	+1.9876	+0.1192	+0.0328	+2.1919	+0.0015
+114.0	+1.5507	+0.1208	+0.0362	+1.7692	+0.0015
+138.5	+1.2760	+0.1221	+0.0400	+1.4134	+0.0013
+173.9	+1.0164	+0.1232	+0.0439	+1.1462	+0.0011
+226.1	+0.7818	+0.1239	+0.0469	+0.8991	+0.0007
+280.3	+0.6306	+0.1248	+0.0520	+0.7062	+0.0009
+329.2	+0.5370	+0.1257	+0.0582	+0.5838	+0.0009
+419.0	+0.4218	+0.1268	+0.0676	+0.4794	+0.0011
+517.7	+0.3415	+0.1277	+0.0773	+0.3816	+0.0009
+636.9	+0.2776	+0.1284	+0.0864	+0.3095	+0.0007
+800.0	+0.2210	+0.1294	+0.1015	+0.2493	+0.0009
+985.6	+0.1794	+0.1303	+0.1204	+0.2002	+0.0009
+1196.6	+0.1477	+0.1311	+0.1382	+0.1635	+0.0007
+1393.9	+0.1268	+0.1316	+0.1528	+0.1373	+0.0005
+1593.2	+0.1110	+0.1323	+0.1767	+0.1189	+0.0007
+1890.1	+0.0935	+0.1330	+0.2054	+0.1022	+0.0007
+2288.6	+0.0772	+0.1340	+0.2504	+0.0854	+0.0010
+2624.7	+0.0674	+0.1349	+0.3023	+0.0723	+0.0009
+3013.9	+0.0587	+0.1356	+0.3481	+0.0630	+0.0007
+3483.3	+0.0507	+0.1363	+0.4011	+0.0547	+0.0007
+4014.6	+0.0440	+0.1375	+0.4987	+0.0474	+0.0012
+4630.0	+0.0382	+0.1384	+0.5900	+0.0411	+0.0009
+5377.3	+0.0329	+0.1400	+0.7692	+0.0355	+0.0016
+6197.8	+0.0285	+0.1412	+0.9191	+0.0307	+0.0011
+7091.6	+0.0249	+0.1428	+1.1554	+0.0267	+0.0016
+8161.2	+0.0217	+0.1441	+1.3889	+0.0233	+0.0014
+9479.9	+0.0186	+0.1453	+1.6154	+0.0202	+0.0011
+10857.1	+0.0163	+0.1464	+1.8745	+0.0175	+0.0011
+12556.8	+0.0141	+0.1473	+2.1149	+0.0152	+0.0009
+14432.2	+0.0122	+0.1482	+2.3901	+0.0132	+0.0009
+16703.3	+0.0106	+0.1491	+2.7064	+0.0114	+0.0009
+19179.5	+0.0092	+0.1498	+2.9804	+0.0099	+0.0007
+22139.2	+0.0080	+0.1502	+3.1927	+0.0086	+0.0005
+25098.9	+0.0070	+0.1505	+3.3162	+0.0075	+0.0002
+29860.8	+0.0059	+0.1509	+3.5932	+0.0065	+0.0004

MICROMERITICS AUTO-PORE 9200 V2.00

FORD, BACON & DAVIS #38178-080-S INTRUSION (PRESSURIZATION) DATA SUMMARY
WG1 MAL #1282
PNTR NUMBER +88

TOTAL INTRUSION VOLUME =	+0.1184	CC/G
TOTAL PORE AREA =	+0.8329	SQ-M/G
MEDIAN PORE DIAMETER (VOLUME) =	+41.1458	MICROMETERS
MEDIAN PORE DIAMETER (AREA) =	+0.0238	MICROMETERS
AVERAGE PORE DIAMETER (4V/A) =	+0.5688	MICROMETERS
BULK DENSITY =	+1.9776	G/CC
APPARENT (SKELETAL) DENSITY =	+2.5825	G/CC

% CAPILLARY = +49.1092

PRESSURE PSIA	PORE DIAMETER MICRO-M	INTRUSION VOLUME CC/G	PORE SURFACE SQ-M/G	MEAN DIAMETER MICRO-M	DV
+1.5	+118.8640	+0.0000	+0.0000	+118.8640	+0.0000
+2.0	+88.0633	+0.0032	+0.0001	+103.4630	+0.0032
+3.0	+58.8521	+0.0406	+0.0022	+73.4576	+0.0373
+4.0	+44.2740	+0.0567	+0.0034	+51.5630	+0.0162
+5.5	+32.4319	+0.0662	+0.0044	+38.3529	+0.0095
+6.9	+25.5067	+0.0712	+0.0051	+28.9693	+0.0050
+8.4	+21.0003	+0.0747	+0.0057	+23.2535	+0.0034
+10.4	+16.9448	+0.0781	+0.0064	+18.9725	+0.0034
+12.9	+13.6633	+0.0813	+0.0072	+15.3040	+0.0032
+15.9	+11.0939	+0.0842	+0.0082	+12.3786	+0.0029
+19.9	+8.8678	+0.0872	+0.0094	+9.9809	+0.0031
+24.9	+7.0948	+0.0897	+0.0107	+7.9813	+0.0025
+28.6	+6.1870	+0.0901	+0.0109	+6.6409	+0.0004
+38.7	+4.5699	+0.0919	+0.0122	+5.3785	+0.0018
+48.6	+3.6339	+0.0937	+0.0140	+4.1019	+0.0018
+58.8	+3.0086	+0.0952	+0.0157	+3.3213	+0.0014
+73.7	+2.3985	+0.0966	+0.0179	+2.7036	+0.0014
+88.9	+1.9892	+0.0979	+0.0202	+2.1939	+0.0013
+114.2	+1.5477	+0.0995	+0.0238	+1.7685	+0.0016
+138.5	+1.2760	+0.1008	+0.0274	+1.4119	+0.0013
+173.7	+1.0177	+0.1019	+0.0313	+1.1468	+0.0011
+227.0	+0.7787	+0.1028	+0.0354	+0.8982	+0.0009
+282.3	+0.6262	+0.1037	+0.0406	+0.7024	+0.0009
+329.2	+0.5370	+0.1048	+0.0482	+0.5816	+0.0011
+418.1	+0.4228	+0.1065	+0.0620	+0.4799	+0.0017
+517.7	+0.3415	+0.1079	+0.0774	+0.3821	+0.0015
+636.9	+0.2776	+0.1092	+0.0942	+0.3095	+0.0013
+799.0	+0.2212	+0.1107	+0.1182	+0.2494	+0.0015
+986.6	+0.1792	+0.1121	+0.1445	+0.2002	+0.0013
+1194.6	+0.1480	+0.1128	+0.1635	+0.1636	+0.0008
+1395.8	+0.1266	+0.1136	+0.1860	+0.1373	+0.0008
+1592.2	+0.1110	+0.1140	+0.1997	+0.1188	+0.0004
+1891.1	+0.0935	+0.1148	+0.2303	+0.1023	+0.0008
+2288.6	+0.0772	+0.1152	+0.2506	+0.0854	+0.0004
+2625.1	+0.0673	+0.1156	+0.2735	+0.0723	+0.0004
+3018.8	+0.0586	+0.1159	+0.2885	+0.0629	+0.0002
+3488.2	+0.0507	+0.1161	+0.3059	+0.0546	+0.0002
+4029.3	+0.0439	+0.1165	+0.3411	+0.0473	+0.0004
+4644.7	+0.0381	+0.1168	+0.3640	+0.0410	+0.0002
+5391.9	+0.0328	+0.1170	+0.3906	+0.0354	+0.0002
+6183.1	+0.0286	+0.1170	+0.3969	+0.0307	+0.0000
+7091.6	+0.0249	+0.1171	+0.4037	+0.0268	+0.0000
+8175.8	+0.0216	+0.1173	+0.4422	+0.0233	+0.0002
+9465.2	+0.0187	+0.1174	+0.4505	+0.0201	+0.0000
+10857.1	+0.0163	+0.1176	+0.4997	+0.0175	+0.0002
+12542.1	+0.0141	+0.1176	+0.4997	+0.0152	+0.0000
+14432.2	+0.0122	+0.1178	+0.5732	+0.0132	+0.0002
+16703.3	+0.0106	+0.1182	+0.7080	+0.0114	+0.0004
+19179.5	+0.0092	+0.1182	+0.7163	+0.0099	+0.0000
+22153.8	+0.0080	+0.1182	+0.7244	+0.0086	+0.0000
+25084.2	+0.0070	+0.1184	+0.8260	+0.0075	+0.0002
+29875.4	+0.0059	+0.1184	+0.8329	+0.0065	+0.0000

MICROMERITICS AUTO-PORE 9200 V2.00

FORD BACON &DAVIS #38178-080-S INTRUSION (PRESSURIZATION) DATA SUMMARY
WG2 MAL#1283
PNTR NUMBER +328

TOTAL INTRUSION VOLUME =	+0.0773	CC/G
TOTAL PORE AREA =	+7.7961	SQ-M/G
MEDIAN PORE DIAMETER (VOLUME) =	+0.1019	MICROMETERS
MEDIAN PORE DIAMETER (AREA) =	+0.0151	MICROMETERS
AVERAGE PORE DIAMETER (4V/A) =	+0.0396	MICROMETERS
BULK DENSITY =	+2.1596	G/CC
APPARENT (SKELETAL) DENSITY =	+2.5921	G/CC

% CAPILLARY = +30.7345

PRESSURE PSIA	PORE DIAMETER MICRO-M	INTRUSION VOLUME CC/G	PORE SURFACE SQ-M/G	MEAN DIAMETER MICRO-M	DV
+1.5	+118.2810	+0.0000	+0.0000	+122.6390	+0.0000
+2.0	+87.7430	+0.0004	+0.0000	+103.0120	+0.0004
+2.9	+60.0232	+0.0007	+0.0000	+73.8831	+0.0004
+4.0	+44.2740	+0.0011	+0.0001	+52.1486	+0.0004
+5.4	+32.4755	+0.0016	+0.0001	+38.3747	+0.0005
+6.9	+25.5337	+0.0020	+0.0002	+29.0046	+0.0004
+8.4	+21.0003	+0.0022	+0.0002	+23.2670	+0.0002
+10.4	+16.9567	+0.0027	+0.0003	+18.9785	+0.0005
+12.9	+13.6788	+0.0031	+0.0004	+15.3177	+0.0004
+15.9	+11.0991	+0.0034	+0.0005	+12.3889	+0.0004
+19.9	+8.8711	+0.0038	+0.0007	+9.9851	+0.0004
+24.9	+7.1010	+0.0042	+0.0009	+7.9861	+0.0004
+28.9	+6.1242	+0.0042	+0.0009	+6.6126	+0.0000
+38.8	+4.5527	+0.0046	+0.0012	+5.3384	+0.0004
+49.3	+3.5853	+0.0049	+0.0015	+4.0690	+0.0004
+59.1	+2.9900	+0.0053	+0.0020	+3.2877	+0.0004
+74.5	+2.3726	+0.0053	+0.0020	+2.6813	+0.0000
+88.6	+1.9942	+0.0057	+0.0027	+2.1834	+0.0004
+113.7	+1.5547	+0.0062	+0.0039	+1.7744	+0.0006
+138.6	+1.2753	+0.0068	+0.0055	+1.4150	+0.0006
+173.8	+1.0168	+0.0073	+0.0074	+1.1461	+0.0006
+200.0	+0.8839	+0.0077	+0.0090	+0.9503	+0.0004
+280.3	+0.6306	+0.0085	+0.0130	+0.7572	+0.0008
+329.2	+0.5370	+0.0092	+0.0181	+0.5838	+0.0007
+417.1	+0.4238	+0.0113	+0.0350	+0.4804	+0.0020
+517.7	+0.3415	+0.0135	+0.0580	+0.3826	+0.0022
+635.9	+0.2780	+0.0166	+0.0982	+0.3097	+0.0031
+796.1	+0.2220	+0.0208	+0.1656	+0.2500	+0.0042
+984.6	+0.1795	+0.0255	+0.2603	+0.2008	+0.0048
+1198.5	+0.1475	+0.0299	+0.3678	+0.1635	+0.0044
+1393.9	+0.1268	+0.0336	+0.4746	+0.1372	+0.0037
+1591.2	+0.1111	+0.0367	+0.5794	+0.1190	+0.0031
+1891.1	+0.0935	+0.0404	+0.7231	+0.1023	+0.0037
+2288.6	+0.0772	+0.0442	+0.9043	+0.0854	+0.0039
+2625.1	+0.0673	+0.0470	+1.0572	+0.0723	+0.0028
+3014.4	+0.0586	+0.0494	+1.2097	+0.0630	+0.0024
+3489.6	+0.0507	+0.0518	+1.3858	+0.0546	+0.0024
+4029.3	+0.0439	+0.0539	+1.5587	+0.0473	+0.0020
+4644.7	+0.0381	+0.0559	+1.7579	+0.0410	+0.0020
+5391.9	+0.0328	+0.0581	+2.0088	+0.0354	+0.0022
+6183.1	+0.0286	+0.0600	+2.2505	+0.0307	+0.0019
+7076.9	+0.0250	+0.0616	+2.4998	+0.0268	+0.0017
+8175.8	+0.0216	+0.0635	+2.8174	+0.0233	+0.0019
+9479.9	+0.0186	+0.0653	+3.1845	+0.0201	+0.0018
+10857.1	+0.0163	+0.0672	+3.6060	+0.0175	+0.0018
+12542.1	+0.0141	+0.0692	+4.1378	+0.0152	+0.0020
+14432.2	+0.0122	+0.0709	+4.6399	+0.0132	+0.0017
+16659.3	+0.0106	+0.0714	+4.8384	+0.0114	+0.0006
+19135.5	+0.0092	+0.0729	+5.4287	+0.0099	+0.0015
+22124.5	+0.0080	+0.0744	+6.1074	+0.0086	+0.0015
+25113.5	+0.0070	+0.0756	+6.7863	+0.0075	+0.0013
+29875.4	+0.0059	+0.0773	+7.7961	+0.0065	+0.0016

MICROMERITICS AUTO-PORE 9200 V2.00

FORD BACON & DAVIS #38178-080-S INTRUSION (PRESSURIZATION) DATA SUMMARY
WG3 MAL#1284
PNTR NUMBER +330

TOTAL INTRUSION VOLUME =	+0.1193	CC/G
TOTAL PORE AREA =	+4.7536	SQ-M/G
MEDIAN PORE DIAMETER (VOLUME) =	+9.7287	MICROMETERS
MEDIAN PORE DIAMETER (AREA) =	+0.0101	MICROMETERS
AVERAGE PORE DIAMETER (4V/A) =	+0.1004	MICROMETERS
BULK DENSITY =	+2.0425	G/CC
APPARENT (SKELETAL) DENSITY =	+2.7008	G/CC

% CAPILLARY = +74.0795

PRESSURE PSIA	PORE DIAMETER MICRO-M	INTRUSION VOLUME CC/G	PORE SURFACE SQ-M/G	MEAN DIAMETER MICRO-M	DV
+1.5	+118.2810	+0.0002	+0.0000	+122.6390	+0.0002
+2.0	+87.7430	+0.0031	+0.0001	+103.0120	+0.0029
+2.9	+60.0232	+0.0145	+0.0007	+73.8831	+0.0113
+4.0	+44.2740	+0.0271	+0.0017	+52.1486	+0.0126
+5.4	+32.4755	+0.0367	+0.0027	+38.3747	+0.0096
+6.9	+25.5337	+0.0426	+0.0035	+29.0046	+0.0059
+8.4	+21.0003	+0.0466	+0.0042	+23.2670	+0.0040
+10.4	+16.9567	+0.0505	+0.0050	+18.9785	+0.0039
+12.9	+13.6788	+0.0542	+0.0060	+15.3177	+0.0037
+15.9	+11.0991	+0.0576	+0.0071	+12.3889	+0.0034
+19.9	+8.8711	+0.0610	+0.0084	+9.9851	+0.0034
+24.9	+7.1010	+0.0630	+0.0095	+7.9861	+0.0021
+28.9	+6.1242	+0.0635	+0.0098	+6.6126	+0.0005
+38.8	+4.5527	+0.0671	+0.0124	+5.3384	+0.0036
+49.3	+3.5853	+0.0697	+0.0151	+4.0690	+0.0027
+59.1	+2.9900	+0.0715	+0.0172	+3.2877	+0.0017
+74.5	+2.3726	+0.0736	+0.0203	+2.6813	+0.0021
+88.6	+1.9942	+0.0750	+0.0228	+2.1834	+0.0014
+113.7	+1.5547	+0.0771	+0.0275	+1.7744	+0.0021
+138.6	+1.2753	+0.0787	+0.0321	+1.4150	+0.0016
+173.8	+1.0168	+0.0804	+0.0382	+1.1461	+0.0017
+200.0	+0.8839	+0.0816	+0.0431	+0.9503	+0.0012
+280.3	+0.6306	+0.0828	+0.0494	+0.7572	+0.0012
+329.2	+0.5370	+0.0842	+0.0590	+0.5838	+0.0014
+417.1	+0.4238	+0.0866	+0.0794	+0.4804	+0.0025
+517.7	+0.3415	+0.0885	+0.0990	+0.3826	+0.0019
+635.9	+0.2780	+0.0903	+0.1218	+0.3097	+0.0018
+796.1	+0.2220	+0.0919	+0.1483	+0.2500	+0.0017
+984.6	+0.1795	+0.0935	+0.1790	+0.2008	+0.0015
+1198.5	+0.1475	+0.0949	+0.2140	+0.1635	+0.0014
+1393.9	+0.1268	+0.0960	+0.2453	+0.1372	+0.0011
+1591.2	+0.1111	+0.0969	+0.2775	+0.1190	+0.0010
+1891.1	+0.0935	+0.0988	+0.3515	+0.1023	+0.0019
+2288.6	+0.0772	+0.1007	+0.4404	+0.0854	+0.0019
+2625.1	+0.0673	+0.1023	+0.5256	+0.0723	+0.0015
+3014.4	+0.0586	+0.1037	+0.6160	+0.0630	+0.0014
+3489.6	+0.0507	+0.1053	+0.7373	+0.0546	+0.0017
+4029.3	+0.0439	+0.1065	+0.8383	+0.0473	+0.0012
+4644.7	+0.0381	+0.1077	+0.9546	+0.0410	+0.0012
+5391.9	+0.0328	+0.1089	+1.0893	+0.0354	+0.0012
+6183.1	+0.0286	+0.1099	+1.2139	+0.0307	+0.0010
+7076.9	+0.0250	+0.1107	+1.3392	+0.0268	+0.0008
+8175.8	+0.0216	+0.1114	+1.4633	+0.0233	+0.0007
+9479.9	+0.0186	+0.1121	+1.6066	+0.0201	+0.0007
+10857.1	+0.0163	+0.1129	+1.7707	+0.0175	+0.0007
+12542.1	+0.0141	+0.1136	+1.9591	+0.0152	+0.0007
+14432.2	+0.0122	+0.1142	+2.1404	+0.0132	+0.0006
+16659.3	+0.0106	+0.1144	+2.2271	+0.0114	+0.0002
+19135.5	+0.0092	+0.1154	+2.6053	+0.0099	+0.0009
+22124.5	+0.0080	+0.1166	+3.2013	+0.0086	+0.0013
+25113.5	+0.0070	+0.1178	+3.8209	+0.0075	+0.0012
+29875.4	+0.0059	+0.1193	+4.7536	+0.0065	+0.0015

MICROMERITICS AUTO-PORE 9200 V2.00

FORD, BACON & DAVIS #38178-080-S INTRUSION (PRESSURIZATION) DATA SUMMARY
WC1 MAL #1281
PNTR NUMBER +73

TOTAL INTRUSION VOLUME =	+0.0591	CC/G
TOTAL PORE AREA =	+2.4512	SQ-M/G
MEDIAN PORE DIAMETER (VOLUME) =	+0.7667	MICROMETERS
MEDIAN PORE DIAMETER (AREA) =	+0.0186	MICROMETERS
AVERAGE PORE DIAMETER (4V/A) =	+0.0964	MICROMETERS
BULK DENSITY =	+2.2785	G/CC
APPARENT (SKELETAL) DENSITY =	+2.6329	G/CC

% CAPILLARY = +28.5724

PRESSURE PSIA	PORE DIAMETER MICRO-M	INTRUSION VOLUME CC/G	PORE SURFACE SQ-M/G	MEAN DIAMETER MICRO-M	DV
+1.5	+121.8650	+0.0002	+0.0000	+121.8650	+0.0002
+2.0	+89.0382	+0.0005	+0.0000	+105.4520	+0.0003
+3.0	+59.2858	+0.0012	+0.0001	+74.1619	+0.0008
+4.0	+44.4371	+0.0017	+0.0001	+51.8614	+0.0005
+5.5	+32.3017	+0.0023	+0.0002	+38.3693	+0.0006
+7.0	+25.4261	+0.0029	+0.0002	+28.8638	+0.0006
+8.5	+20.9093	+0.0034	+0.0003	+23.1677	+0.0005
+10.4	+16.9925	+0.0040	+0.0005	+18.9509	+0.0006
+12.9	+13.6943	+0.0045	+0.0006	+15.3434	+0.0005
+15.9	+11.1093	+0.0054	+0.0009	+12.4018	+0.0009
+19.9	+8.8646	+0.0066	+0.0014	+9.9869	+0.0012
+24.9	+7.0969	+0.0085	+0.0023	+7.9807	+0.0018
+28.6	+6.1712	+0.0088	+0.0025	+6.6340	+0.0003
+38.7	+4.5699	+0.0113	+0.0043	+5.3706	+0.0025
+48.8	+3.6230	+0.0134	+0.0064	+4.0965	+0.0022
+58.8	+3.0086	+0.0154	+0.0089	+3.3158	+0.0020
+73.8	+2.3962	+0.0179	+0.0125	+2.7024	+0.0025
+88.9	+1.9876	+0.0201	+0.0165	+2.1919	+0.0022
+114.0	+1.5507	+0.0228	+0.0227	+1.7692	+0.0028
+138.5	+1.2760	+0.0250	+0.0289	+1.4134	+0.0022
+173.9	+1.0164	+0.0276	+0.0380	+1.1462	+0.0026
+226.1	+0.7818	+0.0294	+0.0457	+0.8991	+0.0017
+280.3	+0.6306	+0.0312	+0.0563	+0.7062	+0.0019
+329.2	+0.5370	+0.0332	+0.0701	+0.5838	+0.0020
+419.0	+0.4218	+0.0359	+0.0922	+0.4794	+0.0026
+517.7	+0.3415	+0.0379	+0.1135	+0.3816	+0.0020
+636.9	+0.2776	+0.0397	+0.1359	+0.3095	+0.0017
+800.0	+0.2210	+0.0412	+0.1614	+0.2493	+0.0016
+985.6	+0.1794	+0.0428	+0.1932	+0.2002	+0.0016
+1196.6	+0.1477	+0.0440	+0.2208	+0.1635	+0.0011
+1393.9	+0.1268	+0.0449	+0.2490	+0.1373	+0.0010
+1593.2	+0.1110	+0.0456	+0.2711	+0.1189	+0.0007
+1890.1	+0.0935	+0.0467	+0.3154	+0.1022	+0.0011
+2288.6	+0.0772	+0.0479	+0.3689	+0.0854	+0.0011
+2624.7	+0.0674	+0.0488	+0.4226	+0.0723	+0.0010
+3013.9	+0.0587	+0.0497	+0.4745	+0.0630	+0.0008
+3483.3	+0.0507	+0.0505	+0.5344	+0.0547	+0.0008
+4014.6	+0.0440	+0.0513	+0.6034	+0.0474	+0.0008
+4630.0	+0.0382	+0.0521	+0.6828	+0.0411	+0.0008
+5377.3	+0.0329	+0.0531	+0.7921	+0.0355	+0.0010
+6197.8	+0.0285	+0.0536	+0.8579	+0.0307	+0.0005
+7091.6	+0.0249	+0.0542	+0.9558	+0.0267	+0.0007
+8161.2	+0.0217	+0.0550	+1.0944	+0.0233	+0.0008
+9479.9	+0.0186	+0.0557	+1.2238	+0.0202	+0.0007
+10857.1	+0.0163	+0.0562	+1.3364	+0.0175	+0.0005
+12556.8	+0.0141	+0.0568	+1.5063	+0.0152	+0.0006
+14432.2	+0.0122	+0.0573	+1.6540	+0.0132	+0.0005
+16703.3	+0.0106	+0.0580	+1.8774	+0.0114	+0.0006
+19179.5	+0.0092	+0.0581	+1.9467	+0.0099	+0.0002
+22139.2	+0.0080	+0.0586	+2.1682	+0.0086	+0.0005
+25098.9	+0.0070	+0.0588	+2.2555	+0.0075	+0.0002
+29860.8	+0.0059	+0.0591	+2.4512	+0.0065	+0.0003

MICROMERITICS AUTO-PORE 9200 V2.00

FORD, BACON, & DAVIS #38178-080-S INTRUSION (PRESSURIZATION) DATA SUMMARY
WC1 MAL #1281
PNTR NUMBER +73

TOTAL INTRUSION VOLUME =	+0.0521	CC/G
TOTAL PORE AREA =	+2.4748	SQ-M/G
MEDIAN PORE DIAMETER (VOLUME) =	+0.5661	MICROMETERS
MEDIAN PORE DIAMETER (AREA) =	+0.0175	MICROMETERS
AVERAGE PORE DIAMETER (4V/A) =	+0.0843	MICROMETERS
BULK DENSITY =	+2.2994	G/CC
APPARENT (SKELETAL) DENSITY =	+2.6127	G/CC

% CAPILLARY = +18.7394 ****

PRESSURE PSIA	PORE DIAMETER MICRO-M	INTRUSION VOLUME CC/G	PORE SURFACE SQ-M/G	MEAN DIAMETER MICRO-M	DV
+1.5	+118.8640	+0.0000	+0.0000	+118.8640	+0.0000
+2.0	+88.0633	+0.0002	+0.0000	+103.4630	+0.0002
+3.0	+58.8521	+0.0010	+0.0001	+73.4576	+0.0008
+4.0	+44.2740	+0.0017	+0.0001	+51.5630	+0.0006
+5.5	+32.4319	+0.0025	+0.0002	+38.3529	+0.0008
+6.9	+25.5067	+0.0033	+0.0003	+28.9693	+0.0008
+8.4	+21.0003	+0.0037	+0.0004	+23.2535	+0.0004
+10.4	+16.9448	+0.0048	+0.0006	+18.9725	+0.0010
+12.9	+13.6633	+0.0058	+0.0009	+15.3040	+0.0010
+15.9	+11.0939	+0.0070	+0.0013	+12.3786	+0.0012
+19.9	+8.8678	+0.0087	+0.0019	+9.9809	+0.0017
+24.9	+7.0948	+0.0100	+0.0026	+7.9813	+0.0012
+28.6	+6.1870	+0.0100	+0.0026	+6.6409	+0.0000
+38.7	+4.5699	+0.0114	+0.0036	+5.3785	+0.0015
+48.6	+3.6339	+0.0129	+0.0051	+4.1019	+0.0015
+58.8	+3.0086	+0.0141	+0.0066	+3.3213	+0.0012
+73.7	+2.3985	+0.0158	+0.0090	+2.7036	+0.0017
+88.9	+1.9892	+0.0170	+0.0113	+2.1939	+0.0013
+114.2	+1.5477	+0.0189	+0.0156	+1.7685	+0.0019
+138.5	+1.2760	+0.0202	+0.0191	+1.4119	+0.0013
+173.7	+1.0177	+0.0220	+0.0257	+1.1468	+0.0019
+227.0	+0.7787	+0.0237	+0.0332	+0.8982	+0.0017
+282.3	+0.6262	+0.0248	+0.0393	+0.7024	+0.0011
+329.2	+0.5370	+0.0267	+0.0522	+0.5816	+0.0019
+418.1	+0.4228	+0.0292	+0.0733	+0.4799	+0.0025
+517.7	+0.3415	+0.0313	+0.0955	+0.3821	+0.0021
+636.9	+0.2776	+0.0328	+0.1149	+0.3095	+0.0015
+799.0	+0.2212	+0.0346	+0.1425	+0.2494	+0.0017
+986.6	+0.1792	+0.0357	+0.1646	+0.2002	+0.0011
+1194.6	+0.1480	+0.0368	+0.1916	+0.1636	+0.0011
+1395.8	+0.1266	+0.0379	+0.2236	+0.1373	+0.0011
+1592.2	+0.1110	+0.0388	+0.2533	+0.1188	+0.0009
+1891.1	+0.0935	+0.0399	+0.2968	+0.1023	+0.0011
+2288.6	+0.0772	+0.0408	+0.3396	+0.0854	+0.0009
+2625.1	+0.0673	+0.0417	+0.3890	+0.0723	+0.0009
+3018.8	+0.0586	+0.0426	+0.4457	+0.0629	+0.0009
+3488.2	+0.0507	+0.0435	+0.5113	+0.0546	+0.0009
+4029.3	+0.0439	+0.0443	+0.5869	+0.0473	+0.0009
+4644.7	+0.0381	+0.0452	+0.6740	+0.0410	+0.0009
+5391.9	+0.0328	+0.0459	+0.7514	+0.0354	+0.0007
+6183.1	+0.0286	+0.0466	+0.8396	+0.0307	+0.0007
+7091.6	+0.0249	+0.0475	+0.9713	+0.0268	+0.0009
+8175.8	+0.0216	+0.0479	+1.0513	+0.0233	+0.0005
+9465.2	+0.0187	+0.0486	+1.1842	+0.0201	+0.0007
+10857.1	+0.0163	+0.0491	+1.2884	+0.0175	+0.0005
+12542.1	+0.0141	+0.0497	+1.4622	+0.0152	+0.0007
+14432.2	+0.0122	+0.0504	+1.6609	+0.0132	+0.0007
+16703.3	+0.0106	+0.0508	+1.8164	+0.0114	+0.0004
+19179.5	+0.0092	+0.0511	+1.9096	+0.0099	+0.0002
+22153.8	+0.0080	+0.0515	+2.1116	+0.0086	+0.0004
+25084.2	+0.0070	+0.0519	+2.3391	+0.0075	+0.0004
+29875.4	+0.0059	+0.0521	+2.4748	+0.0065	+0.0002

MICROMERITICS AUTO-PORE 9200 V2.00

FORD BACON & DAVIS #38247-080-S INTRUSION (PRESSURIZATION) DATA SUMMARY
UE MAL #1328
PNTR NUMBER +222

TOTAL INTRUSION VOLUME =	+0.0079	CC/G
TOTAL PORE AREA =	+1.3134	SQ-M/G
MEDIAN PORE DIAMETER (VOLUME) =	+0.0305	MICROMETERS
MEDIAN PORE DIAMETER (AREA) =	+0.0142	MICROMETERS
AVERAGE PORE DIAMETER (4V/A) =	+0.0240	MICROMETERS
BULK DENSITY =	+2.6636	G/CC
APPARENT (SKELETAL) DENSITY =	+2.7207	G/CC

% CAPILLARY = +22.5136 ◆◆◆◆

PRESSURE PSIA	PORE DIAMETER MICRO-M	INTRUSION VOLUME CC/G	PORE SURFACE SQ-M/G	MEAN DIAMETER MICRO-M	DV
+1.5	+118.8640	+0.0000	+0.0000	+118.8640	+0.0000
+2.0	+88.7108	+0.0000	+0.0000	+103.7870	+0.0000
+3.0	+59.1405	+0.0000	+0.0000	+73.9256	+0.0000
+4.0	+44.1929	+0.0000	+0.0000	+51.6667	+0.0000
+5.4	+32.5193	+0.0000	+0.0000	+38.3561	+0.0000
+7.0	+25.3459	+0.0000	+0.0000	+28.9326	+0.0000
+8.5	+20.8912	+0.0000	+0.0000	+23.1185	+0.0000
+10.4	+16.9925	+0.0000	+0.0000	+18.9418	+0.0000
+12.9	+13.6943	+0.0000	+0.0000	+15.3434	+0.0000
+15.9	+11.1144	+0.0000	+0.0000	+12.4043	+0.0000
+19.9	+8.8678	+0.0000	+0.0000	+9.9911	+0.0000
+24.9	+7.0948	+0.0000	+0.0000	+7.9813	+0.0000
+28.6	+6.1870	+0.0000	+0.0000	+6.6409	+0.0000
+38.5	+4.5873	+0.0001	+0.0001	+5.3872	+0.0001
+48.7	+3.6285	+0.0002	+0.0002	+4.1079	+0.0001
+58.7	+3.0124	+0.0003	+0.0002	+3.3204	+0.0001
+73.7	+2.3985	+0.0004	+0.0004	+2.7055	+0.0001
+88.9	+1.9876	+0.0005	+0.0006	+2.1931	+0.0001
+113.6	+1.5567	+0.0006	+0.0008	+1.7722	+0.0001
+139.3	+1.2693	+0.0007	+0.0010	+1.4130	+0.0001
+174.0	+1.0160	+0.0008	+0.0015	+1.1426	+0.0001
+224.9	+0.7859	+0.0008	+0.0016	+0.9009	+0.0000
+281.3	+0.6284	+0.0010	+0.0028	+0.7071	+0.0002
+329.2	+0.5370	+0.0011	+0.0035	+0.5827	+0.0001
+419.0	+0.4218	+0.0013	+0.0048	+0.4794	+0.0002
+517.7	+0.3415	+0.0014	+0.0059	+0.3816	+0.0001
+640.8	+0.2759	+0.0015	+0.0076	+0.3087	+0.0001
+795.1	+0.2223	+0.0017	+0.0097	+0.2491	+0.0001
+985.6	+0.1794	+0.0019	+0.0119	+0.2008	+0.0001
+1195.6	+0.1479	+0.0018	+0.0134	+0.1636	+0.0001
+1395.8	+0.1266	+0.0020	+0.0165	+0.1372	+0.0001
+1591.2	+0.1111	+0.0020	+0.0193	+0.1189	+0.0001
+1890.1	+0.0935	+0.0022	+0.0245	+0.1023	+0.0001
+2290.6	+0.0772	+0.0023	+0.0321	+0.0853	+0.0002
+2618.3	+0.0675	+0.0025	+0.0395	+0.0723	+0.0001
+3017.8	+0.0586	+0.0026	+0.0479	+0.0630	+0.0001
+3484.7	+0.0507	+0.0028	+0.0633	+0.0547	+0.0002
+4014.6	+0.0440	+0.0030	+0.0830	+0.0474	+0.0002
+4644.7	+0.0381	+0.0033	+0.1132	+0.0410	+0.0003
+5377.3	+0.0329	+0.0037	+0.1537	+0.0355	+0.0004
+6197.8	+0.0285	+0.0041	+0.2103	+0.0307	+0.0004
+7179.5	+0.0246	+0.0046	+0.2757	+0.0266	+0.0004
+8175.8	+0.0216	+0.0050	+0.3462	+0.0231	+0.0004
+9479.9	+0.0186	+0.0055	+0.4423	+0.0201	+0.0005
+10857.1	+0.0163	+0.0059	+0.5413	+0.0175	+0.0004
+12556.8	+0.0141	+0.0064	+0.6617	+0.0152	+0.0005
+14432.2	+0.0122	+0.0067	+0.7546	+0.0132	+0.0003
+16703.3	+0.0106	+0.0070	+0.8704	+0.0114	+0.0003
+19194.1	+0.0092	+0.0073	+0.9833	+0.0099	+0.0003
+22168.5	+0.0080	+0.0075	+1.0780	+0.0086	+0.0002
+25128.2	+0.0070	+0.0077	+1.1727	+0.0075	+0.0002
+29904.7	+0.0059	+0.0079	+1.3134	+0.0065	+0.0002

MICROMERITICS AUTO-PORE 9200 V2.00

FORD BACON & DAVIS #38247-080-S INTRUSION (PRESSURIZATION) DATA SUMMARY
UL MAL #1325
PNTR NUMBER +88

TOTAL INTRUSION VOLUME =	+0.0171	CC/G
TOTAL PORE AREA =	+1.1980	SQ-M/G
MEDIAN PORE DIAMETER (VOLUME) =	+0.1704	MICROMETERS
MEDIAN PORE DIAMETER (AREA) =	+0.0232	MICROMETERS
AVERAGE PORE DIAMETER (4V/A) =	+0.0571	MICROMETERS
BULK DENSITY =	+2.5350	G/CC
APPARENT (SKELETAL) DENSITY =	+2.6498	G/CC

% CAPILLARY = +22.4597 ♦♦♦♦

PRESSURE PSIA	PORE DIAMETER MICRO-M	INTRUSION VOLUME CC/G	PORE SURFACE SQ-M/G	MEAN DIAMETER MICRO-M	DV
+1.5	+118.8640	+0.0001	+0.0000	+118.8640	+0.0001
+2.0	+88.7108	+0.0001	+0.0000	+103.7870	+0.0000
+3.0	+59.1405	+0.0001	+0.0000	+73.9256	+0.0000
+4.0	+44.1929	+0.0001	+0.0000	+51.6667	+0.0000
+5.4	+32.5193	+0.0001	+0.0000	+38.3561	+0.0000
+7.0	+25.3459	+0.0001	+0.0000	+28.9326	+0.0000
+8.5	+20.8912	+0.0001	+0.0000	+23.1185	+0.0001
+10.4	+16.9925	+0.0001	+0.0000	+18.9418	+0.0000
+12.9	+13.6943	+0.0001	+0.0000	+15.3434	+0.0000
+15.9	+11.1144	+0.0001	+0.0000	+12.4043	+0.0000
+19.9	+8.8678	+0.0001	+0.0000	+9.9911	+0.0000
+24.9	+7.0948	+0.0001	+0.0000	+7.9813	+0.0000
+28.6	+6.1870	+0.0001	+0.0000	+6.6409	+0.0000
+38.5	+4.5873	+0.0002	+0.0001	+5.3872	+0.0001
+48.7	+3.6285	+0.0004	+0.0003	+4.1079	+0.0002
+58.7	+3.0124	+0.0006	+0.0006	+3.3204	+0.0002
+73.7	+2.3985	+0.0012	+0.0014	+2.7055	+0.0006
+88.9	+1.9876	+0.0018	+0.0025	+2.1931	+0.0006
+113.6	+1.5567	+0.0028	+0.0047	+1.7722	+0.0010
+139.3	+1.2693	+0.0036	+0.0071	+1.4130	+0.0009
+174.0	+1.0160	+0.0044	+0.0099	+1.1426	+0.0008
+224.9	+0.7859	+0.0049	+0.0120	+0.9009	+0.0005
+281.3	+0.6284	+0.0057	+0.0165	+0.7071	+0.0008
+329.2	+0.5370	+0.0062	+0.0200	+0.5827	+0.0005
+419.0	+0.4218	+0.0069	+0.0253	+0.4794	+0.0006
+517.7	+0.3415	+0.0073	+0.0302	+0.3816	+0.0005
+640.8	+0.2759	+0.0078	+0.0363	+0.3087	+0.0005
+795.1	+0.2223	+0.0081	+0.0420	+0.2491	+0.0004
+985.6	+0.1794	+0.0085	+0.0492	+0.2008	+0.0004
+1195.6	+0.1479	+0.0086	+0.0524	+0.1636	+0.0001
+1395.8	+0.1266	+0.0089	+0.0595	+0.1372	+0.0002
+1591.2	+0.1111	+0.0092	+0.0695	+0.1189	+0.0003
+1890.1	+0.0935	+0.0095	+0.0836	+0.1023	+0.0004
+2290.6	+0.0772	+0.0101	+0.1086	+0.0853	+0.0005
+2618.3	+0.0675	+0.0105	+0.1346	+0.0723	+0.0005
+3017.8	+0.0586	+0.0111	+0.1681	+0.0630	+0.0005
+3484.7	+0.0507	+0.0118	+0.2233	+0.0547	+0.0008
+4014.6	+0.0440	+0.0125	+0.2774	+0.0474	+0.0006
+4644.7	+0.0381	+0.0131	+0.3398	+0.0410	+0.0006
+5377.3	+0.0329	+0.0137	+0.4120	+0.0355	+0.0006
+6197.8	+0.0285	+0.0144	+0.4952	+0.0307	+0.0006
+7179.5	+0.0246	+0.0149	+0.5657	+0.0266	+0.0005
+8175.8	+0.0216	+0.0153	+0.6365	+0.0231	+0.0004
+9479.9	+0.0186	+0.0156	+0.7067	+0.0201	+0.0004
+10857.1	+0.0163	+0.0160	+0.7870	+0.0175	+0.0004
+12556.8	+0.0141	+0.0163	+0.8644	+0.0152	+0.0003
+14432.2	+0.0122	+0.0165	+0.9360	+0.0132	+0.0002
+16703.3	+0.0106	+0.0167	+0.9984	+0.0114	+0.0002
+19194.1	+0.0092	+0.0169	+1.0697	+0.0099	+0.0002
+22168.5	+0.0080	+0.0169	+1.0986	+0.0086	+0.0001
+25128.2	+0.0070	+0.0170	+1.1609	+0.0075	+0.0001
+29904.7	+0.0059	+0.0171	+1.1980	+0.0065	+0.0001

MICROMERITICS AUTO-PORE 9200 V2.00

FORD
CK MAL #132Z
PNTR NUMBER +328

INTRUSION (PRESSURIZATION) DATA SUMMARY

TOTAL INTRUSION VOLUME	=	+0.0689 CC/G
TOTAL PORE AREA	=	+2.6257 SQ-M/G
MEDIAN PORE DIAMETER (VOLUME)	=	+2.3914 MICROMETERS
MEDIAN PORE DIAMETER (AREA)	=	+0.0137 MICROMETERS
AVERAGE PORE DIAMETER (4V/A)	=	+0.1050 MICROMETERS
BULK DENSITY	=	+2.2480 G/CC
APPARENT (SKELETAL) DENSITY	=	+2.6601 G/CC

% CAPILLARY = +35.1750

PRESSURE PSIA	PORE DIAMETER MICRO-M	INTRUSION VOLUME CC/G	PORE SURFACE SQ-M/G	MEAN DIAMETER MICRO-M	DV
+1.4	+125.6740	+0.0000	+0.0000	+125.6740	+0.0000
+2.0	+88.0633	+0.0006	+0.0000	+106.8680	+0.0006
+3.0	+59.5786	+0.0011	+0.0001	+73.8209	+0.0006
+3.9	+44.8501	+0.0015	+0.0001	+52.2143	+0.0004
+5.5	+32.3017	+0.0021	+0.0001	+38.5758	+0.0006
+7.0	+25.3993	+0.0025	+0.0002	+28.8505	+0.0004
+8.4	+20.9820	+0.0028	+0.0002	+23.1906	+0.0003
+10.4	+16.9448	+0.0031	+0.0003	+18.9634	+0.0003
+12.9	+13.6555	+0.0058	+0.0010	+15.3001	+0.0027
+15.9	+11.0888	+0.0110	+0.0027	+12.3722	+0.0052
+19.9	+8.8678	+0.0124	+0.0033	+9.9783	+0.0014
+24.9	+7.0927	+0.0152	+0.0047	+7.9803	+0.0028
+28.6	+6.1712	+0.0170	+0.0058	+6.6319	+0.0018
+38.5	+4.5873	+0.0228	+0.0101	+5.3793	+0.0058
+48.6	+3.6394	+0.0273	+0.0144	+4.1134	+0.0045
+58.6	+3.0162	+0.0306	+0.0183	+3.3278	+0.0032
+73.5	+2.4057	+0.0344	+0.0240	+2.7109	+0.0038
+89.1	+1.9843	+0.0372	+0.0291	+2.1950	+0.0028
+113.6	+1.5557	+0.0399	+0.0352	+1.7700	+0.0027
+138.6	+1.2753	+0.0417	+0.0404	+1.4155	+0.0018
+175.3	+1.0083	+0.0438	+0.0478	+1.1418	+0.0021
+224.4	+0.7879	+0.0451	+0.0535	+0.8981	+0.0013
+280.3	+0.6306	+0.0464	+0.0608	+0.7092	+0.0013
+329.2	+0.5370	+0.0478	+0.0705	+0.5838	+0.0014
+420.0	+0.4209	+0.0498	+0.0872	+0.4789	+0.0020
+516.7	+0.3421	+0.0513	+0.1023	+0.3815	+0.0014
+637.9	+0.2771	+0.0526	+0.1191	+0.3096	+0.0013
+796.1	+0.2220	+0.0537	+0.1379	+0.2496	+0.0012
+985.6	+0.1794	+0.0548	+0.1585	+0.2007	+0.0010
+1194.6	+0.1480	+0.0557	+0.1803	+0.1637	+0.0009
+1393.9	+0.1268	+0.0563	+0.1979	+0.1374	+0.0006
+1592.2	+0.1110	+0.0570	+0.2228	+0.1189	+0.0007
+1891.1	+0.0935	+0.0578	+0.2523	+0.1023	+0.0008
+2290.6	+0.0772	+0.0587	+0.2946	+0.0853	+0.0009
+2619.8	+0.0675	+0.0593	+0.3281	+0.0723	+0.0006
+3014.9	+0.0586	+0.0597	+0.3577	+0.0631	+0.0005
+3475.5	+0.0509	+0.0605	+0.4123	+0.0547	+0.0007
+4014.6	+0.0440	+0.0609	+0.4517	+0.0474	+0.0005
+4644.7	+0.0381	+0.0617	+0.5245	+0.0410	+0.0007
+5377.3	+0.0329	+0.0623	+0.5928	+0.0355	+0.0006
+6183.1	+0.0286	+0.0629	+0.6711	+0.0307	+0.0006
+7179.5	+0.0246	+0.0635	+0.7615	+0.0266	+0.0006
+8175.8	+0.0216	+0.0641	+0.8644	+0.0231	+0.0006
+9465.2	+0.0187	+0.0647	+0.9826	+0.0201	+0.0006
+10842.5	+0.0163	+0.0653	+1.1176	+0.0175	+0.0006
+12542.1	+0.0141	+0.0659	+1.2727	+0.0152	+0.0006
+14432.2	+0.0122	+0.0665	+1.4504	+0.0132	+0.0006
+16659.3	+0.0106	+0.0670	+1.6543	+0.0114	+0.0006
+19179.5	+0.0092	+0.0675	+1.8312	+0.0099	+0.0004
+22139.2	+0.0080	+0.0678	+1.9683	+0.0086	+0.0003
+25113.5	+0.0070	+0.0683	+2.2729	+0.0075	+0.0006
+29890.1	+0.0059	+0.0689	+2.6257	+0.0065	+0.0006

MICROMERITICS AUTO-PORE 9200 V2.00

FORD BACON & DAVIS #38247-080-S INTRUSION (PRESSURIZATION) DATA SUMMARY
CD MAL #1326
PNTR NUMBER +326

TOTAL INTRUSION VOLUME = +0.0413 CC/G
TOTAL PORE AREA = +1.6206 SQ-M/G
MEDIAN PORE DIAMETER (VOLUME) = +3.2824 MICROMETERS
MEDIAN PORE DIAMETER (AREA) = +0.0166 MICROMETERS
AVERAGE PORE DIAMETER (4V/A) = +0.1020 MICROMETERS
BULK DENSITY = +2.4242 G/CC
APPARENT (SKELETAL) DENSITY = +2.6941 G/CC

% CAPILLARY = +23.5354 ****

PRESSURE PSIA	PORE DIAMETER MICRO-M	INTRUSION VOLUME CC/G	PORE SURFACE SQ-M/G	MEAN DIAMETER MICRO-M	DV
+1.4	+125.6740	+0.0000	+0.0000	+125.6740	+0.0000
+2.0	+88.0633	+0.0004	+0.0000	+106.8680	+0.0004
+3.0	+59.5786	+0.0011	+0.0001	+73.8209	+0.0008
+3.9	+44.8501	+0.0015	+0.0001	+52.2143	+0.0004
+5.5	+32.3017	+0.0021	+0.0001	+38.5758	+0.0006
+7.0	+25.3993	+0.0032	+0.0003	+28.8505	+0.0010
+8.4	+20.9820	+0.0043	+0.0005	+23.1906	+0.0011
+10.4	+16.9448	+0.0058	+0.0008	+18.9634	+0.0015
+12.9	+13.6555	+0.0121	+0.0025	+15.3001	+0.0063
+15.9	+11.0888	+0.0139	+0.0030	+12.3722	+0.0018
+19.9	+8.8678	+0.0156	+0.0037	+9.9783	+0.0018
+24.9	+7.0927	+0.0174	+0.0046	+7.9803	+0.0018
+28.6	+6.1712	+0.0178	+0.0048	+6.6319	+0.0004
+38.5	+4.5873	+0.0190	+0.0058	+5.3793	+0.0013
+48.7	+3.6285	+0.0202	+0.0069	+4.1079	+0.0011
+59.1	+2.9900	+0.0211	+0.0080	+3.3092	+0.0009
+74.4	+2.3749	+0.0222	+0.0097	+2.6825	+0.0011
+89.2	+1.9811	+0.0231	+0.0113	+2.1780	+0.0009
+113.6	+1.5567	+0.0241	+0.0136	+1.7689	+0.0010
+139.0	+1.2713	+0.0250	+0.0161	+1.4140	+0.0009
+175.3	+1.0083	+0.0259	+0.0193	+1.1398	+0.0009
+225.6	+0.7837	+0.0264	+0.0216	+0.8960	+0.0005
+282.3	+0.6262	+0.0269	+0.0245	+0.7049	+0.0005
+334.1	+0.5292	+0.0276	+0.0290	+0.5777	+0.0006
+418.1	+0.4228	+0.0284	+0.0356	+0.4760	+0.0008
+520.6	+0.3395	+0.0290	+0.0425	+0.3812	+0.0007
+641.8	+0.2754	+0.0296	+0.0495	+0.3075	+0.0005
+800.0	+0.2210	+0.0302	+0.0603	+0.2482	+0.0007
+989.5	+0.1786	+0.0308	+0.0713	+0.1998	+0.0005
+1201.5	+0.1471	+0.0316	+0.0909	+0.1629	+0.0008
+1400.7	+0.1262	+0.0323	+0.1104	+0.1367	+0.0007
+1597.1	+0.1107	+0.0327	+0.1243	+0.1184	+0.0004
+1890.1	+0.0935	+0.0333	+0.1508	+0.1021	+0.0007
+2288.6	+0.0772	+0.0340	+0.1828	+0.0854	+0.0007
+2622.2	+0.0674	+0.0344	+0.2058	+0.0723	+0.0004
+3020.3	+0.0585	+0.0349	+0.2324	+0.0630	+0.0004
+3489.1	+0.0507	+0.0355	+0.2816	+0.0546	+0.0007
+4014.6	+0.0440	+0.0358	+0.3062	+0.0473	+0.0003
+4630.0	+0.0382	+0.0364	+0.3590	+0.0411	+0.0005
+5377.3	+0.0329	+0.0369	+0.4202	+0.0355	+0.0005
+6197.8	+0.0285	+0.0373	+0.4741	+0.0307	+0.0004
+7164.8	+0.0247	+0.0379	+0.5550	+0.0266	+0.0005
+8175.8	+0.0216	+0.0383	+0.6253	+0.0231	+0.0004
+9465.2	+0.0187	+0.0388	+0.7313	+0.0201	+0.0005
+10871.8	+0.0163	+0.0392	+0.8237	+0.0175	+0.0004
+12542.1	+0.0141	+0.0397	+0.9628	+0.0152	+0.0005
+14432.2	+0.0122	+0.0403	+1.1221	+0.0132	+0.0005
+16717.9	+0.0106	+0.0405	+1.2168	+0.0114	+0.0003
+19179.5	+0.0092	+0.0408	+1.3245	+0.0099	+0.0003
+22124.5	+0.0080	+0.0409	+1.3888	+0.0086	+0.0001
+25084.2	+0.0070	+0.0411	+1.4602	+0.0075	+0.0001
+29875.4	+0.0059	+0.0413	+1.6206	+0.0065	+0.0003

MICROMERITICS AUTO-PORE 9200 V2.01

FORD, BACON, AND DAVIES #38483-050-S INTRUSION (PRESSURIZATION) DATA SUMMARY
ROCK NM-P10-1 SMAL #1407-1-LO-P
PNTR NUMBER +328

TOTAL INTRUSION VOLUME =	+0.0637	CC/G
TOTAL PORE AREA =	+1.9811	SQ-M/G
MEDIAN PORE DIAMETER (VOLUME) =	+3.4777	MICROMETERS
MEDIAN PORE DIAMETER (AREA) =	+0.0218	MICROMETERS
AVERAGE PORE DIAMETER (4V/A) =	+0.1286	MICROMETERS
BULK DENSITY =	+2.2317	G/CC
APPARENT (SKELETAL) DENSITY =	+2.6013	G/CC

% CAPILLARY = +88.6895

PRESSURE PSIA	PORE DIAMETER MICRO-M	INTRUSION VOLUME CC/G	PORE SURFACE SQ-M/G	MEAN DIAMETER MICRO-M	DV
+2.5	+69.5370	+0.0006	+0.0000	+93.9090	+0.0006
+4.0	+44.1829	+0.0014	+0.0001	+56.8649	+0.0008
+5.5	+32.1296	+0.0022	+0.0002	+38.1612	+0.0008
+7.0	+25.2928	+0.0032	+0.0003	+28.7112	+0.0010
+8.5	+20.8912	+0.0041	+0.0005	+23.0920	+0.0009
+10.4	+16.9329	+0.0057	+0.0008	+18.9120	+0.0016
+12.9	+13.6865	+0.0076	+0.0013	+15.3097	+0.0019
+16.0	+11.0634	+0.0108	+0.0023	+12.3750	+0.0032
+20.0	+8.8353	+0.0156	+0.0042	+9.9494	+0.0048
+24.9	+7.0927	+0.0206	+0.0068	+7.9640	+0.0050
+28.9	+6.1087	+0.0229	+0.0082	+6.6007	+0.0023
+38.5	+4.5873	+0.0277	+0.0117	+5.3480	+0.0047
+48.9	+3.6122	+0.0313	+0.0152	+4.0997	+0.0036
+59.2	+2.9863	+0.0339	+0.0184	+3.2992	+0.0026
+74.8	+2.3633	+0.0367	+0.0227	+2.6748	+0.0028
+88.6	+1.9942	+0.0385	+0.0259	+2.1787	+0.0018
+114.7	+1.5418	+0.0407	+0.0309	+1.7680	+0.0022
+139.2	+1.2700	+0.0422	+0.0352	+1.4059	+0.0015
+174.5	+1.0130	+0.0436	+0.0401	+1.1415	+0.0014
+219.0	+0.8073	+0.0446	+0.0446	+0.9101	+0.0010
+273.3	+0.6469	+0.0457	+0.0506	+0.7271	+0.0011
+330.2	+0.5354	+0.0465	+0.0558	+0.5911	+0.0007
+422.0	+0.4189	+0.0475	+0.0639	+0.4772	+0.0010
+519.7	+0.3402	+0.0482	+0.0716	+0.3795	+0.0007
+637.9	+0.2771	+0.0489	+0.0805	+0.3087	+0.0007
+799.0	+0.2212	+0.0496	+0.0915	+0.2492	+0.0007
+985.6	+0.1794	+0.0503	+0.1073	+0.2003	+0.0008
+1204.4	+0.1468	+0.0510	+0.1241	+0.1631	+0.0007
+1403.7	+0.1259	+0.0516	+0.1412	+0.1364	+0.0006
+1594.1	+0.1109	+0.0520	+0.1556	+0.1184	+0.0004
+1900.9	+0.0930	+0.0527	+0.1826	+0.1019	+0.0007
+2294.5	+0.0770	+0.0534	+0.2152	+0.0850	+0.0007
+3021.0	+0.0585	+0.0547	+0.2901	+0.0678	+0.0013
+3490.9	+0.0506	+0.0554	+0.3404	+0.0546	+0.0007
+4023.6	+0.0439	+0.0562	+0.4115	+0.0473	+0.0008
+4634.5	+0.0381	+0.0571	+0.4934	+0.0410	+0.0008
+5394.5	+0.0328	+0.0581	+0.6058	+0.0355	+0.0010
+6184.4	+0.0286	+0.0589	+0.7218	+0.0307	+0.0009
+7093.4	+0.0249	+0.0598	+0.8548	+0.0268	+0.0009
+8196.1	+0.0216	+0.0607	+0.9990	+0.0232	+0.0008
+9462.8	+0.0187	+0.0615	+1.1652	+0.0201	+0.0008
+10848.7	+0.0163	+0.0619	+1.2501	+0.0175	+0.0004
+12532.6	+0.0141	+0.0624	+1.3883	+0.0152	+0.0005
+59712.6	+0.0030	+0.0637	+1.9811	+0.0085	+0.0013
+19283.3	+0.0092	+0.0637	+1.9811	+0.0061	+0.0000
+22353.1	+0.0079	+0.0651	+2.6328	+0.0085	+0.0014
+25080.2	+0.0070	+0.0651	+2.6328	+0.0075	+0.0000
+29953.1	+0.0059	+0.0651	+2.6328	+0.0065	+0.0000

MICROMERITICS AUTO-PORE 9200 V2.01

FORD, BACON, & DAVIS
NM-P10-2 MAL #1408-1-LO-P
PNTR NUMBER +73

INTRUSION (PRESSURIZATION) DATA SUMMARY

TOTAL INTRUSION VOLUME	=	+0.0579 CC/G
TOTAL PORE AREA	=	+4.6062 SQ-M/G
MEDIAN PORE DIAMETER (VOLUME)	=	+0.0918 MICROMETERS
MEDIAN PORE DIAMETER (AREA)	=	+0.0204 MICROMETERS
AVERAGE PORE DIAMETER (4V/A)	=	+0.0503 MICROMETERS
BULK DENSITY	=	+2.1575 G/CC
APPARENT (SKELETAL) DENSITY	=	+2.4655 G/CC

% CAPILLARY = +86.8813

PRESSURE PSIA	PORE DIAMETER MICRO-M	INTRUSION VOLUME CC/G	PORE SURFACE SQ-M/G	MEAN DIAMETER MICRO-M	DV
+2.4	+73.3415	+0.0004	+0.0000	+96.9540	+0.0004
+4.0	+44.1929	+0.0009	+0.0001	+58.7671	+0.0005
+5.5	+32.3450	+0.0012	+0.0001	+38.2689	+0.0003
+7.0	+25.2399	+0.0018	+0.0002	+28.7924	+0.0005
+8.5	+20.8371	+0.0025	+0.0003	+23.0385	+0.0007
+10.4	+16.9686	+0.0037	+0.0005	+18.9028	+0.0011
+13.0	+13.6093	+0.0052	+0.0009	+15.2889	+0.0015
+16.0	+11.0584	+0.0067	+0.0014	+12.3338	+0.0015
+19.9	+8.8743	+0.0083	+0.0021	+9.9663	+0.0015
+24.9	+7.0969	+0.0101	+0.0029	+7.9856	+0.0018
+29.5	+5.9874	+0.0102	+0.0030	+6.5421	+0.0001
+40.3	+4.3872	+0.0118	+0.0042	+5.1873	+0.0016
+50.2	+3.5225	+0.0130	+0.0055	+3.9548	+0.0013
+59.8	+2.9570	+0.0140	+0.0067	+3.2398	+0.0009
+74.7	+2.3656	+0.0152	+0.0085	+2.6613	+0.0012
+91.4	+1.9350	+0.0160	+0.0100	+2.1503	+0.0008
+113.8	+1.5527	+0.0169	+0.0120	+1.7439	+0.0009
+140.4	+1.2587	+0.0177	+0.0143	+1.4057	+0.0008
+175.9	+1.0050	+0.0184	+0.0168	+1.1318	+0.0007
+220.0	+0.8036	+0.0192	+0.0203	+0.9043	+0.0008
+269.6	+0.6558	+0.0198	+0.0236	+0.7297	+0.0006
+333.1	+0.5307	+0.0203	+0.0273	+0.5932	+0.0006
+420.0	+0.4209	+0.0210	+0.0333	+0.4758	+0.0007
+518.7	+0.3408	+0.0217	+0.0401	+0.3808	+0.0007
+636.9	+0.2776	+0.0222	+0.0467	+0.3092	+0.0005
+795.0	+0.2212	+0.0229	+0.0589	+0.2494	+0.0008
+987.5	+0.1790	+0.0238	+0.0761	+0.2001	+0.0009
+1206.3	+0.1465	+0.0247	+0.0985	+0.1628	+0.0009
+1393.9	+0.1268	+0.0257	+0.1264	+0.1367	+0.0010
+1599.0	+0.1105	+0.0268	+0.1654	+0.1187	+0.0012
+1851.1	+0.0935	+0.0286	+0.2380	+0.1020	+0.0018
+2292.5	+0.0771	+0.0318	+0.3836	+0.0853	+0.0031
+3024.5	+0.0584	+0.0373	+0.7103	+0.0678	+0.0055
+3486.3	+0.0507	+0.0398	+0.8895	+0.0546	+0.0024
+4023.8	+0.0439	+0.0421	+1.0879	+0.0473	+0.0023
+4648.4	+0.0380	+0.0441	+1.2830	+0.0410	+0.0020
+5409.5	+0.0327	+0.0462	+1.5205	+0.0353	+0.0021
+6188.5	+0.0287	+0.0478	+1.7292	+0.0307	+0.0016
+7078.5	+0.0250	+0.0493	+1.9530	+0.0268	+0.0015
+8211.0	+0.0215	+0.0508	+2.2112	+0.0233	+0.0015
+9447.8	+0.0187	+0.0520	+2.4401	+0.0201	+0.0012
+10878.5	+0.0162	+0.0531	+2.7035	+0.0175	+0.0012
+12562.4	+0.0141	+0.0541	+2.9545	+0.0152	+0.0010
+14440.1	+0.0122	+0.0549	+3.1982	+0.0132	+0.0009
+16720.1	+0.0106	+0.0557	+3.4789	+0.0114	+0.0008
+19193.9	+0.0092	+0.0563	+3.7219	+0.0098	+0.0006
+22174.3	+0.0080	+0.0569	+4.0012	+0.0086	+0.0006
+25124.8	+0.0070	+0.0574	+4.2673	+0.0075	+0.0005
+28883.5	+0.0058	+0.0579	+4.6062	+0.0065	+0.0005

MICROMERITICS AUTO-PORE 9200 V2.01

FORD, BACON, AND DAVIES #38485-090-S INTRUSION (PRESSURIZATION) DATA SUMMARY
ROCK NM-S23-1 MAL #1405-2-LO-P
PNTR NUMBER +330

TOTAL INTRUSION VOLUME =	+0.0725	CC/G
TOTAL PORE AREA =	+2.2090	SQ-M/G
MEDIAN PORE DIAMETER (VOLUME) =	+10.9385	MICROMETERS
MEDIAN PORE DIAMETER (AREA) =	-0.0143	MICROMETERS
AVERAGE PORE DIAMETER (4V/A) =	+0.1313	MICROMETERS
BULK DENSITY =	+2.2613	G/CC
APPARENT (SKELETAL) DENSITY =	+2.7047	G/CC

% CAPILLARY = +43.7108

PRESSURE PSIA	PORE DIAMETER MICRO-M	INTRUSION VOLUME CC/G	PORE SURFACE SQ-M/G	MEAN DIAMETER MICRO-M	DV
+2.5	+69.5370	+0.0026	+0.0001	+93.9090	+0.0026
+4.0	+44.1929	+0.0074	+0.0004	+56.8645	+0.9048
+5.5	+32.1296	+0.0135	+0.0011	+38.1612	+0.0061
+7.0	+25.2928	+0.0175	+0.0016	+28.7112	+0.0040
+8.5	+20.8912	+0.0220	+0.0024	+23.0920	+0.0045
+10.4	+16.8329	+0.0264	+0.0034	+18.9120	+0.0044
+12.9	+13.6865	+0.0313	+0.0046	+15.3097	+0.0049
+16.0	+11.0634	+0.0360	+0.0061	+12.3750	+0.0046
+20.0	+8.8353	+0.0410	+0.0082	+9.9494	+0.0050
+24.9	+7.0927	+0.0445	+0.0099	+7.9640	+0.0036
+28.9	+6.1087	+0.0452	+0.0103	+6.6007	+0.0006
+38.5	+4.5873	+0.0475	+0.0121	+5.3480	+0.0024
+48.9	+3.6122	+0.0494	+0.0140	+4.0997	+0.0019
+59.2	+2.9863	+0.0505	+0.0153	+3.2992	+0.0011
+74.8	+2.3633	+0.0518	+0.0172	+2.6748	+0.0013
+88.6	+1.9942	+0.0527	+0.0188	+2.1787	+0.0008
+114.7	+1.5418	+0.0540	+0.0218	+1.7680	+0.0013
+139.2	+1.2700	+0.0547	+0.0238	+1.4059	+0.0007
+174.5	+1.0130	+0.0557	+0.0272	+1.1415	+0.0010
+219.0	+0.8073	+0.0562	+0.0293	+0.9101	+0.0005
+273.3	+0.6469	+0.0569	+0.0334	+0.7271	+0.0007
+330.2	+0.5354	+0.0574	+0.0367	+0.5911	+0.0005
+422.0	+0.4189	+0.0586	+0.0469	+0.4772	+0.0012
+519.7	+0.3402	+0.0586	+0.0469	+0.3795	+0.0000
+637.9	+0.2771	+0.0590	+0.0523	+0.3087	+0.0004
+799.0	+0.2212	+0.0603	+0.0720	+0.2492	+0.0012
+985.6	+0.1794	+0.0604	+0.0752	+0.2003	+0.0002
+1204.4	+0.1468	+0.0606	+0.0792	+0.1631	+0.0002
+1403.7	+0.1259	+0.0612	+0.0976	+0.1364	+0.0006
+1594.1	+0.1109	+0.0614	+0.1027	+0.1184	+0.0001
+1900.9	+0.0930	+0.0626	+0.1512	+0.1019	+0.0012
+2294.5	+0.0770	+0.0626	+0.1535	+0.0850	+0.0000
+3021.0	+0.0585	+0.0639	+0.2281	+0.0678	+0.0013
+3490.9	+0.0506	+0.0645	+0.2746	+0.0546	+0.0006
+4023.6	+0.0438	+0.0654	+0.3483	+0.0473	+0.0009
+4634.5	+0.0381	+0.0660	+0.4098	+0.0410	+0.0006
+5394.5	+0.0328	+0.0668	+0.4947	+0.0355	+0.0008
+6184.4	+0.0286	+0.0673	+0.5610	+0.0307	+0.0005
+7093.4	+0.0249	+0.0681	+0.6724	+0.0268	+0.0007
+8196.1	+0.0216	+0.0687	+0.7800	+0.0232	+0.0006
+9462.8	+0.0187	+0.0694	+0.9274	+0.0201	+0.0007
+10848.7	+0.0163	+0.0697	+0.9873	+0.0175	+0.0003
+12532.6	+0.0141	+0.0702	+1.1186	+0.0152	+0.0005
+59712.6	+0.0030	+0.0725	+2.2091	+0.0085	+0.0023
+19283.3	+0.0092	+0.0725	+2.2091	+0.0061	+0.0000
+22353.1	+0.0079	+0.0764	+4.0497	+0.0065	+0.0039
+25080.2	+0.0070	+0.0764	+4.0535	+0.0075	+0.0000
+29953.1	+0.0059	+0.0764	+4.0535	+0.0065	+0.0000

FORD BACON& DAVIS #38485-090-S
NM-S23-2 MAL #1410-3-LO-P
PNTR NUMBER +728

INTRUSION (PRESSURIZATION) DATA SUMMARY

TOTAL INTRUSION VOLUME =	+0.1271	CC/G
TOTAL PORE AREA =	+1.8848	SQ-M/G
MEDIAN PORE DIAMETER (VOLUME) =	+24.1369	MICROMETERS
MEDIAN PORE DIAMETER (AREA) =	+0.0156	MICROMETERS
AVERAGE PORE DIAMETER (4V/A) =	+0.2698	MICROMETERS
BULK DENSITY =	+1.9486	G/CC
APPARENT (SKELETAL) DENSITY =	+2.5904	G/CC

% CAPILLARY = +35.3103

PRESSURE PSIA	PORE DIAMETER MICRO-M	INTRUSION VOLUME CC/G	PORE SURFACE SQ-M/G	MEAN DIAMETER MICRO-M	DV
+2.4	+73.1192	+0.0023	+0.0001	+101.0760	+0.0023
+4.0	+44.2740	+0.0067	+0.0004	+58.6966	+0.0044
+5.5	+32.2154	+0.0261	+0.0024	+38.2447	+0.0194
+7.0	+25.2663	+0.0592	+0.0070	+28.7408	+0.0331
+8.5	+20.7832	+0.0765	+0.0100	+23.0248	+0.0173
+10.4	+16.9567	+0.0866	+0.0122	+18.8698	+0.0101
+12.9	+13.6710	+0.0923	+0.0137	+15.3138	+0.0057
+16.0	+11.0685	+0.0964	+0.0150	+12.3697	+0.0041
+19.9	+8.8743	+0.0993	+0.0161	+9.9714	+0.0028
+25.0	+7.0823	+0.1024	+0.0177	+7.9783	+0.0031
+30.3	+5.8283	+0.1024	+0.0177	+6.4553	+0.0000
+40.2	+4.3951	+0.1024	+0.0177	+5.1117	+0.0000
+49.6	+3.5642	+0.1029	+0.0182	+3.9796	+0.0005
+60.1	+2.9390	+0.1042	+0.0198	+3.2516	+0.0013
+76.1	+2.3224	+0.1058	+0.0222	+2.6307	+0.0016
+89.9	+1.9865	+0.1068	+0.0241	+2.1444	+0.0010
+116.3	+1.5195	+0.1081	+0.0272	+1.7430	+0.0013
+141.1	+1.2526	+0.1092	+0.0302	+1.3861	+0.0011
+175.2	+1.0088	+0.1103	+0.0339	+1.1308	+0.0011
+220.2	+0.8029	+0.1108	+0.0364	+0.9058	+0.0005
+268.7	+0.6579	+0.1113	+0.0394	+0.7304	+0.0005
+331.1	+0.5338	+0.1122	+0.0448	+0.5958	+0.0008
+420.0	+0.4209	+0.1127	+0.0496	+0.4773	+0.0006
+518.7	+0.3402	+0.1133	+0.0557	+0.3805	+0.0006
+638.8	+0.2767	+0.1139	+0.0633	+0.3084	+0.0006
+798.0	+0.2215	+0.1148	+0.0770	+0.2491	+0.0009
+986.6	+0.1792	+0.1151	+0.0839	+0.2003	+0.0003
+1201.5	+0.1471	+0.1157	+0.0988	+0.1632	+0.0006
+1395.8	+0.1266	+0.1163	+0.1161	+0.1369	+0.0006
+1598.0	+0.1106	+0.1169	+0.1359	+0.1186	+0.0006
+1880.1	+0.0935	+0.1175	+0.1598	+0.1021	+0.0006
+2294.5	+0.0770	+0.1184	+0.2013	+0.0853	+0.0009
+2620.7	+0.0675	+0.1190	+0.2342	+0.0722	+0.0006
+3017.2	+0.0586	+0.1198	+0.2686	+0.0630	+0.0009
+3482.6	+0.0508	+0.1204	+0.3325	+0.0547	+0.0006
+4023.6	+0.0439	+0.1213	+0.4050	+0.0473	+0.0009
+4648.4	+0.0380	+0.1218	+0.4381	+0.0410	+0.0003
+5364.7	+0.0330	+0.1222	+0.5051	+0.0355	+0.0006
+6184.4	+0.0286	+0.1231	+0.6153	+0.0308	+0.0008
+7078.5	+0.0250	+0.1234	+0.6637	+0.0268	+0.0003
+8188.1	+0.0218	+0.1240	+0.7638	+0.0233	+0.0006
+9477.7	+0.0187	+0.1243	+0.8272	+0.0201	+0.0003
+10883.6	+0.0163	+0.1248	+0.8581	+0.0175	+0.0003
+12562.4	+0.0141	+0.1252	+1.0473	+0.0152	+0.0006
+14435.0	+0.0122	+0.1257	+1.2171	+0.0132	+0.0006
+16680.3	+0.0106	+0.1260	+1.3208	+0.0114	+0.0003
+19134.2	+0.0092	+0.1263	+1.4368	+0.0099	+0.0003
+22189.2	+0.0080	+0.1265	-1.5889	+0.0086	+0.0003
+25085.3	+0.0071	+0.1268	+1.7153	+0.0075	+0.0003
+25938.2	+0.0069	+0.1271	+1.8848	+0.0065	+0.0003

MICROMERITICS AUTO-PORE 9200 V2.01

FORD ,BACON & DAVIS
NMS -23-3 MAL#244 -3
PNTR NUMBER +73

INTRUSION (PRESSURIZATION) DATA SUMMARY

TOTAL INTRUSION VOLUME	=	+0.0447 CC/G
TOTAL PORE AREA	=	+1.8428 SQ-M/G
MEDIAN PORE DIAMETER (VOLUME)	=	+0.7814 MICROMETERS
MEDIAN PORE DIAMETER (AREA)	=	+0.0242 MICROMETERS
AVERAGE PORE DIAMETER (4V/A)	=	+0.0970 MICROMETERS
BULK DENSITY	=	+2.3354 G/CC
APPARENT (SKELETAL) DENSITY	=	+2.6076 G/CC

% CAPILLARY = +38.6901

PRESSURE PSIA	PORE DIAMETER MICRO-M	INTRUSION VOLUME CC/G	PORE SURFACE SQ-M/G	MEAN DIAMETER MICRO-M	DV
+1.5	+118.2810	+0.0001	+0.0000	+118.2810	+0.0001
+2.1	+85.5650	+0.0001	+0.0000	+101.9230	+0.0000
+3.0	+58.1430	+0.0005	+0.0000	+71.8539	+0.0004
+4.0	+43.7918	+0.0009	+0.0001	+50.9674	+0.0004
+5.5	+32.2585	+0.0013	+0.0001	+38.0251	+0.0003
+7.0	+25.3459	+0.0018	+0.0002	+28.8022	+0.0005
+8.5	+20.9093	+0.0022	+0.0002	+23.1276	+0.0003
+10.4	+16.9567	+0.0024	+0.0003	+18.9330	+0.0003
+12.9	+13.6555	+0.0031	+0.0005	+15.3061	+0.0007
+15.9	+11.1093	+0.0036	+0.0006	+12.3824	+0.0005
+20.0	+8.8483	+0.0064	+0.0017	+9.9788	+0.0028
+29.1	+6.0779	+0.0064	+0.0017	+7.4631	+0.0000
+39.0	+4.5356	+0.0077	+0.0027	+5.3068	+0.0013
+48.6	+3.6394	+0.0090	+0.0040	+4.0875	+0.0013
+59.0	+2.9937	+0.0106	+0.0060	+3.3166	+0.0016
+73.5	+2.4057	+0.0126	+0.0089	+2.6997	+0.0020
+89.1	+1.9843	+0.0140	+0.0116	+2.1950	+0.0015
+114.1	+1.5497	+0.0158	+0.0157	+1.7670	+0.0018
+138.4	+1.2774	+0.0176	+0.0205	+1.4135	+0.0017
+174.1	+1.0155	+0.0192	+0.0263	+1.1465	+0.0016
+219.7	+0.8045	+0.0221	+0.0388	+0.9100	+0.0028
+270.6	+0.6533	+0.0239	+0.0488	+0.7289	+0.0018
+329.2	+0.5370	+0.0248	+0.0546	+0.5952	+0.0009
+419.0	+0.4218	+0.0258	+0.0634	+0.4794	+0.0011
+518.7	+0.3408	+0.0269	+0.0744	+0.3813	+0.0011
+635.9	+0.2780	+0.0278	+0.0869	+0.3094	+0.0010
+796.1	+0.2220	+0.0288	+0.1025	+0.2500	+0.0010
+987.5	+0.1790	+0.0299	+0.1236	+0.2005	+0.0011
+1199.5	+0.1474	+0.0309	+0.1497	+0.1632	+0.0011
+1397.8	+0.1265	+0.0317	+0.1730	+0.1369	+0.0008
+1599.0	+0.1105	+0.0325	+0.1999	+0.1185	+0.0008
+1891.1	+0.0935	+0.0339	+0.2550	+0.1020	+0.0014
+2285.7	+0.0773	+0.0351	+0.3090	+0.0854	+0.0012
+2617.2	+0.0675	+0.0360	+0.3627	+0.0724	+0.0010
+3017.2	+0.0586	+0.0370	+0.4244	+0.0631	+0.0010
+3493.0	+0.0506	+0.0380	+0.4957	+0.0546	+0.0010
+4023.6	+0.0439	+0.0389	+0.5707	+0.0473	+0.0009
+4634.5	+0.0381	+0.0393	+0.6152	+0.0410	+0.0005
+5409.5	+0.0327	+0.0403	+0.7251	+0.0354	+0.0010
+6184.4	+0.0286	+0.0409	+0.8066	+0.0306	+0.0006
+7093.4	+0.0249	+0.0416	+0.8999	+0.0268	+0.0006
+8166.3	+0.0216	+0.0421	+0.9921	+0.0233	+0.0005
+9477.7	+0.0187	+0.0427	+1.1156	+0.0201	+0.0006
+10833.8	+0.0163	+0.0430	+1.1784	+0.0175	+0.0003
+12562.4	+0.0141	+0.0434	+1.2733	+0.0152	+0.0004
+14455.0	+0.0122	+0.0437	+1.3821	+0.0132	+0.0004
+16660.5	+0.0106	+0.0439	+1.4465	+0.0114	+0.0002
+19208.8	+0.0092	+0.0442	+1.5547	+0.0099	+0.0003
+22189.2	+0.0080	+0.0443	+1.6387	+0.0086	+0.0002
+25695.1	+0.0070	+0.0445	+1.7332	+0.0075	+0.0002
+29553.1	+0.0059	+0.0447	+1.8428	+0.0065	+0.0002

MICROMERITICS AUTO-PORE 9200 V2.01

FORD ,BACON & DAVIS
SCHWARZWALDER MAL#
PNTR NUMBER +222

INTRUSION (PRESSURIZATION) DATA SUMMARY

TOTAL INTRUSION VOLUME =	+0.0107	CC/G
TOTAL PORE AREA =	+0.7011	SQ-M/G
MEDIAN PORE DIAMETER (VOLUME) =	+0.1082	MICROMETERS
MEDIAN PORE DIAMETER (AREA) =	+0.0351	MICROMETERS
AVERAGE PORE DIAMETER (4V/A) =	+0.0611	MICROMETERS
BULK DENSITY =	+2.9965	G/CC
APPARENT (SKELETAL) DENSITY =	+3.0959	G/CC

% CAPILLARY = +41.9290

PRESSURE PSIA	PORE DIAMETER MICRO-M	INTRUSION VOLUME CC/G	PORE SURFACE SQ-M/G	MEAN DIAMETER MICRO-M	DV
+1.5	+118.2810	+0.0000	+0.0000	+118.2810	+0.0000
+2.1	+85.5650	+0.0000	+0.0000	+101.9230	+0.0000
+3.0	+58.1430	+0.0001	+0.0000	+71.8539	+0.0001
+4.0	+43.7919	+0.0001	+0.0000	+50.9674	+0.0000
+5.5	+32.2585	+0.0001	+0.0000	+38.0251	+0.0000
+7.0	+25.3459	+0.0001	+0.0000	+28.8022	+0.0000
+8.5	+20.9093	+0.0001	+0.0000	+23.1276	+0.0000
+10.4	+16.9567	+0.0001	+0.0000	+18.9330	+0.0000
+12.9	+13.6555	+0.0001	+0.0000	+15.3061	+0.0000
+15.9	+11.1093	+0.0001	+0.0000	+12.3824	+0.0000
+20.0	+8.8483	+0.0001	+0.0000	+9.9788	+0.0000
+28.9	+6.1087	+0.0001	+0.0000	+7.4785	+0.0000
+38.8	+4.5527	+0.0001	+0.0000	+5.3307	+0.0000
+48.7	+3.6285	+0.0001	+0.0000	+4.0906	+0.0000
+58.6	+3.0162	+0.0001	+0.0000	+3.3223	+0.0000
+74.1	+2.3867	+0.0001	+0.0000	+2.7014	+0.0000
+88.6	+1.9942	+0.0001	+0.0000	+2.1904	+0.0000
+113.6	+1.5567	+0.0001	+0.0000	+1.7754	+0.0000
+139.0	+1.2720	+0.0001	+0.0000	+1.4144	+0.0000
+175.2	+1.0092	+0.0001	+0.0000	+1.1406	+0.0000
+220.0	+0.8033	+0.0001	+0.0000	+0.9063	+0.0000
+269.6	+0.6557	+0.0001	+0.0001	+0.7295	+0.0000
+332.1	+0.5323	+0.0002	+0.0010	+0.5940	+0.0001
+418.1	+0.4228	+0.0004	+0.0027	+0.4775	+0.0002
+517.7	+0.3415	+0.0009	+0.0072	+0.3821	+0.0004
+637.9	+0.2771	+0.0014	+0.0136	+0.3093	+0.0005
+796.1	+0.2220	+0.0019	+0.0228	+0.2496	+0.0006
+987.5	+0.1790	+0.0029	+0.0409	+0.2005	+0.0009
+1198.5	+0.1475	+0.0038	+0.0649	+0.1632	+0.0010
+1393.9	+0.1268	+0.0044	+0.0816	+0.1372	+0.0006
+1590.2	+0.1112	+0.0052	+0.1089	+0.1190	+0.0008
+1892.1	+0.0934	+0.0061	+0.1421	+0.1023	+0.0009
+2294.5	+0.0770	+0.0070	+0.1838	+0.0852	+0.0009
+2625.7	+0.0673	+0.0074	+0.2105	+0.0722	+0.0005
+3015.2	+0.0586	+0.0079	+0.2400	+0.0630	+0.0005
+3482.1	+0.0508	+0.0083	+0.2659	+0.0547	+0.0004
+4023.6	+0.0439	+0.0087	+0.3021	+0.0473	+0.0004
+4649.4	+0.0380	+0.0090	+0.3331	+0.0410	+0.0003
+5394.5	+0.0328	+0.0093	+0.3648	+0.0354	+0.0003
+6199.3	+0.0285	+0.0095	+0.3966	+0.0306	+0.0002
+7093.4	+0.0249	+0.0097	+0.4302	+0.0267	+0.0002
+8191.2	+0.0216	+0.0099	+0.4594	+0.0233	+0.0002
+9492.6	+0.0186	+0.0101	+0.4894	+0.0201	+0.0002
+10378.5	+0.0162	+0.0102	+0.5239	+0.0174	+0.0002
+12517.7	+0.0141	+0.0104	+0.5586	+0.0152	+0.0001
+14440.1	+0.0122	+0.0104	+0.5873	+0.0132	+0.0001
+16779.7	+0.0105	+0.0105	+0.6205	+0.0114	+0.0001
+19238.6	+0.0092	+0.0106	+0.6511	+0.0099	+0.0001
+22129.6	+0.0080	+0.0107	+0.6690	+0.0086	+0.0000
+25065.3	+0.0071	+0.0107	+0.6891	+0.0075	+0.0000
+29893.5	+0.0059	+0.0107	+0.7011	+0.0065	+0.0000

MICROMERITICS AUTO-PORE 9200 V2.01

FORD ,BACON &DAVIS
MADAWASKA MAL#
PNTR NUMBER +218

INTRUSION (PRESSURIZATION) DATA SUMMARY

TOTAL INTRUSION VOLUME =	+0.0017	CC/G
TOTAL PORE AREA =	+0.0358	SQ-M/G
MEDIAN PORE DIAMETER (VOLUME) =	+0.8656	MICROMETERS
MEDIAN PORE DIAMETER (AREA) =	+0.0597	MICROMETERS
AVERAGE PORE DIAMETER (4V/A) =	+0.1944	MICROMETERS
BULK DENSITY =	+2.6128	G/CC
APPARENT (SKELETAL) DENSITY =	+2.6247	G/CC

% CAPILLARY = +5.8490 ****

PRESSURE PSIA	PORE DIAMETER MICRO-M	INTRUSION VOLUME CC/G	PORE SURFACE SQ-M/G	MEAN DIAMETER MICRO-M	DV
+1.5	+118.2810	+0.0000	+0.0000	+118.2810	+0.0000
+2.1	+85.5650	+0.0000	+0.0000	+101.9230	+0.0000
+3.0	+58.1430	+0.0000	+0.0000	+71.8539	+0.0000
+4.0	+43.7919	+0.0001	+0.0000	+50.9674	+0.0000
+5.5	+32.2585	+0.0001	+0.0000	+38.0251	+0.0000
+7.0	+25.3459	+0.0001	+0.0000	+28.8022	+0.0000
+8.5	+20.9093	+0.0001	+0.0000	+23.1276	+0.0000
+10.4	+16.9567	+0.0001	+0.0000	+18.9330	+0.0000
+12.9	+13.6555	+0.0001	+0.0000	+15.3061	+0.0000
+15.9	+11.1093	+0.0002	+0.0000	+12.3824	+0.0000
+20.0	+8.8483	+0.0002	+0.0000	+9.9788	+0.0000
+28.9	+6.1087	+0.0002	+0.0001	+7.4785	+0.0000
+38.8	+4.5527	+0.0003	+0.0001	+5.3307	+0.0000
+48.7	+3.6285	+0.0003	+0.0001	+4.0906	+0.0000
+58.6	+3.0162	+0.0003	+0.0002	+3.3223	+0.0000
+74.1	+2.3867	+0.0004	+0.0003	+2.7014	+0.0001
+88.6	+1.9942	+0.0005	+0.0004	+2.1904	+0.0001
+113.6	+1.5567	+0.0006	+0.0007	+1.7754	+0.0001
+139.0	+1.2720	+0.0006	+0.0007	+1.4144	+0.0000
+175.2	+1.0092	+0.0007	+0.0011	+1.1406	+0.0001
+220.0	+0.8033	+0.0009	+0.0019	+0.9063	+0.0002
+269.6	+0.6557	+0.0010	+0.0022	+0.7295	+0.0000
+332.1	+0.5323	+0.0010	+0.0026	+0.5940	+0.0001
+418.1	+0.4228	+0.0011	+0.0032	+0.4775	+0.0001
+517.7	+0.3415	+0.0012	+0.0037	+0.3821	+0.0000
+637.9	+0.2771	+0.0012	+0.0046	+0.3093	+0.0001
+796.1	+0.2220	+0.0012	+0.0047	+0.2496	+0.0000
+987.5	+0.1790	+0.0013	+0.0057	+0.2005	+0.0001
+1198.5	+0.1475	+0.0014	+0.0080	+0.1632	+0.0001
+1393.9	+0.1268	+0.0014	+0.0080	+0.1372	+0.0000
+1590.2	+0.1112	+0.0014	+0.0084	+0.1190	+0.0000
+1892.1	+0.0934	+0.0015	+0.0112	+0.1023	+0.0001
+2294.5	+0.0770	+0.0015	+0.0136	+0.0852	+0.0001
+2625.7	+0.0673	+0.0015	+0.0152	+0.0722	+0.0000
+3015.2	+0.0586	+0.0016	+0.0183	+0.0630	+0.0000
+3482.1	+0.0508	+0.0016	+0.0183	+0.0547	+0.0000
+4023.6	+0.0439	+0.0016	+0.0231	+0.0473	+0.0001
+4649.4	+0.0380	+0.0017	+0.0237	+0.0410	+0.0000
+5394.5	+0.0328	+0.0017	+0.0293	+0.0354	+0.0000
+6199.3	+0.0285	+0.0017	+0.0293	+0.0306	+0.0000
+7093.4	+0.0249	+0.0017	+0.0293	+0.0267	+0.0000
+8181.2	+0.0216	+0.0017	+0.0358	+0.0233	+0.0000
+9492.6	+0.0186	+0.0017	+0.0358	+0.0201	+0.0000
+10878.5	+0.0162	+0.0017	+0.0358	+0.0174	+0.0000
+12517.7	+0.0141	+0.0017	+0.0358	+0.0152	+0.0000
+14440.1	+0.0122	+0.0017	+0.0358	+0.0132	+0.0000
+16779.7	+0.0105	+0.0017	+0.0358	+0.0114	+0.0000
+19238.6	+0.0092	+0.0017	+0.0358	+0.0099	+0.0000
+22129.6	+0.0080	+0.0017	+0.0358	+0.0086	+0.0000
+25065.3	+0.0071	+0.0017	+0.0358	+0.0075	+0.0000
+29393.5	+0.0059	+0.0017	+0.0358	+0.0065	+0.0000

MICROMERITICS AUTO-PORE 9200 V2.01

FORD , BACON & DAVIS
SYNTHETIC ORE #3 MAL#247
PNTR NUMBER +68

INTRUSION (PRESSURIZATION) DATA SUMMARY

TOTAL INTRUSION VOLUME =	+0.1554 CC/G
TOTAL PORE AREA =	+4.4865 SQ-M/G
MEDIAN PORE DIAMETER (VOLUME) =	+4.9588 MICROMETERS
MEDIAN PORE DIAMETER (AREA) =	+0.0155 MICROMETERS
AVERAGE PORE DIAMETER (4V/A) =	+0.1383 MICROMETERS
BULK DENSITY =	+1.7570 G/CC
APPARENT (SKELETAL) DENSITY =	+2.4172 G/CC

% CAPILLARY = +46.4784

PRESSURE PSIA	PORE DIAMETER MICRO-M	INTRUSION VOLUME CC/G	PORE SURFACE SQ-M/G	MEAN DIAMETER MICRO-M	DV
+1.5	+118.2810	+0.0000	+0.0000	+118.2810	+0.0000
+2.1	+85.5650	+0.0010	+0.0000	+101.9230	+0.0010
+3.0	+58.1430	+0.0027	+0.0001	+71.8539	+0.0017
+4.0	+43.7915	+0.0052	+0.0003	+50.9674	+0.0025
+5.5	+32.2585	+0.0110	+0.0009	+38.0251	+0.0057
+7.0	+25.3459	+0.0209	+0.0023	+28.8022	+0.0100
+8.5	+20.9093	+0.0314	+0.0041	+23.1276	+0.0105
+10.4	+16.9567	+0.0428	+0.0065	+18.9330	+0.0114
+12.9	+13.6555	+0.0503	+0.0085	+15.3061	+0.0075
+15.9	+11.1093	+0.0550	+0.0100	+12.3824	+0.0047
+20.0	+8.8483	+0.0699	+0.0160	+9.9788	+0.0149
+29.1	+6.0779	+0.0734	-0.0179	+7.4631	+0.0034
+39.0	+4.5356	+0.0784	+0.0224	+5.3068	+0.0060
+48.6	+3.6394	+0.0846	+0.0275	+4.0875	+0.0052
+59.0	+2.9937	+0.0888	+0.0326	+3.3166	+0.0042
+73.5	+2.4057	+0.0943	+0.0407	+2.6997	+0.0055
+89.1	+1.9843	+0.0981	+0.0475	+2.1950	+0.0037
+114.1	+1.5497	+0.1021	+0.0566	+1.7670	+0.0040
+138.4	+1.2774	+0.1056	+0.0665	+1.4135	+0.0035
+174.1	+1.0155	+0.1093	+0.0796	+1.1465	+0.0038
-219.7	+0.8045	+0.1153	-0.1060	+0.9100	+0.0060
+270.6	+0.6533	+0.1196	+0.1294	+0.7289	+0.0043
+329.2	+0.5370	+0.1206	+0.1363	+0.5952	+0.0010
+419.0	+0.4218	+0.1224	+0.1513	+0.4794	+0.0018
+518.7	+0.3408	+0.1242	+0.1702	+0.3813	+0.0018
+635.5	+0.2780	+0.1260	+0.1935	+0.3094	+0.0018
+796.1	+0.2220	+0.1273	+0.2147	+0.2500	+0.0013
+987.5	+0.1790	+0.1289	+0.2462	+0.2005	+0.0016
+1199.5	+0.1474	+0.1300	+0.2727	+0.1632	+0.0011
+1397.8	+0.1265	+0.1311	+0.3039	+0.1369	+0.0011
+1589.0	+0.1105	+0.1321	+0.3398	+0.1185	+0.0011
+1891.1	+0.0935	+0.1332	+0.3822	+0.1020	+0.0011
+2285.7	+0.0773	+0.1353	+0.4803	+0.0854	+0.0021
+2617.2	-0.0675	+0.1361	+0.5257	+0.0724	+0.0008
+3017.2	+0.0586	+0.1379	+0.6412	+0.0631	+0.0018
+3493.0	+0.0506	+0.1395	+0.7586	+0.0546	+0.0016
+4023.6	+0.0439	+0.1413	+0.9316	+0.0473	+0.0021
+4634.3	+0.0381	+0.1432	+1.0845	+0.0410	+0.0019
+5408.5	+0.0327	+0.1450	+1.2903	+0.0354	+0.0018
+6184.4	+0.0286	+0.1460	+1.4269	+0.0306	+0.0011
+7083.4	+0.0246	-0.1471	+1.5872	+0.0268	+0.0011
+8166.3	+0.0216	+0.1484	+1.8114	+0.0233	+0.0013
-9477.7	+0.0187	+0.1492	+1.9714	+0.0201	+0.0008
+10833.8	+0.0163	+0.1500	+2.1532	+0.0175	+0.0008
+12562.4	+0.0141	+0.1511	+2.4278	+0.0152	+0.0010
+14455.0	-0.0122	+0.1516	+2.5913	+0.0132	+0.0005
+13680.5	+0.0106	+0.1521	+2.7776	+0.0114	+0.0005
+15208.8	+0.0092	+0.1526	-2.9806	+0.0099	+0.0005
+22189.2	+0.0060	-0.1537	+3.4656	-0.0066	+0.0010
+25085.1	+0.0070	-0.1544	+3.6719	+0.0075	+0.0008
+29853.1	+0.0059	+0.1554	+4.4965	+0.0065	+0.0010

Appendix B. Calculated exhalation relations for self-generated radon

Suppose that the disc is first sealed as shown in Figure B-1. It has arbitrary gaps g_o and g_L (cm) at the respective flat surfaces and assumed leak-rate constants c_o and c_L at the same surfaces. The curved surfaces are assumed to be completely sealed. The sample is left thus for several half-lives of radon after which the radon concentration C is unchanging with time in equation 4-17 and the equilibrium value C_{eq} (atoms/cm^3) in the air of the pores is of the form.

$$C_{eq} = \frac{E_\mu S}{\lambda(p+\rho k+\rho_w k_w)}\left(1+ae^{\sqrt{\frac{\lambda}{D_{obs}}}x}+be^{-\sqrt{\frac{\lambda}{D_{obs}}}x}\right) \qquad \text{(B-1)}$$

where $\underline{a}$ and $\underline{b}$ are constants not involving $\underline{x}$ or $\underline{t}$. The constants $\underline{a}$ and $\underline{b}$ are determinable from the boundary conditions which are as follows in terms of radon concentrations C_{g_o} and C_{g_L} in the gaps g_o and g_L, respectively:

$$C_{g_0} = C_{eq}\Big|_{x=0} \qquad \text{(B-2)}$$

$$C_{g_L} = C_{eq}\Big|_{x=L} \qquad \text{(B-3)}$$

$$J_{x=0} = (+)(p+\rho k+\rho_w k_w) D_{obs} \left.\frac{\partial C}{\partial x}\right|_{x=0} = g_0 C_{g_0}(\lambda+c_0) \qquad \text{(B-4)}$$

$$J_{x=L} = (-)(p+\rho k+\rho_w k_w) D_{obs} \left.\frac{\partial C}{\partial x}\right|_{x=L} = g_L C_{g_L}(\lambda+c_L) \qquad \text{(B-5)}$$

The flux J and the exhalation rate are considered to be positive if they are outward from the disc. Equations B-2 to B-5 suffice to determine the four unknown constants, a, b, C_{g_o} and C_{g_L}. However, it is unnecessary to write the complicated solutions for these constants because they will not enter into the final results.

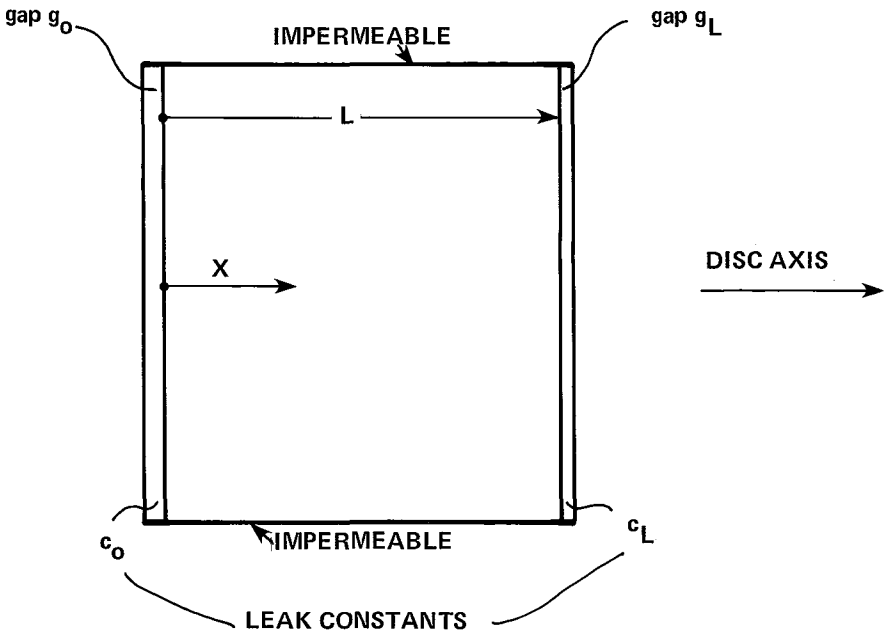

Figure B-1. The sealed disc for self generation of radon

After the end plates have been removed from the flat surfaces and air has been passed over the surfaces for a long time, a steady-state radon concentration C_{ss} (atoms/cm^3) results within the air of the pores such that

$$C_{ss} = \frac{E_\mu S}{\lambda(p+\rho k+\rho_w k_w)}\left[1- \frac{\cosh\left(\sqrt{\frac{\lambda}{D_{obs}}}\,(x-\frac{L}{2})\right)}{\cosh\left(\sqrt{\frac{\lambda}{D_{obs}}}\,\frac{L}{2}\right)}\right] \qquad \text{(B-6)}$$

It is assumed that the air stream reduces the radon concentration to essentially zero at the exposed surface of the solid at all times after the end plates have been removed.

The radon concentration C (atoms/cm^3) in the pore air will now be given for the general time t(sec) after the end plates are removed. The derivation for C is principally that of Dr. R.F. Holub of the U.S. Bureau of Mines, Denver, CO. The solution is of the form

$$C = C_{ss} + e^{-\lambda t}F(x)f(t) \qquad \text{(B-7)}$$

where

$$F(x)f(t) = \sum_{n=1}^{\infty}\alpha_n \sin\frac{n\pi x}{L}\, e^{-n^2\pi^2 D_{obs}t/L^2} \qquad \text{(B-8)}$$

and

$$\alpha_n = \frac{2}{L}\int_0^L (C_{eq}-C_{ss})\, \sin\frac{n\pi x}{L}\, dx \qquad \text{(B-9)}$$

Substituting equations B-1 and B-6 into equation B-9 and performing the integration gives

$$\alpha_n = \frac{2E_\mu S}{L\lambda(p+\rho k+\rho_w k_w)}\left[\frac{\frac{n\pi}{L}}{\frac{\lambda}{D_{obs}}+\frac{n^2\pi^2}{L^2}}\right]\cdot$$

$$\left[\left(a+\frac{1}{1+e^{\sqrt{\frac{\lambda}{D_{obs}}}L}}\right)\left(1-(-1)^n e^{\sqrt{\frac{\lambda}{D_{obs}}}L}\right)+\left(b+\frac{e^{\sqrt{\frac{\lambda}{D_{obs}}}L}}{1+e^{\sqrt{\frac{\lambda}{D_{obs}}}L}}\right)\left(1-(-1)^n e^{-\sqrt{\frac{\lambda}{D_{obs}}}L}\right)\right]$$

(B-10)

Combining equations B-6 through B-8 and B-10 yields the result

$$C = \frac{E_\mu S}{\lambda(p+\rho k+\rho_w k_w)}\left[1- \frac{\cosh\left(\sqrt{\frac{\lambda}{D_{obs}}}\left(x-\frac{L}{2}\right)\right)}{\cosh\left(\sqrt{\frac{\lambda}{D_{obs}}}\frac{L}{2}\right)}\right.$$

$$+ \frac{2}{L} e^{-\lambda t}\sum_{n=1}^{\infty}\left[\frac{\frac{n\pi}{L}}{\frac{\lambda}{D_{obs}}+\frac{n^2\pi^2}{L^2}}\right]\sin\frac{n\pi x}{L}\, e^{-n^2\pi^2 Dt/L^2}\cdot$$

$$\left.\left[\left(a+\frac{1}{1+e^{\sqrt{\frac{\lambda}{D_{obs}}}L}}\right)\left(1-(-1)^n e^{\sqrt{\frac{\lambda}{D_{obs}}}L}\right)+\left(b+\frac{e^{\sqrt{\frac{\lambda}{D_{obs}}}L}}{1+e^{\sqrt{\frac{\lambda}{D_{obs}}}L}}\right)\left(1-(-1)^n e^{-\sqrt{\frac{\lambda}{D_{obs}}}L}\right)\right]\right] \qquad \text{(B-11)}$$

Counting the exhalation rate EXR (atoms/s) to be positive if it is outward from the flat faces each of area A(cm^2) gives the expression

$$EXR = AD_e \left.\frac{\partial C}{\partial x}\right|_{x=0} - AD_e \left.\frac{\partial C}{\partial x}\right|_{x=L} \qquad \text{(B-12)}$$

with the aid of equation 4-14. Performing the operations of equation B-12 on B-11, and using equation 4-18, results in the relation,

$$EXR = EXR_{ss} + \frac{4AD_{obs}E_\mu S}{\lambda L} e^{-\lambda t}\left[2+(a+b)\left(1+e^{\sqrt{\frac{\lambda}{D_{obs}}}L}\right)\right]\sum_{n=0}^{\infty}\frac{e^{-(2n+1)^2\pi^2 D_{obs}t/L^2}}{1+\frac{\lambda L^2}{(2n+1)^2\pi^2 D_{obs}}} \qquad \text{(B-13)}$$

where the steady-state exhalation rate EXR_{ss} is

$$EXR_{ss} = 2AE_\mu S\sqrt{\frac{D_{obs}}{\lambda}}\tanh\left(\sqrt{\frac{\lambda}{D_{obs}}}\frac{L}{2}\right) \qquad \text{(B-14)}$$

Both EXR and EXR_{ss} are directly measurable although the accuracy of measuring EXR_{ss} is usually limited because of low levels of radioactivity. It is not necessary to know $E_\mu S$, a and b in order to use equation B-13 to determine D_{obs} because the equation can be rearranged to eliminate the constants of lesser interest using measurements at two different times t_1 and t_2. Thus, the sample in the air stream at two different times t_1 and t_2 has

$$(EXR_{t_1}-EXR_{ss})/(EXR_{t_2}-EXR_{ss}) =$$

$$e^{-\lambda(t_1-t_2)}\left[\sum_{n=0}^{\infty} e^{-(2n+1)^2\pi^2 D_{obs}t_1/L^2/\{1+\lambda L^2/((2n+1)^2\pi^2 D_{obs})\}}\right] \Bigg/$$

$$\sum_{n=0}^{\infty} e^{-(2n+1)^2\pi^2 D_{obs}t_2/L^2/\{1+\lambda L^2/((2n+1)^2\pi^2 D_{obs})\}} \qquad (4\text{-}20)$$

Equation 4-20 is thought to be rigorously valid in spite of unknown gaps and leakages at the planar faces during equilibration.[1] It allows the experimental determination of D_{obs} from pairs of points.

---

[1] An equation number without the B prefix refers to an equation in the main text.

Appendix C. Program BJT06·PRE315.6

This program was written for use with EXEC 8 on an UNIVAC 1108.

```
      C     SEE THAMER'S EQN (20) OF 4/1/80 LETTER TO HOLUB.
      C     THIS DETERMINES D FROM (EXRT1-EXRSS)/(EXRT2-EXRSS)=RATIO
      C     USING A SEARCH METHOD.
      C     CGS UNITS EXCEPT EXR VALUES IN CONSISTENT UNITS.
      C     T1 IS LESS THAN T2 AND ON UPPER PART OF CURVE.
      C     AN EXEC 8 USER CAN TERMINATE PGM WITH BREAK @@X TIO
            REAL*8 RATIO,DOMIN,DOMAX,D,T,SUM,ARG,STEP,XN,
           $EEXP,XINC,EXPRN,F,ESUM,RAD,SUM1,SUM2,DMAX,ERROR
            DATA RN,P,ERMAX
           1     /0.2098E-5,3.14159265,0.01/
   20       WRITE(6,1)
    1       FORMAT(' PGM TO DETERMINE D FROM')
            WRITE(6,30)
   30       FORMAT(' (EXRT1-EXRSS)/(EXRT2-EXRSS) USING')
            WRITE(6,31)
   31       FORMAT(' A SEARCH METHOD.')
            WRITE(6,2)
    2       FORMAT(' THE VALUE OF XL (DISC THICKNESS) IS :')
            READ(5,3)XL
    3       FORMAT()
            WRITE(6,4)
    4       FORMAT(' THE VALUE OF EXRSS IS:')
            READ(5,3)EXRSS
            WRITE(6,5)
    5       FORMAT(' THE VALUE OF LOWER TIME T1 IS :')
            READ(5,3)T1
            WRITE(6,6)
    6       FORMAT(' THE VALUE OF HIGHER TIME T2 IS :')
            READ(5,3)T2
            WRITE(6,7)
    7       FORMAT(' THE VALUE OF EXRT1 IS :')
            READ(5,3)EXRT1
            WRITE(6,8)
    8       FORMAT(' THE VALUE OF EXRT2 IS :')
            READ(5,3)EXRT2
            WRITE(6,9)
    9       FORMAT(' AN ESTIMATED VALUE OF D (CM**2/S) IS :')
            READ(5,3)DEST
            RATIO=(EXRT1-EXRSS)/(EXRT2-EXRSS)
            DOMIN=DEST/10.
            DOMAX=DEST*10.
            STEP=0.01*DOMAX
            D=DOMIN-STEP
   13       DO 10 I=1,111
1           D=D+STEP
1           T=T1
1           CALL ELSUM(RATIO,DOMIN,DOMAX,D,T,SUM,ARG,STEP,XN,
1          $EEXP,XINC,EXPRN,F,ESUM,RAD,SUM1,SUM2,DMAX,ERROR)
1           SUM1=ESUM
1           T=T2
1           CALL ELSUM(RATIO,DOMIN,DOMAX,D,T,SUM,ARG,STEP,XN,
1          $EEXP,XINC,EXPRN,F,ESUM,RAD,SUM1,SUM2,DMAX,ERROR)
1           SUM2=ESUM
1           RAD=SUM1/SUM2
1           IF (RAD.GT.RATIO) GO TO 12
1       10  CONTINUE
```

```
      12    ERROR=STEP/D
            IF (ERROR.LT.ERMAX) GO TO 14
            DMAX=D
            DMIN=DMAX-STEP
            STEP=0.01*(DMAX-DMIN)
            D=DMIN-STEP
            GO TO 13
      14    WRITE(6,15)
      15    FORMAT(' THE VALUE FOUND FOR D (CM**2/S) IS')
            WRITE(6,16)D
      16    FORMAT(1E10.4)
            WRITE(6,17)
      17    FORMAT(' FOR WHICH THE FRACTIONAL UNCERTAINTY IS')
            WRITE(6,18)ERMAX
      18    FORMAT(1E10.3)
            GO TO 20
            SUBROUTINE ELSUM(RATIO,DOMIN,DOMAX,D,T,SUM,ARG,STEP,XN,
           $EEXP,XINC,EXPRN,F,ESUM,RAD,SUM1,SUM2,DMAX,ERROR)
            REAL*8 RATIO,DOMIN,DOMAX,D,T,SUM,ARG,STEP,XN,
           $EEXP,XINC,EXPRN,F,ESUM,RAD,SUM1,SUM2,DMAX,ERROR
            DATA RN,P /0.2098E-5,3.14159265/
            SUM=0.
            XN=-1.
            DO 11 J=1,101
     1      XN=XN+1.
     1      ARG=-(2.*XN+1.)**2*P*P*T*D/(XL*XL)
     1      EEXP=DEXP(ARG)
     1      XINC=EEXP/(1.+(RN*XL*XL/((2.*XN+1.)**2*P*P*D)))
     1  11  SUM=SUM+XINC
            EXPRN=-RN*T
            F=DEXP(EXPRN)
            ESUM=F*SUM
            RETURN
            END
```

Appendix D. Calculated exhalation relations with the prior injection of radon

A disc that is permanently sealed on its curved sides is considered. Compare Figure B-1. Assume first that the planar surfaces are sealed with No Injection of radon, that there are no appreciable gaps or leaks at the seals, and a uniform pore-air concentration C_{ONI} (atoms/cm^3) is obtained after several half lives of radon. Using equation 4-17 with the derivatives equal to zero then gives

$$C_{ONI} = \frac{E_\mu S}{\lambda(p+\rho k+\rho_w k_w)} \qquad (D\text{-}1)$$

which is equation B-1 with a = b = o. However, if external radon is placed in the sample at atmospheric pressure before sealing, then in a few days a uniform pore-air concentration C_o (atoms/cm^3) is obtained such that $C_o > C_{ONI}$. Hence C_o and C_{ONI} are two alternative replacements for the equilibrium pore-air concentration C_{eq} (atoms/cm^3) of Equation B-1. However, equation B-6 of the pore-air concentration C_{ss} a long time after the inception of exhalation is still valid. Equations B-7 and B-9 are also valid except that C_{eq} becomes either C_o or C_{ONI}. With C_{eq} considered not to be a function of $\underline{x}$, equation B-9 is now solved to give

$$\alpha_n = \frac{2}{n\pi}\left[C_{eq} - \frac{E_\mu S}{\lambda(p+\rho k+\rho_w k_w)}\right](1-(-1)^n) + \frac{2E_\mu S(\frac{n\pi}{L})(1-(-1)^n)}{L\lambda(p+\rho k+\rho_w k_w)\left[\frac{\lambda}{D} + \frac{n^2\pi^2}{L^2}\right]} \qquad (D\text{-}2)$$

Inserting equation D-2 into equations B-7 and B-8 results in

$$C = \frac{E_\mu S}{\lambda(p+\rho k+\rho_w k_w)}\left[1 - \frac{\cosh\left[\sqrt{\frac{\lambda}{D_{obs}}}\left(x-\frac{L}{2}\right)\right]}{\cosh\left[\sqrt{\frac{\lambda}{D_{obs}}}\frac{L}{2}\right]}\right]$$

$$+ \frac{4}{L} e^{-\lambda t}\left(C_{eq} - \frac{E_\mu S}{\lambda(p+\rho k+\rho_w k_w)}\right)\sum_{n=0}^{\infty} \frac{L}{(2n+1)\pi}\sin\frac{(2n+1)\pi x}{L}\, e^{-(2n+1)^2\pi^2 D_{obs} t/L^2}$$

$$+ \frac{4E_\mu S e^{-\lambda t}}{L\lambda(p+\rho k+\rho_w k_w)}\sum_{n=0}^{\infty} \frac{(2n+1)\pi/L}{\frac{\lambda}{D_{obs}} + \left[\frac{(2n+1)\pi}{L}\right]^2}\sin\frac{(2n+1)\pi x}{L}\, e^{-(2n+1)^2\pi^2 D_{obs} t/L^2}$$

(D-3)

Applying equation B-12 to the latter equation gives the following for the exhalation rate EXR (atoms/s):

$$EXR = EXR_{ss}$$

$$+ \frac{8A}{L} e^{-\lambda t}\sum_{n=0}^{\infty}\left(C_{eq} D_e - \frac{E_\mu S}{\lambda} D_{obs}\left[\frac{1}{1+\frac{(2n+1)^2\pi^2 D_{obs}}{L^2\lambda}}\right]\right) e^{-(2n+1)^2\pi^2 D_{obs} t/L^2}$$

(D-4)

where EXR_{ss} is described by Equation B-14.

The exhalation rate with No Injection (EXR_{NI}, atom/s) has equation D-1 for C_{eq} in equation D-4. This and equation 4-18 give

$$EXR_{NI} =$$

$$EXR_{ss} + \frac{8AE_{\mu}SD_{obs}}{\lambda L} e^{-\lambda t} \sum_{n=0}^{\infty} \frac{(2n+1)^2\pi^2 D_{obs}/L^2\lambda}{1+\frac{(2n+1)^2\pi^2 D_{obs}}{L^2\lambda}} e^{-(2n+1)^2\pi^2 D_{0bs} t/L^2} \qquad (D\text{-}5)$$

Now reserving the designation EXR (atom/s) for equation D-4 with radon injection and $C_{eq} = C_o$, and combining equations D-4 and D-5 gives the relation

$$EXR\text{-}EXR_{NI} = \frac{8A}{L}(C_0 D_e - E_{\mu} SD/\lambda)\ e^{-\lambda t} \sum_{n=0}^{\infty} e^{-(2n+1)^2\pi^2 D_{obs} t/L^2} \qquad (D\text{-}6)$$

A disc's unknown quantity $(C_o D_e - E_{\mu} SD/\lambda)$ may be eliminated by taking the ratio of Equation D-6 at two different times; hence,

$$\frac{(EXR\text{-}EXR_{NI})_{t_1}}{(EXR\text{-}EXR_{NI})_{t_2}} = e^{\lambda(t_2 - t_1)} \frac{\sum_{n=0}^{\infty} e^{-(2n+1)^2\pi^2 D_{obs} t_1/L^2}}{\sum_{n=0}^{\infty} e^{-(2n+1)^2\pi^2 D_{obs} t_2/L^2}} \qquad (D\text{-}7)$$

Equation D-7 may be put in the form of equation 4-21 using the following identity taken from the text by H.S. Carslaw and J.C. Jaeger:[1]

$$\sum_{n=0}^{\infty} e^{-(2n+1)^2 \pi^2 D_{obs} t/L^2} = \frac{L}{4\sqrt{(\pi D_{obs} t)}}\left(1 + 2\sum_{n=1}^{\infty} (-1)^n \, e^{-n^2 L^2/4 D_{obs} t}\right) \qquad \text{(D-8)}$$

[1] H.S. Carslaw and J.C. Jaeger, "Conduction of Heat in Solids," 2nd ed. (1959), p. 97, equations 12-13.

This program was written for use with EXEC 8 on an UNIVAC 1108.

```
      C     THIS PGM SEARCHES OUT CORRECT VALUE OF D FOR
      C     EXPTL VALUES OF EXR AND EXRN AT TIMES T1 AND T2.
      C     SEE THAMER'S LETTER OF 4/21/80 TO HOLUB,
      C     ESPECIALLY EQN 18.
      C     UNITS OF CM AND MIN.
      C     PGM CREATED ON 9/12/80 BY THAMER.
      C     AN EXEC 8 USER CAN TERMINATE PGM WITH BREAK @@X TIO
            REAL*8 RATIO,DOMIN,DOMAX,STEP,D,T,NUM,FFSUM,DEN,
           $RAD,ERROR,DMAX,DMIN,SUM,XN,ARG,EXPAR,EXPRN,RNT,S,RN,XL
            DATA RN,P,ERMAX
           $     /.12588D-3,3.14159265,0.01/
         90 WRITE(6,1)
          1 FORMAT(' PGM TO SEARCH FOR VALUE OF D FROM')
            WRITE(6,30)
         30 FORMAT(' EXPTL EXR AND EXRN AT TWO TIMES.')
            WRITE(6,40)
         40 FORMAT(' USE UPPER PART OF CURVE.')
      C     L IS TWICE THICKNESS IF ONLY ONE END IS OPEN.
            WRITE(6,2)
          2 FORMAT(' THE VALUE OF L IS')
            READ(5,3)XL
          3 FORMAT()
            WRITE(6,4)
          4 FORMAT(' THE VALUE OF TIME T1 IS')
            READ(5,3)T1
            WRITE(6,5)
          5 FORMAT(' THE VALUE OF EXR1 IS')
            READ(5,3)EXR1
            WRITE(6,6)
          6 FORMAT(' THE VALUE OF EXRN1 IS')
            READ(5,3)EXRN1
            WRITE(6,7)
          7 FORMAT(' THE VALUE OF TIME T2 IS')
            READ(5,3)T2
            WRITE(6,8)
          8 FORMAT(' THE VALUE OF EXR2 IS')
            READ(5,3)EXR2
            WRITE(6,9)
          9 FORMAT(' THE VALUE OF EXRN2 IS')
            READ(5,3)EXRN2
            WRITE(6,10)
         10 FORMAT(' AN EXPECTED VALUE OF D (CM**2/MIN) IS')
            READ(5,3)DEX
            RATIO=(EXR1-EXRN1)/(EXR2-EXRN2)
            DOMIN=DEX/10.
            DOMAX=DEX*10.
            STEP=0.01*DOMAX
            D=DOMIN-STEP
         13 DO 11 I=1,101
1           D=D+STEP
1           T=T1
1           CALL FSUM(XL,RN,D,T,FFSUM,SUM,XN,ARG,EXPAR,EXPRN,RNT,S)
1           NUM=FFSUM
1           T=T2
1           CALL FSUM(XL,RN,D,T,FFSUM,SUM,XN,ARG,EXPAR,EXPRN,RNT,S)
1           DEN=FFSUM
```

```
1          57.            RAD=NUM/DEN
1          58.            IF (RAD.GT.RATIO) GO TO 12
1          59.         11 CONTINUE
           60.         12 ERROR=STEP/D
           61.            IF (ERROR.LT.ERMAX) GO TO 14
           62.            DMAX=D
           63.            DMIN=DMAX-STEP
           64.            STEP=0.01*(DMAX-DMIN)
           65.            D=DMIN-STEP
           66.            GO TO 13
           67.         14 WRITE(6,15)
           68.         15 FORMAT(' THE VALUE FOUND FOR D (CM**2/MIN) IS')
           69.            WRITE(6,16)D
           70.         16 FORMAT(1E10.4)
           71.            WRITE(6,17)
           72.         17 FORMAT(' FOR WHICH THE FRACTIONAL UNCERTAINTY IS')
           73.            WRITE(6,18)ERROR
           74.         18 FORMAT(1E10.3)
           75.            GO TO 90
           76.            SUBROUTINE FSUM(XL,RN,D,T,FFSUM,SUM,XN,ARG,EXPAR,EXPRN,RNT
,S)
           77.            REAL*8 XL,RN,D,T,FFSUM,SUM,XN,ARG,EXPAR,EXPRN,RNT,S
           78.            DATA P /3.14159265/
           79.            SUM=0.
           80.            XN=0.
           81.            S=1.
           82.            DO 19 J=1,100
1          83.            S=-1.*S
1          84.            XN=XN+1.
1          85.            ARG=-XN*XN*XL*XL/(4.*D*T)
1          86.            EXPAR=DEXP(ARG)
1          87.            SUM=SUM+S*EXPAR
1          88.         19 CONTINUE
           89.            RNT=-RN*T
           90.            EXPRN=DEXP(RNT)
           91.            FFSUM=EXPRN*(1.+2.*SUM)/SQRT(T)
           92.            RETURN
           93.            END
```

Appendix F. Program BJT06*UC359PROG9.1

This program was written for use with EXEC 8 on an UNIVAC 1108.

```
      C     THIS PGM CALCULATES EX2=(EXR2-EXRNI2) AT
      C     T2 IF EX1=(EXR1-EXRNI1) AT T1 AND D ARE KNOWN.
      C     SEE THAMER'S LETTER OF 4/21/80 TO HOLUB.
      C     UNITS OF CM AND MINUTES.
      C     PGM CREATED ON 5/13/81 BY THAMER.
      C     L IS TWICE THICKNESS IF ONLY ONE END IS OPEN.
            REAL*8 XL,RN,DOBS,T,GFSUM,SUM,XN,ARG,EXPAR,EXPRN,RNT,S,GF1
     ,YN,
           $GF2,T2,EX2
            DATA RN /.125880D-3/
            WRITE(6,1)
          1 FORMAT(' PGM TO CALCULATE EX2 =')
            WRITE(6,2)
          2 FORMAT(' (EXR2-EXRNI2) WHEN D,')
            WRITE(6,3)
          3 FORMAT(' EX1 = (EXR1-EXRNI1), AND T1')
            WRITE(6,4)
          4 FORMAT(' ARE KNOWN.')
            WRITE(6,5)
          5 FORMAT(' THE VALUE OF EX1 IS')
            READ(5,6)EX1
          6 FORMAT()
            WRITE(6,7)
          7 FORMAT(' THE VALUE OF T1 IS')
            READ(5,6)T1
            WRITE(6,8)
          8 FORMAT( ' THE VALUE OF L IS')
            READ(5,6)XL
            WRITE(6,9)
          9 FORMAT(' MAX T2 OF INTEREST IS')
            READ(5,6)T2MAX
            WRITE(6,20)
         20 FORMAT(' THE MINIMUM TIME OF INTEREST IS')
            READ(5,6)TMIN
            WRITE(6,10)
         10 FORMAT(' THE VALUE OF DOBS IS')
            READ(5,6)DOBS
            WRITE(6,11)
         11 FORMAT(' T2(MIN)    EX2=(EXR2-EXRNI2)')
            T=T1
            CALL FSUM(XL,RN,DOBS,T,GFSUM,SUM,XN,ARG,EXPAR,EXPRN,RNT,S)
            GF1=GFSUM
            YN=-1.
            DO 13 J=1,1000
     1      YN=YN+1.
     1      T2=TMIN*1.414**YN
     1      IF (T2.GT.T2MAX) GO TO 14
     1      T=T2
     1      CALL FSUM(XL,RN,DOBS,T,GFSUM,SUM,XN,ARG,EXPAR,EXPRN,RNT,S)
     1      GF2=GFSUM
     1      EX2=EX1*GF1/GF2
     1      WRITE(6,16)T2,EX2
     1   16 FORMAT(1X,G9.4,1X,E15.4)
     1   13 CONTINUE
         14 STOP
            END
```

```
      56.           SUBROUTINE FSUM(XL,RN,DOBS,T,GFSUM,SUM,XN,ARG,EXPAR,EXPRN,
RNT,S)
      57.           REAL*8 XL,RN,DOBS,T,GFSUM,SUM,XN,ARG,EXPAR,EXPRN,RNT,S
      58.           SUM=0
      59.           XN=0
      60.           S=1
      61.           DO 12 I=1,100
     1  62.           S=-1.*S
     1  63.           XN=XN+1.
     1  64.           ARG=-XN*XN*XL*XL/(4.*DOBS*T)
     1  65.           EXPAR=DEXP(ARG)
     1  66.           SUM=SUM+S*EXPAR
     1  67.        12 CONTINUE
      68.           RNT=RN*T
      69.           EXPRN=DEXP(RNT)
      70.           GFSUM=EXPRN*SQRT(T)/(1.+2.*SUM)
      71.           RETURN
      72.           END
```

Appendix G. Program BJT06*UC359PGM1.1

This program was written for use with EXEC 8 on an UNIVAC 1108.

```
      C     THIS PGM CALCULATES EX2=(EXRT2-EXRSS) AT
      C     T2 IF EX1=(EXRT1-EXRSS) AT T1 AND D ARE KNOWN.
      C     SEE THAMER'S LETTER OF 4/1/80 TO HOLUB.
      C     UNITS OF CM AND MINUTES.
      C     PGM CREATED ON 5/18/81 BY THAMER.
            REAL*8 XL,RN,DOBS,T,TMIN,TMAX,T1,T2,EXRSS,EXRT1,SUM,XN,ARG
     ,GFSUM,
           $GF1,YN,EX2
            DATA RN,P /.125880D-3,3.14159265/
            WRITE(6,1)
          1 FORMAT(' PGM TO CALCULATE EX2=')
            WRITE(6,2)
          2 FORMAT(' (EXRT2-EXRSS) WHEN D,')
            WRITE(6,3)
          3 FORMAT(' EX1=(EXRT1-EXRSS), AND T1')
            WRITE(6,4)
          4 FORMAT(' ARE KNOWN.')
            WRITE(6,5)
          5 FORMAT(' THE VALUE OF L IS')
            READ(5,7)XL
          7 FORMAT()
            WRITE(6,8)
          8 FORMAT(' THE VALUE OF EXRSS IS')
            READ(5,7)EXRSS
            WRITE(6,9)
          9 FORMAT(' THE VALUE OF EXRT1 IS')
            READ(5,7)EXRT1
            WRITE(6,10)
         10 FORMAT(' THE VALUE OF T1 IS')
            READ(5,7)T1
            WRITE(6,12)
         12 FORMAT(' THE VALUE OF DOBS IS')
            READ(5,7)DOBS
            WRITE(6,13)
         13 FORMAT(' THE MINIMUM TIME OF INTEREST IS')
            READ(5,7)TMIN
            WRITE(6,14)
         14 FORMAT(' THE MAXIMUM TIME OF INTEREST IS')
            READ(5,7)TMAX
            WRITE(6,15)
         15 FORMAT('    T2(MIN)     EX2=EXRT2-EXRSS')
            T=T1
            CALL FSUM(XL,RN,DOBS,T,TMIN,TMAX,T1,T2,EXRSS,EXRT1,
           $ SUM,XN,ARG,GFSUM)
            GF1=GFSUM
            YN=-1.
            DO 17 J=1,1000
     1      YN=YN+1.
     1      T2=TMIN*1.414**YN
     1      IF (T2.GT.TMAX) GO TO 18
     1      T=T2
     1      CALL FSUM(XL,RN,DOBS,T,TMIN,TMAX,T1,T2,EXRSS,EXRT1,
     1     $ SUM,XN,ARG,GFSUM)
     1      GF2=GFSUM
     1      EX2=(EXRT1-EXRSS)*GF2/GF1
     1      WRITE(6,19)T2,EX2
```

```
  1        56.       19 FORMAT(1X,G9.4,3X,E15.4)
  1        57.       17 CONTINUE
           58.       18 STOP
           59.          END
           60.          SUBROUTINE FSUM(XL,RN,DOBS,T,TMIN,TMAX,T1,T2,EXRSS,EXRT1,S
UM,XN,
           61.         $ARG,GFSUM)
           62.          REAL*8 XL,RN,DOBS,T,TMIN,TMAX,T1,T2,EXRSS,EXRT1,SUM,XN,ARG
,GFSUM
           63.          DATA P /3.14159265/
           64.          SUM=0
           65.          XN=-1.
           66.          DO 16 I=1,100
  1        67.          XN=XN+1.
  1        68.          ARG=-(2.*XN+1.)**2*P*P*DOBS*T/(XL*XL)
  1        69.          SUM=SUM+(DEXP(ARG))/(1.+RN*XL*XL/((2.*XN+1.)**2*P*P*DOBS))
  1        70.       16 CONTINUE
           71.          GFSUM=(DEXP(-RN*T))*SUM
           72.          RETURN
           73.          END
```

Appendix H. Program for calculating emanation coefficients

This program was written for use with EXEC 8 on an UNIVAC 1108.

```
C   PROGRAM NAME EMANAT
C
C
C
C
C
      DIMENSION SAMPLE(10),RAD(60),DIA(60),VOL(60),ANUM(60),W(13)
      DIMENSION SAT(15),E(15),AM(60)
      DATA W/0.,11.,5.,2.,1.,.5,.2,.07,.015,.003,.001,.0003,.0001/
      DATA QUIT/'STOP'/
C
C
C GET INPUT DATA
C
C
   99 WRITE(6,100)
  100 FORMAT(1X,'ENTER SAMPLE ID')
      READ(5,200)(SAMPLE(I),I=1,10)
  200 FORMAT (10A4)
      IF (SAMPLE(1).EQ.QUIT)GOTO 999
      WRITE(6,103)
  103 FORMAT(1X,'ENTER DENSITY,TM,FR')
      READ(5,202)DENS,TM,FR
      WRITE(6,101)
  101 FORMAT(1X,'ENTER POROSITY(CC/G)& NO. OF PORE SIZES:')
      READ(5,202)POROS,IP
       WRITE(6,102)
  102 FORMAT(1X,'ENTER PORE DIA.(UM)& DV',/,2X,'NNN.NNNN N.NNNN')
      READ(5,202)(DIA(I),VOL(I),I=1,IP)
  202 FORMAT()
      JSTEP=19
      KSTEP=20
      RANGE=0.036
      AR=0.48
      THRESH=0.01
C
C
C
C LIST INPUT DATA FOR VERIFICATION
C
C
      IF(JSTEP.LT.100)GO TO 2
      DO 1 I=1,IP
    1 WRITE(6,104) I, DIA(I),VOL(I)
  104 FORMAT (1X,I2,F11.4,F9.4)
    3 WRITE(6,105)
  105 FORMAT(1X,'CORRECTIONS?  ENTER LINE#  AND DIA. AND VOL. ZERO TERMI
     CNATES')
      READ(5,204)I,DIAN,VOLN
```

```
 204 FORMAT(I2,F11.4,F9.4)
     IF(I.EQ.0)GOTO2
     DIA(I)=DIAN
     VOL(I)=VOLN
     GOTO 3
   2 CONTINUE
C
C
C  DEFINE ROCK MATRIX PARAMETERS
C
C
     RAIR=64.
      DENS=DENS/10.**12
      POROS=POROS*10.**12
     SUMP=0.
     DO 4 I=1,IP
     RAD(I)=DIA(I)/2.
      VOL(I)=VOL(I)*10.**12
   4 SUMP=SUMP +VOL(I)
     SUMD=0.
     PA=0.
     SN=0.
      SDN=0.
     DO 5 I=1,IP
     VOL(I)=VOL(I)*POROS/SUMP
     ANUM(I)=VOL(I)*DENS/RAD(I)/RAD(I)/3.14159/(1.-FR)
     AM(I)=ANUM(I)*3.14159*((RAD(I)+TM)**2-RAD(I)*RAD(I))
     PA=PA+ANUM(I)*3.14159*RAD(I)*RAD(I)
     SUMD=SUMD+AM(I)
     SN=SN+ANUM(I)
   5 SDN=SDN+ANUM(I)*ALOG(2.*RAD(I))
     DIAV=EXP(SDN/SN)
     UCELL=SQRT(2./SN)
     DIP=UCELL/1.414214
     DMAXP=UCELL/2.-DIAV/2.
     X=1.
     Y=RANGE-THRESH
     RMAX=RANGE
     IF(TM.LT.RMAX)RMAX=TM
     Q=SUMD
     IF(PA+SUMD.GT.1.) Q=1.-PA
     IF(Q.GT.1.) Q=1.
C
C
C  LOOP OVER VARIOUS MOISTURE CONTENTS.
C
C
     DO 60 L=1,13
     SWRN=0.
     SR2N=0.
     DO 6 N=1,IP
```

```
101:       WW=W(L)
102:       IF(WW.GT.RAD(M))WW=RAD(M)
103:       SWRN=SWRN+WW*(2.*RAD(M)-WW)*ANUM(M)
104:     6 SR2N=SR2N+RAD(M)*RAD(M)*ANUM(M)
105:       SAT(L)=SWRN/SR2N
106:       RG2=RANGE*RANGE
107:C
108:C  SUMMATION LOOP OVER PORE SIZES
109:C
110:C
111:       SUMF=0.
112:       DO 50 I=1,IP
113:       WW=W(L)+(RAD(I)-W(L))*RANGE/AR/RAIR
114:       IF(WW.GT.RAD(I))WW=RAD(I)
115:C
116:C
117:C  INTEGRAL LOOP OVER DISTANCE FROM PORE
118:C
119:C
120:       SUMR=0.
121:       DO 40 K=1,KSTEP
122:        R=RAD(I)+FLOAT(K)*RMAX/FLOAT(KSTEP)
123:C
124:C   INTEGRAL LOOP OVER ANGLE THETA
125:C
126:C
127:       SUMT=0.
128:       DO 30 JJ=1,JSTEP + 1
129:       J=JJ-1
130:       T=ACOS((R-RAD(I))/RANGE)/FLOAT(JSTEP)*FLOAT(J)
131:       CT=COS(T)
132:       B=ASIN(RAD(I)/R)
133:       IF(R.LT.SQRT(RG2*CT*CT +RAD(I)*RAD(I)))GOTO 15
134:       B=(R*R-RAD(I)*RAD(I)+RG2*CT*CT)/2./R/RANGE/CT
135:       IF(B.GT.1.) B=1.
136:       B=ACOS(B)
137:    15 CHI=0.
138:       IF(R.GT.(RAD(I)-2.*AR*WW+Y*CT))GOTO 16
139:        C1=2.*Y*(1.-AR)/(2.*AR-1.)
140:       C2=(2.*AR*(RAD(I)*RAD(I)-R*R)+4.*AR*AR*WW*(WW-2.*RAD(I))-Y*Y*CT*CT
141:      C)/(CT*CT*(2.*AR-1.))
142:       C3=(2.*AR*Y*(R*R-RAD(I)*RAD(I)))/CT/CT/(2.*AR-1.)
143:       C4=(3.*C2-C1*C1)/9.
144:       C5=(9.*C1*C2-27.*C3-2.*C1*C1*C1)/54.
145:       XB=C4*C4*C4+C5*C5
146:       IF(XB.LT.0.) GO TO 17
147:       XB=SQRT(XB)
148:        XA1=C5+XB
149:        XA2=C5-XB
150:       ZI=-C1/3.
151:       IF(XA1.NE.0.)ZI=ZI+SIGN(EXP(ALOG(ABS(XA1))/3.),XA1)
```

```
152:      IF(XA2.NE.0.)ZI=ZI+SIGN(EXP(ALOG(ABS(XA2))/3.),XA2)
153:      CHI=(R*R-RAD(I)*RAD(I)+ZI*ZI*CT*CT)/2./R/ZI/CT
154:      IF(CHI.GT.1.) GO TO 17
155:      CHI=ACOS(CHI)
156:      IF(CHI.LT.ASIN((RAD(I)-WW)/R)) GOTO16
157:      A1=-2.*Y/(1.-AR*AR)
158:      A2=(Y*Y*CT*CT+2.*AR*AR*(R*R-RAD(I)*RAD(I)))/CT/CT/(1.-AR*AR)
159:      A4=-AR*AR*(R*R-RAD(I)*RAD(I))**2/CT/CT/CT/CT/(1.-AR*AR)
160:      A5=(-12.*A4-A2*A2)/9.
161:      A6=(36.*A2*A4-27.*A4*(4.*A2-A1*A1)+2.*A2*A2*A2)/54.
162:      A7=ACOS(A6/SQRT(-A5*A5*A5))
163:      A8=2.*SQRT(-A5)*COS(A7/3.)+A2/3.
164:      A9=SQRT(A1*A1/4.-A2+A8)
165:      A10=SQRT(3.*A1*A1/4.-A9*A9-2.*A2+(4.*A1*A2-A1*A1*A1)/4./A9)
166:      ZII=-A1/4.+A9/2.-A10/2.
167:      CHI=(R*R-RAD(I)*RAD(I)+ZII*ZII*CT*CT)/2./R/ZII/CT
168:      IF(CHI.GT.1.)GO TO 17
169:      CHI=ACOS(CHI)
170:      GO TO 16
171:   17 CHI=ASIN(RAD(I)/R)
172:   16 CONTINUE
173:   30 IF((B-CHI).GT.0.) SUMT=SUMT+B-CHI
174:      SUMT=SUMT/FLOAT(JSTEP+1)
175:   40 SUMR=SUMR+R*SUMT
176:      SUMR=SUMR/FLOAT(KSTEP)
177:   50 SUMF=SUMF+SUMR*ANUM(I)*((RAD(I)+RMAX)**2-RAD(I)*RAD(I))
178:      E(L)=SUMF*4./Q
179:      WRITE(6,119)SAT(L),E(L)
180:   60 CONTINUE
181:C
182:C
183:C   PRINTOUT OF RESULTS
184:C
185:C
186:      WRITE(6,106) (SAMPLE(I),I=1,10)
187:  106 FORMAT(///,1X,10A4,//)
188:      POROS=POROS/10.**12
189:      DENS=DENS*10.**12
190:       SN=SN*10.**8
191:      WRANGE=RANGE/AR
192:      WRITE(6,107) POROS
193:  107 FORMAT(6X,'TOTAL POROSITY=',F8.4,' CUBIC CENTIMETERS PER GRAM.')
194:      WRITE(6,108)DENS
195:  108 FORMAT(6X,'SAMPLE DENSITY=',F8.4,' GRAMS PER CUBIC CENTIMETER.')
196:      WRITE(6,109)RANGE
197:  109 FORMAT(5X,'RN RECOIL RANGE=',F8.4,' MICROMETERS IN ROCK.')
198:      WRITE(6,111)WRANGE
199:  111 FORMAT(5X,'RN RECOIL RANGE=',F8.4,' MICROMETERS IN WATER.')
200:      WRITE(6,110)THRESH
201:  110 FORMAT(2X,'THRESH.EQUIV.RANGE=',F8.4,' MICROMETERS FOR ROCK IMPACT
202:     CION.')
```

```
203:      WRITE (6,112)TM
204:  112 FORMAT(3X,'MINERAL THICKNESS=',F8.4,' MICROMETERS')
205:      WRITE(6,122) Q
206:  122 FORMAT(2X,'MINERAL/CEMENT FR.=',F8.4,' CM3/CM3')
207:      WRITE(6,126)RAIR
208:  126 FORMAT(5X,'RN RECOIL RANGE=',F8.4,' MICROMETERS IN AIR.')
209:      WRITE(6,124)FR
210:  124 FORMAT(1X,'INERT ROCK FRACTION=',F8.4)
211:      WRITE (6,113) DIAV
212:  113 FORMAT(2X,'MEAN PORE DIAMETER=',F8.4,' MICROMETERS (NUMBER WEIGHTE
213:     CD)')
214:      WRITE(6,114)UCELL
215:  114 FORMAT(1X,'UNIT CELL DIMENSION=',F8.4,' MICROMETERS (ON A SIDE)')
216:      WRITE(6,115)DIP
217:  115 FORMAT(1X,'AVG.INTERPORE DIST.=',F8.4,' MICROMETERS MINIMUM BETWEE
218:     CN CENTERS')
219:      WRITE(6,116)DMAXP
220:  116 FORMAT(3X,'MAXIMUM ROCK PATH=',F8.4,' MICROMETERS TO AVERAGE PORE'
221:     C)
222:      WRITE(6,123)SN
223:  123 FORMAT(8X,'PORE DENSITY=',F13.0,' PORES/SQUARE CENTIMETER')
224:      WRITE(6,117) JSTEP+1,KSTEP
225:  117 FORMAT (1X,'NUMERICAL INTEGRATION INCREMENTS=',I3,' FOR THETA AND'
226:     C,I3,' FOR R',//)
227:      WRITE(6,118)
228:  118 FORMAT(1X,'SATURATION  WATER FILM (UM)  EMANATION',/,1X,
229:     C'----------  ---------------  ---------')
230:      WRITE(6,119)(SAT(I),W(I),E(I),I=1,13)
231:  119 FORMAT(3X,F6.4,8X,F7.4,6X,F9.5)
232:      WRITE(6,120)
233:  120 FORMAT(1X,////,1X,'PORE DIAM.(UM)  PORES/CM**2  CM**3/GRAM',2X,
234:     C'MINERAL',/,1X,'--------------  ----------  ----------  -------')
235:       DO 71 I=1,IP
236:        ANUM(I)=ANUM(I)*10.**8
237:   71 VOL(I)=VOL(I)/10.**12
238:      WRITE (6,121)(DIA(I),ANUM(I),VOL(I),AM(I),I=1,IP)
239:  121 FORMAT(4X,F8.4,3X,F13.0,3X,F7.4,2X,F9.6)
240:      GOTO 99
241:  999 STOP
242:      END
```